UNIVERSITY OF SOUTHAMPTON

Faculty of Engineering and Physical Sciences
Department of Mechanical Engineering
Bioengineering Science Research Group

Additively Manufactured Porous Metamaterials: An Investigation of Mechanical Behaviour and the Effects of Geometry Variations within Uniform and Stochastic Lattices

by

Maria Stagno Navarra
ORCiD: 0009-0000-0816-7356

A thesis for the degree of
Doctor of Philosophy

June 2025

University of Southampton

Abstract

Faculty of Engineering and Physical Sciences
Department of Mechanical Engineering

Doctor of Philosophy

Additively Manufactured Porous Metamaterials: An Investigation of Mechanical Behaviour and the Effects of Geometry Variations within Uniform and Stochastic Lattices

by Maria Stagno Navarra

Natural porous materials have evolved over millennia to optimise lightweight mechanical performance, including properties such as stiffness, strength and energy absorption at low density. As a result, these natural materials occupy a large range of material property space, enabling properties to be efficiently matched to performance requirements. As manufacturing techniques have developed, the property space occupied by synthetic materials has expanded accordingly, but often without the combined performance and efficiency of natural materials. Advances in additive manufacturing (AM) have enabled the synthetic material property space to be expanded further by enabling porous materials with variations in relative density, pore shapes and spatial distribution to achieve tailored mechanical properties.

Synthetic structures consist of assemblies of repeated unit cells. Analytical models based on axial (stretching-dominated) or bend (bending-dominated) modes of loading for different unit cells can predict the mechanical response of uniform (regular) lattice structures, but these models break down with increasing relative density as they are based on slender beam assumptions that become invalid, and are also not applicable to non-uniform (spatially varying) lattices. A large region of the accessible material property space is therefore not described by these analytical models. Additionally, an often under-reported feature of additively manufactured porous materials is the presence of distortion due to residual stress, which can alter their boundary conditions and consequently their apparent properties. This project aimed to further our understanding of how relative density, geometry, and distortion affect the behaviour of additively manufactured lattice structures by characterising the geometries, and mechanical behaviour of both uniform and non-uniform bending- and stretching-dominated lattices over a range of relative densities.

Lattice specimens were manufactured using stereolithography AM of a commercial glass-reinforced thermosetting resin with a high base elastic modulus but low strain to failure. Height distortions were observed in all types of lattices but decreased with relative density and for non-uniform structures. An adapted version of Winkler's elastic foundation model determined that a typical distortion of 100 μm reduced the initial apparent elastic modulus by approximately 50%, with greater distortions reducing this further. The as-built density was greater than as-designed for all lattice geometries, and analytical models from literature were empirically adjusted to account for the increase in strut diameters observed. Other analytical models from literature that described the relationships between relative density and mechanical properties for uniform lattice structures were validated over a wide relative density range (15 to 70% depending on geometry type), with improvements suggested using empirical fits. These revealed that the apparent elastic modulus relationship was similar to natural materials such as wood and bone. For all uniform lattices, relative density increased the apparent elastic modulus, maximum stress and energy absorption. Further increases for non-uniform geometries were observed for the apparent elastic modulus and maximum stress, thought to be due to the accumulation of excess material at the joints between dissimilar adjacent cells. The failure strains for all geometries were at least double that of the base material with trends dependent upon the geometry of the unit cells. They increased with relative density for uniform stretching-dominated lattices, but decreased for uniform bending-dominated geometries. Non-uniform structures had similar or reduced levels of energy absorption and failure strains to uniform structures, with the lower-density unit cells often resulting in catastrophic failure at lower strain.

Both the uniform and non-uniform lattices produced in this project added to the material property space in regions that overlap with cancellous bone, an example of an evolutionary optimised natural porous material. The methodologies developed in this project provide a good basis for designing and characterising further non-uniform lattice geometries to continue expanding this space.

Contents

List of Figures ix

List of Tables xix

List of Additional Material xxi

Declaration of Authorship xxiii

Acknowledgements xxv

List of Abbreviations xxvii

List of Notation xxix

1 Introduction 1
- 1.1 Aims and Objectives 2
  - 1.1.1 Novel Contributions 2
- 1.2 Thesis Structure 3

2 Background 5
- 2.1 Introduction 5
- 2.2 Porous Metamaterials 5
  - 2.2.1 Unit Cell Geometries 12
  - 2.2.2 Joining Unit Cells 15
  - 2.2.3 Non-Uniform Porous Metamaterials 16
- 2.3 Additive Manufacturing 18
- 2.4 Conclusion 33

3 Additively Manufactured Porous Metamaterials and the Mechanical Effects of Distortion 35
- 3.1 Abstract 35
- 3.2 Introduction 36
- 3.3 Methodology 36
  - 3.3.1 Porous Metamaterial Fabrication 36
  - 3.3.2 Mechanical Testing and Geometry Characterisation 38
  - 3.3.3 Winkler′s Elastic Foundation Model 40
- 3.4 Results and Discussion 43
  - 3.4.1 Endplate Distortions 43
  - 3.4.2 Post-Processing Variations 47
- 3.5 Conclusions 51

4 Effects of Relative Density on Distortion and Apparent Compressive Properties of Uniform Lattice Metamaterials 53
4.1 Abstract 53
4.2 Introduction 54
4.3 Methodology 54
4.3.1 Porous Metamaterial Fabrication 54
4.3.2 Mechanical Testing 58
4.3.3 Geometry Characterisation 59
4.4 Results and Discussion 62
4.4.1 Geometry Characterisation 62
4.4.1.1 Determination of Relative Density 62
4.4.1.2 As-designed versus As-built 65
4.4.2 Endplate Distortions 66
4.4.3 Elastic Behaviour 69
4.4.4 Failure Behaviour 76
4.5 Conclusions 81

5 Distortion and Apparent Compressive Properties of Graded and Stochastic Lattice Metamaterials 83
5.1 Abstract 83
5.2 Introduction 84
5.3 Methodology 84
5.3.1 Porous Metamaterial Fabrication 84
5.3.1.1 Graded Lattices 86
5.3.1.2 Stochastic Lattices 88
5.3.2 Mechanical Testing 91
5.3.3 Geometrical Characterisation 92
5.4 Results and Discussion 92
5.4.1 Geometry Characterisation 92
5.4.2 Endplate Distortions 95
5.4.3 Elastic Behaviour 97
5.4.4 Failure Behaviour 101
5.5 Conclusion 112

6 Conclusions and Future Work 115
6.1 Conclusions 115
6.2 Future Work 120

References 123

7 Appendix A 145
7.1 Post-processing Variation 145
7.2 MatchID Noise Study 147
7.3 Integration of Elastic Foundation Model for Dome with Peak in the Centre 148
7.4 Integration of Elastic Foundation Model for Dome with Peak in the Corner 151
7.5 Method for accounting for the ′toe-in′ region adapted from NPL′s 'Measurement Good Practice Guide No. 98: Elastic Modulus Measurement' [129] 152

8 Appendix B **159**
8.1 Analysing Height Distortions 159
8.2 Applying the Compliance Correction 162

9 Appendix C **163**
9.1 Using Voronoi Cells to Create Stochastic Lattices 163

10 Appendix D **169**

List of Figures

2.1 Evolution of the material property space adapted from [3] 6
2.2 Rods and plates seen in cancellous bone, from [23] 8
2.3 Cubic unit cell for open-celled foams [28]. t is the strut thickness and l is the strut length 9
2.4 A periodic, square 2D lattice with a dashed box highlighting a joint where four edges meet (nodal connectivity is 4). Image taken from [3] . 10
2.5 3 types of 2D frames as defined by Maxwell's criterion Eq. 2.2.3. a) M <0, mechanism and bending-dominated, b) M = 0, fully defined and stretching-dominated, c) M >0, over-defined and stretching-dominated [30] 11
2.6 a) BCC and b) BCCz unit cell geometries. 14
2.7 a) Diamond, b) FCCm and c) Octet unit cell geometries. 14
2.8 Rhombic Dodecahedron (RD) Cell 15
2.9 a) visual representative varying levels of disorder as defined by Aranguren *et al.* [1], [2] and b) corresponding measured cell areas of 1000 Voronoi cells. Figure adapted from Aranguren *et al.*, [1] 16
2.10 Examples of using Voronoi structures to represent a natural porous material with the yellow dots indicating the centroids of Voronoi cells and blue lines as the Voronoi cell walls. Variation of measured disorder for a range of porous materials is also shown with N equal to the number of images analysed. Figure adapted from Aranguren *et al.*, [1]. . 17
2.11 Impact of disorder (δ) on normalised a) apparent elastic modulus, b) maximum stress and c) energy absorption. Figure adapted from Aranguren *et al.*, [1]. 18
2.12 Labelled diagram of the FFF process, figure taken from [60] 19
2.13 Labelled diagram of the SLS process, figure taken [63] 20
2.14 Labelled diagram of the Polyjet process, figure taken from [64] 20
2.15 Labelled diagram of the SLA process, figure taken from [68] 21
2.16 Examples of defects from L-PBF parts: a) warping observed in an overhang, taken from [76], b) increased waviness and roughness observed in horizontal struts, taken from [86], c) internal porosities observed using micro CT, taken from [89], d) variation of normalised apparent elastic modulus as a function of strut waviness and strut diameter variation, taken from [88], e) variation of surface roughness on struts as a build direction (0° is horizontal) and strut diameter, taken from [87] and f) examples of strut waviness and strut diameter variation, taken from [85]. 23

2.17 Examples of defects from SLA parts: a) warping observed for fully supported overhangs, taken from [81], b) influence of build direction on geometrical accuracy of various shapes including cylinders and spheres, taken from [93], c) types of pore based defects caused by excess resin observed with micro CT, taken from [95]. 24
2.18 Polymerisation reaction of microdroplet-jet printing, a vat photopolymerisation technique showing thermal reactions that lead to residual stresses and warping. Figure taken from [106]. 26
2.19 Variation of porosity with inclination and position for the up (zone A) and down-skin (zone B) portions of struts. Figure taken from [72] and [109]. 27
2.20 a) Representation of stair-stepping, seen in all forms of additive manufacture, figure taken from [110]. b) Example of balling in L-PBF manufacture, figure taken from [112]. c) Evidence of loose powder on parts, figure taken from [110]. d) increase surface roughness and dross on the down-skin, e) compared to the uk-skin, figure taken from [110]. . 29
2.21 Variation of eccentricity with inclination angle and strut diameter, from [87]. 31
2.22 Figure adapted from [117]. a) High friction at contact surfaces causes barrelling in the sample, b) misalignment between platens and sample causes non-uniform loading and c) localised crushing/failure of the sample 33

3.1 BCCz lattice where vertical struts are aligned with the build direction and endplates protect the top and bottom struts. Dots marked on the front back for optical strain measurement with a maximum virtual gauge length of 20 mm. Enlarged view of single BCCz unit cell shown. . 37
3.2 Strut diameter measurement example for vertical and angled struts . . . 39
3.3 a) Elastic foundation model assumed geometry. b) Elastic foundation geometry adapted for the height distortion in the lattices with the peak of the dome in the centre. c) Elastic foundation geometry adapted for the height distortions in the lattices with the peak of the dome at the corner of the sample. P is applied force, x is the displacement of the indenter as a result of force P, a is the semi-major axis of the indenter at displacement x, h is the thickness of elastic material, d_h is the maximum height distortion of the dome and w is the width, depth, and height of the cube. 41
3.4 Typical height distortion of top endplate, showing an off-centred dome-like pattern. Maximum height distortion for this example is 450 μm. 43
3.5 a) Representative stress-strain plots for both unadhered (dashed lines) and adhered (solid lines) PP2 samples up to maximum load and b) up to 0.5% strain. Representative local strain results are shown in c) and the result of the increased spread in local strain is reflected by d) the local apparent elastic modulus. Average and standard deviation (SD) of all adhered (red) and unadhered (blue) samples are 339.4 MPa and 49.3 MPa and 393.6 MPa and 104.7 respectively. 44

3.6 Representative compressive force-displacement of adhered (green) and unadhered (red) samples with adapted Winkler's model prediction shown, which is valid until the displacement equals the maximum height distortion (d, black dashed line). Also shown (purple) is the range of physiological strains for bone growth on tissue scaffolds. 46
3.7 a) Average apparent elastic modulus (n = 6) with error bars noting one standard deviation for PP1 and PP2 post-processing procedures. As-designed and as-built moduli predictions are from the geometry specific analytical model (Eq. 2.2.10) from Zhang *et al.* [40]. b) Variation in strut diameter as a function of strut type and post-processing procedure, compared with a designed diameter of 0.46 mm. 47
3.8 Stair-stepping diagram for angled struts 48
3.9 Inter-strut variation of base material elastic modulus measured using nano-indentation as a function of a) post-processing procedure (PP1 or PP2), location on either the inside (In) or outside (Out) of the lattice and sample number (1 or 2), and also as a function of b) post-processing procedure 49

4.1 a) BCCz and b) BCC, lattice geometries with endplates to protect the top and bottom struts and dots marked on the front back for optical strain measurement with a maximum virtual gauge length of 20 mm. Enlarged view of single BCCz and BCC unit cells shown. Vertical struts in the BCCz lattice are aligned with the build direction. 56
4.2 Representative stress-strain plot of a) bending-dominated and b) stretching-dominated lattices showing similar shapes of results from optical strain measurements (solid), uncorrected platen strain measurements (dotted) and corrected platen measurements (dashed). . . 60
4.3 Labelled diagram of lattice prepared for manufacture during slicing, highlighting the endplates, support material and raft. 60
4.4 Minimum height distortion positions on endplate overlaid on example height distortion map with front and left sides of the printer. Scanning direction is back to front and left to right. 61
4.5 Plot showing the two methods of calculating relative density for both BCC (blue) and BCCz (orange) geometries over a wide relative density range. 63
4.6 Variation of the coefficient of variation of average strut diameter for BCC (blue) and BCCz (orange) geometries at varying relative densities for both angled (circle) and vertical (square) struts. The coefficient of variation is the ratio between the standard deviation and the average strut diameter, as a percentage. 64
4.7 Comparison between as-designed and as-built relative density for bending- (BCC, blue) and stretching-dominated (BCCz, orange) lattices. As-built relative density is calculated based on adjusted volume and mass measurements. The ideal trend (dashed black line) is for as-designed matched as-built. First-order fits performed to as-designed versus as-built data to correct relative density in future designs. Shaded regions indicate the range of data (maximum to minimum). 66

4.8 Average height distortion on top endplate for BCC (blue) and BCCz (orange) lattices as a function of relative density a) before and b) after secondary cure phase during post-processing. Shaded regions indicate the range of data (maximum to minimum). Representative height distortion plots before the secondary cure phase and the corresponding height distortion plots after the secondary cure phase are shown. Colour bars scaled to the maximum height distortion observed across all plots (BCC, after the secondary cure phase). 67
4.9 Position of minimum height distortion on endplate after the secondary cure phase for BCC (blue) and BCCz (orange) lattices. Position is in accordance with Fig. 4.4. 68
4.10 Effect of distortion on the apparent elastic modulus of a porous metamaterial determined within the physiological strain range that encourages bone growth for bone scaffolds, 0.15 - 0.3% strain. a) Apparent elastic modulus is given as a normalised percentage of the target apparent elastic modulus and calculated based on the adapted elastic foundation model using Eq. 3.3.2. b) shows effects of distortion for target apparent elastic modulus of 1000 MPa as behaviour is independent of the target elastic modulus. 69
4.11 Representative stress-strain curve of virtual extensometers with height distortion map of the sample after the secondary cure phase, a) full curve and b) zoomed-in section to 0.2% strain, the range over which the apparent elastic modulus is determined. Solid lines are virtual extensometers from the front face and dotted lines are virtual extensometers from the back face. The coordinate system is looking at the sample from the front face i.e. the front left (FL) and back left (BL) extensometers are on the same side of the sample. 70
4.12 Example stress-strain curve of a virtual extensometer for a sample that was excluded from summarised data with linear fit for apparent elastic modulus shown (red line). 71
4.13 Stress-strain curve of virtual extensometers for sample that was excluded from summarised data, a) full curve and b) zoomed-in section to 0.2% strain. Solid lines are virtual extensometers from the front face and dotted lines are virtual extensometers from the back face. The coordinate system is looking at the sample from the front face i.e. the front left (FL) and back left (BL) extensometers are on the same side of the sample. 71
4.14 As-designed versus as-built apparent elastic modulus for both BCC (blue) and BCCz (orange) lattices over a range of relative densities. As-designed apparent elastic modulus is calculated using Eq. 4.4.3 and Eq. 4.3.3 for BCC and BCCz geometries respectively. 72
4.15 As-built relative density versus as-built apparent elastic modulus for both BCC (blue) and BCCz (orange) lattices over a range of relative densities with range (shaded regions) and analytical models for BCC (blue dotted) and BCCz (orange dotted). a) full plot and b) zoomed-in plot over the range of as-built results. 73

4.16 As-built relative density versus as-built apparent elastic modulus for both BCC (blue) and BCCz (orange) lattices over a range of relative densities with range (shaded regions). Ashby-Gibson equations (Eq. 4.4.4), fitted for C and n for 2 regions, for relative densities less than 30% and greater than 30% for both the BCC (blue line) and BCCz geometries (orange line). 74
4.17 Log-log plot of as-built relative density versus as-built apparent elastic modulus for both BCC (blue) and BCCz (orange) lattices over a range of relative densities with range (shaded regions). Log-log equation 4.17 fitted for n (similar to Eq. 4.4.4) and c (intercept) for 2 regions, for relative densities less than 30% and greater than 30% for both the BCC (blue line) and BCCz geometries (orange line). 75
4.18 Representative image for the failure of a) bending-dominated lattices with the shear band highlighted in blue and representative image for the failure of stretching-dominated lattices with b) the initial point of failure and c) the shear band highlighted in orange. 76
4.19 As-built relative density versus strain at sample failure for both BCC (blue) and BCCz (orange) uniform lattices over a range of relative densities. BCCz samples at the highest designed relative density did not fail completely during the test so are not shown here. Range (maximum to minimum) of results are shown with shaded regions. . . . 77
4.20 As-built relative density versus maximum stress for both BCC (blue) and BCCz (orange) uniform lattices over a range of relative densities. Range (maximum to minimum) results are shown with shaded regions. Trends with relative density for average results are shown by the solid lines. 78
4.21 As-built relative density versus coefficient of variation for the maximum stress for both BCC (blue) and BCCz (orange) uniform lattices over a range of relative densities. 79
4.22 As-built relative density versus energy absorbed to sample failure for both BCC (blue) and BCCz (orange) uniform lattices over a range of relative densities. BCCz samples at the highest designed relative density did not fail completely during the test so are not shown here. Range (maximum to minimum) results are shown with shaded regions. Trends with relative density for average results are shown by the solid lines. 80
4.23 As-built relative density versus coefficient of variation for energy absorbed to sample failure for both BCC (blue) and BCCz (orange) uniform lattices over a range of relative densities. BCCz samples at the highest designed relative density did not fail completely during the test so are not shown here. 80

5.1 Graded a) & c) bending-dominated, BCC and b) & d) stretching-dominated, BCCz lattices where vertical struts are aligned with the build direction. H and L indicate the highest and lowest relative density from the relative density range with arrows indicating the variation along the page (X- direction). Blue and orange circles indicate the direction of relative density gradient into the page (Y- direction). Endplates protect the top and bottom struts. Dots marked on the front and back for optical strain measurement with a maximum virtual gauge length of 20 mm. c) and d) are examples of samples prior to testing. 87
5.2 Relative density variation in a) X- and b) Y- direction within a layer for a bending-dominated sample. H and L indicate the highest and lowest relative density from the relative density range, with arrows indicating the direction of variation. The same pattern of variation is also implemented in the stretching-dominated samples. 88
5.3 Example variation of average strut diameter across two layers for a lattice with a) the relative density varying in the X- and Y- direction in alternating layers and b) the relative density varying in both the X- and Y- directions within each layer. 88
5.4 Example of variation of stochastic a) bending-dominated, BCC and b) stretching-dominated, BCCz lattice with $\delta = 0.4$. The colour bar indicates the relative density of the individual unit cells, with the maximum of the range as red and the minimum as blue. 90
5.5 Mixed stochastic lattice built up from both bending- (BCC) and stretching-dominated (BCCz) unit cells with varying relative densities. High relative density cells (> 0.34) are BCCz and lower relative density cells ($=< 0.34$) are set to BCC. $\delta = 0.8$. 91
5.6 Comparison between as-designed and as-built relative density for graded (circle) and stochastic (square and diamond) bending- (BCC, blue) and stretching-dominated (BCCz, orange) lattices. The mixed stochastic lattice is given by the red star. Shaded regions indicate the range of data (maximum to minimum). First-order trend lines of the BCC (blue) and BCCz (orange) lattices derived in the previous investigation (Chapter 4) are shown for comparison. 93
5.7 Excess material between neighbouring cells in stochastic BCC (b) and BCCz (d) lattices. Uniform lattices (a and c) at the same approximate as-built relative density are shown for comparison. Stochastic lattice with $\delta = 0.8$ shown. 94
5.8 Average height distortion on the top endplate for graded (circle) and stochastic (square and diamond) BCC (blue) and BCCz (orange) lattices a) before and b) after the secondary cure phase. Data for a mixed stochastic lattice is also shown (red star). The shaded area indicates the range of average height distortion. Representative height distortion plots before the secondary cure phase and the corresponding height distortion plots after the secondary cure phase are shown. Colour bars scaled to the maximum height distortion observed across all plots (BCCz, after the secondary cure phase). 95

5.9 Average height distortion on the top endplate for graded (circle) and stochastic (square and diamond) BCC (blue) and BCCz (orange) lattices a) before and b) after the secondary cure phase. Data for a mixed stochastic lattice is also shown (red star) compared to results from uniform lattices in Chapter 4. The shaded area indicates the range of average height distortion, for both the uniform and non-uniform lattices. 96
5.10 As-built relative density versus as-built apparent elastic modulus for graded (circle) and stochastic (square and diamond) BCC (blue) and BCCz (orange) lattices, compared to results from uniform lattices from previous investigation (Chapter 4) including range. Data for a mixed stochastic lattice is also shown (red star). Shaded areas/bars indicate the range of apparent elastic modulus, for both the uniform and non-uniform lattices. The mixed stochastic lattice (red star) had a very small range of 885 to 871 MPa, so the range bar is not observable on the plot. 97
5.11 As-built relative density versus normalised as-built apparent elastic modulus for graded (circle) and stochastic (square, δ = 0.4 and diamond, δ = 0.8) BCC (blue) and BCCz (orange) lattices, compared to results from uniform lattices from previous investigation (Chapter 4). Plots for both the uniform and non-uniform lattices were normalised by trend lines developed for the uniform lattices in the previous investigation (Chapter 4), with Eq. 5.4.1, Eq. 5.4.2, Eq. 5.4.3 and Eq. 5.4.4, to account for any changes due to relative density. Data for a mixed stochastic lattice is also shown (red star), normalised by the trend for uniform stretching-dominated (BCCz) lattices. Shaded areas/bars indicate the range of normalised apparent elastic modulus, for both the uniform and non-uniform lattices. The mixed stochastic lattice (red star) had a very small range of 1.10 to 1.08, so the range bar is not observable on the plot. 99
5.12 Representative image for the failure of a) bending-dominated lattices with the shear band highlighted in blue, representative image for the failure of stretching-dominated lattices with b) the initial point of failure and c) the shear band highlighted in orange, representative image for the failure of stochastic mixed (bending- and stretching-dominated) lattices with the d) initial random points of failure, e) bottom layer failure and f) the shear band highlighted in red. 102
5.13 As-built relative density versus strain at sample failure for graded (circle) and stochastic (square and diamond) BCC (blue) and BCCz (orange) lattices, compared to results from uniform lattices from previous investigation (Chapter 4). Data for a mixed stochastic lattice is also shown (red star). The shaded areas/bars indicate the range of failure strain, for both the uniform and non-uniform lattices. 103
5.14 Variation of failure strain with δ for the stochastic lattices in this investigation (blue and orange) and the 2D Voronoi based lattices investigated by Aranguren *et al.* (green), Results are taken from [2] with error bars determined from 12 repeats for levels of δ and 24 repeats when δ = 0.8 and 1.0. 104

5.15 Stress-strain curves produced from corrected platen data for uniform a) bending- and c) stretching-dominated lattices non-uniform b) bending- and d) stretching-dominated lattices. A mixed stochastic lattice is shown on both plots for the non-uniform lattices (b and d). 104
5.16 Stress strain curve for highly disordered stochastic stretching-dominated lattice 105
5.17 As-built relative density versus maximum stress for graded (circle) and stochastic (square and diamond) BCC (blue) and BCCz (orange) lattices, compared to results from uniform lattices from the previous investigation (Chapter 4). Data for a mixed stochastic lattice is also shown (red star). Shaded areas/bars indicate the range of maximum stress, for both the uniform and non-uniform lattices. The mixed stochastic lattice (red star), graded (circle) and highly ordered stochastic (diamond, $\delta = 0.8$) BCC lattices all had small ranges, so the range bar is not observable on the plot. 107
5.18 As-built relative density versus normalised maximum stress for graded (circle) and stochastic (square and diamond) BCC (blue) and BCCz (orange) lattices, compared to results from uniform lattices from previous investigation (Chapter 4). Data for a mixed stochastic lattice is also shown (red star). Plots for both the uniform and non-uniform lattices were normalised by trend lines developed for the uniform lattices in the previous investigation (Chapter 4), with Eq. 5.4.5 and Eq. 5.4.6), to account for any changes due to relative density. Data for a mixed stochastic lattice is also shown (red star), normalised by the trend for uniform stretching-dominated (BCCz) lattices. Shaded areas/bars indicate the range of normalised maximum stress, for both the uniform and non-uniform lattices. 108
5.19 As-built relative density versus energy absorbed to sample failure for graded (circle) and stochastic (square and diamond) BCC (blue) and BCCz (orange) lattices, compared to results from uniform lattices from previous investigation (Chapter 4). Data for a mixed stochastic lattice is also shown (red star). Shaded areas/bars indicate the range of energy absorbed, for both the uniform and non-uniform lattices. The non-uniform bending-dominated lattices (BCC) and graded stretching-dominated lattices (BCCz) all had small ranges, so the range bar is not observable on the plot. 110
5.20 As-built relative density versus normalised energy absorbed to sample failure for graded (circle) and stochastic (square and diamond) BCC (blue) and BCCz (orange) lattices, compared to results from uniform lattices from previous investigation (Chapter 4). Data for a mixed stochastic lattice is also shown (red star). Plots for both the uniform and non-uniform lattices were normalised by trend lines developed for the uniform lattices in the previous investigation (Chapter 4), with Eq. 5.4.7 and Eq. 5.4.8), to account for any changes due to relative density. Data for a mixed stochastic lattice is also shown (red star), normalised by the trend for uniform stretching-dominated (BCCz) lattices. Shaded areas/bars indicate the range of normalised energy absorbed, for both the uniform and non-uniform lattices. 111

6.1 Ashby map of relative density versus apparent elastic modulus for common natural and synthetic porous materials produced with Granta Selector [170] along with the data for both uniform and non-uniform lattices investigated in this study. A limited number of natural porous materials are shown as there is limited relative density data for them on Granta Selector [170]. The light and dark green, and bright blue shaded regions indicate general property spaces of foams, natural materials and cancellous bone respectively. The smaller bubbles within the shaded regions show the range of properties for more specific materials, examples of which are shown on the plot. Graded (circle) and stochastic (square and diamond) BCC (blue) and BCCz (orange) lattices, compared to results from uniform lattices (shaded regions and lines). Data for a mixed stochastic lattice is also shown (red star). 116

7.1 Variation in apparent elastic modulus for six different post-processing methods calculated using both optical strain measurements and cross-head displacement. 146
7.2 Variation in strain across an unloaded sample with varying subset size. . 148
7.3 151

List of Tables

2.2.1 Summary of equations that describe the behaviour of bending- and stretching-dominated structures [15], [28], [30], [31]. 12
2.3.1 AM process comparison. Note that Z is the build direction, and XY is the plane of layered material deposition. Green blue and red shading indicates better, equal, and worse performance compared to SLA. 21

3.4.1 Summary of average and standard deviation of vertical and angled strut diameters for PP1 and PP2 samples 50
3.4.2 Summary of variations in strut diameters for PP1 and PP2 samples and how that impacts the variation in elastic modulus calculated using Eq. 2.2.10 50

4.3.1 Summary of designed and predicted parameters for BCCz lattice geometries. The relative density is predicted using Eq. 4.3.1 and apparent elastic modulus is predicted using the geometric specific analytical model, Eq. 4.3.3 56
4.3.2 Summary of designed and predicted parameters for BCC lattice geometries. The relative density is predicted using Eq. 4.3.2 and apparent elastic modulus is predicted using the geometric specific analytical model, Eq. 4.3.4 57
4.4.1 Summary of powers R^2 for bending- and stretching-dominated uniform lattices fitted to Ashby-Gibson relationship for relative density and apparent elastic modulus over two relative density ranges. 74
4.4.2 Summary of powers R^2 for bending- and stretching-dominated uniform lattices fitted to logarithmic Ashby-Gibson relationship for relative density and apparent elastic modulus over two relative density ranges. 76
4.4.3 Summary of powers R^2 for bending- and stretching-dominated uniform lattices fitted to Ashby-Gibson relationship for relative density and maximum stress over two relative density ranges. 78

5.3.1 Summary of Design Parameters for Graded and Stochastic Lattices. Relative density was based on the as-built relative density of uniform lattices, observed in Chapter 4. 85

7.1.1 Post-processing conditions trialled in phase one with key differences being highlighted with boxes. UB – ultrasonic bath. 145
7.2.1 Subset and step size variation for noise study. Subsets were chosen in increments of 100 pixels with 245 pixels chosen to try and improve upon 199 and 299 pixels. 147

List of Additional Material

Dataset: https://doi.org/10.5258/SOTON/D3519

Declaration of Authorship

I declare that this thesis and the work presented in it is my own and has been generated by me as the result of my own original research.

I confirm that:

1. This work was done wholly or mainly while in candidature for a research degree at this University;
2. Where any part of this thesis has previously been submitted for a degree or any other qualification at this University or any other institution, this has been clearly stated;
3. Where I have consulted the published work of others, this is always clearly attributed;
4. Where I have quoted from the work of others, the source is always given. With the exception of such quotations, this thesis is entirely my own work;
5. I have acknowledged all main sources of help;
6. Where the thesis is based on work done by myself jointly with others, I have made clear exactly what was done by others and what I have contributed myself;
7. None of this work has been published before submission

Signed:... Date:..................

Acknowledgements

I would first like to thank my supervisors, Professor Martin Browne and Doctors Andrew Hamilton and Charles Burson-Thomas, for their support, advice and feedback, and without whom this PhD would not have been possible.

I’d also like to thank all my friends and family for supporting me throughout the PhD and listening to my frequent ramblings about the project.

List of Abbreviations

AM	Additive Manufacturing
BCC	Body Centered Cubic
BCCz	Body Centered Cubic with z strut
FCC	Face Centered Cubic
FCCm	modified Face Centered Cubic
RD	Rhombic Dodecahedron
FFF	Fused Filament Fabrication
SLS	Selective Laser Sintering
SLA	Stereolithography
L-PBF	Laser-powder bed fusion
UV	Ultraviolet
IPA	Isopropyl Alcohol
FE	Finite Element
PP1	Post-Process 1
PP2	Post-Process 2
CT	Computed Tomography
DVC	Digital Volume Correlation

List of Notation

In order of appearance

ρ_s	Density of the solid material (material density)
ρ^*	Density of the porous structure (apparent density)
E^*	Elastic modulus of porous solid (apparent elastic modulus)
G^*	Shear modulus of porous solid (apparent shear modulus)
ν^*	Poisson's ratio of porous solid (apparent Poisson's ratio)
E_s	Elastic modulus of solid material (material elastic modulus)
C	Constant based on geometry (used in Ashby and Gibson equations)
n	Index related to structure type and loading/failure model (used in Ashby and Gibson equations)
M	Maxwell's criterion
b	Number of struts
j	Number of joints
s	Number of self stress states
m	Number of mechanisms
σ^*_{el}	Buckling elastic collapse stress of porous solid (apparent buckling collapse stress)
σ^*_{pl}	Plastic collapse strength of porous solid (apparent plastic collapse strength)
$\sigma_{y,s}$	Yield strength of solid material (material yield strength)
σ^*_{cr}	Brittle collapse stress of porous solid (apparent brittle collapse stress)
σ_{fs}	Modulus of rupture of solid material (material modulus of rupture)
E^*_z	Apparent elastic modulus of lattice for loading parallel to the build direction
d_{ang}	Diameter of angled struts
L	Overall unit cell size
d_{vert}	Diameter of vertical struts
δ	Disorder parameter is defined by Aranguren *et al.* [1], [2].
E_r	Reduced elastic modulus (for Oliver Pharr method)
E_i	Elastic modulus of the indenter (for Oliver Pharr method)

ν_s	Poisson's ratio of solid (for Oliver Pharr method)
ν_i	Poisson's ratio of indenter (for Oliver Pharr method)
P	Applied force (for elastic foundation model)
E	Elastic modulus (for elastic foundation model)
w	Width/Depth/Height of lattice (for elastic foundation model)
x	Displacement of the indenter as a result of force P (for elastic foundation model
d_h	Maximum height distortion of the lattice (for elastic foundation model)
h	Height/thickness of elastic material (for elastic foundation model)
a	semi-major axis of indenter at displacement δ (for elastic foundation model)
R_c	Radius of curvature of the indenter (for elastic foundation model)
d	Strut diameter
k_{eq}	Combined stiffness of the load frame and sample (for compliance correction)
k_L	Stiffness of the load frame (for compliance correction)
k_{PT}	Stiffness of the sample determined from point tracking (for compliance correction
F	Force for compliance correction (Hooke's law)
k	Spring constant of Hooke's law
A	Area for axial stiffness relationship
L_s	Original length of sample parallel to loading direction (for axial stiffness relationship and compliance correction)
E_{PT}	Elastic modulus as determined by point tracking (for compliance correction)
E_{eq}	Elastic modulus calculated from uncorrected platen data (for compliance correction)
$disp_{CPL}$	Corrected displacements from platen data (for compliance correction)
$disp_{PL}$	Uncorrected displacements from platen data (for compliance correction)
σ^*_{max}	Apparent maximum stress
U^*	Apparent energy absorption
A_V	Voronoi cell area

Chapter 1

Introduction

This project aims to further our understanding of how additive manufacturing (AM) can be used to manufacture porous metamaterials and how these porous materials can be tailored to elicit specific and predictable mechanical responses. Density versus mechanical property relationships for uniform lattices built up from simplified unit cells will help inform the response and design of non-uniform porous structures (designed for AM) built up from the same simplified unit cells. These porous structures will expand the design space of polymers by taking inspiration from natural materials, which currently occupy a wide material design space, efficiently tailoring properties to demands, difficult to achieve with many synthetic materials.

Synthetic porous materials, such as foams, have been developed to overcome some of the limitations of synthetic and natural materials. They are used in a wide range of applications ranging from energy absorbing applications to particulate filters to light-weighting materials. This range of applications is possible via a variety of manufacturing methods, for example metallic foams made by injecting gas into the melt, ceramic porous materials made using sacrificial moulds, or polymeric porous metamaterials manufactured using AM. AM can create complex structures such as lattices with relative ease compared to traditional manufacturing methods, leveraging the shapes of certain geometries to alter apparent responses. For example, simplified unit cells can be categorised (based on their response to mechanical deformation), as either bending- or stretching-dominated. Structures with bending-dominated unit cells are more compliant and suited to energy absorbing applications, whereas stretching-dominated unit cells are stiffer and more suited to lightweight structural applications. Unit cell geometries with common points of intersection and features compatible with AM ensure manufacturability. A direct relationship between the geometrical properties and resultant mechanical properties can then be determined. This informs the behaviour of non-uniform lattices, created by combining different uniform geometries and increasing the material property space through careful consideration of lattice design.

1.1 Aims and Objectives

The aim of this project is to further our understanding of the mechanical behaviour of additively manufactured uniform and non-uniform porous metamaterials and how these are affected by relative density. This knowledge can be useful in the development of porous metamaterials for specific applications such as light-weighting in aerospace or engineered bone tissue scaffolds in biomedical applications.

The following objectives are set to help fulfil the aim:

- Understand the mechanical behaviour of a stretching-dominated geometry and how this varies for two different builds and post-processing methods.
- Verify the apparent elastic modulus analytical models for bending- and stretching-dominated unit cells over a range of relative densities.
- Develop empirical fits for both elastic and failure properties of bending- and stretching-dominated geometries.
- Determine how non-uniform porosity distribution for bending- and stretching-dominated lattices impacts distortions and mechanical properties, compared to uniform lattices.
- Determine how non-uniform porosity distribution for a combined bending- and stretching-dominated lattice impacts distortions and mechanical properties, compared to uniform lattices.

1.1.1 Novel Contributions

This project uses cutting-edge techniques to manufacture, test, analyse and characterise porous metamaterials, expanding the material property space of synthetic materials to match that of natural porous materials. Key novel contributions from this project are highlighted below.

- Novel application of point tracking technique for both bending- and stretching-dominated additively manufactures structures.
- Understanding of the behaviour (both elastic and failure) of a bending- and stretching-dominated unit cell over a wide range of porosities.

- Verification of analytical models and development of empirical fits for the bending- and stretching-dominated unit cells (for both elastic and failure properties).
- Application of analytical models from uniform porous metamaterials to describe the relationships of non-uniform porous metamaterials.

1.2 Thesis Structure

Following a review of the relevant literature, three technical chapters are presented, each with separate methodology and discussion sections. The final chapter focuses on conclusions and proposes areas for further investigation based on the findings of this work. A brief summary of each chapter is given below:

Chapter 2, presents relevant background literature, initially discussing both natural and synthetic porous metamaterials, including how one can predict the properties of such materials with both generic and geometry specific analytical models. This is followed by a comparison of different additive manufacturing methods, often used to manufacture porous metamaterials, discussing how various defects can influence apparent properties. Finally, compressive mechanical testing methods for porous metamaterials are explored with expected behaviours discussed.

The first technical chapter, Chapter 3, focuses on characterising distortions observed for a uniform stretching-dominated porous metamaterial and understanding the influence on apparent properties. Height distortions were most commonly identified, and an established analytical model (elastic foundation model), was adapted to quantify the loss of stiffness due to the distortions. Additionally, greater than expected intra- and inter-sample variability was observed and explained in terms of geometrical and base-material property variation.

The second technical chapter, Chapter 4, extends the methodologies from the first investigation to a wider range of relative densities as well as a uniform bending-dominated geometry. Distortions were strongly density dependent for bending-dominated geometries while a weaker trend was observed for stretching-dominated geometries. Empirically models were developed to describe density and mechanical property trends such as apparent elastic modulus and energy absorbed for both geometries. This was to better predict behaviour when designing tailored structures and for comparison with non-uniform geometries as in the following chapter. The two geometry types generally behaved as expected with increased mechanical properties with relative density and greater mechanical properties such as apparent elastic modulus observed for stretching-dominated compared to bending-dominated geometries.

The final technical chapter, Chapter 5, applies the methodologies and results from the previous chapters to explain the behaviour of three types of non-uniform geometries: bending- or stretching-dominated graded lattices, bending- or stretching-dominated stochastic lattices, and a mixed bending- and stretching-dominated stochastic lattice. The influence of randomness is also investigated for the single geometry stochastic lattices. Distortions are generally reduced for the non-uniform lattices, also resulting in increased apparent elastic modulus and maximum stress, but reduced energy absorption compared to uniform lattices. These results contribute to our know-how with regards to expanding the material property space and understanding the behaviour fo brittle non-uniform metamaterials with controllable porosity.

Finally, Chapter 6 summarises key conclusions from this project and suggests areas for future work focusing on applying other techniques for geometry or mechanical property characterisation or expanding the range of geometries evaluated.

Chapter 2

Background

2.1 Introduction

A review of the literature is presented in this chapter, focusing on two areas: porous metamaterials and additive manufacturing. The first section (Section 2.2) concerns both synthetic and natural porous metamaterials with cancellous bone presented as an example of an efficient porous material that has evolved over millennia to optimise mechanical properties such as stiffness and energy absorption, in relation to weight. A range of simplified unit cell geometries are discussed together with generic and geometry-specific analytical models that predict mechanical behaviour from density. The impact of random density variations in porous metamaterials is also explored, with a focus on how such materials have advantageous mechanical properties compared to uniform porous materials and with this randomness observed in natural porous materials such as cancellous bone. Finally, Section 2.3 then reviews various polymeric additive manufacturing techniques, highlighting stereolithography as a suitable manufacturing method for porous materials and the method chosen for this project. A discussion of commonly observed defects in the additive manufacture of porous metamaterials is also presented highlighting the need to accurately characterise as-built geometries.

2.2 Porous Metamaterials

Throughout history, as new materials have been discovered, the material property space available to manufacture products has increased (Fig. 2.1) [3].

Early natural materials such as wood, ceramics and stone possessed a limited but optimised range of mechanical properties such as stiffness, strength and ductility. As more materials were discovered and developed, the material property space

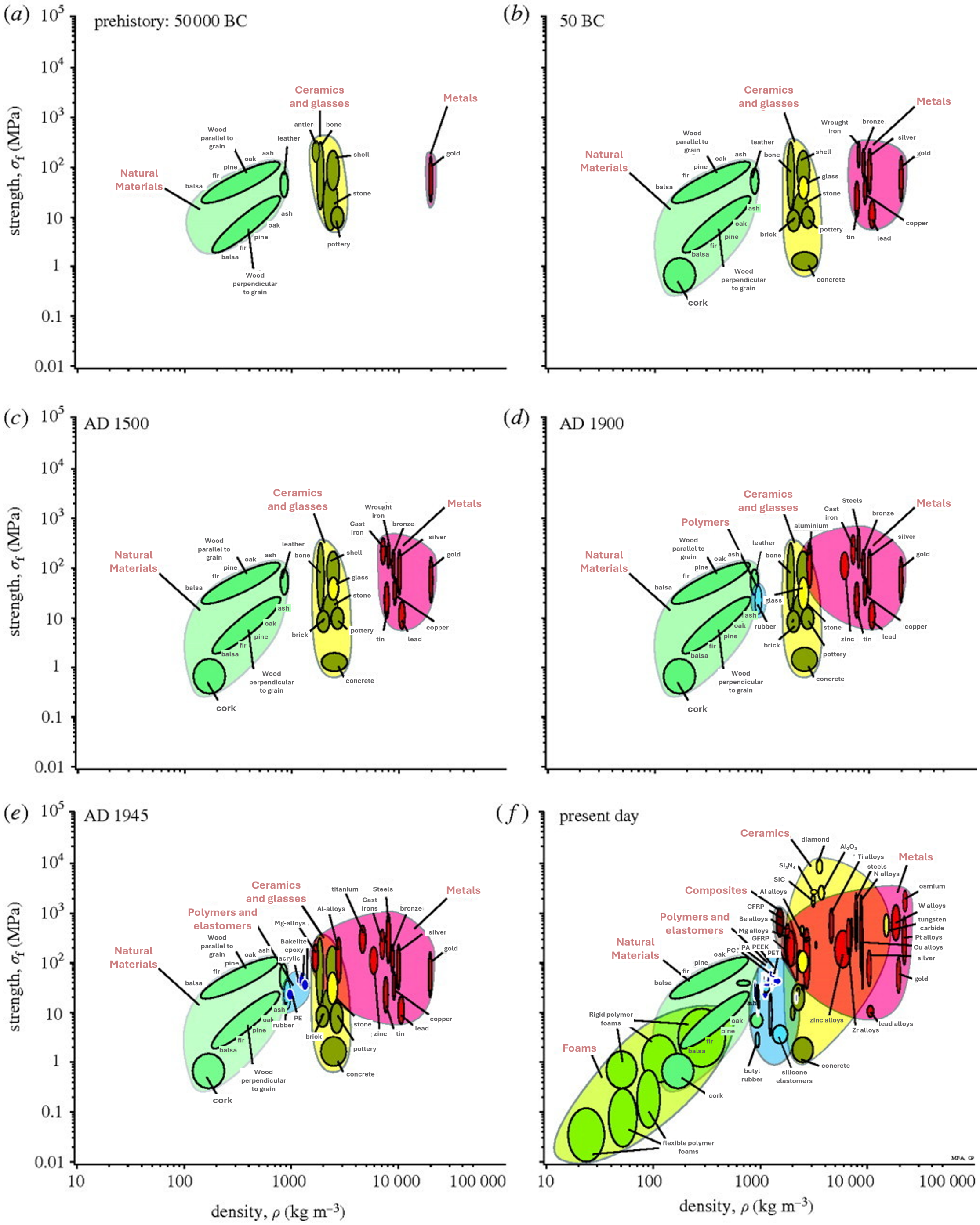

FIGURE 2.1: Evolution of the material property space adapted from [3]

increased, resulting in more innovations. The Roman roads we know today, for example, only came about after the development of concrete [4], and the second industrial revolution would not have been possible without the mass production of steel [5]. These examples highlight why accessing greater areas of the material property space is important and has been the focus of much research. In the past, this has been achieved by altering the chemical make up of the materials, for example, by making new metallic alloys or by changing the microstructure of the material to control the distribution of different phases, particularly in metals. As a result of extensive research, further improvements in the property space are becoming increasingly limited for solid materials [3]. The development of porous metamaterials (where a metamaterial is defined as a synthetic architected material that spatially varies material distribution to outperform natural materials [6]–[8]) presents an opportunity to expand the material property space further, providing alternatives to traditional solid materials [3]. Composites have also been developed to overcome the limitations of solid materials, however, they target a different area of the material property space and are not the focus of this project.

A porous material can be defined as a solid which contains cavities. This broad definition encompasses a large range of both synthetic and natural materials with a wide range of applications and target properties. Examples of synthetic materials include acoustic foams [9], which have high energy absorption capabilities to reduce reflected sound (porosity ranges between 16 - 90 %) and water filter cartridges that use the pores to remove unwanted particulates [10], [11] (porosity ranges between 35 - 50%). These two applications are vastly different and use distinct base materials (polymers and ceramics respectively), however, both are classed as porous materials.

Improved specific mechanical properties (property x divided by mass) are one of the key advantages of porous materials over solid materials. Honeycomb sections of sandwich structures and the infill of 3D printed parts, for example, both achieve increased stiffness for a reduced weight. The resultant increase in design space offered by porous materials is evident in Ashby plots (Fig. 2.1f, foams). The goal of maximising specific properties is not limited to synthetic materials. Nature has shown that this can be achieved with wood [12] and cancellous/trabecular bone [13]. Such biological porous materials have evolved over millennia to be efficient, optimising physical and mechanical properties such as stiffness and energy absorption, typically in relation to weight [14]. As a result, they occupy a wide material property space [3] compared to solid synthetic materials as seen in Fig. 2.1. Cancellous bone is described here in more detailed as it is a good example of a tailored porous metamaterial, with the wide range of properties due to both the base material (discussed below) and geometric variation/randomness discussed in Section 2.2.3.

Cancellous bone is highly porous with porosities ranging between 40 and 95 % [15]–[17] and is very metabolically active, constantly being remodelled [18], [19]. It is made up of mineral (mostly as hydroxyapatite) and organic compounds (mostly various forms of collagen) as well as water (65%, 25% and 10% weighted respectively) with the exact ratio of the different components varying between individuals [19]–[21]. It has a tissue/material density (ρ_s, density not including porosity) similar to cortical bone (lower porosity than cancellous bone at between 5 and 20 % [15]–[17]) of between 1.6 and 2.0 gcm^{-3} [15], [17], [20], [22]. When porosity is included, cancellous bone has an apparent density (ρ^*, density including porosity) of between 0.05 and 1.3 gcm^{-3} [15], [17], [20], [22]. Cancellous bone can be described as being made up of struts/trabeculae that come in two forms: rods and plates (Fig. 2.2) [15], [17], [20].

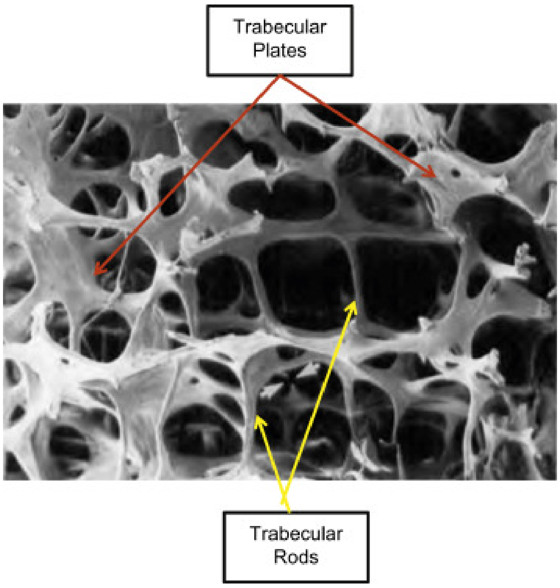

FIGURE 2.2: Rods and plates seen in cancellous bone, from [23]

The number of rods versus plates depends on location; areas with a higher apparent density (lower porosity), have more plates and conversely, areas with a lower apparent density (higher porosity) have more rods [20], [24], [25]. This can be seen in measurements of average trabecular thickness which depend on location and typically ranges between 100 and 300 µm [20], [24]. The geometric variation translates to variations in mechanical properties such as the compressive elastic modulus. The base material compressive elastic modulus (without porosity) ranges between 10 and 20 GPa depending on location, geometry and test method [17], [26]. When porosity is considered for cancellous bone (apparent elastic modulus), these values are significantly reduced to between 10 and 300 MPa [17] with between 70 and 90% of the variability due to apparent density differences. Unlike apparent elastic modulus, yield strain and ultimate strain are not strongly related to apparent density and are more isotropic (there is a slightly stronger dependence of yield strain on apparent density at low densities) [17]. Yield strain is reported to vary between 0.7 - 0.85% in compression and between 0.6 - 0.71% in tension; variability is mostly seen between locations, with yield strain remaining relatively constant within the same site (standard deviations are approximately 1/10th of the mean) [17], [20]. Ultimate strain is reported to vary between 1 and 2.5% [17].

Additive manufacturing (AM) can be used to create complex geometries like lattices that attempt to match a range of properties and performance for many applications including aerospace, automotive and biomedical [27], with analytical models used to predict their behaviour. The seminal work of Ashby and Gibson details how the apparent elastic modulus, E^* (elastic modulus of porous material), of an opened-cell porous material (material distributed along cell edges instead of along solid faces connecting cells) can be estimated by classifying the response as either bending- or stretching-dominated and assuming a generic unit cell geometry, useful when little is known about the internal geometry as in stochastic foams [28]. A cubic unit cell geometry can be used (Fig. 2.3) with unit cells connected by strut midpoints. This geometry allows isotropic material assumptions to be applied and only two of the following properties are required to describe the material: E^*, G^*, the apparent shear modulus and ν^*, the apparent Poisson's ratio.

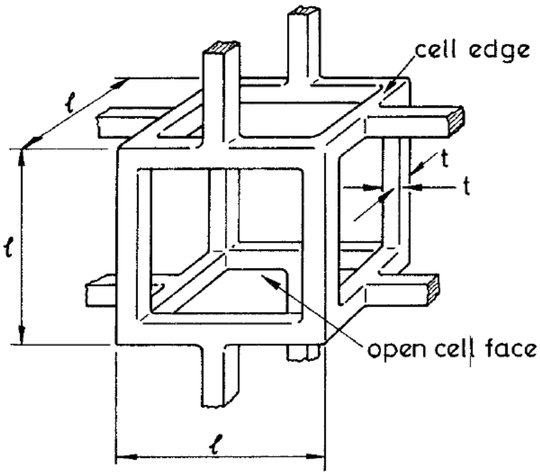

FIGURE 2.3: Cubic unit cell for open-celled foams [28]. t is the strut thickness and l is the strut length

The general Ashby-Gibson expression for the apparent response is given in Eq. 2.2.1,

$$E^* = E_s \left(\frac{\rho^*}{\rho_s}\right)^n \cdot C \qquad \text{(Eq. 2.2.1)}$$

where, E_s is the base material elastic modulus, (ρ^*/ρ_s) is the density of the porous material (ρ^*) relative to the density of the solid base material (ρ_s), and C is an empirical constant for stochastic geometries. The power, n, is dependent on the mechanical response of the porous material and is equal to 2 or 1 for bending- and stretching-dominated materials, respectively, with the latter being stiffer at the same relative density [29]–[31]. Stretching-dominated structures are therefore better suited to light-weighting applications such as those in aerospace whilst bending-dominated structures are better suited to energy absorbing applications such as soundproofing. A low (less than 5) nodal connectivity is characteristic of bending-dominated

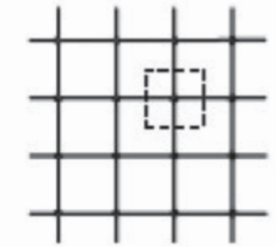

FIGURE 2.4: A periodic, square 2D lattice with a dashed box highlighting a joint where four edges meet (nodal connectivity is 4). Image taken from [3]

structures, where nodal connectivity is defined as the number of cell edges/struts that meet at a joint (Fig. 2.4). Most foams (a widely used synthetic porous metamaterial) have a nodal connectivity of three to four and tend to be bending-dominated [32]. The same relationships can be used for cancellous bone with the apparent elastic modulus related to apparent density by a power law with exponents of between 2 and 3, however, the exponent can be set to 1 if the range of apparent density is small [17], [20], [33]. Along with analytical models of porous solids, the exponent of the power laws suggests the dominant deformation mechanisms of cancellous bone and how it might fail [33]. For apparent elastic modulus, indices of 2 and 3 suggest that cancellous bone behaves like open- and mostly closed-cell structures, respectively, where bending dominates [28], [33], [34]. An index of 1, however, suggests open-celled structures where stretching dominates [28], [33], [34].

Maxwell's stability criterion, (M), can be applied in 2D (Eq. 2.2.2) and 3D (Eq. 2.2.3) to predict the behaviour of geometries, like those in Fig. 2.5, based on nodal connectivity [29], [30], where b, is the number of struts and j, is the number of joints.

$$M = b - 2j + 3 \tag{Eq. 2.2.2}$$

$$M = b - 3j + 6 \tag{Eq. 2.2.3}$$

The number associated with the number of joints (the 2j and 3j terms in Eq. 2.2.2 and Eq. 2.2.3) is based on the number of dimensions in the system, i.e. 2D or 3D, whilst the number of struts term, b is the same for both. To determine the other term in the equations, one must look at the statically and kinematically determinate case in Fig. 2.5 b. Here, b is 5, and j is 4. As it is statically and kinematically determinate, Eq. 2.2.4 is valid, with x needing to be found. Rearranging Eq. 2.2.4, and letting b = 5 and j = 4, x becomes -3. Maxwell's criterion/number is found when rearranging Eq. 2.2.4 to equal 0, giving Eq. 2.2.2.

$$b = 2j + x \qquad \text{(Eq. 2.2.4)}$$

When M < 0 (Fig. 2.5a, M = - 1 from Eq. 2.2.2), it is classed as a mechanism and has at least one degree of freedom. When loaded in compression, the struts of a mechanism can rotate about the joints, which if fixed, results in the individual struts bending, leading to a bending-dominated structure. A fully defined structure (Fig. 2.5b), when M = 0, has no degrees of freedom and when loaded, and the struts experience both tension and compression; the struts can only deform by stretching. When the joints are fixed, as in a lattice structure, there is negligible effect on the struts and the structure remains stretching-dominated.

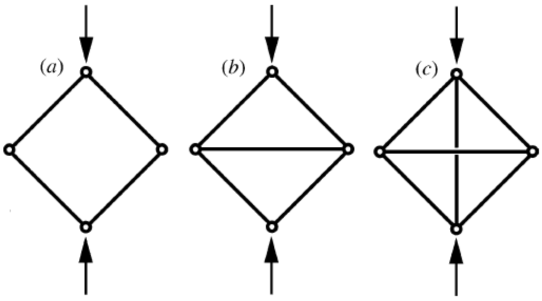

FIGURE 2.5: 3 types of 2D frames as defined by Maxwell's criterion Eq. 2.2.3. a) M <0, mechanism and bending-dominated, b) M = 0, fully defined and stretching-dominated, c) M >0, over-defined and stretching-dominated [30]

When another strut is added (Fig. 2.5c, M = 1), the structure becomes over-defined (M > 0) and may be subject to a state of self-stress. The structure is still stretching-dominated but Eq. 2.2.2 and Eq. 2.2.3 are not suitable as Maxwell's criterion is only concerned with statically and kinematically determinate trusses. An expanded version of Maxwell's equations in 3D (developed by Calladine [35]) can be used instead (Eq. 2.2.5), with s, the number of self-stress states and m, the number of mechanisms. With Calladine's equations, if M < 0 the structure is bending-dominated and if M ≥ 0, the structure is stretching-dominated.

$$M = b - 3j + 6 = s - m \qquad \text{(Eq. 2.2.5)}$$

Eq. 2.2.1 describes the relationship of open-celled porous materials when behaving linear elastically, but if loaded past the linear elastic region, a porous structure will generally either fail by strut buckling (Eq. 2.2.6), plastic collapse where plastic hinges form at the joints (Eq. 2.2.7), or by strut fracture (Eq. 2.2.8).

$$\frac{\sigma^*_{el}}{E_s} = C\left(\frac{\rho^*}{\rho_s}\right)^n \qquad \text{(Eq. 2.2.6)}$$

$$\frac{\sigma^*_{pl}}{\sigma_{y,s}} = C\left(\frac{\rho^*}{\rho_s}\right)^n \quad \text{(Eq. 2.2.7)}$$

$$\frac{\sigma^*_{cr}}{\sigma_{fs}} = C\left(\frac{\rho^*}{\rho_s}\right)^n \quad \text{(Eq. 2.2.8)}$$

where, σ^*_{el} is the apparent buckling elastic collapse stress, σ^*_{pl}, is the apparent plastic collapse strength, $\sigma^*_{y,s}$ is the base material yield strength, σ^*_{cr} is the apparent brittle collapse stress, and σ_{fs} is the base material modulus of rupture. The constants (C) and index/slope (n) vary depending on the property and deformation mode of the porous metamaterial. Table 2.2.1 summarises the relevant values for each loading scenario. The constants are calculated from experimental and numerical data where possible [15], [28], [30], [31].

TABLE 2.2.1: Summary of equations that describe the behaviour of bending- and stretching-dominated structures [15], [28], [30], [31].

Equation	Bending		Stretching	
	C	n	C	n
Eq. 2.2.1 - Linearly elastic	1.00	2.00	$\frac{1}{3}$	1.00
Eq. 2.2.6 - Strut buckling	0.05	2.00	-	2.00
Eq. 2.2.7 - Plastic collapse	0.30	1.50	$\frac{1}{3}$	1.00
Eq. 2.2.8 - Brittle fracture	0.65	1.50	-	1.00

As there is limited data for bending-dominated structures that fail by brittle fracture (Eq. 2.2.8), the constant is estimated by comparing to the equations for plastic collapse (Eq. 2.2.7). The constants for stretching-dominated structures are less certain as failure is heavily dependent on defects, and is therefore not provided. In the buckling case (Eq. 2.2.6) for stretching-dominated structures, the constant is not known but thought to be material dependent (elastomeric versus rigid polymers) and of a similar order of magnitude to that for bending-dominated structures [28], [30].

2.2.1 Unit Cell Geometries

Alternatively, the specific geometry of the unit cell can be used to predict the apparent response, with three main groups of non-parametric simplified unit cell models: body-centred cubic (BCC), diamond/face-centred cubic (FCC) and rhombic dodecahedron. Other unit cell types such as those defined by curved surfaces like gyroids [31], [36] have been explored to create porous metamaterials. In this investigation, simplified unit cells are examined, as they are comparatively easy to manufacture, reproduce and vary, and have established analytical expressions for their behaviour.

Body-Centered Cubic

BCC unit cell geometries are simple to design and manufacture and consist of inclined struts between the corners of a cube and its centre (Fig. 2.6a). This geometry is bending-dominated (M = - 13) and isotropic. Several investigations derived analytical equations for behaviour of BCC geometries with differences being limited to the different beam bending theories, Euler-Bernoulli [37], [38] (e.g. Eq. 2.2.9 which predicts the apparent elastic modulus E_z^*, from d_{ang} the diameter of the angled struts and L, the overall length of the unit cell) versus Timoshenko [38], [39], and relative density calculations accounting ([38], [39]) and not accounting ([37]) for beam overlap. Timoshenko beam theory accounts for shear and rotational effects, important factors when the diameter-to-length ratio of the struts is greater than 0.1 [38], typically when the relative density (ρ^*/ρ_s) is greater than 30%. If not included, the accuracy of the analytical model decreases with increasing relative density and the initial stiffness of the geometry is under-predicted. Relative density is also over-predicted if beam overlap is not accounted for.

$$E_z^* BCC = \frac{\sqrt{3}\pi}{2} \cdot \left(\frac{d_{ang}}{L}\right)^4 \cdot E_s \qquad \text{(Eq. 2.2.9)}$$

To increase the stiffness for the same density and add anisotropy (a key feature in many applications including engineered bone tissue scaffolds), vertical struts can be added between the corners or in the centre (Fig. 2.6b) to create a BCCz unit cell. This geometry appears as bending-dominated using Maxwell's equations (Eq. 2.2.5), as M = -9. However, if loaded parallel to the extra vertical strut, this strut dominates the response parallel to loading, greatly increasing stiffness and resulting in stretching-dominated behaviour. As with the BCC geometry, its performance can also be predicted using analytical models, as in Eq. 2.2.10 which predicts E_z^*, the apparent elastic modulus in the direction aligned with the vertical strut [40].

$$E_z^* BCC_z = \frac{\sqrt{3}\pi}{2} \cdot \left(\frac{d_{ang}}{L}\right)^4 \cdot E_s + \frac{\pi}{4} \cdot \left(\frac{d_{vert}}{L}\right)^2 \cdot E_s \qquad \text{(Eq. 2.2.10)}$$

where, d_{ang} is the designed diameter of the angled struts as in the BCC equation and d_{vert} is the designed diameter of the vertical struts. The response of the BCCz unit cell provided is a sum of the response of the angled struts, which form a BCC unit cell and the response of the single vertical strut. At low relative densities, when the ratio between strut diameter and unit cell length is reduced, higher order terms such as the response of the BCC component can be ignored, further highlighting the stretching-dominated response of the unit cell. As with the BCC unit cell, the accuracy of this analytical model decreases at approximately 30% relative density [28], [41] for both the BCC component and the deformation of the vertical strut as slender beam assumptions apply to both parts of the model.

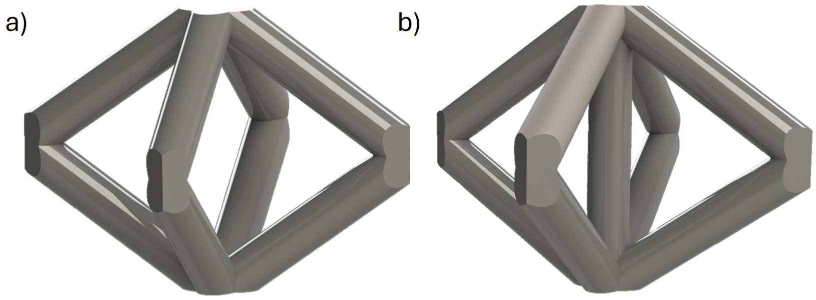

FIGURE 2.6: a) BCC and b) BCCz unit cell geometries.

Diamond/Face-Centered Cubic

Diamond and FCC unit cell geometries are more complex than the BCC geometries but still manufacturable using AM techniques. The diamond geometry (Fig. 2.7a) is bending-dominated (M= -20) and isotropic. A modified FCC geometry (FCCm, Fig. 2.7b), is also bending-dominated, but with a higher Maxwell's number, -14. Within the category of FCC geometries, the octet geometry (Fig. 2.7c) is an anisotropic stretching-dominated geometry and is kinematically and statically fully defined with M equal to 0 [30], [42]–[46] and is shown to be beneficial for energy absorbing applications [47].

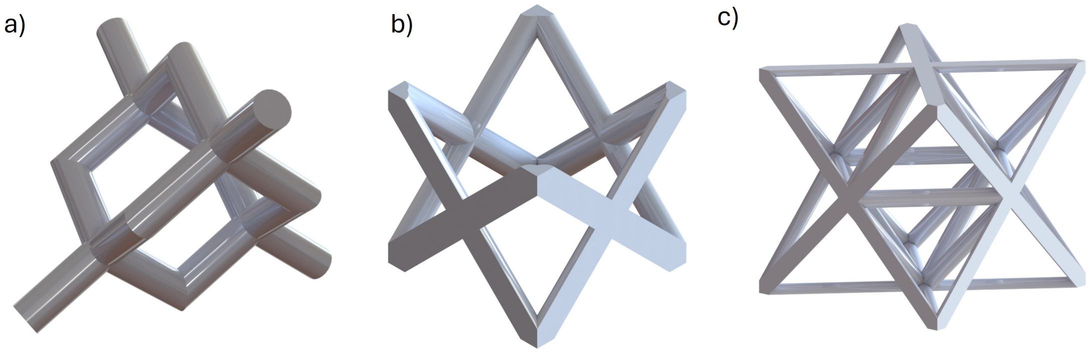

FIGURE 2.7: a) Diamond, b) FCCm and c) Octet unit cell geometries.

Rhombic Dodecahedron

Rhombic dodecahedron (RD, Fig. 2.8) unit cell geometries are centrally symmetric, isotropic and bending-dominated, with M = -6. The RD geometry is more complex than the BCC unit cells, however, is still manufacturable using AM techniques.

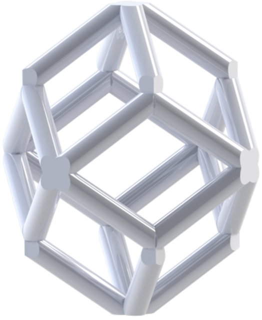

FIGURE 2.8: Rhombic Dodecahedron (RD) Cell

2.2.2 Joining Unit Cells

Four approaches have been identified for joining simplified unit cells for the additive manufacture of porous metamaterials. The appropriate joining method will depend on how widely the target properties, and therefore the geometry of each unit cell, vary [36].

A **uniform design** involves selecting one optimal geometry and repeating this geometry for the overall target shape. Using this format, compatibility between neighbouring cells is guaranteed and modelling is straightforward (the analytical models can be used without modification) [36]. However, this does not offer any variation throughout the full lattice structure.

A **layered gradient** involves selecting several optimised geometries and staggering them based on the goal structure. Potential issues include stress concentrations at points where different unit cells join (this becomes significant when the geometry and size of struts between neighbouring unit cells differ greatly) rendering certain cell combinations non-manufacturable [36].

A **continuous gradient** design is similar to the layered gradient, however, the change between layers is more gradual. This format reduces the chance of stress concentrations at neighbouring cells and subsequent non-manufacturable designs [36].

A **stochastic** design is built up from randomly varied unit cells, varied for either relative density, design or both. As with the layered gradient, stress concentrations and issues with manufacturability are likely between neighbouring unit cells due to the random build of the porous material. Predicting as-built properties is more complex as the analytical models of simplified unit cells cannot be used.

Designs based on **topology optimisation** involve optimising the material layout based on the predicted properties of the unit cells [36], [48]–[51]. Compared to the gradient methods, the variation is typically more discrete, with reduced stress concentrations. Non-manufacturable designs, however, are still possible. Additionally, the application of analytical models and prediction of behaviour is considerably more complex than other methods and depends on the approach taken. One could either use a single cell design but vary strut diameter, or use a library of unit cells with a fixed strut diameter. Both offer similar performance increases compared to a uniform design [48].

2.2.3 Non-Uniform Porous Metamaterials

Stochastic structures offer numerous advantages over more uniform structures and are often found in natural porous materials which tend to have some level of stochasticity [1], [2], [52], [53]. To determine the influence of stochasticity and the level present in natural porous materials, Aranguren et al., [1], defined a disorder parameter, δ. δ, is defined as the ratio between the minimum centroid to centroid distance of random 2D Voronoi cells by the centroid to centroid distance of a regular hexagonal-based 2D lattice, with 1.0 for a fully regular arrangement and 0.1, for a highly disordered structure (Fig. 2.9a). The level of disorder also influences the cell size and cell size distribution with a higher level of disorder (lower δ) resulting in more varied cell sizes and an increase in the number of smaller cells, Fig. 2.9b).

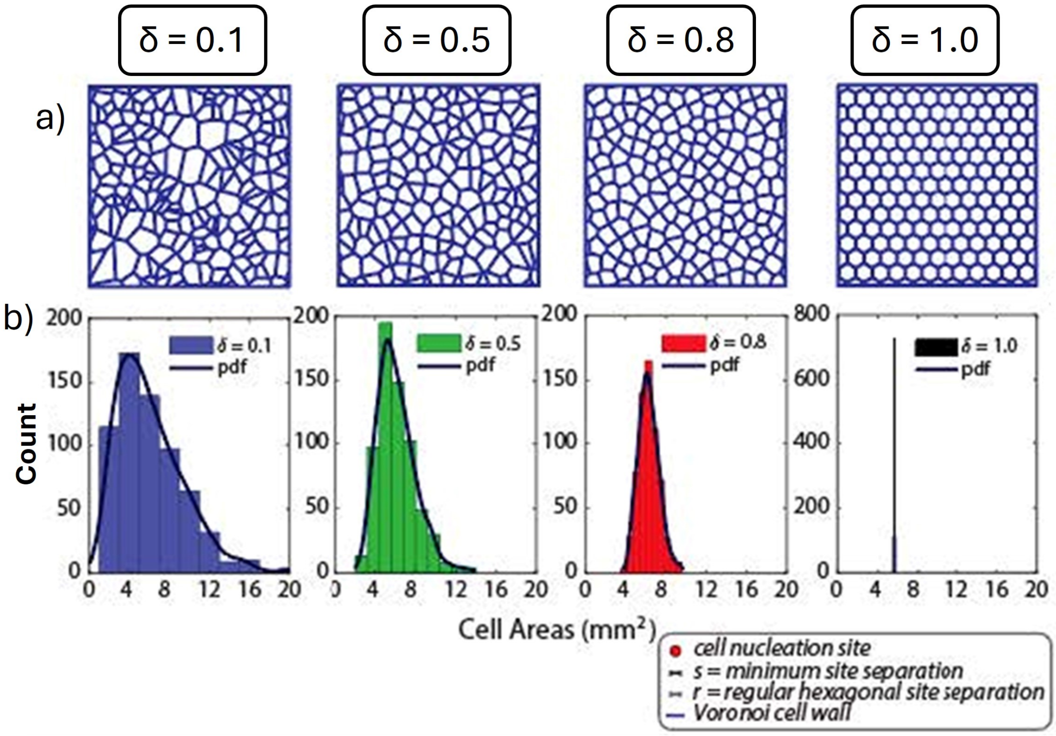

FIGURE 2.9: a) visual representative varying levels of disorder as defined by Aranguren *et al.* [1], [2] and b) corresponding measured cell areas of 1000 Voronoi cells. Figure adapted from Aranguren *et al.*, [1]

Natural porous materials can often be represented by Voronoi structures. Aranguren *et al.* [1], made use of this to generate representative Voronoi-based 2D structures for a wide range of natural porous materials (examples in Fig. 2.10) and a select number of synthetic porous materials including polymer foams. This allowed for δ to be calculated (Fig. 2.10). Interestingly, natural porous metamaterials are all relatively ordered with a minimum median disorder of 0.55, compared to polymer and metallic foams which have median disorders of 0.4 and 0.5 respectively. Additionally, porous materials have distinct comparatively narrow disorder ranges. Whale vertebrae were found to have the greatest range varying between 0.48 and 0.7, whilst metal foams have a range between 0.25 and 0.6.

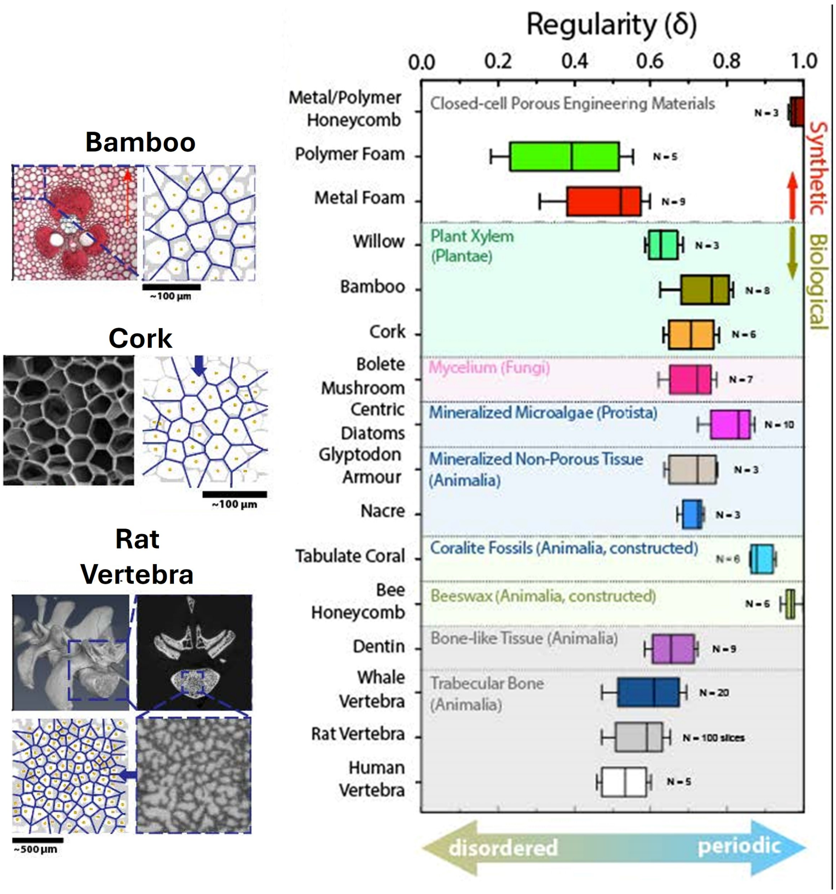

FIGURE 2.10: Examples of using Voronoi structures to represent a natural porous material with the yellow dots indicating the centroids of Voronoi cells and blue lines as the Voronoi cell walls. Variation of measured disorder for a range of porous materials is also shown with N equal to the number of images analysed. Figure adapted from Aranguren *et al.*, [1].

From Fig. 2.10, one might conclude that natural porous materials have evolved to optimise disorder (shown by the narrow ranges) in order to optimise certain mechanical properties. To test this hypothesis, Aranguren *et al.*, manufactured a range of 2D Voronoi lattices using additive manufacturing techniques with δ ranging from 0.1 to 1.0. They characterised how disorder impacted a range of tensile mechanical properties, including apparent elastic modulus and energy absorption as well as analysing crack growth mechanics (Fig. 2.11). Values were normalised by results from fully ordered lattices. From Fig. 2.11, they determined that highly ordered Voronoi lattices, when $\delta \geq 0.6$, had a comparable normalised apparent elastic modulus, maximum stress and energy absorption to failure as fully ordered hexagonal lattices. This was likely due to the increasingly uniform cell size distribution as δ approaches 1.0 (2.9b). Decreasing δ beyond 0.6 generally resulted in decreasing mechanical properties due to earlier catastrophic fracture. The one exception to this was the normalised apparent elastic modulus, which generally remained constant, independent of disorder. Beyond these mechanical properties, the highly ordered stochastic structures were shown to have multi-stage failure and, through crack propagation tests, improved survivability characteristics such as fracture toughness (calculated via the J integral method) compared to fully ordered structures. Disorder inhibits catastrophic crack propagation, encouraging crack deflection (most significant for highly ordered lattices) and increasing fracture toughness. For fully ordered or highly disordered lattices, fast fracture was observed with straight undeflected crack paths. Highly ordered lattices ($0.6 \leq \delta \leq 0.8$) showed improved failure characteristics whilst maintaining elastic properties. The level of disorder for natural porous materials is similar and therefore likely plays a role in the mechanical advantages that natural porous materials have over synthetic ones. Building upon this to expand the synthetic disordered lattices characterised to include simplified unit cells as well as 3D lattices would help in expanding the material property space accessible.

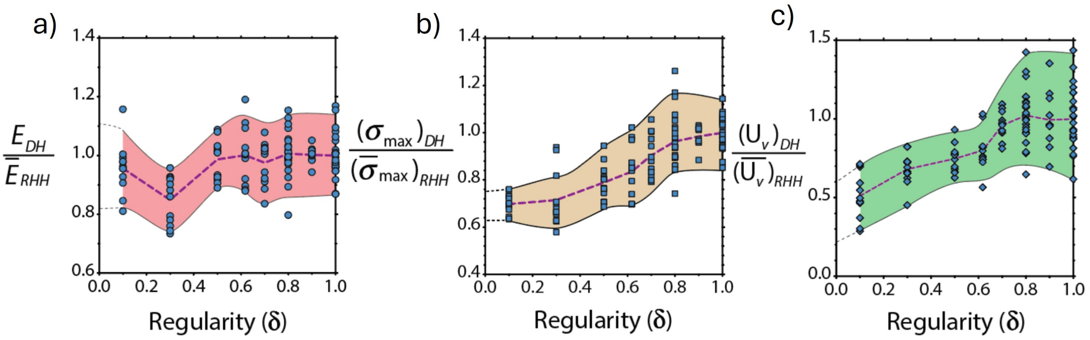

FIGURE 2.11: Impact of disorder (δ) on normalised a) apparent elastic modulus, b) maximum stress and c) energy absorption. Figure adapted from Aranguren *et al.*, [1].

2.3 Additive Manufacturing

AM can produce complex geometries with relative ease and works on the principle of adding material layer-by-layer, rather than removing it as with traditional subtractive manufacturing techniques [54]. It is typically used for prototyping as it allows companies to manufacture on-site and is more economical for small-batch production runs [55]. Metals, ceramics and polymers are all compatible with AM and use a wide range of processing techniques, resulting in varying size scales and roughnesses [54]. The focus of this investigation will be limited to polymers; this enables a material property space similar to biological materials to be accessed. Common polymeric AM techniques include fused filament fabrication (FFF), selective laser sintering (SLS), Polyjet and stereolithography (SLA). A comparison between these four methods is discussed here and summarised in Table 2.3.1.

In FFF, material is extruded through a nozzle and deposited layer-by-layer with the high viscosity of the melted polymer limiting the smallest nozzle size and therefore layer height (Z resolution) [56] (Fig. 2.12). The requirement to start/stop extrusion within each layer greatly limits the smallest in-plane feature size (XY resolution). The cooling rate of the material determines the printable overhang; sections of a part not supported by the part and would typically require additional support and therefore post-processing [57]. A high material modulus for FFF is achieved using composites, with short glass or carbon fibres embedded into normal filament [58]. This only increases the stiffness in the XY plane as stiffness in the Z direction is still limited by layer adhesion; directional properties are further emphasised [59]. Additionally, composite FFF materials require larger nozzle sizes and therefore decrease resolution in both the XY and Z directions.

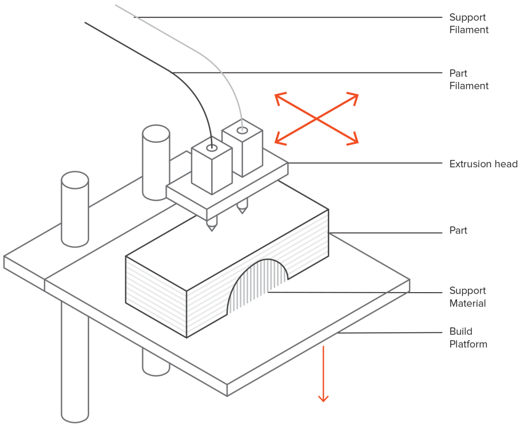

FIGURE 2.12: Labelled diagram of the FFF process, figure taken from [60]

In SLS, a type of laser-powder bed fusion (L-PBF) the powdered material is sintered using a laser along a predetermined path, similar to the path of FFF [61] (Fig. 2.13). The laser spot size and power limit the volume of powder that can be sintered and therefore layer height. The unsintered powder is able to support the part when being built up, so no additional supports are required [62]. The range of materials compatible with SLS is limited, with nylon and nylon-based composites most commonly used [62].

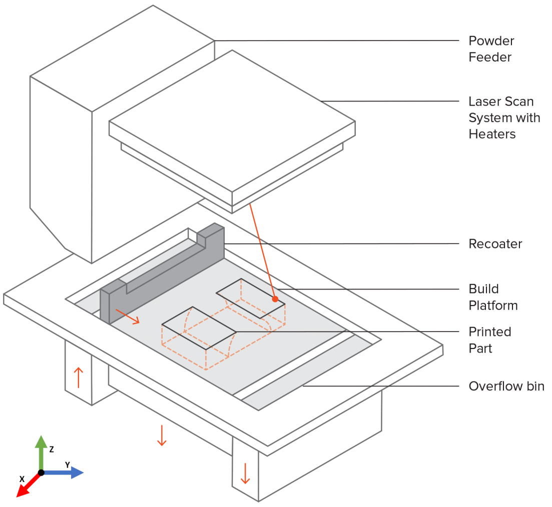

FIGURE 2.13: Labelled diagram of the SLS process, figure taken [63]

Polyjet works similarly to inkjet printing, whereby droplets of material are deposited layer-by-layer and then cured using an ultraviolet (UV) light [62] (Fig. 2.14). The size of the droplets means a full support structure is required; no overhangs are possible making this less suitable for porous metamaterials [62]. The range of materials compatible with polyjet is also limited as this method is typically used for aesthetic and non-functional parts [62].

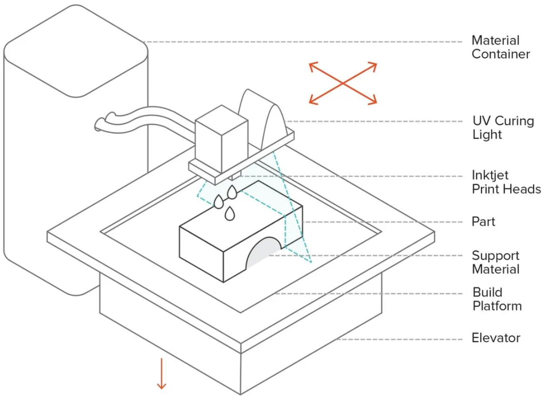

FIGURE 2.14: Labelled diagram of the Polyjet process, figure taken from [64]

SLA is a type of vat photopolymerisation that builds parts from the bottom up (parts are inverted during manufacture) with a UV laser curing a photoinitiated resin along a predetermined path [65] (Fig. 2.15). Once a layer is cured, it is peeled from the flexible film of the resin tank, the resin is mixed, levelled and the part is lowered ready to continue part manufacture. Once the part is complete, it is then washed (typically with isopropyl alcohol, IPA) to remove excess resin, and undergoes a final UV curing step. XY and Z resolution depend on the laser spot size and layer height respectively as well as material. They also have similar support requirements to FFF although optimal print orientation to reduce surface area often results in a large number of supports. Commercial SLA machines are compatible with a large range of materials with elastic moduli ranging from 1 – 11.7 GPa [66], [67] for parts that have undergone a specific post-processing methodology. On balance, SLA offers many advantages for producing porous metamaterials.

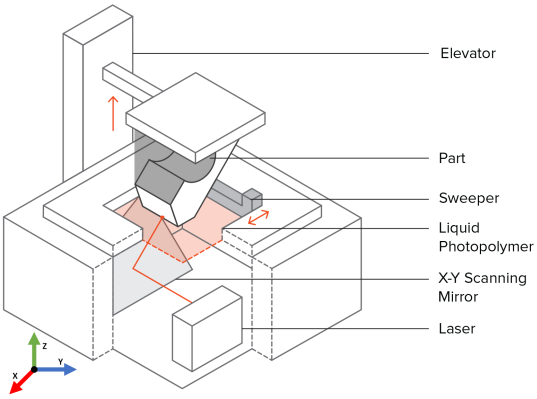

FIGURE 2.15: Labelled diagram of the SLA process, figure taken from [68]

TABLE 2.3.1: AM process comparison. Note that Z is the build direction, and XY is the plane of layered material deposition. Green blue and red shading indicates better, equal, and worse performance compared to SLA.

Process	Resolution Layer height (Z)	 In-plane (XY)	Cost	Support	Base Material Elastic Modulus Range (GPa)
SLA	$> 25\ \mu$m	$> 85\ \mu$m	Med.	<20°	1 - 11.7
FFF	$> 50\ \mu$m	$> 200 - 1000\ \mu$m	Low	<30°	0.5 - 6.7
SLS	$> 50\ \mu$m	$> 100\ \mu$m	High	None	1.6 - 5.3
Polyjet	$> 16\ \mu$m	$> 42\ \mu$m	High	Full	0.9 - 3

Variations in post-processing procedures are also known to affect the mechanical response of AM parts [69], [70] including initial stiffness and energy absorption, resulting in deviations from analytical models. For SLA, an increase in washing time with IPA decreases the flexural modulus and tensile strength of dog-bone samples with a low surface area-to-volume ratio. After washing for 90 minutes or 12 hours the flexural modulus reportedly decreased by 15% and 50%, respectively, and after washing for 30 minutes the tensile strength decreased by 13% [69]–[71]. This is suggested to be due to the IPA permeating the printed part during washing, relaxing the polymer chains, resulting in part softening as well as unreacted monomer removal by the IPA leaving voids in the printed part, decreasing mechanical properties.

Deviations from the as-designed geometry have also been shown to impact the apparent properties of metallic AM lattices. For example, shape distortions such as warping are commonly observed in additive manufacturing, affecting loading [72]–[81]. The analytical models developed, however, assume uniform loading resulting in differences between as-designed and as-built apparent properties. These distortions range from approximately 20 to 600 μm for parts manufactured with L-PBF, and between 15 μm and 2.5 mm for SLA parts varying depending on geometry type (unsupported versus supported), manufacturing processing conditions and cross-sectional area and have the potential to impact loading behaviour [73]–[78], [80], [81]. For example, distortions of up to 300 μm were reported L-PBF parts over a length of 2 mm (15%) [73], [76], and 500 μm over a length of 80 mm (0.63%) [81] for SLA parts (Fig. 2.17a). Though the level of distortion for the SLA example given appears small, especially when compared to the distortion of the L-PBF part, the SLA parts were thicker and, more importantly, fully supported, whereas in the L-PBF example, they we not supported, increasing the excepted distortion in the L-PBF parts. Though the processes of L-PBF differ from SLA, understanding the influence of these can still highlight potential variables that will increase intra- and inter-sample variability and influence mechanical properties. With both L-PBF and SLA, warping (caused by residual stresses), missing struts, surface roughness and deviations from the designed geometry such as inclusions, porosities, non-circular strut cross-sections and the waviness of struts (Figs. 2.16 and Fig. 2.17 , examples of defects in L-PBF lattices and SLA parts respectively) have all been found to affect mechanical properties such as strength and modulus and [72], [76]–[98].

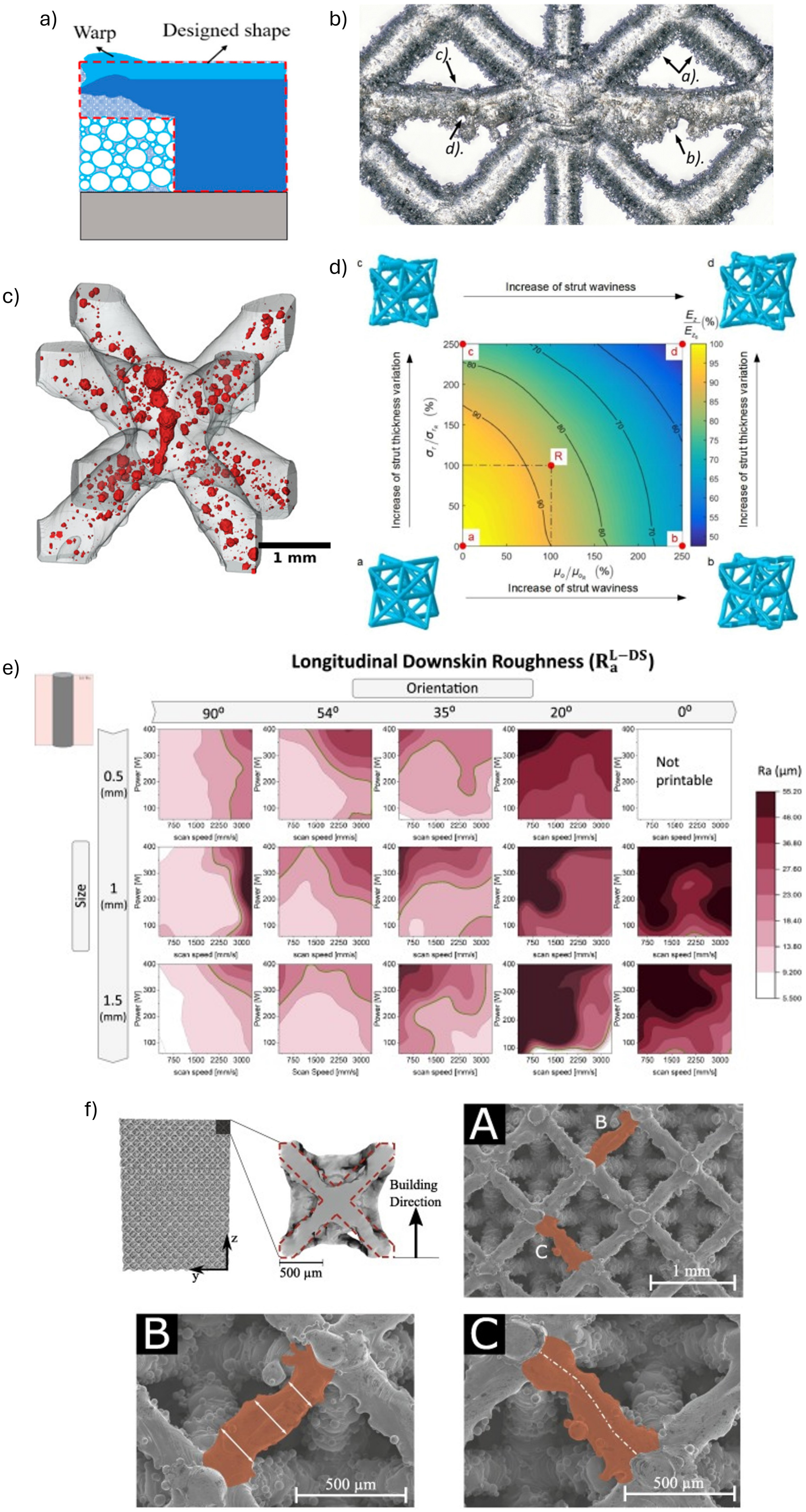

FIGURE 2.16: Examples of defects from L-PBF parts: a) warping observed in an overhang, taken from [76], b) increased waviness and roughness observed in horizontal struts, taken from [86], c) internal porosities observed using micro CT, taken from [89], d) variation of normalised apparent elastic modulus as a function of strut waviness and strut diameter variation, taken from [88], e) variation of surface roughness on struts as a build direction (0° is horizontal) and strut diameter, taken from [87] and f) examples of strut waviness and strut diameter variation, taken from [85].

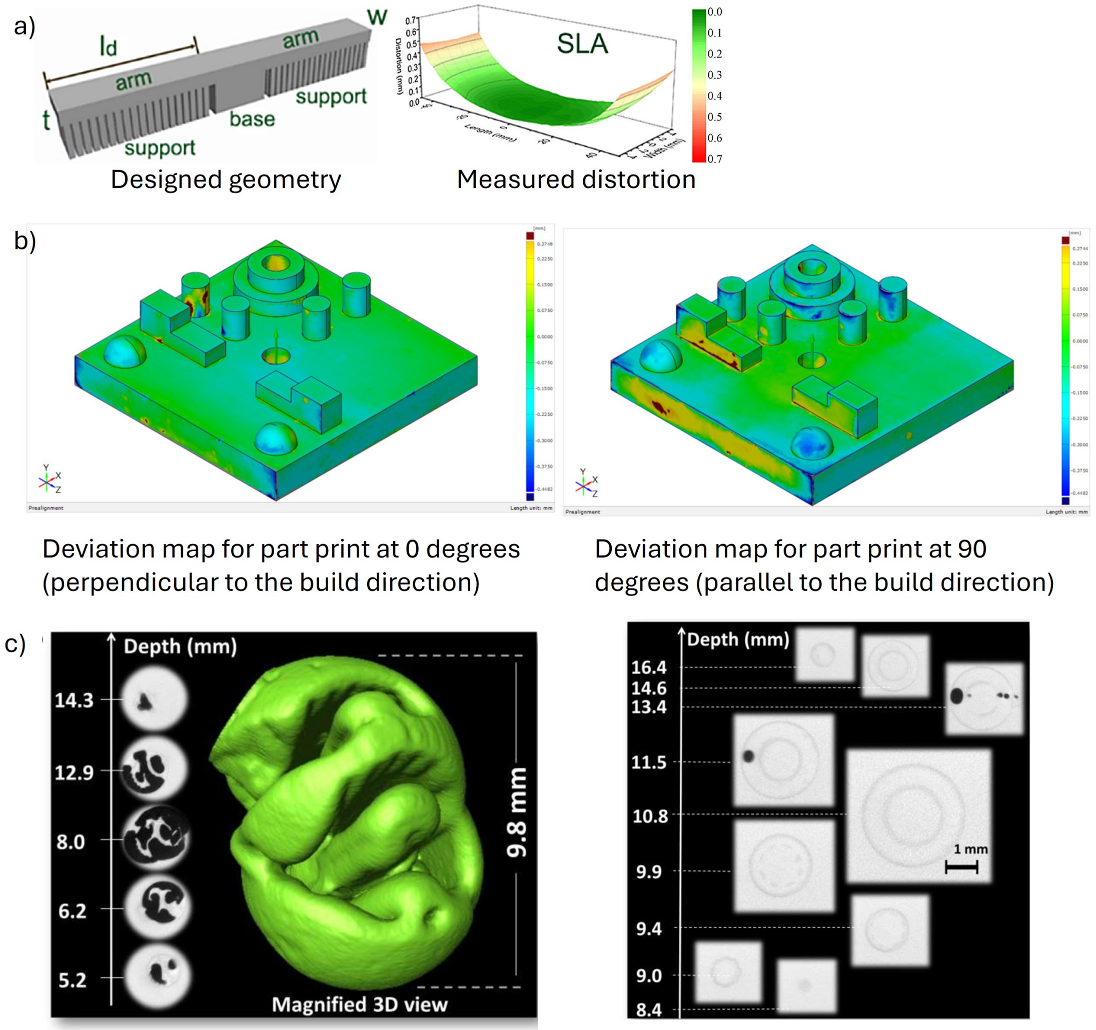

Designed geometry

Measured distortion

Deviation map for part print at 0 degrees (perpendicular to the build direction)

Deviation map for part print at 90 degrees (parallel to the build direction)

Excess resin pooling in pore as a result of a poor pore network

Incomplete pores formed due to excess resin

FIGURE 2.17: Examples of defects from SLA parts: a) warping observed for fully supported overhangs, taken from [81], b) influence of build direction on geometrical accuracy of various shapes including cylinders and spheres, taken from [93], c) types of pore based defects caused by excess resin observed with micro CT, taken from [95].

These geometric deviations depend on part orientation relative to the print direction. For example, for L-PBF lattices, struts aligned with the build direction (vertical struts) are manufactured to a higher degree of accuracy, reducing waviness, differences to the designed geometry and surface roughness compared to horizontal struts [72], [86]–[88], [99]. Arabnejad *et al.* [100], found that the vertical struts of L-PBF lattices were undersized by up to 45%, whereas the horizontal struts were oversized by approximately 130%. Similarly, L-PBF struts were found to have a mean surface roughness (Ra) of approximately 17 and 74 μm for vertical and horizontal struts, respectively [101]. Similar conclusions can be drawn for parts manufactured via SLA. Kalilayeva *et al.* [93] found that cylindrical features (like struts in lattices) were typically undersized by between 7.3 and 4.8%, depending on the angle, with cylinders parallel to the build direction (vertical), resulting in the least amount of deviation from designed dimensions (Fig. 2.17b). Similar, although slightly reduced deviations from the designed geometry were also observed for spherical parts (similar to the nodes between struts in lattices), with hemispheres manufactured with the flat face parallel to the build direction resulting in a 2.5% deviation from designed dimensions [93]. These undersized parts are thought to be due to resin shrinkage, a known phenomenon in the SLA process, which can also result in warping as a result of residual stresses [77]–[80].

L-PBF parts experience both high temperature gradients and cooling rates during manufacture, leading to residual stresses and often part warping and cracking. During part manufacture, the top layer(s) are subject to higher temperatures than the solidified layers below. The higher temperature layer(s) are prevented from expanding by these solidified layers inducing compressive residual stresses [72], [102]. Additionally, during melt pool cooling, layers are unable to contract due to the solidified layers below, inducing tensile residual stresses. When residual stresses exceed the strength of the material, this leads to plastic deformation and warping [76].

Similarly, in vat photopolymerization techniques such as multijet fusion and stereolithography, the polymerisation of resin results in warping through two key mechanisms. During polymerisation, the liquid resin is converted into a solid, resulting in an increase in density and therefore a decrease in volume [103]–[105]. This leads to layer/part shrinkage, inducing residual stresses and ultimately warping [77]–[81]. Residual stresses are also introduced due to the cyclic nature of the SLA process, during which a part is repeatedly peeled off a thin flexible film and pushed back onto it once the resin has been levelled off. This process cyclically stresses the part, potentially introducing deformations and warping [98]. Non-symmetrical curing due to laser scan patterns will amplify the warping behaviour [104]. Polymerisation reactions also produce heat as a by-product (Fig. 2.18), transferred through convection and conduction. Some of the excess heat is convected to the surrounding air, warming the chamber/environment. The rest of the excess heat is then typically conducted to the cured layers below (microns thick), resulting in further layer curing (penetration curing) and the accumulation of stresses that lead to warping. If the manufacturing technique requires a heated bed, as with microdroplet-jet printing shown in Fig. 2.18, heat transfer from the heated bed to the printed part increases the penetration curing and therefore residual stress formation [106]. Alternatively, if the post-processing method employs a heat treatment, this will induce further residual stresses, amplifying any distortions present [79]. The layer height also controls the level of penetrative curing, with a reduced layer height increasing the amount of penetrative curing that a part experiences, increasing residual stresses and therefore warping [77]. As such, both Vatani *et al.* [77] and Wiedemann *et al.* [78] determined that increasing the layer height decreased distortion, with layer heights of 0.1 and 0.15 mm resulting in maximum distortions of 2.5 and 0.7 mm, respectively, over a length of 200 mm [77]. However, increasing the layer height to decrease distortion comes at a cost of decreasing the resolution and therefore dimensional accuracy of parts in the build direction, which can in turn impact as-built properties. Chockalingam *et al.* [107] found that increasing layer height decreased the yield tensile strength, ultimate tensile strength and impact energy of samples manufactured using SLA and was thought to be due to an increase in the number and size of voids that were evident with increasing layer height.

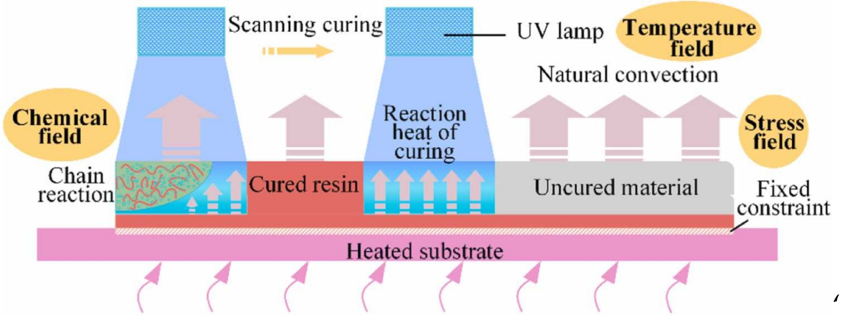

FIGURE 2.18: Polymerisation reaction of microdroplet-jet printing, a vat photopolymerisation technique showing thermal reactions that lead to residual stresses and warping. Figure taken from [106].

The methods used in L-PBF lend themselves to creating unintentional porosities, even when processing parameters are optimised, with a porosity of approximately 1% expected for lattice structures [72]. However, for a gyroid-based lattice, increasing the unit cell size was found to result in an increase in porosity to approximately 10% [108]. Increasing the cell size increased scanning paths and the time spent at each layer, allowing more pores to form before the next layer was built up. Further optimising processing parameters, however, can overcome these size scale effects. Pores form due to a number of reasons. Impurities or certain constituents within the powder may have a lower melting point than the main powder, evaporating during part manufacturing and forming gases. Gases can also be formed through gaps within the powder bed. These gases then become incorporated and entrapped into the melt pool and due to the high cooling rates form pores. Pores can also form due to the improper flow of the melt pool which could be the result of ridges/overhangs from a previous layer blocking the flow path, incomplete fusion due to insufficient energy, or the oxidation of layers decreasing wettability resulting in incomplete fusion. Porosities form stress concentrations when loaded, acting as initiation points for failure, impacting both static and fatigue properties. Dong *et al.*, [109], reported a

14% increase in elastic modulus for struts manufactured parallel to the build direction compared to struts manufactured at 35° from the build platform, attributing the difference partially due to the decrease in porosity observed, 1.95% to 0.11%. The inclined struts are supported by more unsintered powder thus reducing cooling rates. This increases the temperature of each build layer, resulting in melt pool instability, both of which contribute to the formation of hydrogen and argon pores. A higher level of porosity is observed in the lower half of the inclined struts (Fig. 2.19), increasing as the inclination decreases, further supporting the reasoning for the increase in porosity. Pores can form in SLA from gases being trapped within the resin, albeit to a much lesser extent (negligible), due to the differences in manufacturing methods and are reported to result in an increase in porosity of approximately 0.02% for a solid part [95].

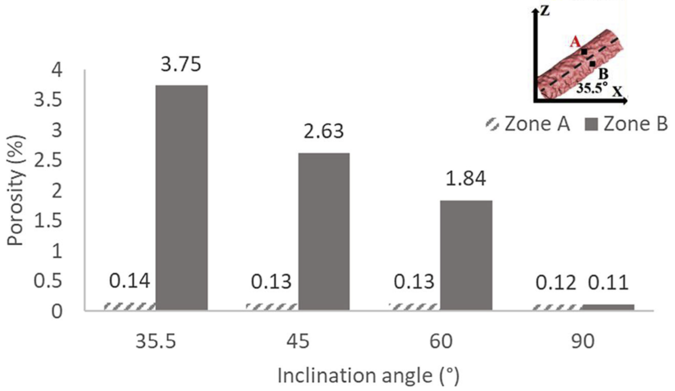

FIGURE 2.19: Variation of porosity with inclination and position for the up (zone A) and down-skin (zone B) portions of struts. Figure taken from [72] and [109].

Some level of surface roughness is expected for any process. In L-PBF, surface roughness is often due to un-sintered particles from a lack of fusion (Fig. 2.20c), adhering to solid parts [84]. Print orientation greatly impacts surface roughness, with inclined struts resulting in greater surface roughness than struts printed parallel to the build direction, Fig. 2.16f). This is mainly due to stair-stepping (Fig. 2.20a), caused by a difference between the designed geometry and the geometry possible based on scan patterns. Stair-stepping leads to an increase in surface roughness for inclined struts compared to vertical struts, with the effect amplified on the down-skin of inclined struts (Fig. 2.20d and e). The powder that supports the struts is a poor conductor of heat, leading to increased cooling times and allowing molten material to sink due to gravity and capillary force and form a drop, also known as dross, resulting in increased roughness [110]. The up-skin experiences decreased cooling times as heat is conducted through the solid and then convected away. Surface roughness can also increase due to balling (Fig. 2.20b), commonly observed when the length of the melt pool is less than twice the width, occurring when the molten powder solidifies into spheres instead of flat layers. It is caused by the surface tension of the molten sphere preventing the molten powder from joining with the solid layer below and resulting in reduced interlayer adhesion [72], [82]. Severe balling can also affect the distribution of powder on subsequent layers, impacting the build-up of parts, and potentially further increasing surface roughness. Surface roughness, regardless of how it formed, results in stress concentrations, impacting mechanical properties. Dressler *et al.*, [99], determined that there was a 20% drop in ultimate stress for struts manufactured perpendicular to the build direction compared to parallel. While as previously discussed, porosity, which is affected by print orientation, does have an impact, they showed through FE models that stress experienced by the rougher perpendicular struts was greater than for the parallel struts. Surface roughness and effects on mechanical properties are also a consideration for parts produced via stereolithography with stair-stepping, affected by build angle, being the main contributor as it is not a powdered based process and any heating effects are minimal in comparison to L-PBF so dross does not form to the same extent [97], [98], [111]. Yang *et al.* [97] found that thin flat plates manufactured parallel to the build direction resulted in a reduced surface roughness (Ra) of 3 μm compared to thin flat plates manufactured at 10 degrees to the build plate which had a surface roughness of 17 μm, over five times greater.

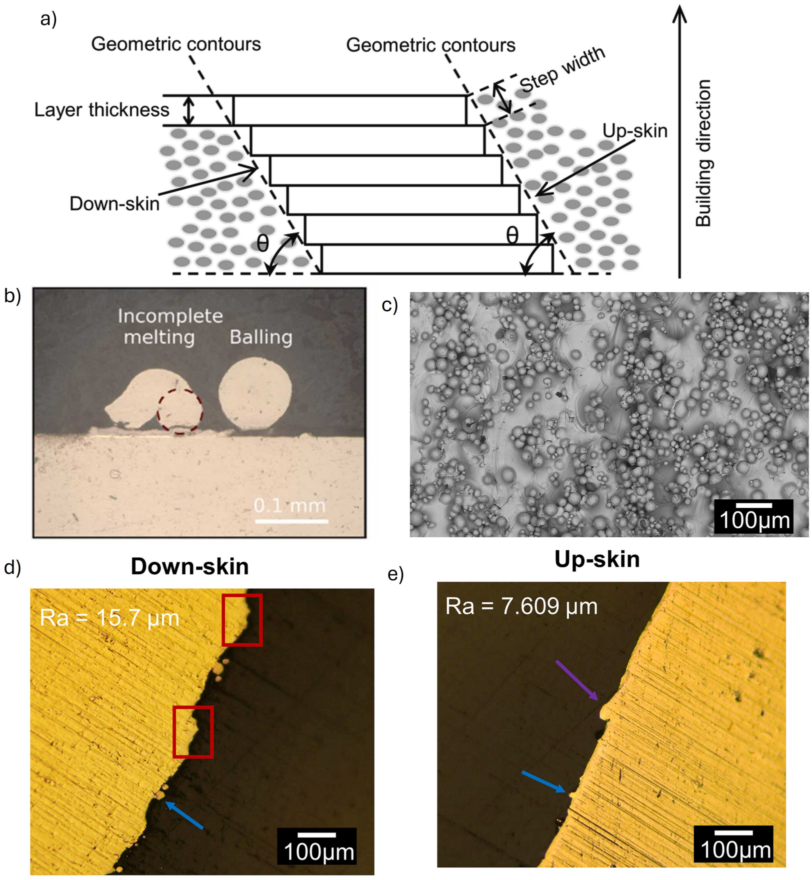

FIGURE 2.20: a) Representation of stair-stepping, seen in all forms of additive manufacture, figure taken from [110]. b) Example of balling in L-PBF manufacture, figure taken from [112]. c) Evidence of loose powder on parts, figure taken from [110]. d) increase surface roughness and dross on the down-skin, e) compared to the uk-skin, figure taken from [110].

Geometry variations such as strut waviness and variations in strut diameter are commonly observed in L-PBF lattices (Fig. 2.16c) as they are often manufactured at the limits of resolution and accuracy. It is often observed in the form of ellipsoidal struts instead of circular, and the degree of variation dependent on print orientation, with struts parallel to the build direction normally undersized (reported at 30 and 45%) and those perpendicular to the build direction oversized (reported at 54 and 128 %) [100], [113]. Although the values from the different investigations vary, the same trends are observed. Struts parallel to the build direction are typically undersized due to shrinkage, whilst struts perpendicular to the build direction are typically oversized due to stair-stepping and dross formation from the melt pool being pulled down by gravity and capillary forces. Similar trends are observed concerning strut waviness, defined as deviations of the central strut axis. Struts perpendicular to the build direction are found to have a greater strut waviness than those parallel to the build direction and this difference also decreases as the perpendicular struts become more inclined and aligned with the parallel struts. It is these perpendicular struts, which experience tensile loads during compression that fail first and initiate lattice failure, highlighting the impact of geometry variations. Eccentricity (a ratio between the semi-major and semi-minor axes of the strut cross-section), a function of strut shape and linked with strut diameter variation, is also influenced by the print orientation. Casata *et al.*, [87], determined that eccentricity, increases with inclination angle and designed diameter, with thick struts parallel to the build direction more circular and thin struts perpendicular to the build direction the most elliptical (Fig. 2.21). Increased strut diameter variation, waviness and decrease in eccentricity have all been linked to reduced mechanical properties [88]. Liu et al, [88], determined that for an octet lattice, increasing the strut waviness by 250% (normalised by representative octet lattice with a relative density of 10.6%), but keeping strut variation the same, decreased the apparent elastic modulus by approximately 40% and the compressive strength by approximately 35% (Fig. 2.16e). Additionally, increasing the strut diameter variation but keeping strut waviness the same now, decreased the apparent elastic modulus by 25% and the compressive strength by 45% (Fig. 2.16e). Strut waviness influences the apparent elastic modulus to a greater extent than the strut diameter variation and the reverse is observed for the compressive strength (Fig. 2.16e). In SLA, the main deviations/variations from the as-designed geometry are due to resin shrinkage leading to distortions and deformations as previously discussed [98], stair-stepping as in the L-PBF case, which is dependent on the layer height and is the main cause of the surface roughness evident on SLA parts and excess resin pooling within the part Fig. 2.17c [95], [96]. Liu *et al.* and Guessasma *et al.* manufactured a series of solid blocks with varying levels (0 - 60% porosity) of randomly distributed spherical voids/macro-sized pores using SLA and assessed the geometrical accuracy using X-ray micro tomography. For a porous solid (when porosity is greater than 30% as defined by Ashby and Gibson [28]), there was good agreement between the as-designed and as-built level of porosity, with differences of less than 1.5% observed. This was reflected by their compressive behaviour, which was similar to as-designed. However, for a solid with distributed pores (when the porosity is less than or equal to 30%), the geometrical accuracy was reduced with the as-built porosity up to 8% less than as-designed. This decrease in porosity is mainly due to excess resin remaining in pores due to poor pore network connectivity, not allowing excess resin to be drained/washed out of the part Fig. 2.17c. This excess resin can then also close off other pores, resulting in incomplete pores forming, further decreasing the as-built porosity (Fig. 2.17c). Even adjusting for the as-built porosity, measured mechanical properties such as elastic modulus and yield strength differed greatly from analytical models and thought to be due to strain localisation due to the excess resin, followed by cell collapse and densification. The amount of pooled excess resin can be reduced by ensuring that pores are sufficiently interconnected, a difficulty when designing randomly distributed pores as in the investigations by Liu *et al.* [95] and Guessesma *et al.* [96] but more possible if using strut-based lattices as is the case in this project.

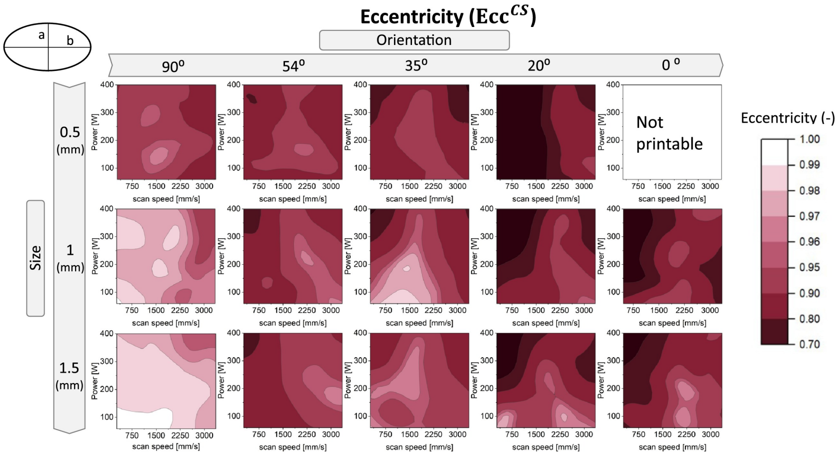

FIGURE 2.21: Variation of eccentricity with inclination angle and strut diameter, from [87].

Defects in horizontal struts decrease the apparent elastic modulus of lattices to a greater extent than defects in vertical struts, and an increase in the number of defects, surface roughness, strut waviness and non-circularity in both directions reduces the apparent elastic modulus and strength of parts [84], [88], [114], [115]. Goodall *et al.* [114] determined that even only removing 1% of struts (representative of an extreme defect), reduced the yield strength of L-PBF lattices by up to 8 MPa from 34 MPa.

Part orientation in SLA can also impact the as-built mechanical properties of parts, largely due to the difference in geometric accuracy observed at varying orientations, as discussed previously. For example, Saini *et al.* determined that for tensile dog-bone specimens, the tensile modulus was greater (approximately 1750 MPa from 1500 MPa) for parts manufactured parallel to the build direction compared to perpendicular to the build direction. This increase is due to the build layers being perpendicular to the applied load. This is also why the maximum compressive load of parts manufactured parallel to the build direction is considerably greater (40 kN compared to 10 kN) than that for parts manufactured perpendicular to the build direction. Similar patterns are observed for the flexural strength as demonstrated by Unkovskiy *et al.* [94] with flexural strengths of 135.7 and 117.5 MPa for parts manufactured parallel and perpendicular to the build direction. This difference was thought to be due to the improved geometrical accuracy observed for the parts manufactured parallel to the build direction, as with L-PBF parts. Additionally, although it is generally considered that SLA produces isotropic parts, Quintata *et al.* [91] determined that tensile dog-bone specimens manufactured parallel to the build direction had a statistically greater ultimate tensile strength and elastic modulus than samples manufactured perpendicular to the build direction. This was thought to be due to the directionality of the layer build up relative to the loading direction. It should be noted that the differences were less than 5% for both the ultimate tensile strength and elastic modulus. SLA can therefore still be considered to produce isotropic parts.

Defects are shown to considerably affect the apparent properties of lattices and are heavily dependent on geometry, particularly inclination angle. Understanding and categorising these defects in AM lattices is important for explaining mechanical properties variation as well as any trends observed between geometry types.

The testing method can also impact the apparent properties of porous materials due to machine compliance. As noted in the ASTM standard for the compressive properties of cellular plastics [116], machine compliance is present in all testing systems and is evidenced by a difference between the cross-head displacement and the displacement samples experience, potentially considerably affecting the measured response [117]–[120]. The effect of machine compliance is amplified for samples that experience small strains such as for brittle materials or if samples experience large cross-sectional area changes as they will often result in high loads increasing the non-sample machine displacement [118].

A common method for accounting for machine compliance (and recommended by the ASTM standard for compressive cellular plastics [116]), involves running a test without a sample but under the same conditions samples are subject to. The measured displacement for each force value should then be subtracted from the test data. This method is simple to apply and therefore commonly used. Alternatively, strain gauges or differential variable reluctance transducers can be used to measure the strain of samples directly [119]; these are often used in the characterisation of bone samples as they are subject to low strains [17], [119]. Although directly measuring strain using strain gauges accounts for machine compliance, they can only be used for a limited range of strain and under normal operating conditions. Finally, optical strain measurement techniques such as point tracking and digital image correlation can be used to indirectly measure strain and account for machine compliance [117], [119]. Both techniques involve applying a pattern to the surface of a sample and tracking displacement throughout the test with cameras. Additionally, optical strain measurement techniques are able to account for three more sources of error, highlighted in Fig. 2.22. Friction between the sample and platens can cause sample barrelling (Fig. 2.22a) where the contact surfaces do not experience strain while the rest of the sample does, leading to a non-uniform stress state, an assumption made throughout the test. Non-uniform loading (Fig. 2.22b), caused by misalignment of platens or non-parallel contact surfaces, results in inaccurate strain measurements and can lead to localised failure (Fig. 2.22c) meaning properties might be determined outside the elastic region. Marter *et al.*, [117], [121] demonstrated that point tracking accurately captures the surface strains of a porous material, with results comparable to digital volume correlation, the 'gold standard' for strain measurement. With points relatively easy to apply to surfaces, this is the preferred technique for porous materials.

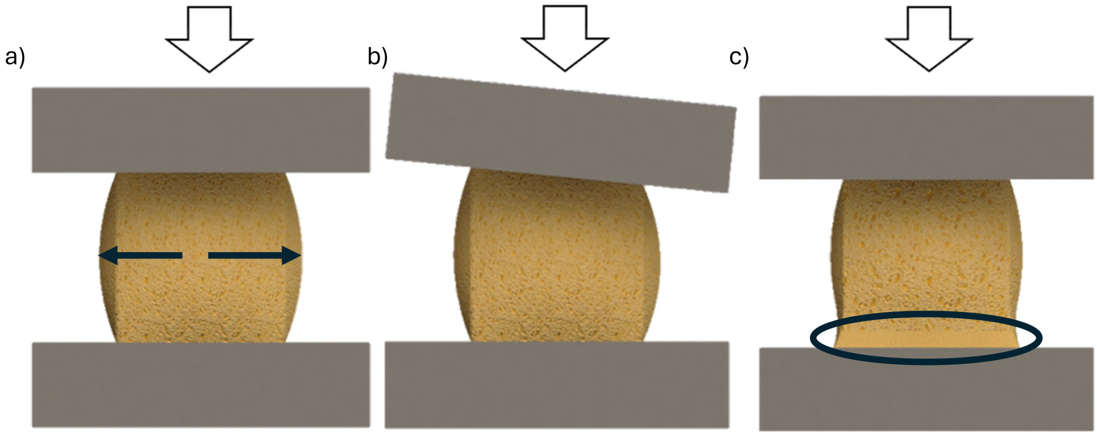

FIGURE 2.22: Figure adapted from [117]. a) High friction at contact surfaces causes barrelling in the sample, b) misalignment between platens and sample causes non-uniform loading and c) localised crushing/failure of the sample

2.4 Conclusion

Natural porous metamaterials such as cancellous bone have been shown to occupy a wide material property space due to geometric and mechanical property optimisation that has occurred over millennia. The large range of mechanical properties observed for cancellous bone is partially due to variations in architecture. Previous work determined that the semi-random variation in density observed in cancellous bone improves failure properties such as energy absorption whilst maintaining elastic properties such as apparent elastic modulus in comparison to fully regular porous materials like honeycomb structures. Building upon this, creating a uniform and non-uniform porous metamaterial from simplified unit cells is beneficial as these types of geometries are comparatively easy to manufacture whilst also having analytical models that can predict the as-built behaviour. Such geometries are commonly manufactured using additive manufacturing techniques. Several types of polymeric based additive manufacturing techniques are presented, and stereolithography is highlighted as a suitable technique for producing the porous metamaterials required in these investigations. As with any manufacturing technique, additive manufacturing presents its own unique series of commonly observed defects, with some more prevalent for porous metamaterials as they are generally at the limit of manufacturability. Deviations from the designed geometry are frequently observed including greater than designed strut diameters and warping. Such defects influence the apparent response of porous materials with warping altering the boundary conditions leading to non-uniform loading. It is important that defects are identified and characterised for authentic mechanical behaviour to be captured, allowing tailored non-uniform porous metamaterials to be designed and manufactured with predictable responses.

Non-uniform lattices built up from simplified unit cells are advantageous for lightweight load-bearing applications as in aerospace or biomedical applications for engineered tissue bone scaffolds, where matching the stiffness and geometry to the surrounding native bone is crucial for function [122]. The first step towards expanding the material property space with such structures is characterising their repeatability and understanding the effect distortions have on the initial compressive elastic modulus. This is the focus of the following chapter.

Chapter 3

Additively Manufactured Porous Metamaterials and the Mechanical Effects of Distortion

3.1 Abstract

Biological porous materials like cancellous bone have evolved over millennia to optimise both physical and mechanical properties. Such materials occupy a large material property space, efficiently balancing properties to achieve certain performance requirements. This efficiency is difficult to replicate using synthetic materials. Additively manufactured, (AM) porous metamaterials could address this shortcoming but shape distortions like warping are common, affecting boundary and loading conditions, altering the apparent mechanical response. In this study, it is hypothesized that Winkler's elastic foundation model can be used to analyse the effects of warping on the apparent response of porous metamaterials. To test this hypothesis, stereolithography was used to produce porous metamaterials made up of repeating body-centred cubic (BCCz, 30 x 30 x 30 mm) lattices with integrated endplates. Height distortions on endplates resulting from AM were measured, and lattices were quasi-statically compressed with endplates either adhered or unadhered to the loading platens in order to observe the effects of uniform and non-uniform loading on the apparent mechanical response. Optical point tracking was used to note local strain variation. Endplate distortions were observed ranging from 235 to 450 µm and resulted in large variations in the local strain in unadhered compressed samples. The elastic foundation model accurately predicted the reduced initial apparent stiffness due to distortions and can also be used to determine the pre-loading or dimensional tolerances required to ensure a given apparent stiffness. These outcomes

are useful for the development and manufacture of load-bearing porous structures, such as bone tissue scaffolds for regenerative medicine, for which reduced apparent stiffness is detrimental to performance and function.

3.2 Introduction

Natural porous metamaterials occupy a large material property space. They balance both physical and mechanical properties and through evolution, are efficiently tailored for each application. Additive manufacturing can be used to develop complex geometries such as lattices that attempt to match this property space and efficiency for synthetic material for a range of applications including aerospace, automotive, safety and biomedical. However, defects such as distortions are commonly observed in additive manufacturing, altering boundary conditions and therefore the apparent behaviour of synthetic porous metamaterials. Understanding and characterising these differences is essential to being able to consistently create tailored synthetic porous metamaterials with predictable properties, especially when needing to match the mechanical and geometrical properties as with engineering bone tissue scaffolds [122].

This study aims to assess the effects of distortion and post-processing on the apparent elastic modulus. Following this section’s relevant background and research justification, the methodology for sample manufacture, mechanical and geometric characterisation (including distortions) is detailed in Section 3.3. This study assesses the impact that distortion has on the boundary conditions of porous metamaterials using Winkler’s elastic foundation model and how this alters the apparent mechanical response, focusing on the initial stiffness in Section 3.4.1. To the author’s knowledge, this use of the elastic foundation model has not been explored. This is followed by a brief discussion regarding the difference post-processing methods have on mechanical and geometric properties such as strut diameter and a more in-depth analysis regarding inherent intra- and inter-sample variability in Section 3.4.2. Key results are summarised in Section 3.5 with potential use cases for the adapted elastic foundation model.

3.3 Methodology

3.3.1 Porous Metamaterial Fabrication

Lattices of BCCz (body-centred cubic with an extra z direction strut, Fig 3.1) unit cells were manufactured using a Formlabs Form3 stereolithography printer with Rigid10K resin (Formlabs, Massachusetts, United States of America, see Appendix 10 for material data sheets), a glass-particle reinforced (55-75 % weighting) acrylic based resin (E_s = 10 GPa) [123] and a layer height of 0.05 mm. Parts were manufactured with a 405 nm wavelength laser with a spot size of 85 μm. Other parameters including scan time per layer and scan speed could not be altered and were set by the manufacturer. This geometry is stretching-dominated when the loading direction is aligned with the extra z strut and is, therefore, stiffer for the same relative density compared to bending-dominated unit cell geometries, essential for light-weighting applications as in aerospace and biomedical industries [124]. Additionally, the geometry is self-supporting ensuring compatibility and printability with SLA. Samples were post-processed to remove excess resin and induce further curing either via UV exposure only (60 minutes, referred to as PP1 subsequently, n = 11) or using both heat and UV exposure (held at 60 °C for 120 minutes and cured with UV light for 60 minutes, referred to as PP2 subsequently, n = 11). Prior to curing, samples were washed using IPA in an ultrasonic bath to remove excess resin for 20 and 12 minutes for PP1 and PP2, respectively and then left to air dry for at least 30 minutes. PP2 samples were placed under a vacuum of 5 Pa for 120 minutes following washing and prior to heating. These conditions were chosen based on an assessment of several different conditions (the results of which can be found in Appendix 7.1) that concluded PP1 and PP2 resulted in the minimum and maximum apparent elastic modulus, respectively.

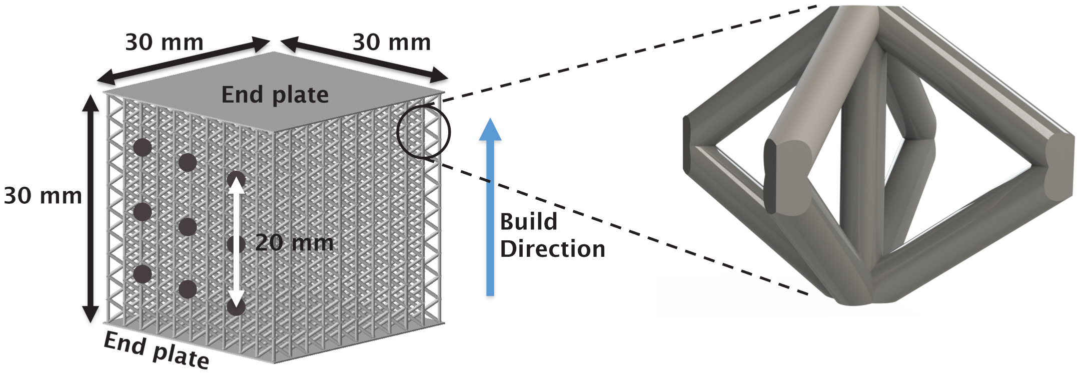

FIGURE 3.1: BCCz lattice where vertical struts are aligned with the build direction and endplates protect the top and bottom struts. Dots marked on the front back for optical strain measurement with a maximum virtual gauge length of 20 mm. Enlarged view of single BCCz unit cell shown.

The BCCz lattices were manufactured with an overall unit cell size (L) of 3 mm, a designed strut diameter (d_{ang} and d_{vert}) of 0.46 mm for all struts and endplates on the top and bottom faces (endplate dimensions = 31 x 31 x 0.2 mm, width, depth and thickness) for improved load distribution. Samples were made up of 10 unit cells in each direction (overall dimensions: 30 x 30 x 30 mm, the same order of magnitude as used in the testing standard of rigid polymers [125]) to minimise size-scale and random defect effects [6], [28], [41]. White *et al.* suggest that 1000 struts are required to overcome the influence of random defects, resulting in a ratio between standard deviation and average apparent elastic modulus of 0.026 [6]. From Eq. 2.2.10, the apparent elastic modulus and standard deviation for this investigation are therefore predicted to be 199.7 and 5.2 MPa, respectively. The geometry was chosen to ensure manufacturability (minimum recommended manufacturable diameter is 0.2 mm) and result in a designed relative density and apparent elastic modulus similar to that of low density cancellous bone [126]. Matching the geometric and mechanical environment of the surrounding tissue is essential for the development of bone tissue scaffolds to encourage bone growth.

3.3.2 Mechanical Testing and Geometry Characterisation

Samples (n = 9 for PP1 and PP2) were quasi-statically compressed (Instron 5569 equipped with a 50 kN load cell and loaded at 1 mm/minute (to minimise visco-elastic effects [119], [127] and similar to a testing standard for rigid polymers [125]) with a 20 N preload and a spherically seated upper platen) and both platen (using overall system displacement) measurements and optical point tracking [117] were used to measure overall strain and local strain distributions. For point tracking, nine dots (maximum gauge length of 20 mm, Fig. 3.1) were marked onto two opposing faces (front and back) of the sample using a marker pen and stencil to ensure consistency. Manta cameras [2452x2056], 50 mm or 105 mm lenses (Nikkor) and Nila lights, along with MatchID software (MatchID, Ghent, Belgium) [128] were used to capture images of the sample during testing at a rate of at least four frames per second. At least 10 images were captured prior to loading and analysed using MatchID (MatchID, Ghent, Belgium) [128] to determine the subset and step sizes for which noise converged to values of less than 100 µstrain (details are given in Appendix 7.2).

Force data and nominal cross-sectional area from average width and depth measurements (three measurements per direction, measured with SPI callipers (Swiss Precision Instruments, accurate to 0.02 mm)) were used to determine global stress. Strain for each virtual extensometer was calculated in MatchID (MatchID, Ghent, Belgium) [128] and plotted against stress with a linear regression analysis performed from 0 to 0.2% strain to determine apparent elastic modulus. If the specimen experienced an initial toe-in region (most likely due to incomplete contact between the specimen and loading platen), the line of best fit from the linear regression would result in a non-zero intercept which, in a procedure adapted for NPL's 'Measurement Good Practice Guide No. 98: Elastic Modulus Measurement', was used to shift the stress-strain data to account for the toe-in [129]. Further linear fits and data shifts were performed until the toe-in region was removed before a final linear fit was performed, the code for which can be found in Appendix 7.5.

For both post-processing methods, the endplates of six samples were adhered to flat metal plates using a cyanoacrylate based adhesive to ensure uniform contact. Three other samples acted as a control and were not adhered. Selected endplates (n = 3) from both post-processing methods were imaged using an Alicona infinite focus microscope (at 2.5x magnification, Bruker Alicona, Graz, Austria) to evaluate height distortions. A 3D general image field was captured over the full surface of the endplates through a vertical distance of at least 1 mm ensuring that all features were in focus. The 3D image of the surface was then viewed in the pseudo colour view (as in Fig. 3.4) with the varying colours corresponding to the height of the sample. The range of the colour bar was set manually, ensuring that the full potential range of the colour bar was evident on the sample. This was then used to determine the maximum total height distortion experienced by the sample for use with the analytical model as described in Section 3.3.3.

The strut diameters of selected samples from both post-processing methods (PP1 and PP2, n = 3 for both) were measured using optical microscopy (Olympus BX41M LED microscope at five times magnification, Olympus, Toyko, Japan). For each strut type (angled struts, external vertical struts and internal vertical struts), 10 images at random locations on at least two faces were captured. The images were analysed with ImageJ [130] to measure the strut diameter at three locations per image (example measurement shown in Fig. 3.2), for a total of 30 measurements per strut type per sample.

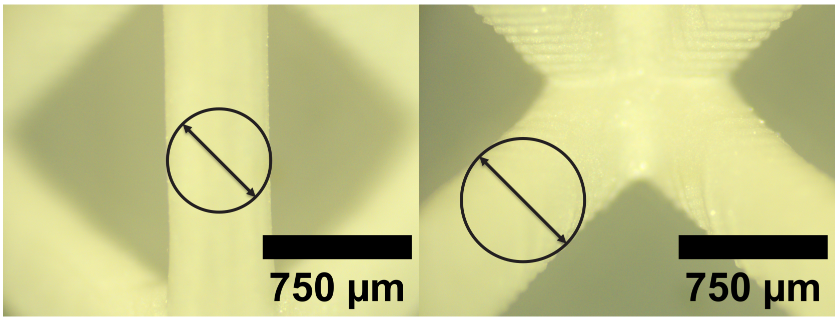

FIGURE 3.2: Strut diameter measurement example for vertical and angled struts

The cross-sections of struts from varying locations (at least 32 internal and external struts) of two samples from each post-processing method were nano-indented with a Berkovich diamond tip. This was to investigate the intra- and inter-sample base material modulus variation to determine if there was a trend with strut location and link it to the apparent elastic modulus variation observed. Samples were embedded in cold-cure epoxy (Epoxfix) and cut in half with the plane of cut orthogonal to the build direction. The top surface of the sample was ground and polished with a rotary polisher (Spectrographic OmegaPol) and emery paper with increasing grit size (up to 2000 grit) and finished with a 1 µm diamond suspension polishing fluid. The nanoindentation was performed on a MicroMaterials Vantage system [131] in depth control to a maximum of 1µm, with a loading rate of 0.5 mN/s, an unloading rate of 1 mN/s and a 40 second dwell at the maximum load. Another 40 second hold was also applied after 90% of the unloading to account for thermal drift.

The Oliver and Pharr method [132] was used to calculate reduced elastic modulus, E_r from the unloading curve of the indents from which the base material modulus, E_s was determined using Eq. 3.3.1 [132], [133]

$$E_s = \frac{(E_r E_i) \cdot (1 - v_s^2)}{E_i - E_r(1 - v_i^2)} \qquad \text{(Eq. 3.3.1)}$$

where E_i is the modulus of the diamond indenter (1141 GPa), v_i is the Poisson ratio of the indenter (0.07) and v_s is the Poisson ratio of the base material (taken as 0.35 [7]).

3.3.3 Winkler's Elastic Foundation Model

In this study, it is proposed that Winkler's elastic foundation model [134] can be used to account for the effects of warping commonly observed in AM. The elastic foundation model predicts the load required to deform an elastic material of a specified thickness with a rigid indenter for a set deformation depth and indenter geometry [134]. Since it was developed in 1867, it has been used in a variety of applications including quantifying the contact of a joint on cartilage, modelling soil-pipe interactions and understanding the behaviour of railway tracks and will now be applied to porous metamaterials [135]–[137]. The elastic foundation model assumes that the deformed elastic material is made up of independent springs with the Poisson effect ignored. Assumptions that are true for the lattice as the height/width of the sample is much greater than the thickness of the height distortion, the layer is sufficiently thin for the elastic foundation model to still apply [138]. The shape of the height distortion in lattices is equivalent to that of a dome, similar to the elliptic paraboloid of the indenter assumed in the elastic foundation model when the paraboloid is axisymmetric (Fig. 3.3a). The height distortion geometry places the peak of the dome in the bottom right-hand corner of the sample which, compared to a situation where the dome is in the centre (Fig. 3.3b), increases the radius of the dome at the base so the change in contact area under compressive deformation is more gradual (Fig. 3.3c).

Applying the elastic foundation model to the lattice geometry, with an adjusted dome shape results in Eq. 3.3.2, the full derivation of which is shown subsequently.

$$P = \frac{E\pi x^2}{w + d_h} \cdot \frac{w^2 + d_h^2}{8d_h} \qquad \text{(Eq. 3.3.2)}$$

where P is the applied force, E is the apparent elastic modulus of the lattice, x is the displacement as a result of the force P, w is the width, depth and height of the cubic lattice and d_h is the maximum height distortion of the domed distortion. The geometry assumed by the elastic foundation model, shown in Fig. 3.3a, can be adapted to represent the geometry of the lattice with the height distortion, as shown in Fig. 3.3b.

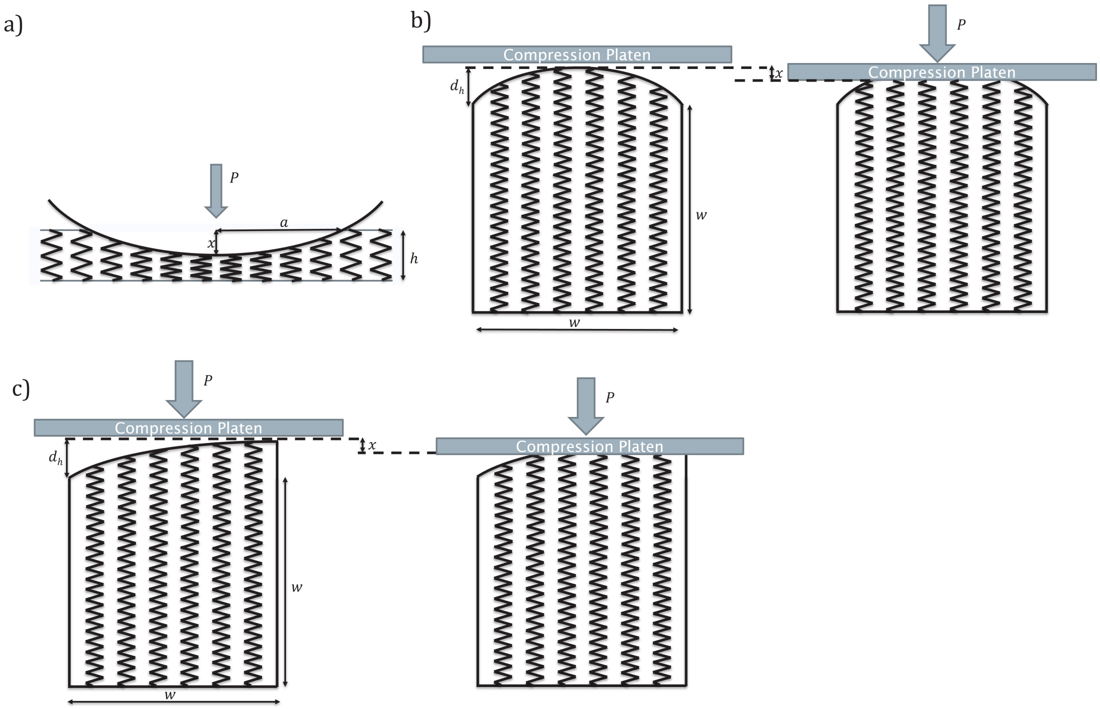

FIGURE 3.3: a) Elastic foundation model assumed geometry. b) Elastic foundation geometry adapted for the height distortion in the lattices with the peak of the dome in the centre. c) Elastic foundation geometry adapted for the height distortions in the lattices with the peak of the dome at the corner of the sample. P is applied force, x is the displacement of the indenter as a result of force P, a is the semi-major axis of the indenter at displacement x, h is the thickness of elastic material, d_h is the maximum height distortion of the dome and w is the width, depth, and height of the cube.

Through integration (see Appendix 7.3 for full integration), and following the nomenclature in Fig. 3.3a, the elastic foundation model for an axisymmetric elliptic paraboloid where the major and minor semi-axes (a) are equal, is:

$$P = \frac{E\pi a^2 x}{2h} \qquad \text{(Eq. 3.3.3)}$$

The semi-major axis can be derived from the displacement and the radius of curvature (R_c) of the indenter as:

$$a = (2xR_c)^{\frac{1}{2}} \tag{Eq. 3.3.4}$$

Replacing a in Eq. 3.3.3 gives

$$P = \frac{E\pi x^2 R_c}{h} \tag{Eq. 3.3.5}$$

where h is the height of the elastic material in the elastic foundation model, and therefore the initial height of the springs. In the lattice case (Fig. 3.3b), when $w \gg d_h$, the initial height of all the springs is assumed to be the same and is $w + d_h$, so Winkler's formula now becomes

$$P = \frac{E\pi x^2 R_c}{w + d_h} \tag{Eq. 3.3.6}$$

To derive the indenter radius of curvature, R_c, the dome can be assumed equivalent to a cap of a spherical dome, and so

$$R_c = \frac{(\frac{w}{2})^2 + d_h^2}{2d_h} \tag{Eq. 3.3.7}$$

where $\frac{w}{2}$ is the radius of the dome at the base and d_h is the height of the dome and therefore equal to the maximum height distortion. Winkler's formula then becomes:

$$P = \frac{E\pi x^2}{w + d_h} \cdot \frac{(\frac{w}{2})^2 + d_h^2}{2d_h} \tag{Eq. 3.3.8}$$

This is the case when the peak of the dome is in the middle of the endplate (Fig. 3.3b). If, however, the peak of the distortion is in the corner of the sample (Fig. 3.3c), the change in contact area would be more gradual as the radius of the dome at the base would double. Adjusting the integration for the new shape reveals that the force is a quarter of that for a full dome (see appendix 7.4 for full integration). This geometric change results in Equation Eq. 3.3.2.

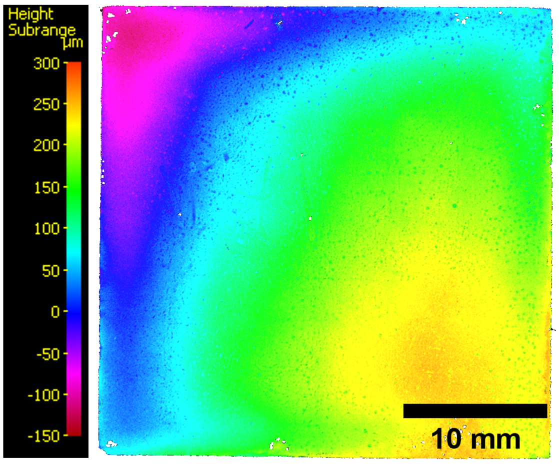

FIGURE 3.4: Typical height distortion of top endplate, showing an off-centred dome-like pattern. Maximum height distortion for this example is 450 μm.

3.4 Results and Discussion

3.4.1 Endplate Distortions

Evidence of endplate distortions were seen on all samples (representative plot shown in Fig. 3.4), with a range of 235 – 450 μm maximum height difference observed, comparable to that observed in literature for L-PBF geometries which range from approximately 20 to 600 μm [73]–[76]. The height distortion observed takes the shape of a dome with the peak in the corner (bottom right in Fig. 3.4), similar to the height distortion used in the adapted elastic foundation model. The height distortion on the endplate is likely to result in non-uniform contact and therefore non-uniform load distribution during compression, evidenced by comparing the stress-strain plots from local optical strain measurements, Fig. 3.5.

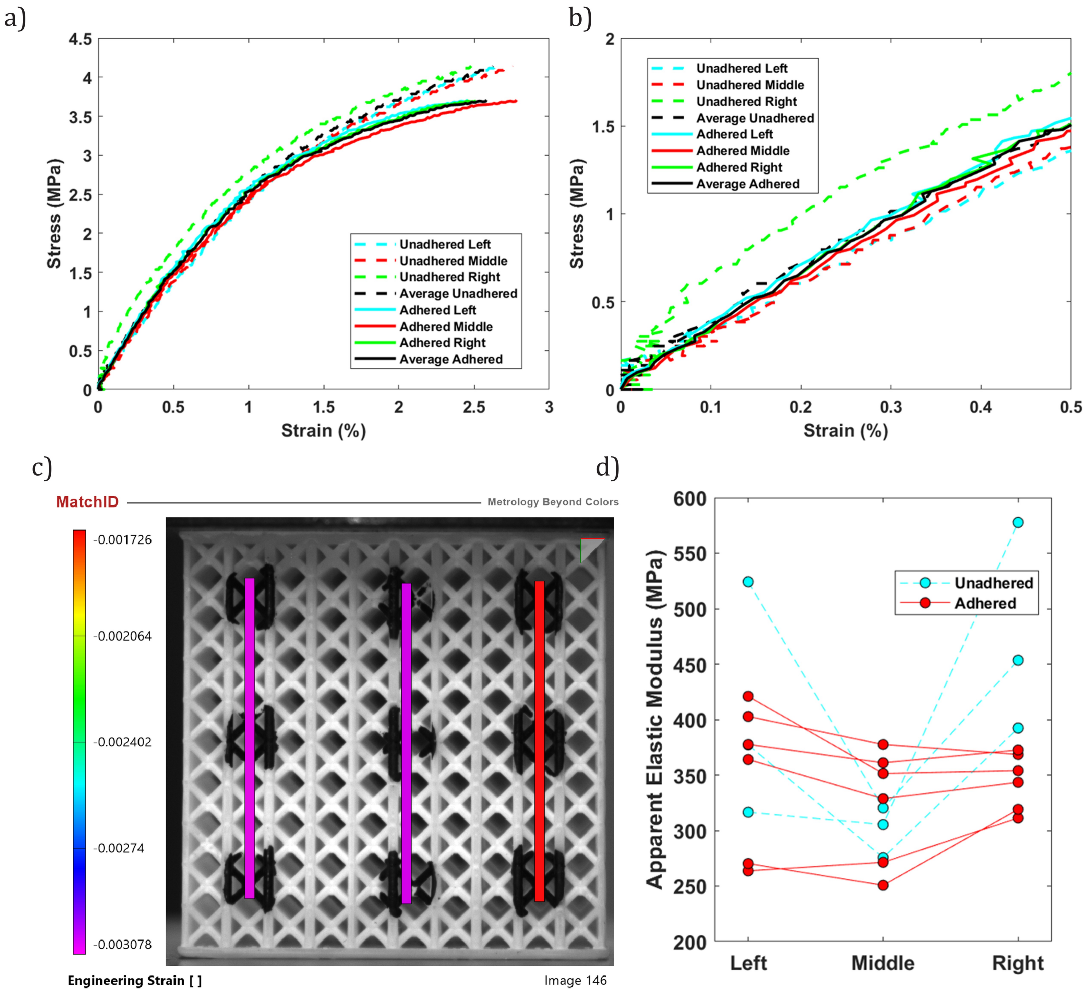

FIGURE 3.5: a) Representative stress-strain plots for both unadhered (dashed lines) and adhered (solid lines) PP2 samples up to maximum load and b) up to 0.5% strain. Representative local strain results are shown in c) and the result of the increased spread in local strain is reflected by d) the local apparent elastic modulus. Average and standard deviation (SD) of all adhered (red) and unadhered (blue) samples are 339.4 MPa and 49.3 MPa and 393.6 MPa and 104.7 respectively.

Even with the compliant 'toe-in' region removed, the local stress-strain plots from the unadhered samples vary more between each other than the adhered samples. For a given stress, the adhered samples experience very similar levels of strain (Fig. 3.5b, solid lines) implying that they experienced uniform contact and load, a response not seen for the unadhered sample (dashed lines). In the representative optical strain results in Fig. 3.5c, the right extensometer experiences the least compressive strain whilst the left and middle extensometers experience similar high compressive strains for the same stress, almost twice that of the right extensometer. This suggests that due to the height distortion, the left and middle of the sample were loaded first. This is reflected by the local apparent elastic modulus results in Fig. 3.5d. The local elastic moduli vary across the sample with the middle of the samples typically exhibiting a reduced modulus due to high strains, an important observation as a uniform load distribution is assumed when calculating apparent properties. The adhered samples, which experience more uniform contact and loading show similar elastic moduli across the sample. The degree of variation in the adhered sample is minor in comparison. It could be attributed to several reasons including, variation in strut diameters, potential changes in the transitional geometry when going from unit cells to the endplates, variations in adhesive distribution or the presence of defects.

The effect of height distortions on the initial behaviour and its effect on the apparent compressive response of unadhered samples can be estimated using the adapted version of the elastic foundation model (Eq. 3.3.2). The cube width and height without distortion were taken as 30 mm (i.e. as-designed), and E was taken as 353.22 MPa with a standard deviation of 58.7 MPa, the average as-built apparent elastic modulus for the six PP2 samples (an average is taken across the three virtual extensometers for the front and back faces, which are then also averaged together to give an average per sample). Crosshead displacement was used as the elastic foundation model predicts the global response and Eq. 3.3.2 was fitted to the experimental force-displacement data using MATLAB's curve fitting toolbox to estimate the height distortion. Initially, the analytical model was fitted over the full data range, however, the model is only valid whilst the displacement is less than or equal to the maximum height distortion. The maximum displacement over which the model was fitted was therefore compared to the calculated maximum height distortion. If this difference was greater than 1 μm, the maximum displacement over which the model was fitted was set to the calculated maximum height distortion with the process repeated until the difference was less than 1 μm.

The elastic foundation model agrees with the experimental data showing an initial compliant region until the maximum height distortion (≈0.35 mm for this particular sample) and deviates thereafter. In contrast, the adhered sample is relatively linear. For many applications, the response in this initial region is crucial and deviations from the designed behaviour can be detrimental to performance, for example in bone scaffolds for regenerative medicine [100], [139]–[141]. According to Wolff's law and the mechanostat model, bone grows in response to loading with strains approximately between 0.15% and 0.3% strain resulting in bone modelling that increases bone mass [13], [142]–[144]. Strains less than 0.15% are likely to result in bone resorption, while high levels of strain above 0.3% can result in fractures. Ensuring the mechanical response of lattices is within the optimal physiological strain range, as designed and predicted, is key to tissue repair in synthetic bone scaffolds. The analytical model can also be used to determine the effect of height distortions on the apparent elastic modulus within this physiological range.

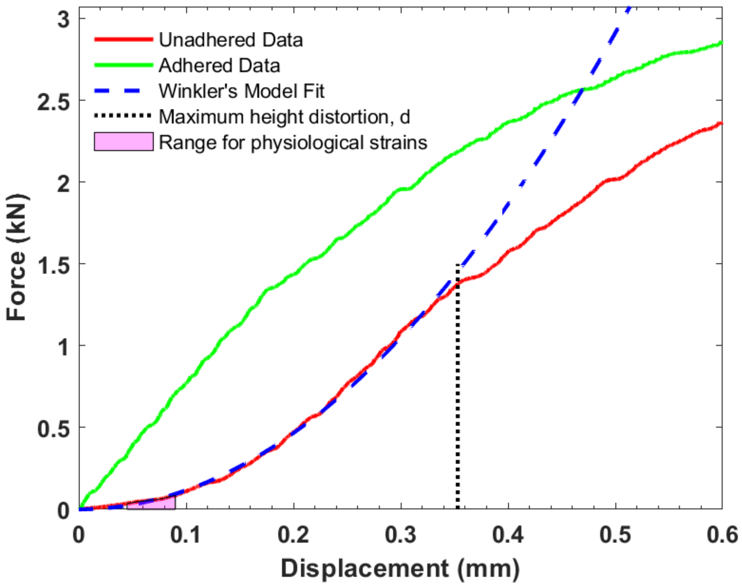

FIGURE 3.6: Representative compressive force-displacement of adhered (green) and unadhered (red) samples with adapted Winkler's model prediction shown, which is valid until the displacement equals the maximum height distortion (d, black dashed line). Also shown (purple) is the range of physiological strains for bone growth on tissue scaffolds.

Using the adapted elastic foundation model (Eq. 3.3.2), for a height distortion of 450 μm (in line with the representative height map in Fig. 3.4), the apparent elastic modulus for the example unadhered sample shown in Fig. 3.6 between 0.15% and 0.3% strain is 41 MPa, an order of magnitude lower than the as-built apparent elastic modulus of 353.22 MPa for adhered samples. Additionally, if the boundary conditions and loading between the surrounding tissue and scaffold are unknown and do not match the controlled test conditions, the effects can be estimated using the elastic foundation model. While the present work analyses a specific case of lattice geometry and distortion, the following outcomes apply to lattice structures in general:

- The difference between as-designed and as-built geometries is important because minor height distortions can greatly affect the initial stiffness.
- The elastic foundation model can be used effectively to predict the influence of height distortions on mechanical response, helping to derive an acceptable height distortion tolerance.
- For applications where the initial mechanical response is critical to performance, mitigation procedures such as changing the interval over which modulus is calculated, adhering specimens to a flat plate or increasing the targeted as-designed mechanical properties can be applied to correct for the height distortion.

- When using optical strain measurement techniques, the loading response of adhered samples is reflective of more uniform loading due to more controlled boundary conditions.

3.4.2 Post-Processing Variations

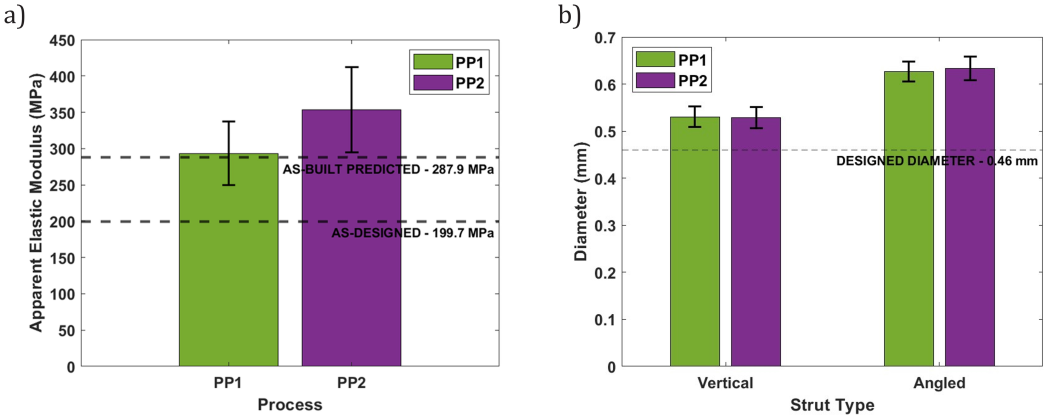

FIGURE 3.7: a) Average apparent elastic modulus (n = 6) with error bars noting one standard deviation for PP1 and PP2 post-processing procedures. As-designed and as-built moduli predictions are from the geometry specific analytical model (Eq. 2.2.10) from Zhang *et al.* [40]. b) Variation in strut diameter as a function of strut type and post-processing procedure, compared with a designed diameter of 0.46 mm.

As shown in Fig. 3.7a, the apparent elastic modulus of both post-processing methods, PP1 and PP2, was greater than as-designed, predicted to be 199.7 MPa using Eq. 2.2.10, and assuming an elastic modulus of 10 GPa for the base material as specified by the manufacturer. The analytical model used to predict apparent elastic modulus is heavily dependent upon geometry, suggesting that the as-built geometry differs from as-designed, as confirmed by strut diameter measurements (Fig. 3.7b) from micrographs. For both post-processing methods, there are two distinct average strut diameters corresponding to the two types of struts in the unit cell geometry: vertical and angled. The as-built strut diameter was larger than designed (0.46 mm, equivalent to a relative density of 12.56% from Eq. 3.4.1), at 0.53 (SD = 0.024) and 0.63 (SD = 0.024) mm for the vertical and angled struts, respectively, resulting in an average as-built relative density of 23.86% and 24.79% for PP1 and PP2, Eq. 3.4.1. The slight difference between the calculated as-built relative densities is due slight differences that are not represented by the averages due to rounding. The increased strut diameter from as-designed for both the vertical and angled struts is partially likely due to the designed diameter not being an integer multiple of the laser spot size, it would need to be either 0.425 mm or 0.51 mm. Additionally, small features, like the struts are likely to be greater than designed due to the forces experienced by the part during manufacture. Parts manufactured on inverted SLA printers like for the Form 3, experience two types of print force; peel forces from when the cured part is being removed from the flexible film of the resin tank and compressive forces when the part is returned to the flexible film after resin mixing [98]. Both the peel and compressive forces can cause layer shifting and part deformation, decreasing dimensional accuracy and increasing the minimum printable feature size [98], [145]. Resin viscosity can also impact the dimensional accuracy of parts, if too low, then smudging or resin shrinkage may occur [146], but, if too high, the resin may not level properly between layers [147]–[149]. Finally, exposure time and energy and dwell times between layers can impact dimensional accuracy with over exposure causing distortions [150]. At the time of sample manufacture, the author was not able to modify print settings beyond layer height, orientation and support and as such had to use the manufacturer-optimised settings, optimised for speed and dimensional accuracy and less likely to cause the deviations from as-designed dimensions observed here.

$$\frac{\rho^*}{\rho_s} = \frac{(1+4\sqrt{3})\pi}{4} \cdot \left(\frac{d}{L}\right)^2 - \frac{11\pi}{6} \cdot \left(\frac{d}{L}\right)^3 \qquad \text{(Eq. 3.4.1)}$$

The as-built diameter of the angled struts is greater than that of the vertical struts because of the cross-sectional geometry. The cross-section of the vertical struts is completely circular – the same shape as the laser. However, the cross-section of the angled struts is an elongated oval and is made up of more laser path lines, accumulating dimensional inaccuracies. Additionally, the angled struts experience stair-stepping (Fig. 3.8), and excess material from the ‘overhang’ can partially merge with the layer below, increasing the as-built diameter and surface roughness, a common result of stair-stepping [72], [82], [110], [151].

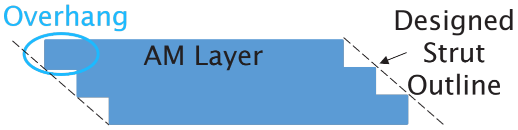

FIGURE 3.8: Stair-stepping diagram for angled struts

The as-built strut diameter measurements can be used to update the as-designed apparent elastic modulus (predicted to be 287.9 MPa using Eq. 2.2.10), which aligns more closely with the average apparent elastic modulus of PP1 but is still less than the average apparent elastic modulus of PP2 (Fig. 3.7a).

The average apparent elastic modulus of PP2 samples (353.22 MPa) is greater than PP1 samples (293.46 MPa), however, the differences between the two groups are within the standard deviation of 43.8 and 58.7 MPa for PP1 and PP2 respectively. Given these means and standard deviations, a sample size of 13 would be required to determine if there was a statistical difference between the two means with a two-sample t-test with a power of 0.8 and alpha of 0.05 (using MATLAB's 'samplesizepwr' function from the Statistics and Machine Learning Toolbox). There are, therefore, not enough samples in this investigation for any statistical analysis. This variation is greater than expected based on the conclusions of White et al [6], who studied L-PBF face-centred cubic and body-centred cubic stainless-steel lattices and determined the influence of the number of struts on the variability of apparent elastic modulus and strength with relative density. The coefficient of variation is 0.16 and 0.13 for PP1 and PP2, respectively, an order of magnitude greater than the 0.026 expected. White *et al.* note that for more brittle materials (as in this case), variability may increase as the individual struts are less damage and defect tolerant. However, the apparent elastic modulus should not be affected by failure mechanisms, so the increase in variability ought to be minimal. Variations in strut diameter, although modest, contribute to a varied response within and between samples. Using the BCCz specific geometry analytical model (Eq. 2.2.10) and the variation in strut diameter (standard deviation of 0.022 and 0.021 for the vertical and angled struts in PP1 and 0.023 and 0.025 for the vertical and angled struts in PP2, Table 3.4.1), the range of predicted moduli can be determined as ±26 and ±28.4 MPa for the PP1 and PP2 groups respectively (Table 3.4.2), approximately 59 and 48% of the variation seen in experimental results for PP1 and PP2. Strut waviness, another geometric defect known to influence the variation of, and the average apparent mechanical properties of porous AM structures [84], was not observed in the micrographs as seen in Fig. 3.2.

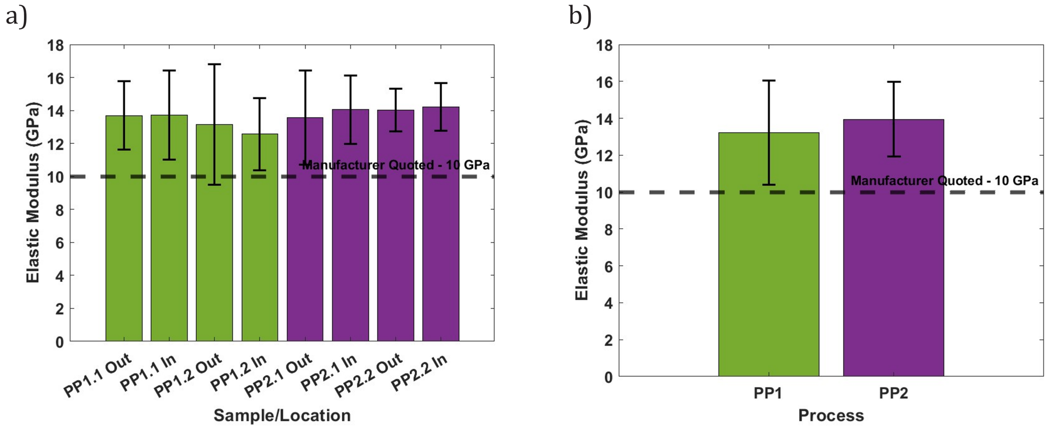

FIGURE 3.9: Inter-strut variation of base material elastic modulus measured using nano-indentation as a function of a) post-processing procedure (PP1 or PP2), location on either the inside (In) or outside (Out) of the lattice and sample number (1 or 2), and also as a function of b) post-processing procedure

TABLE 3.4.1: Summary of average and standard deviation of vertical and angled strut diameters for PP1 and PP2 samples

	PP1		**PP2**	
	Average Strut Diameter (mm)	Standard Deviation (mm)	Average Strut Diameter (mm)	Standard Deviation (mm)
Vertical	0.530	0.0216	0.529	0.0227
Angled	0.627	0.0210	0.634	0.0249

TABLE 3.4.2: Summary of variations in strut diameters for PP1 and PP2 samples and how that impacts the variation in elastic modulus calculated using Eq. 2.2.10

		PP1		**PP2**	
		Strut Diameter (mm)	Corresponding Apparent Elastic Modulus (MPa)	Strut Diameter (mm)	Corresponding Apparent Elastic Modulus (MPa)
Upper Bound	Vertical	0.5516	313.8	0.5517	317.7
	Angled	0.6480		0.6589	
Lower Bound	Vertical	0.5084	261.8	0.5063	260.9
	Angled	0.6060		0.6091	

Analytical model predictions are also based on the base material modulus, and so variations in this could explain the remaining intra- and inter-sample variability. The average base material elastic modulus as determined from nano-indentation (Fig. 3.9) within and between samples for both post-processing methods are similar (especially considering the large standard deviation present) and do not depend on location with no difference between struts inside the lattice and outside on the lattice surface, Fig. 3.9a. The source of the large intra- and inter-sample variations could be attributed to the composite nature of the resin. The resin has an acrylic resin base with glass-particle inclusions to increase stiffness. Not much is known about the particle size and distribution, however, it is likely that their size is similar to the size-scale of the nano-indenter tip. This would influence elastic modulus measurements, with a greater elastic modulus measured closer to individual glass particles and a comparatively reduced elastic modulus when measured over just the acrylic resin without the influence of the glass particles. Comparing the effects of post-processing methods, the average base material moduli are 13.22 and 13.95 GPa for PP1 and PP2, respectively, which are greater than the 10 GPa quoted by the manufacturer and used for predictions with the analytical model in Fig. 3.7a. This difference could be due to the difference in testing methods as the modulus provided by the manufacturer was derived from the tensile testing of dog bone specimens. The viscoelastic nature of polymers means the base material elastic modulus is typically overestimated with nanoindentation, and direct comparisons cannot be drawn between studies [133], [152], [153]. Nevertheless, the coefficients of variation can indicate the level of variability expected in analytical predictions due to the variation in the base material and are 0.21 and 0.15 for PP1 and PP2, respectively, similar to the variability in the apparent elastic modulus. Together with strut diameter variability, base material modulus variation is another contributing factor that can account for the metamaterial mechanical property variability.

3.5 Conclusions

Differences in the average apparent mechanical response of lattices manufactured using the two post-processing methods in this work were observed. Applying heat during curing increased the average apparent elastic modulus by 60 MPa from 293 MPa. These differences, however, are within the inter-sample variability and are predominantly due to base material property variations between individual struts shown with nanoindentation, as well as geometrical variation between strut diameters.

Local apparent elastic modulus variation (shown by optical strain measurements) within a sample can be attributed to height distortions observed on the endplates, which lead to non-uniform contact and loading. Using the elastic foundation model, the height distortions of unadhered samples are shown to result in a more compliant initial response and a decrease in apparent stiffness compared to adhered samples, appearing as a ‘toe-in’ region of the stress-strain curve. This stiffness reduction is relevant for load-bearing structures such as scaffolds for bone tissue, a biological porous material that experiences small strains. The elastic foundation model can be used to predict the influence of lattice distortions on the apparent mechanical response of various porous geometries, enabling the identification of acceptable height distortion tolerances and the prediction of the response under non-uniform loading. Pre-loading requirements to avoid reduced stiffness can be determined after the height distortion is fully compressed, the response of the unadhered lattice becomes similar to adhered and the stiffness recovers. If characterisation prior to testing identifies substantial distortion such that the apparent mechanical response will be altered, adhering samples prior to testing or application can reduce the effect of distortions, leading to apparent properties that are more representative of uniform loading.

This investigation only looked at the height distortion for a set stretching-dominated unit cell geometry (BCCz) for one as-built relative density, approximately 24%. When accessing the material property space of biological materials with lattices, a wide range of relative densities as well as a bending-dominated geometry are likely to be required. Additionally, understanding potential causes and trends of the height distortion present at lattice boundaries can help develop strategies to mitigate this. Height distortions and trends in mechanical properties such as apparent elastic modulus with relative density are therefore characterised in the following chapter.

Chapter 4

Effects of Relative Density on Distortion and Apparent Compressive Properties of Uniform Lattice Metamaterials

4.1 Abstract

Quantifying and understanding the behaviour of uniform porous metamaterials over a range of relative densities is important for designing non-uniform structures relevant to many applications including aerospace and biomedical. The previous investigation demonstrated how distortions affect the apparent response of an additively manufactured porous metamaterial, and is expanded in this investigation with the response of both bending- and stretching-dominated geometries over a range of relative densities analysed. Characterisation of lattice endplates (manufactured for uniform loading) revealed significant distortions for both geometries across all densities, with a commonly measured distortion of 100 μm, predicted to reduce the initial apparent elastic modulus by 50%. The additively manufactured lattices were also quasi-statically compressed to determine relative density and mechanical property relationships using power law fits such as those developed by Ashby and Gibson. Fits for the apparent elastic modulus were developed over two density ranges, less than and greater than 30% relative density for when the slender beam assumptions used in the analytical models are no longer valid (>30% relative density). The powers for the apparent elastic modulus relationship were greater than expected for the geometry types but similar to that for natural porous materials such as bone. Uniform lattices were shown to have improved strain to failure compared to

the base material and behave as expected concerning the maximum stress and energy absorption with the stretching-dominated lattices greater than bending-dominated for the same relative density. These trends are useful for understanding and developing non-uniform porous metamaterials which are thought to have improved failure properties compared to uniform structures.

4.2 Introduction

Chapter 3 highlighted that the intra- and inter-sample variability of compressive apparent elastic modulus is primarily the result of base material property variations between individual struts as well as geometrical variation between strut diameters. Additionally, the most notable influence on apparent elastic modulus was found to be from height variations due to sample distortions as demonstrated using an adapted version of the elastic foundation model. The extent and influence of the distortion were evaluated for a stretching-dominated geometry at a nominal density to demonstrate the elastic foundation model, however, bending-dominated geometries can also offer a wide range of lightweight properties, potentially useful in aerospace or biomedical applications such as engineered tissue bone scaffolds, and have not yet been considered.

In this study, the influence of the relative density of stretching- and bending-dominated uniform lattices, on distortion, apparent elastic modulus, and failure characteristics is investigated. This will lay the foundation for investigations into non-uniform lattices in Chapter 5. Following this section's brief introduction and research justification, the methodology for sample manufacture, mechanical and geometric characterisation is detailed in Section 4.3. This study assesses the impact of geometry and relative density on the distortion of lattices both before and after a secondary curing phase in Section 4.4.2. This is followed by an in-depth discussion regarding the difference geometry and relative density can have on mechanical properties such as apparent elastic modulus and failure strain in Sections 4.4.3 and 4.4.4, using equations to describe relationships where possible for later use. Key results are summarised in Section 4.5 mechanical property versus density relationships highlighted for when designing non-uniform porous metamaterials.

4.3 Methodology

4.3.1 Porous Metamaterial Fabrication

Uniform lattices made up of either BCCz (body-centred cubic with an extra z direction strut, Fig. 4.1a) or BCC (body-centred cubic, Fig. 4.1b) unit cells (3 mm overall unit cell size) were designed in MATLAB [154] to span a range of relative densities (predicted using Eq. 4.3.1 [40] and Eq. 4.3.2 [37]) summarised in Tables 4.3.1 and 4.3.2 with the corresponding elastic moduli predicted using Eq. 4.3.3, [40] and Eq. 4.3.4, [37]. The BCCz geometry is stretching-dominated when the loading is aligned with the extra z-strut, whilst the BCC geometry is bending-dominated; between the two geometries, a wide range of material properties are covered with the BCCz geometries being stiffer for a BCC geometry with the same relative density.

$$\frac{\rho^*}{\rho_s}BCCz = \frac{(1+4\sqrt{3})\pi}{4} \cdot \left(\frac{d}{L}\right)^2 - \frac{11\pi}{6} \cdot \left(\frac{d}{L}\right)^3 \qquad \text{(Eq. 4.3.1)}$$

$$\frac{\rho^*}{\rho_s}BCC = \sqrt{3}\pi \left(\frac{d}{L}\right)^2 \qquad \text{(Eq. 4.3.2)}$$

$$E_z^* BCCz = \frac{\sqrt{3}\pi}{2} \cdot \left(\frac{d_{ang}}{L}\right)^4 \cdot E_s + \frac{\pi}{4} \cdot \left(\frac{d_{vert}}{L}\right)^2 \cdot E_s \qquad \text{(Eq. 4.3.3)}$$

$$E_z^* BCC = \frac{\sqrt{3}\pi \left(\frac{d_{ang}}{L}\right)^2 \cdot E_s}{1 + 2\left(\frac{L}{d_{ang}}\right)^2} \qquad \text{(Eq. 4.3.4)}$$

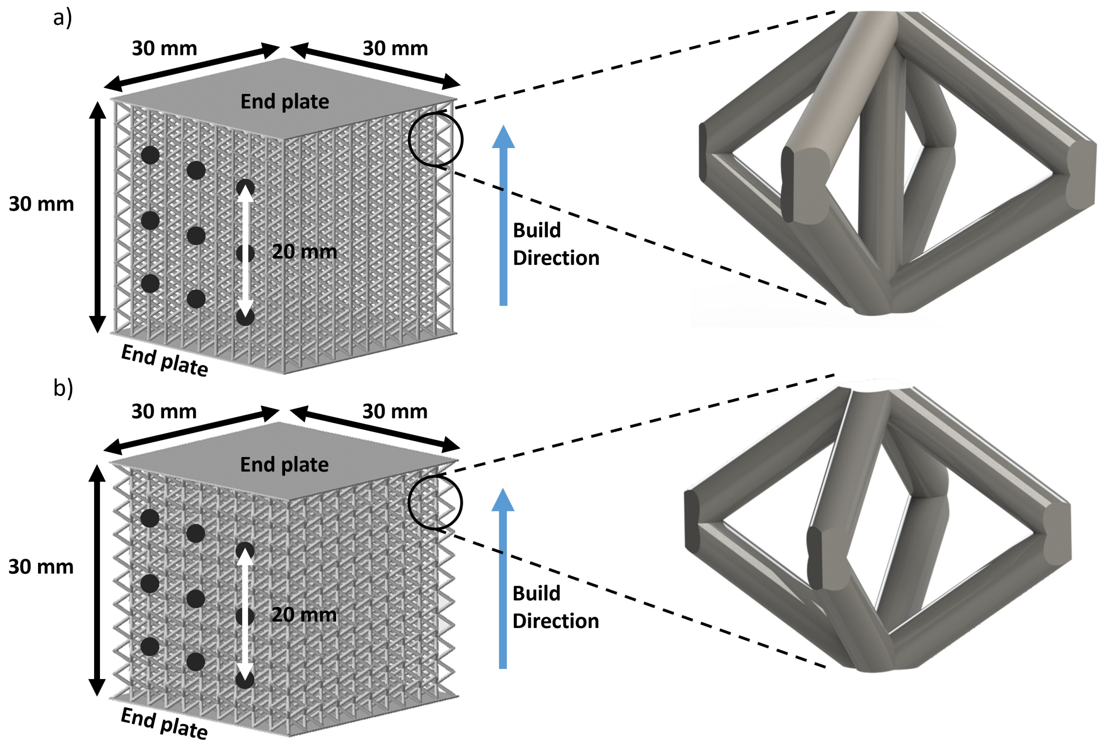

FIGURE 4.1: a) BCCz and b) BCC, lattice geometries with endplates to protect the top and bottom struts and dots marked on the front back for optical strain measurement with a maximum virtual gauge length of 20 mm. Enlarged view of single BCCz and BCC unit cells shown. Vertical struts in the BCCz lattice are aligned with the build direction.

TABLE 4.3.1: Summary of designed and predicted parameters for BCCz lattice geometries. The relative density is predicted using Eq. 4.3.1 and apparent elastic modulus is predicted using the geometric specific analytical model, Eq. 4.3.3

Designed Diameter (mm)	**Relative Density**	**Predicted Apparent Elastic Modulus (MPa)**
0.30	0.057	81.3
0.46	0.126	199.7
0.55	0.174	249.7
0.70	0.266	508.3
0.85	0.369	805.8
1.00	0.479	1208.6
1.15	0.581	1741.6

TABLE 4.3.2: Summary of designed and predicted parameters for BCC lattice geometries. The relative density is predicted using Eq. 4.3.2 and apparent elastic modulus is predicted using the geometric specific analytical model, Eq. 4.3.4

Designed Diameter (mm)	Relative Density	Predicted Apparent Elastic Modulus (MPa)
0.31	0.058	3.1
0.46	0.128	14.9
0.54	0.176	28.1
0.66	0.263	62.2
0.78	0.368	120.3
0.89	0.479	201.9
0.99	0.593	306.0

The BCCz geometry with a designed diameter of 0.46 mm was selected as it corresponded to the first data point in the previous investigation (Chapter 3) which looked at a specific stretching-dominated geometry. The designed relative density and apparent elastic modulus of this geometry are within the typical range for a cancellous bone/bone scaffold, a biological porous material that exhibits a wide range of mechanical properties [15]–[17], [20], [22]. For such a scaffold, matching the mechanical and geometric properties is essential to performance [122]. The other target strut diameters for the BCCz geometry were chosen to achieve an even porosity distribution for a range of as-designed strut diameters, limited by manufacturability, approximately 0.2 - 1.15 mm for an overall unit cell size of 3 mm. Chapter 3 noted that the designed diameter was not a multiple integer of the laser spot size, potentially increasing the as-built diameter. However, compared to the effect of overhangs and the peel and compressive forces, this is likely minimal and therefore the focus of the designed diameter selection was on an even porosity distribution rather than matching the laser spot size. The BCC unit cell as-designed strut diameters were selected to match the as-designed relative density of the BCCz unit cells as closely as possible, considering the minimum precision of 0.01 mm.

As in the previous investigation (Chapter 3), lattices had 10 unit cells in each direction to minimise edge and boundary effects [28], [41]. Parts were also manufactured with endplates on the top and bottom faces to protect struts during post-processing, further reduce boundary condition effects and provide more uniform loading. Samples were manufactured using a Form3 stereolithography printer (layer height = 0.05 mm) with Rigid10K resin, a glass-particle reinforced acrylic based resin with a base material modulus of 10 GPa (Formlabs, Massachusetts, United States of America, see Appendix 10 for material data sheets) [123]. All specimens were manufactured across six builds; any conclusions drawn are therefore representative of samples being manufactured between various builds and different build locations. Samples were post-processed according to PP2 in Chapter 3, which involved washing samples in IPA for 12 minutes in an ultrasonic bath, followed by at least a 30 minute air dry, 120 minutes under a 5 Pa vacuum, 120 minutes in an oven at 60 °C and an additional 60 minute cure under UV light.

4.3.2 Mechanical Testing

The compressive testing procedure was identical to that of Chapter 3, Section 3.3.2. Key parameters are outlined here. A total of 39 samples were quasi-statically compressed with the endplates of all samples adhered to flat metal plates using a cyanoacrylate-based adhesive to minimise the effects of height distortions on the loading behaviour of the lattices. Both platen and optical measurements were used to measure strain, allowing both failure behaviour and local measurements to be captured. The latter accounts for machine compliance and more accurately captures surface strains [117]. For optical measurements, point tracking was employed. Nine dots (Fig. 4.1) were marked on the front and rear faces of the samples using a marker pen and stencil to ensure consistency. Manta cameras [2452x2056], 105 mm lenses (Nikkor) and Nila lights, along with MatchID software (MatchID, Ghent, Belgium) [128] were used to capture images of the sample during testing at a rate of four frames per second. At least 10 images were captured prior to loading and analysed using MatchID (MatchID, Ghent, Belgium) [128] to verify the validity of the subset and step sizes determined previously in Chapter 3, with details given in Appendix 7.2).

The apparent elastic modulus of the samples was calculated as in Chapter 3, Section 3.3.2, following a procedure adapted from NPL's 'Measurement Good Practice Guide No. 98: Elastic Modulus Measurement' [129]. The apparent elastic modulus from each virtual strain gauge per face (n = 3 per face) were averaged to provide an apparent elastic modulus per face per sample. The apparent elastic modulus for the two opposing faces were also averaged to result in an apparent elastic modulus per sample, which were then grouped and averaged to determine the average, standard deviation, maximum and minimum apparent elastic modulus for similar samples (same designed relative density and geometry type). One sample was rejected due to a non-linear initial behaviour, incompatible with analysis methods employed as discussed in greater depth in Section 4.4.3.

Although samples are taken to failure where possible, point tracking is unable to provide data beyond the yield point, when the points are either too deformed or have broken off the sample. For failure characteristics such as total energy absorption, strain from platen measurements were corrected for machine compliance and used instead with the following assumptions: the load frame deforms elastically, the apparent elastic modulus calculated from point tracking is without any influence of machine compliance, and the load frame and sample are in series with their combined behaviour estimated by springs in series, Eq. 4.3.5 where k_{eq} is the combined stiffness of the load frame and sample, k_L is the stiffness of the load frame and k_{PT} is the stiffness of the sample determined from point tracking [155]. By modelling the behaviour as springs in series, a linear relationship is assumed between platen and point tracking measurements, an assumption that was validated when comparing graphs with similar shapes observed (Fig. 4.2).

$$\frac{1}{k_{eq}} = \frac{1}{k_L} + \frac{1}{k_{PT}} \tag{Eq. 4.3.5}$$

The springs in series relationship (Eq. 4.3.5) can be used with Hooke's law, $F = kx$, where F is the force applied, k is the spring constant and x is the displacement, and with the axial stiffness relationship (Eq. 4.3.6), where E is the elastic modulus of the material, A is the cross-sectional area of the material, perpendicular to the loading direction and L_s is the original length of the material, parallel to the loading direction to determine the corrected displacement Eq. 4.3.7.

$$k = \frac{E \cdot A}{L_s} \tag{Eq. 4.3.6}$$

Rearranging Eq. 4.3.5, Eq. 4.3.5, and Eq. 4.3.6 and cancelling out the cross-sectional area, gives Eq. 4.3.7 which was divided by sample height to give corrected strain, where E_{PT} is the apparent elastic modulus as determined by point tracking, E_{eq} is the apparent elastic modulus calculated from uncorrected platen data, and $disp_{CPL}$ and $disp_{PL}$ are the corrected and uncorrected displacements from platen data.

$$disp_{CPL} = disp_{PL} - \frac{FL_s}{A} \cdot \frac{E_{PT} - E_{eq}}{E_{PT} E_{eq}} \tag{Eq. 4.3.7}$$

With force-displacement plots from the test machine corrected for compliance, the failure strain is calculated as the strain when the sample experiences near 0 force. The energy absorbed is determined by integrating the stress-strain curve between the 0 and the final strain.

4.3.3 Geometry Characterisation

The height distortions of all samples after washing and after the secondary UV cure were measured using an Alicona infinite focus microscope (at 2.5x magnification, Bruker Alicona, Graz, Austria). A 3D general image field was captured over the full

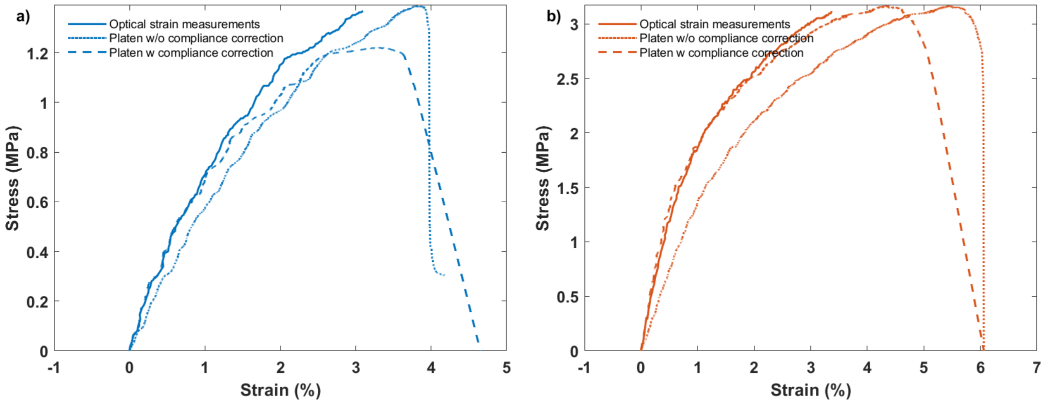

FIGURE 4.2: Representative stress-strain plot of a) bending-dominated and b) stretching-dominated lattices showing similar shapes of results from optical strain measurements (solid), uncorrected platen strain measurements (dotted) and corrected platen measurements (dashed).

surface of the top endplates through a vertical distance of at least 1 mm ensuring that all features were in focus. Samples were imaged before removal from the raft and supporting material, generated during slicing when preparing the part for manufacture (Fig. 4.3) and manufactured directly on the build plate, minimising potential height distortions. The height of the supports was set to 5.00 mm with a touchpoint size (point of contact between the raft support and part) of 0.50 mm. Only the top endplate could be imaged with the distortion on the bottom endplate assumed to be similar.

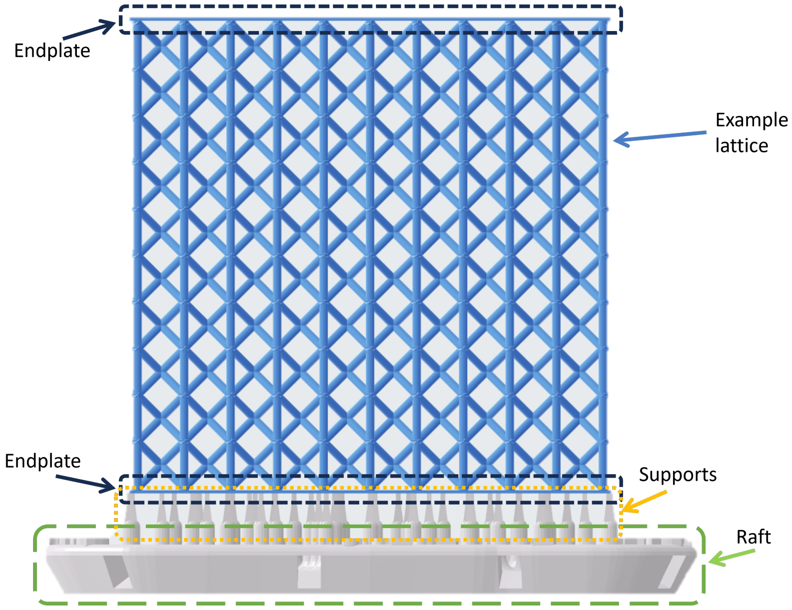

FIGURE 4.3: Labelled diagram of lattice prepared for manufacture during slicing, highlighting the endplates, support material and raft.

Height distortion area-based averages for all samples were calculated using the Alicona height data, with the maximum and minimum distortion manually set to ensure the full potential range of the distortions was clearly evident on the sample. Additionally, points within 0.5 mm of the maximum and minimum X- and Y- coordinates were identified as noise and spurious data, and were removed. Distortions were then zeroed and summed to give the total height distortion across the endplate. The total height distortion was then normalised by the total endplate area to give the average height distortion. The position on the endplate with reduced distortion was determined by the author and grouped according to Fig. 4.4. This was correlated to laser scanning direction during sample manufacture which goes from back to front and left to right.

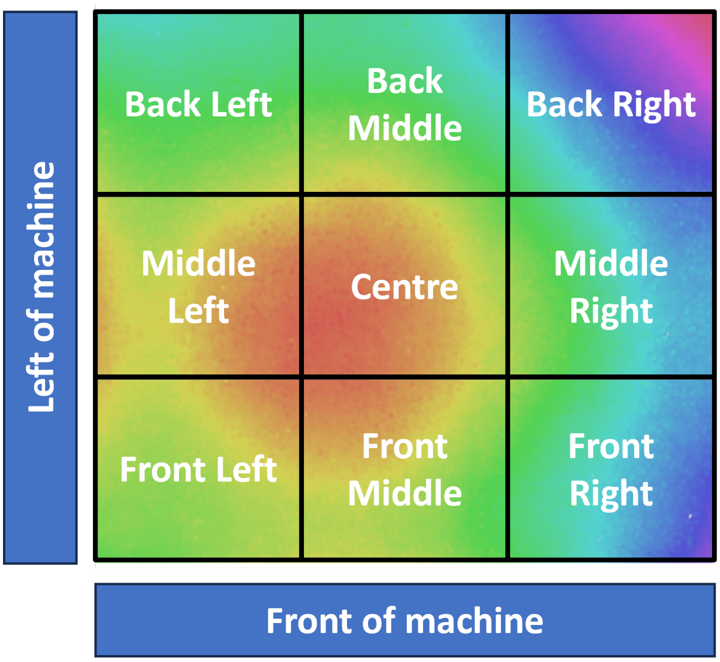

FIGURE 4.4: Minimum height distortion positions on endplate overlaid on example height distortion map with front and left sides of the printer. Scanning direction is back to front and left to right.

Additionally, height data was input into the adapted elastic foundation model developed in Chapter 3 to determine how the distortions observed would affect the initial apparent elastic modulus (up to 0.3% strain).

Prior to mechanical testing, images of all four faces were taken of all samples using Manta cameras [2452x2056]. The images were analysed with ImageJ (as in Chapter 3, Section 3.3.2) [130] to measure the strut diameter of 10 randomly selected vertical and angled struts per face for a total of 40 measurements per strut type per sample. This equates to sampling 0.5% of the angled struts in the BCCz and BCC lattices, and 4% of the vertical struts in the BCCz lattice or 2.5% of the external angled struts in the

BCCz and BCC lattices, and 10% of the outermost vertical struts in the BCCz lattice. Overall dimensions (to determine volume) of the samples were taken as an average of three repeats for each dimension, measured using SPI callipers (Swiss Precision Instruments, accurate to 0.02 mm)). Mass was measured using an AE 240 Mettler Toledo (Ohio, United States) balance accurate to 4 decimal places.

4.4 Results and Discussion

4.4.1 Geometry Characterisation

4.4.1.1 Determination of Relative Density

The relative density of the samples was calculated from measured values using two different methods to account for the endplates; i) using measured strut diameters with the manufacturer-specified solid density of the resin and analytical models (Eq. 4.3.1, Eq. 4.3.2, Eq. 4.4.1, and Eq. 4.4.2), and ii) using specimen mass and volume measurements. When using strut diameter measurements, each strut is treated as a cylinder, with the overlap between the struts at joints often ignored. At low strut diameter-to-length ratios, generally, when the relative density is less than 30%, the volume of overlap is minimal compared to the volume of the struts and has a negligible impact on relative density. The relative density can therefore be calculated without accounting for the overlapping material as in Eq. 4.3.2 and Eq. 4.4.1 for the BCC and BCCz geometries respectively. With increasing strut diameters, the volume of the overlap tends towards the volume of the struts and has an increasingly noticeable effect on the relative density. The excess material therefore needs to be accounted for when calculating relative density as in Eq. 4.4.2 and Eq. 4.3.1 for the BCC and BCCz geometries respectively. The term $\frac{55\pi}{36} \cdot \left(\frac{d}{L}\right)^3$, in Eq. 4.4.2 which accounts for the overlapping material is the same term used for the BCCz geometry (determined by Zhang *et al.* [40] using geometrical relationships multiplied by a constant term estimated empirically through comparison with 3D renderings) scaled by the ratio between the number of overlapping joints for the BCC and BCCz unit cell geometries. For the BCC analytical models (Eq. 4.3.2 and Eq. 4.4.2), strut diameter, d, is the average measured strut diameter, and L, the unit cell size is as designed, 3 mm. For the BCCz geometry, L, is the same at 3 mm, however, using the predefined analytical models, the strut diameter is based on the average strut diameter from both vertical and angled struts, normalised by the ratio between the total number of vertical and angled struts; there are 8 angled struts for every vertical strut.

$$\frac{\rho^*}{\rho_s}BCCz = \frac{(1+4\sqrt{3})\pi}{4} \cdot \left(\frac{d}{L}\right)^2 \qquad \text{(Eq. 4.4.1)}$$

$$\frac{\rho^*}{\rho_s} BCC = \sqrt{3}\pi \left(\frac{d}{L}\right)^2 - \frac{55\pi}{36} \cdot \left(\frac{d}{L}\right)^3 \qquad \text{(Eq. 4.4.2)}$$

Unlike when using strut diameter measurements, when using mass and volume measurements, the endplates need to be taken into account. The designed dimensions of the endplate were 31 x 31 x 0.2 mm. Assuming that the as-built dimensions match this, and the density of the cured resin is 1.63 gcm^{-3}, the mass contribution of both endplates is 0.627 g. When measuring the overall size of the samples, the height is the only dimension which the endplates influence. The volume contribution of both the endplates is, therefore, 30 x 30 x 0.2 mm x 2, or 360 mm^3. These values can then be used to provide a more accurate measurement of the relative density of the samples without the influence of the endplates.

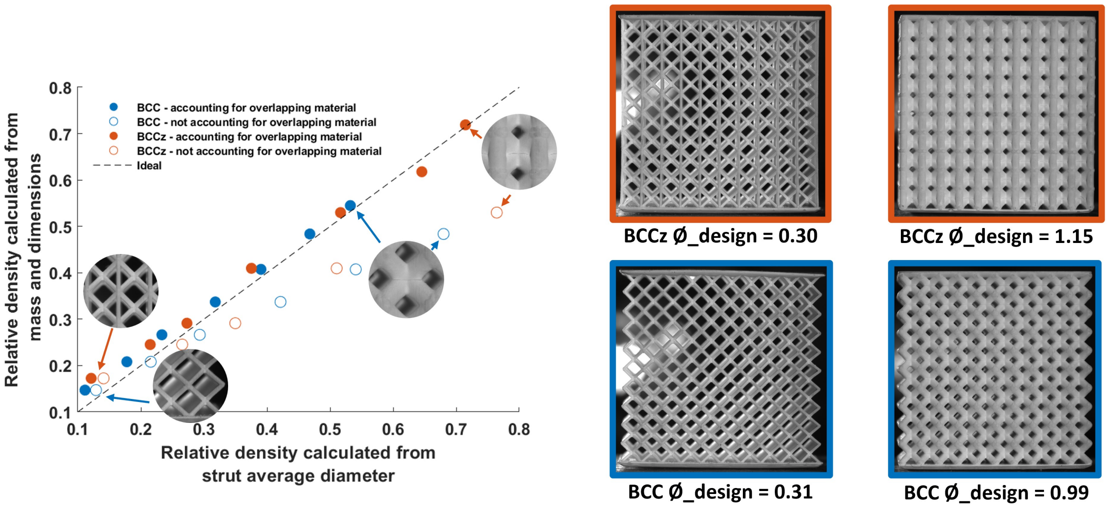

FIGURE 4.5: Plot showing the two methods of calculating relative density for both BCC (blue) and BCCz (orange) geometries over a wide relative density range.

The two methods for calculating relative density are compared in Fig. 4.5 with strut-diameter-based estimates on the X-axis and specimen mass-and-volume-based measurements on the Y-axis. For both unit cell geometry types (BCC and BCCz), the influence of not accounting for excess/double material at the joints between struts is given by the unfilled points. Representative images of the unit cell geometries at the highest and lowest relative densities are shown with zoomed-in sections showing the overlap between struts/junctions on the plot.

Fig. 4.5, shows that for all plots there is good agreement between the two methods up to approximately 30% relative density, the limit generally given for the assumptions of porous material validity [28]. Up to 30%, the contribution from overlapping material is minimal and can be ignored. Beyond this, the relative density calculated without accounting for the overlapping material consistently overpredicts as-built relative density. This is evidenced in the detailed views of the junctions at the extreme relative densities (Fig. 4.5). For designed diameters of 0.3 and 0.31 mm for BCCz and BCC geometries respectively, the material at the joint is minimal. However, at the highest relative density, the overlap between struts is considerable, even making it difficult to pick out the vertical strut in the BCCz geometry detail view (Fig. 4.5). The analytical models that do not account for material overlap are therefore invalid at low relative densities. An alternative method for determining relative density is needed to span the full density range of samples manufactured in this investigation.

For the analytical models that account for the overlapping material (solid points), there is good agreement with calculating relative density using mass and volume measurements across the full relative density range (Fig. 4.5). The mass and volume measurements generally predict a relative density that is on average 2% greater than from strut diameter measurements for both BCC and BCCz geometries. This difference is likely due to either the use of as-designed measurements when accounting for the relative density contribution of the endplates, or variation in as-built strut diameters. Only a limited number of struts were measured, 40 per strut type per sample. The previous investigation (Chapter 3), found a standard deviation for vertical and angled struts of 0.022 and 0.025 mm respectively for an as-built strut diameter of 0.53 and 0.63 mm, equating to a coefficient of variation of approximately 4%, comparable to that in this investigation, Fig. 4.6.

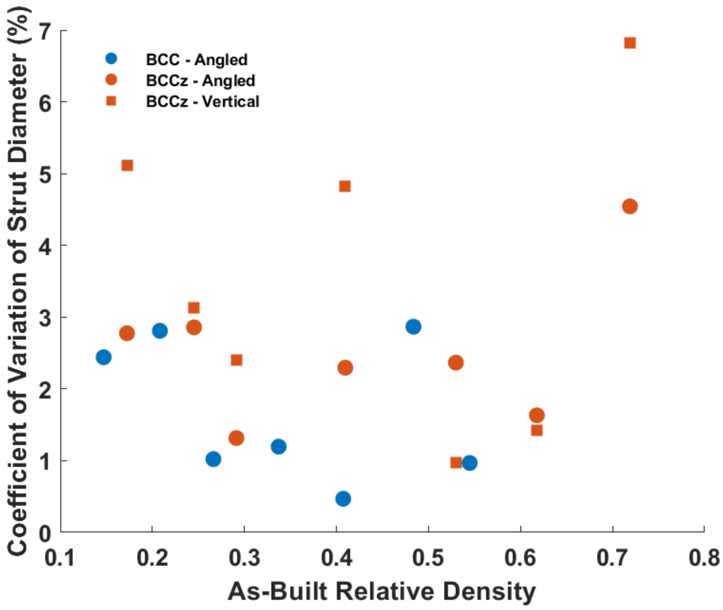

FIGURE 4.6: Variation of the coefficient of variation of average strut diameter for BCC (blue) and BCCz (orange) geometries at varying relative densities for both angled (circle) and vertical (square) struts. The coefficient of variation is the ratio between the standard deviation and the average strut diameter, as a percentage.

In either case, the difference between the two methods is minor, and as using mass and volume measurements is applicable to gradient and stochastic structures (investigated in Chapter 5) as well as the uniform structures in this investigation, it is taken forward to calculate as-built relative density.

4.4.1.2 As-designed versus As-built

Comparing the as-designed and as-built relative density in Fig. 4.7, the as-built relative density is consistently greater than the as-designed relative density. The first order (y = mx + c) equations fitted to both the BCC and BCCz results indicate that the relationship between as-designed and as-built relative density is relatively linear; the ′m′ constant is low in both cases, 1.09 and 1.04 for the BCC and BCCz lattices. The greater difference comes from the ′c′ constant; the as-built relative density is just shifted up on the Y-axis, with c as 0.1 and 0.12 for the BCC and BCCz lines of best fit. These equations, along with the analytical models which predict the relative density of unit cells whilst accounting for overlapping material, can be used when designing new lattices. These equations should be used with caution, however, as they only apply to lattices manufactured as described in this investigation, with a Form3 stereolithography printer and Rigid10K resin. Nevertheless, the present investigation has demonstrated a framework for assessing other manufacturing methods and materials that are likely to result in variations in print accuracy and deviations from the designed geometry.

The differences between as-designed and as-built relative densities are likely due to those hypothesised in Chapter 3: the manufactured geometries tending towards the limit of manufacturability; designed diameters not being a multiple integer of the laser spot size; peel and compressive print forces causing layer smudging, shifting and part deformation; and the angled struts resulting in an overhang during manufacture, likely to be the dominant effect. The peel and compressive print forces occur when the part is removed from the flexible film prior to the resin being levelled and when the part is brought back down onto the flexible film [98], [145]. Additionally, most (89%) of the struts in the BCCz lattice and all of the struts in the BCC lattice are angled. Even with a layer height of 0.05 mm, the angled struts experience stair-stepping (described in Section 3.4.2), and any overhanging excess material is able to merge with the layer below, increasing the as-built strut diameter.

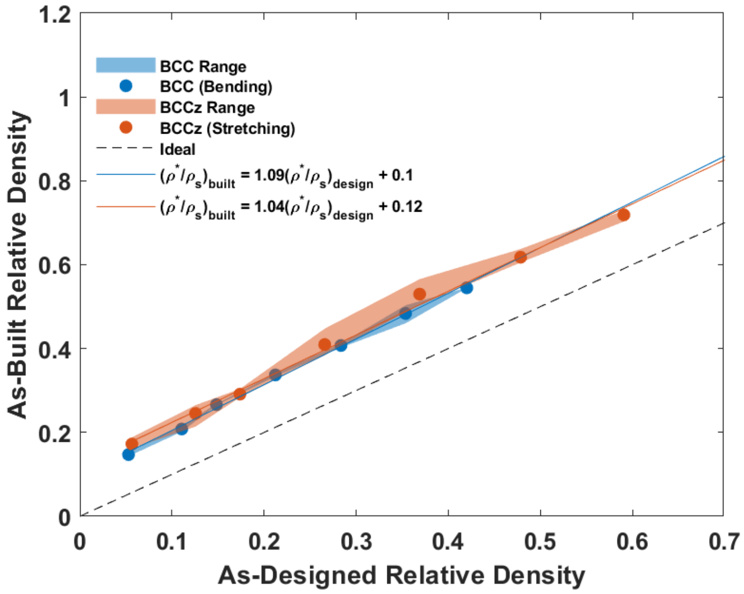

FIGURE 4.7: Comparison between as-designed and as-built relative density for bending- (BCC, blue) and stretching-dominated (BCCz, orange) lattices. As-built relative density is calculated based on adjusted volume and mass measurements. The ideal trend (dashed black line) is for as-designed matched as-built. First-order fits performed to as-designed versus as-built data to correct relative density in future designs. Shaded regions indicate the range of data (maximum to minimum).

4.4.2 Endplate Distortions

The average endplate height distortion was assessed as the area-based average height position of all measurement points on the top surface of each specimen endplate. Evidence of endplate distortions were seen on all samples, both before and after the secondary cure phase, Fig. 4.8, with the average distortion ranging from approximately 60 - 150 μm to 70 - 450 μm respectively. This is in line with that seen in L-PBF geometries which range from approximately 20 to 600 μm for aluminium alloy, titanium alloy and steel parts [73]–[76] and for SLA parts which range from 15 to 2500 μm [77], [78], [80], [81]. The height distortions are greater after the secondary cure phase for both the BCC and BCCz lattices across the relative density ranges. The secondary cure phase involves both heating the samples and curing using a UV light, encouraging further cross-linking of the polymer chains to fully cure the sample, but also resulting in residual stresses [156] which are the main cause of warping in SLA structures [77], [78], [80], [81], [98].

Prior to the secondary cure phase (Fig. 4.8 a), there was little change in the distortion of both BCC and BCCz lattices with relative density (approximately 90 μm on average). The average distortion was greater at the lowest relative density of BCC lattices ($\approx$ 150 μm at a relative density of 0.15); however, the range was considerable, and further precise conclusions cannot be drawn without additional data points.

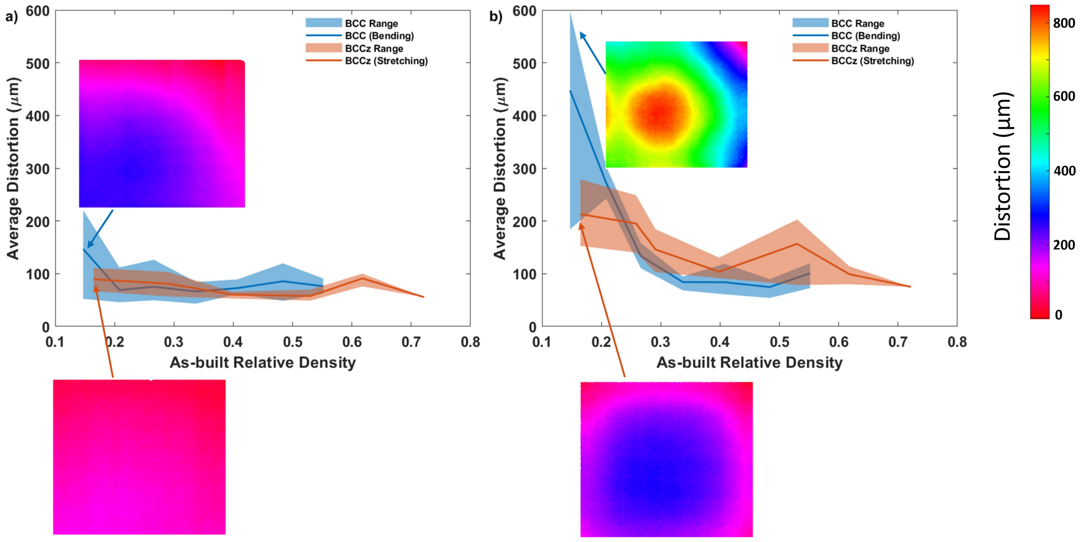

FIGURE 4.8: Average height distortion on top endplate for BCC (blue) and BCCz (orange) lattices as a function of relative density a) before and b) after secondary cure phase during post-processing. Shaded regions indicate the range of data (maximum to minimum). Representative height distortion plots before the secondary cure phase and the corresponding height distortion plots after the secondary cure phase are shown. Colour bars scaled to the maximum height distortion observed across all plots (BCC, after the secondary cure phase).

The same trend was not observed after the secondary cure phase in Fig. 4.8 b. The highest distortion for both geometries was at the lowest relative density, but these were also accompanied by a large range. For the BCC geometry, increasing the relative density resulted in decreased distortion, plateauing when the relative density exceeded 30% at a height distortion of approximately 60 μm. The relationship for the BCCz geometry was less clear due to the wide range of results. Taking instead the general shape rather than average results, as the relative density increased, the height distortion decreased, and similar to the BCC geometry, it plateaued at a relative density of approximately 30%. As the relative density increases, the stiffness of the individual struts and unit cells will increase, as will their resistance to shrinkage from curing and distortion.

Comparing the two geometry types, BCC and BCCz, after the secondary cure phase (as there is minimal difference before), at lower relative densities, greater distortion is observed for the BCC geometry compared to the BCCz geometry. This is true, even considering the overlap of the ranges. However, as the relative density increases, the height distortion of the BCCz geometry becomes greater than that for the BCC geometry. This is most probably due to the upright z-strut. Assuming that the struts shrink by the same amount from curing, the effect will be more pronounced for the upright struts than the angled struts, increasing the out-of-plane distortion in the BCCz lattices.

As shown in the representative plots in Fig. 4.8, the shape of the height distortions changes after the sample undergoes the secondary curing phase. For both the BCC and BCCz geometries, the distortion is more of a dome-like shape, similar to that observed in the previous investigation (Chapter 3). When the sample is being built up, the laser scanning pattern goes from back to front and left to right. One would, therefore, expect the back left of the endplate to consistently experience reduced height distortions. This is not reflected in Fig. 4.9, with the minimum height distortion position observed at all four corners for both the BCC and BCCz samples. For the BCC lattices, the minimum distortion is typically observed at the back left or front right corners corresponding to the beginning or end of the laser scan path. For the BCCz geometry, however, the minimum height distortion is generally observed at the back right corner, which would have been manufactured towards the end of sample manufacture.

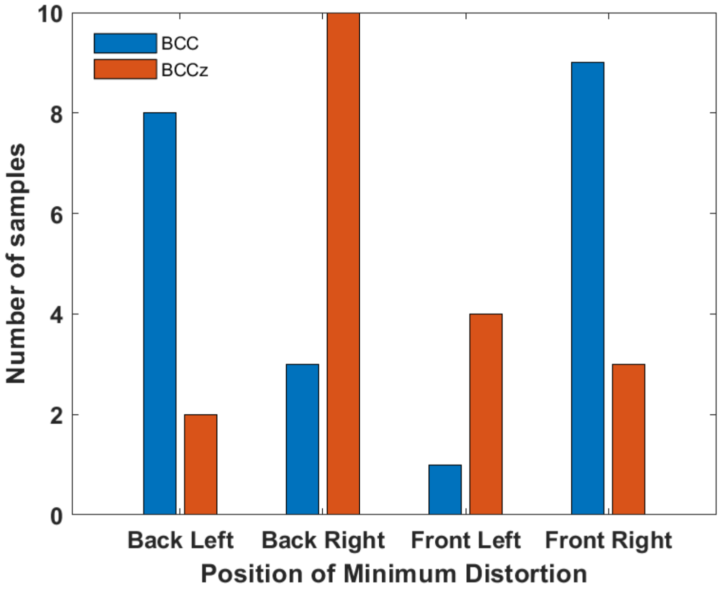

FIGURE 4.9: Position of minimum height distortion on endplate after the secondary cure phase for BCC (blue) and BCCz (orange) lattices. Position is in accordance with Fig. 4.4.

The adapted elastic foundation model (Eq. 3.3.2) showed that height distortions can considerably alter the apparent properties of a porous metamaterial. Taking bone scaffolds as an example, the apparent elastic modulus of a porous metamaterial can be determined between the physiologically relevant strains (0.15 to 0.3% for bone growth), to give a physiological apparent elastic modulus, normalised by the target apparent elastic modulus for better comparison across a range of relative densities, Fig. 4.10. As the target apparent elastic modulus increases, the physiological normalised apparent elastic modulus remains constant. The total distortion, however, has an increasing effect on the apparent elastic modulus. As the distortion increases, the resultant modulus decreases with a decreasing difference between height distortion steps. Fig. 4.10a, is a visual representation of Eq. 3.3.2, where the normalised apparent elastic modulus (and therefore normalised force) is independent of the base material/target elastic modulus (shown by the constant horizontal lines) but affected by level of distortion. From Fig. 4.10b, with a commonly observed distortion of 100 μm, the physiological apparent elastic modulus is approximately 52% of the target. At the most extreme case, but still observed at the lowest relative density, the resultant apparent elastic modulus is approximately 9% of the target. With distortions observable across the full range evaluated here, this plot highlights the important effect of height distortions on apparent mechanical properties like apparent elastic modulus.

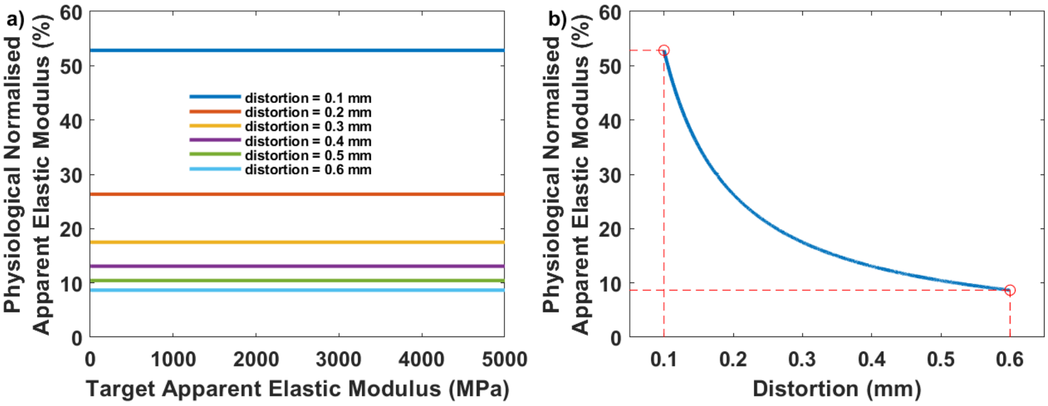

FIGURE 4.10: Effect of distortion on the apparent elastic modulus of a porous metamaterial determined within the physiological strain range that encourages bone growth for bone scaffolds, 0.15 - 0.3% strain. a) Apparent elastic modulus is given as a normalised percentage of the target apparent elastic modulus and calculated based on the adapted elastic foundation model using Eq. 3.3.2. b) shows effects of distortion for target apparent elastic modulus of 1000 MPa as behaviour is independent of the target elastic modulus.

4.4.3 Elastic Behaviour

When averaging the apparent elastic modulus (determined up to 0.2% strain) over a group of samples to determine key parameters such as average apparent elastic modulus and maximum and minimum values, the pattern of the virtual extensometers (as determined by the strain from a pair of points that were tracked, with one point close to the upper endplate and the other point close to the lower endplate) correlated well with the distortion observed after the secondary cure phase (Fig. 4.11). For the example shown, the front-left (FL, solid blue) extensometer had a slightly higher stress for the same strain than the back-left (BL, dashed blue) extensometer, seen more clearly in Fig 4.11b. Similar, although reduced differences were observed for the other positions. This suggests that there was minimal difference between the front-to-back loading, and therefore minimal distortion in this direction, as observed in the height distortion map (Fig. 4.11) and was possible because of the hemispherical seated platen. The height distortion map also reflects the greater difference between front-to-back loading on the left side.

Next looking left to right, for the same stress, the front-left (FL, solid blue) extensometer experiences the least strain, followed by the front-middle (ML, solid orange) and then the front-right (FR, solid yellow), with the ML and FR plots overlapping each other greatly (Fig. 4.11). This would suggest that the left side of the sample was loaded first, followed by almost simultaneous loading of the middle and right side. From the height distortion map (Fig. 4.11a), the greatest distortion is experienced by the middle of the sample and one would therefore expect the middle to experience the greatest strain for the same stress as it would be loaded first. This does not occur due to the adherence of the endplates to platens. Finally, all virtual extensometers show initial linear regions with the back virtual extensometers experiencing more noise possibly due to lighting differences.

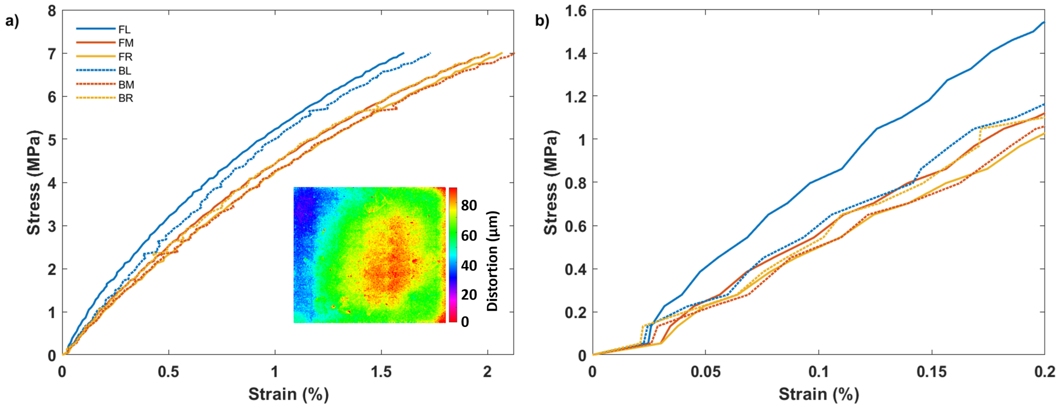

FIGURE 4.11: Representative stress-strain curve of virtual extensometers with height distortion map of the sample after the secondary cure phase, a) full curve and b) zoomed-in section to 0.2% strain, the range over which the apparent elastic modulus is determined. Solid lines are virtual extensometers from the front face and dotted lines are virtual extensometers from the back face. The coordinate system is looking at the sample from the front face i.e. the front left (FL) and back left (BL) extensometers are on the same side of the sample.

Linear regions were not observed for all the virtual extensometers of one BCC sample (designed strut diameter of 0.99 mm) was therefore excluded from averaging (Fig. 4.12 and Fig. 4.13). The front extensometers all showed a relatively linear response with some spread. The back extensometers are more varied, even after accounting for the ’toe-in’ region with a procedure adapted from NPL’s ‘Measurement Good Practice Guide No. 98: Elastic Modulus Measurement’ [129] and appear to have a less distinct starting point. Although the back virtual extensometers across all samples tend to be more noisy than the front extensometers, possibly due to lighting, other samples were not discounted and it is unclear why this particular sample had a non-linear response. Additionally, the average R^2 of this sample was 0.76, with the R^2 for the virtual extensometer shown in Fig. 4.12 equal to 0.41 for an apparent elastic modulus calculated between 0 and 0.2% strain. Whereas the average R^2 for the other samples was 0.94 and 0.97 for the BCC and BCCz geometries respectively, for the same strain range.

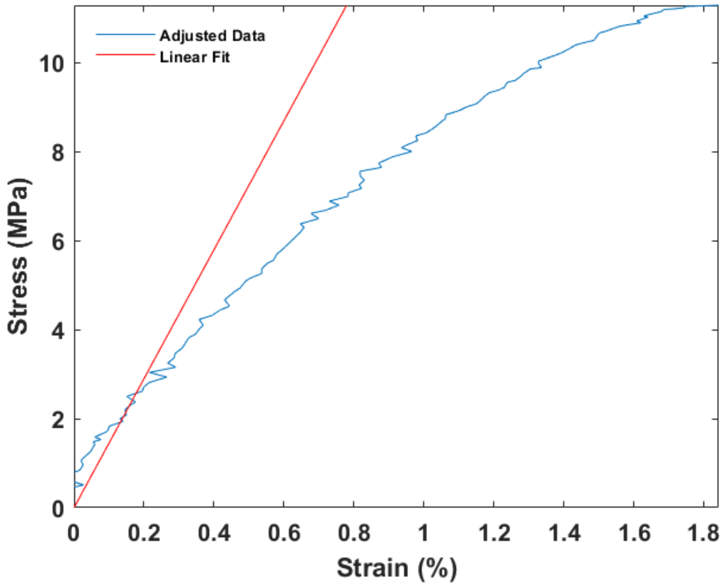

FIGURE 4.12: Example stress-strain curve of a virtual extensometer for a sample that was excluded from summarised data with linear fit for apparent elastic modulus shown (red line).

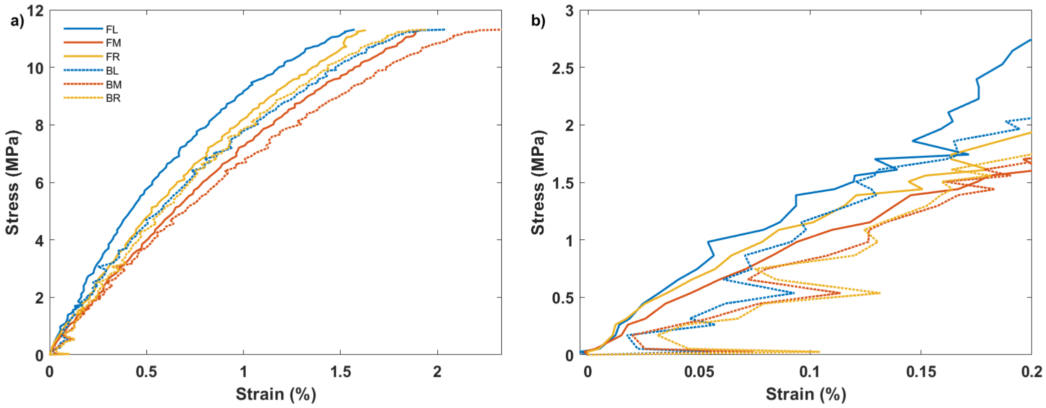

FIGURE 4.13: Stress-strain curve of virtual extensometers for sample that was excluded from summarised data, a) full curve and b) zoomed-in section to 0.2% strain. Solid lines are virtual extensometers from the front face and dotted lines are virtual extensometers from the back face. The coordinate system is looking at the sample from the front face i.e. the front left (FL) and back left (BL) extensometers are on the same side of the sample.

As in Chapter 3, the as-built apparent elastic modulus was greater than as-designed, Fig. 4.14, due to the greater than designed relative density. Additionally, the difference between designed and as-built apparent elastic modulus greater for the BCC geometries than for the BCCz geometries. Interestingly, the apparent elastic modulus does not follow the same trend of being uniformly shifted up as for the relative density. The apparent elastic modulus for both geometries (Eq. 4.4.3 and Eq. 4.3.3) are not related to the relative density by a constant. For the BCC case, it is related to the relative density divided by the ratio between the length and diameter of the struts squared and is even more complex for the BCCz case. It is therefore not as simple as multiplying the relative density by an empirical constant.

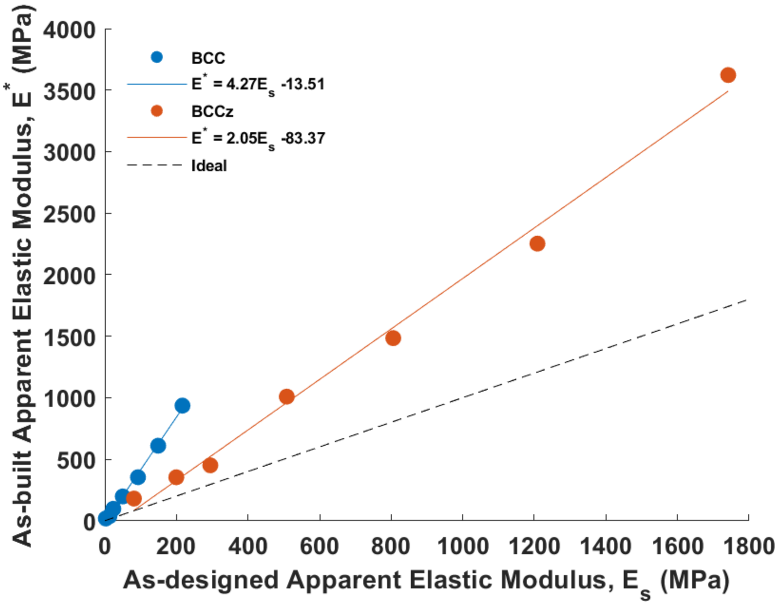

FIGURE 4.14: As-designed versus as-built apparent elastic modulus for both BCC (blue) and BCCz (orange) lattices over a range of relative densities. As-designed apparent elastic modulus is calculated using Eq. 4.4.3 and Eq. 4.3.3 for BCC and BCCz geometries respectively.

$$E_z^* BCC = \frac{\left(\sqrt{3}\pi\left(\frac{d_{ang}}{L}\right)^2 - \left(\frac{55\pi}{36}\cdot\left(\frac{d_{ang}}{L}\right)^3\right)\right)\cdot E_s}{1+2\left(\frac{L}{d_{ang}}\right)^2} \qquad \text{(Eq. 4.4.3)}$$

When as-built relative densities are used (Fig. 4.15), there is good agreement between the as-built results and the analytical models that predict the apparent elastic moduli for low relative densities. The model agrees with as-built results up to a relative density of approximately 27% for BCC geometries and approximately 50% for BCCz geometries, although the range of apparent elastic modulus makes it harder to discern. With increasing relative density, slender beam assumptions become less accurate, resulting in increasing deviations for the apparent elastic modulus from analytical models as demonstrated by both the BCC and BCCz lattices. Additionally, as the relative density increases, so does the excess material at strut joints. The joints become increasingly rigid, having a stiffening effect on the lattice greater than that due to the density increase [157]. The extra upright z-strut in the BCCz lattice is subject to stretching and not bending, with deviations from the slender beam assumptions having a reduced impact. The apparent elastic modulus of the BCCz lattice is therefore similar to the analytical model for a larger relative density range.

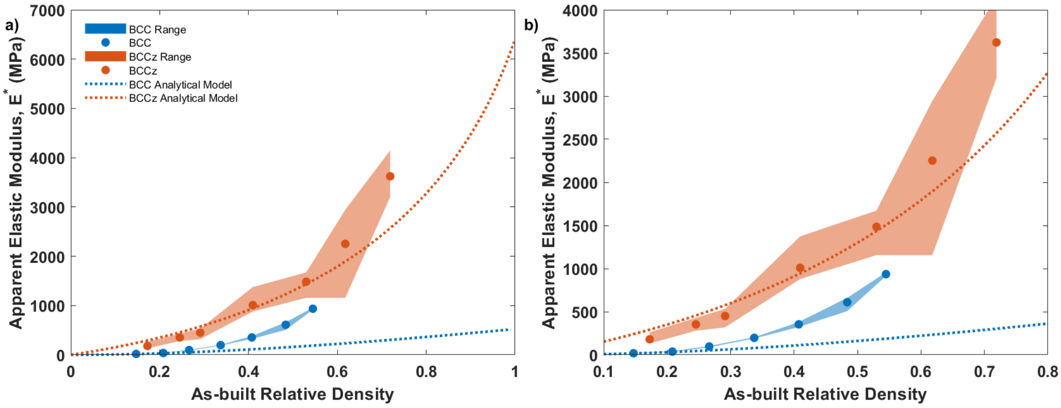

FIGURE 4.15: As-built relative density versus as-built apparent elastic modulus for both BCC (blue) and BCCz (orange) lattices over a range of relative densities with range (shaded regions) and analytical models for BCC (blue dotted) and BCCz (orange dotted). a) full plot and b) zoomed-in plot over the range of as-built results.

Empirically fitting as-built results to the Ashby and Gibson analytical model for porous solids Eq. 4.4.4, across two regions, for relative densities less than 30% and greater than 30% for both the BCC and BCCz geometries shows good agreement (Fig. 4.16 and Table 4.4.1). The lattices can still be treated as porous solids but need to have different relationships for low and high relative densities and according to Ashby and Gibson, a change is expected at a relative density of 30% [28]. A fit was also performed across the full relative density range for the BCC geometries as the powers for the two density ranges (Table 4.4.1) where similar.

$$E^* = E_s \left(\frac{\rho^*}{\rho_s}\right)^n \cdot C \qquad \text{(Eq. 4.4.4)}$$

According to Ashby and Gibson [28], the power, n, should be 2 and 1 for bending- and stretching-dominated open-celled porous solids respectively. Although the power for all the fits are greater than expected (Table 4.4.1), the powers for the bending-dominated (BCC) plots are greater than that of the stretching-dominated (BCCz) plots, as expected.

The greater than expected power for the low relative density stretching-dominated plot of 1.7 is likely because angled struts are expected to deform in bending

Geometry Type	Relative Density Range	Power	R^2
BCC (expected bending)	$\leq 30\%$	3.41	0.986
	$> 30\%$	3.34	0.999
	all	3.30	0.999
BCCz (expected stretching)	$\leq 30\%$	1.70	0.993
	$> 30\%$	2.64	0.981

TABLE 4.4.1: Summary of powers R^2 for bending- and stretching-dominated uniform lattices fitted to Ashby-Gibson relationship for relative density and apparent elastic modulus over two relative density ranges.

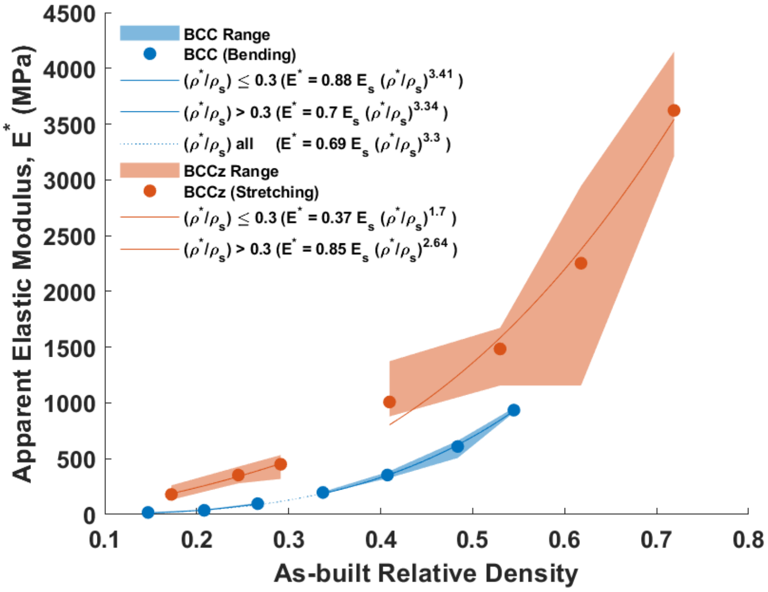

FIGURE 4.16: As-built relative density versus as-built apparent elastic modulus for both BCC (blue) and BCCz (orange) lattices over a range of relative densities with range (shaded regions). Ashby-Gibson equations (Eq. 4.4.4), fitted for C and n for 2 regions, for relative densities less than 30% and greater than 30% for both the BCC (blue line) and BCCz geometries (orange line).

(corresponding to the higher power law of 2), and only the z-strut is expected to deform by stretching (corresponding to a power of 1). Beyond a relative density of 30%, the BCCz geometry appears to become even more bending-dominated with a power of 2.64, similar to that of natural porous materials such as wood and cancellous bone [158] which both have powers between 2 and 3.

The powers for the bending-dominated plots are 3.41 and 3.34 for less than and greater than 30% relative density and 3.30 for the full relative density range. This differs from that predicted for bending-dominated open-celled porous solid with a power of 2 expected, but aligns more closely with the behaviour of foams produced by replication, which have a power closer to 3 and natural porous metamaterials such as wood and bone [158]–[160]. These foams are modelled with most of the material concentrated at the joints between struts instead of on the struts themselves, somewhat similar to the material accumulation at the joints for high-density uniform lattices.

Although the power law fits appear to fit well with the experimental data, with R^2s greater than 0.98 in all cases, further confirmation of this is possible by plotting the experimental data in Fig. 4.16 on a logarithmic plot as in Fig. 4.17 and determining the logarithmic fits, using Eq. 4.4.5, where n should be similar to the power in the Ashby-Gibson based equations Eq. 4.4.4. Eq. 4.4.5, is a standard linear fit where y is $ln(E^*)$ and x is $ln\left(\frac{\rho^*}{\rho_s}\right)$. A summary of the n terms and corresponding R^2 is provided in Table 4.4.2.

$$ln(E^*) = \left(n \cdot ln\left(\frac{\rho^*}{\rho_s}\right)\right) + c \qquad \text{(Eq. 4.4.5)}$$

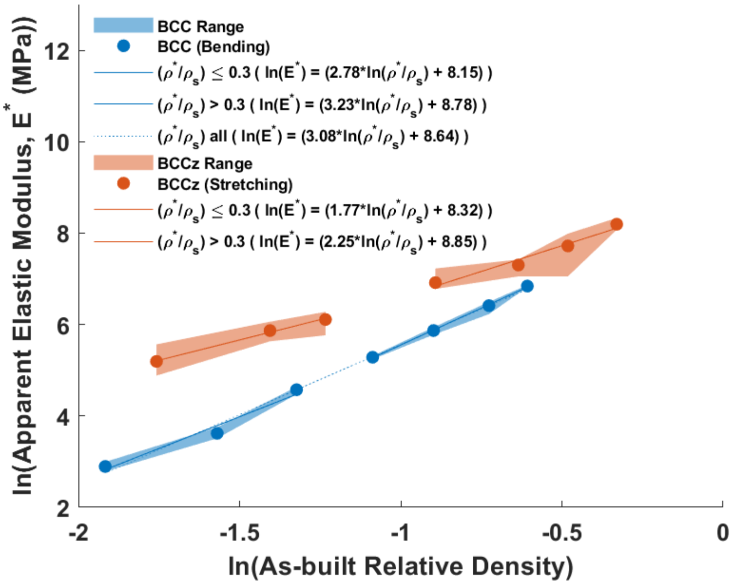

FIGURE 4.17: Log-log plot of as-built relative density versus as-built apparent elastic modulus for both BCC (blue) and BCCz (orange) lattices over a range of relative densities with range (shaded regions). Log-log equation 4.17 fitted for n (similar to Eq. 4.4.4) and c (intercept) for 2 regions, for relative densities less than 30% and greater than 30% for both the BCC (blue line) and BCCz geometries (orange line).

A clear linear relationship is evident on the log-log plot in Fig. 4.17, evidenced by the high R^2 for all linear fits (Table 4.4.2). The n terms are similar to those for the Ashby-Gibson based fits (summary in Table 4.4.1), confirming their suitability.

Geometry Type	Relative Density Range	n	R^2
BCC (expected bending)	$\leq 30\%$	2.78	0.969
	$> 30\%$	3.23	0.999
	all	3.08	0.995
BCCz (expected stretching)	$\leq 30\%$	1.77	0.995
	$> 30\%$	2.25	0.968

TABLE 4.4.2: Summary of powers R^2 for bending- and stretching-dominated uniform lattices fitted to logarithmic Ashby-Gibson relationship for relative density and apparent elastic modulus over two relative density ranges.

4.4.4 Failure Behaviour

The bending- and stretching-dominated lattices exhibited distinct failure patterns. The bending-dominated lattices fail suddenly; all of the struts and therefore load paths are angled, resulting in a shear force effects causing failure due to shear bands [161] (Fig. 4.18a), with failure initiating at the joints between struts as these are known points of stress concentrations. However, for the stretching-dominated lattices, failure is more progressive, initiating and progressing along the bottom layer (Fig. 4.18b), before shear bands are observed along the angled struts (Fig. 4.18c). For the stretching-dominated lattices, failure initiates at the joints between struts as well as within vertical struts due to buckling. As the top and bottom faces are adhered to the platens, the boundary conditions can be treated as contacts with infinite friction. However, the top compression platen was hemispherically seated and had more rotational degrees of freedom than the bottom plate which was fully fixed. Stress is therefore likely to concentrate at the fixed bottom layer causing it to fail there first.

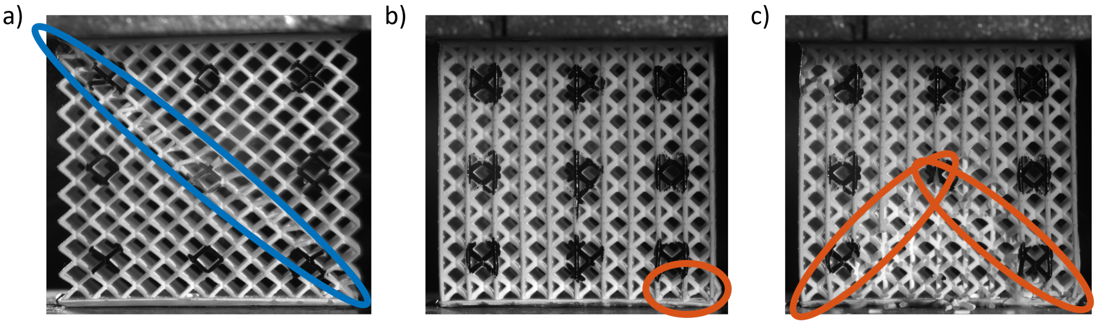

FIGURE 4.18: Representative image for the failure of a) bending-dominated lattices with the shear band highlighted in blue and representative image for the failure of stretching-dominated lattices with b) the initial point of failure and c) the shear band highlighted in orange.

For all the lattices investigated, there was an increase in the failure strain compared to that of the base material of 1.7% (Fig. 4.19). This is expected, for lattice structures, the loading is more heterogeneous, with manufacturing defects resulting in more localised failure instead of global failure. This increases the deformation and therefore strain to failure compared to a solid uniform material. Additionally, the failure strain of all samples, was greater than that of cancellous bone which varies between 1 to 2.5 % [17].

The relationship between failure strain and relative density appears opposite for bending- and stretching-dominated geometries. For BCC geometries, increasing relative density decreases failure strain until a relative density of approximately 30% where it plateaus at approximately 3% strain. For the BCCz geometries, there is a general trend of increasing failure strain with relative density. This trend, however, is less distinct as the BCCz geometries show large ranges. Failure strain was determined using platen measurements corrected for machine compliance as determined from optical strain measurements. Upon examining the individual stress strain curves and images to failure, no clear reason for this was observed with samples behaving as expected.

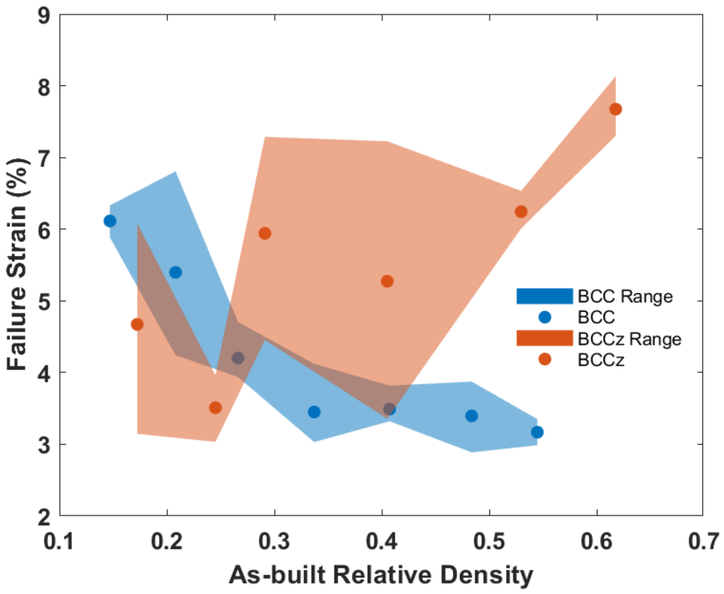

FIGURE 4.19: As-built relative density versus strain at sample failure for both BCC (blue) and BCCz (orange) uniform lattices over a range of relative densities. BCCz samples at the highest designed relative density did not fail completely during the test so are not shown here. Range (maximum to minimum) of results are shown with shaded regions.

The maximum stress is greater for stretching-dominated samples than for bending-dominated samples at the same relative density (Fig. 4.20). The extra z-strut in the loading direction of the stretching-dominated geometries increases the resistance to loading, increasing the maximum stress reached. Interestingly, the stretching-dominated geometries appear to have a greater variation in results than the bending-dominated geometries, as evidenced by the coefficient of variation for maximum stress (Fig. 4.21). Stretching-dominated lattices are known to be more

Geometry Type	Power	R^2
BCC (expected bending)	2.88	0.9995
BCCz (expected stretching)	2.323	0.992

TABLE 4.4.3: Summary of powers R^2 for bending- and stretching-dominated uniform lattices fitted to Ashby-Gibson relationship for relative density and maximum stress over two relative density ranges.

sensitive to defects and failure than bending-dominated lattices [162], of which both these structures are already sensitive to due to the brittle nature of the base material, thereby increasing the failure to strain variation for the stretching-dominated lattices. Fitting the average maximum stress data to relative density, as with Ashby-Gibson equations, reveals good fits (high R^2) and powers similar to that of cancellous bone, which has powers of 2 [17], Table 4.4.3.

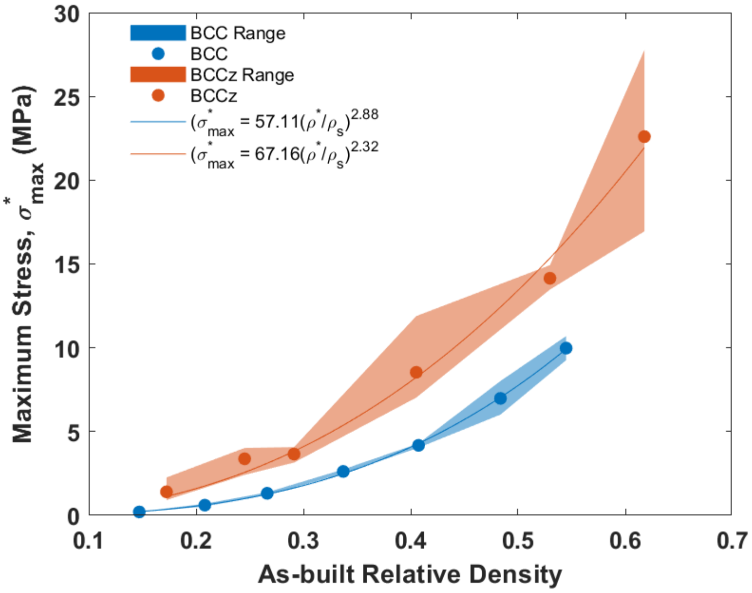

FIGURE 4.20: As-built relative density versus maximum stress for both BCC (blue) and BCCz (orange) uniform lattices over a range of relative densities. Range (maximum to minimum) results are shown with shaded regions. Trends with relative density for average results are shown by the solid lines.

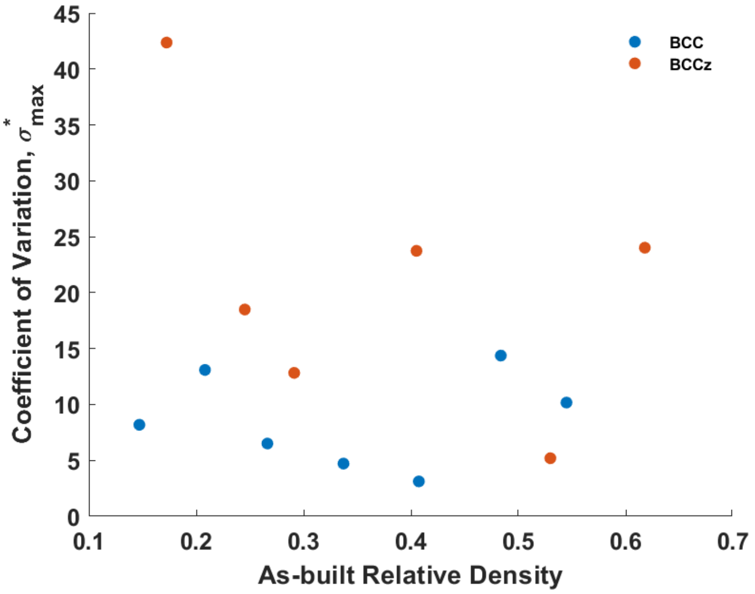

FIGURE 4.21: As-built relative density versus coefficient of variation for the maximum stress for both BCC (blue) and BCCz (orange) uniform lattices over a range of relative densities.

The energy absorbed to failure is greater for stretching-dominated samples than for bending-dominated samples at the same relative density (Fig. 4.22). The stretching-dominated lattices withstand a greater maximum stress, and for relative densities greater than 30% have a greater failure strain, resulting in increased energy absorption. The stretching-dominated lattices also have increased variation, reflected in the coefficient of variation plot (Fig. 4.23) as with the maximum stress. As before, the stretching-dominated lattices are likely more sensitive to defects resulting in more varied failure behaviour.

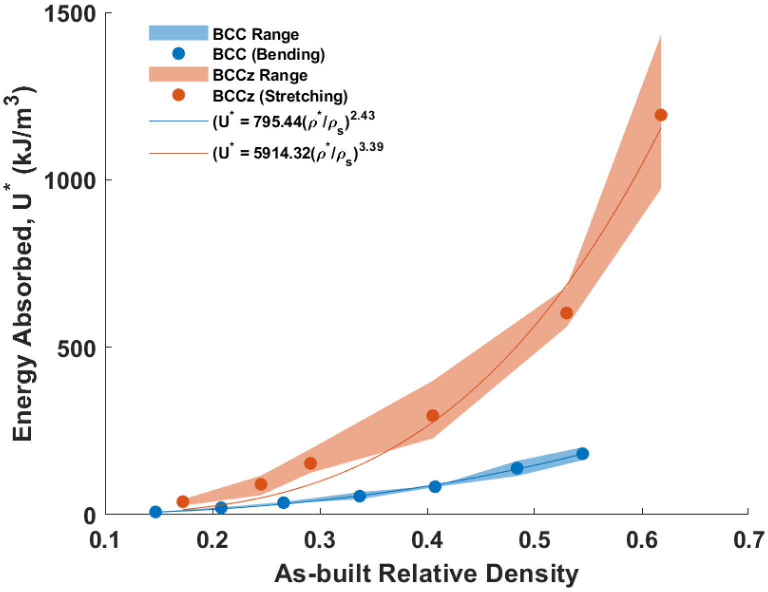

FIGURE 4.22: As-built relative density versus energy absorbed to sample failure for both BCC (blue) and BCCz (orange) uniform lattices over a range of relative densities. BCCz samples at the highest designed relative density did not fail completely during the test so are not shown here. Range (maximum to minimum) results are shown with shaded regions. Trends with relative density for average results are shown by the solid lines.

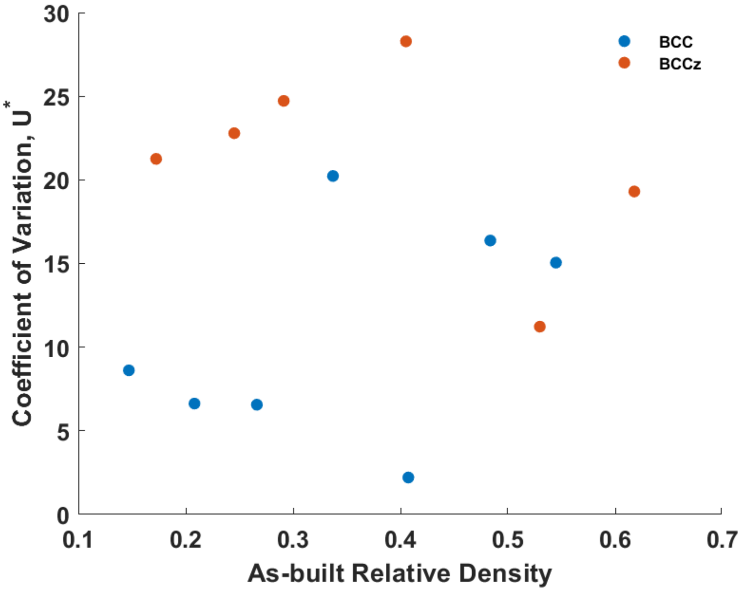

FIGURE 4.23: As-built relative density versus coefficient of variation for energy absorbed to sample failure for both BCC (blue) and BCCz (orange) uniform lattices over a range of relative densities. BCCz samples at the highest designed relative density did not fail completely during the test so are not shown here.

4.5 Conclusions

Distortions are seen for all samples, increasing after the secondary cure phase and taking on a more dome-like shape with the centre of the dome resting in the middle or at a corner of endplates. This is likely due to an increase in residual stresses from curing as a result of polymer chains cross-linking resulting in part shrinkage [156]. Additionally, the bending-dominated geometries initially have high levels of distortion, decreasing as the relative density decreases and levelling off at a relative density of approximately 30%. The relationship is less distinct for the stretching-dominated geometries due to the considerable variation but generally follows a similar although more gradual trend. Using the adapted elastic foundation model (Chapter 3), the observed distortion ranging from 70 - 600 μm is predicted to reduce the initial apparent elastic response of lattices (up to 0.3% strain), with a distortion of 100 μm resulting in approximately a 50% decrease in initial apparent elastic modulus, over a range of strain which encourages bone growth in engineered tissue scaffolds (0.15 to 0.3 % strain).

The as-built relative density is consistently greater than as-designed by 10 and 12% for bending- and stretching-dominated geometries respectively. This difference between as-built measurements and as-designed predictions persisted despite accounting for errors in predictions due to double-counting of overlapping material at cell junctions. The difference is consistent with as-built cell strut diameters larger than as-designed. Using as-built relative densities, the geometry specific analytical models for the bending-dominated geometries accurately predicts the apparent elastic response for low relative densities. Deviations from the analytical model increase with increasing relative density due to greater deviations from slender-beam assumptions and the increased impact of the rigid strut joint [41], [157]. For the stretching-dominated geometries, these analytical models are accurate up to higher relative densities of $\approx$ 50%, due to the extra z-strut that deforms by stretching and thus are not affected by the slender-beam assumption. Ashby-Gibson based power law fits were developed for both geometry types over two relative density ranges, less than and greater than 30%. These showed higher than expected powers based on loading type, greater than 3 for the bending-dominated geometries and 1.7 and 2.6 for the stretching-dominated geometries, but similar powers to natural porous materials such as bone and wood.

Concerning failure properties, the strain to failure was at least double for all samples than for the base material. For bending-dominated geometries, strain to failure decreases with relative density and the opposite is observed for the stretching-dominated geometries. Additionally, as expected, the maximum stress, and therefore energy absorbed for the stretching-dominated geometries is greater than for the bending-dominated geometries with the same relative density. Greater variation in properties is observed for the stretching-dominated geometries as they are more sensitive to defects that affect failure properties. However, there is considerable variation for both the bending- and stretching-dominated geometries, across all the mechanical properties evaluated. This is likely primarily due to the base material modulus variation between struts as discussed in the previous investigation (Chapter 3) as well as geometric variations between samples.

The relationships investigated here are for uniform porous metamaterials which have limited real-world applications compared to non-uniform lattices often used for light-weighting applications. They are predicted to perform similarly to uniform lattices where elastic properties are concerned but outperform in regards to failure characteristics. The relationships developed here can be used to explain the trends and relationships for non-uniform porous metamaterials as in the next investigation (Chapter 5), required for the design of lattices for a tailored response.

Chapter 5

Distortion and Apparent Compressive Properties of Graded and Stochastic Lattice Metamaterials

5.1 Abstract

Non-uniform structures with varying densities are useful for many applications including light-weighting and are often found in natural porous materials for example in bone and wood. It is hypothesised that the semi-random density variations (described by a disorder parameter) in natural porous materials contribute to the enhanced mechanical properties compared to uniform synthetic materials and was verified in a previous investigation using 2D lattice structures [1], [2]. This investigation applies a similar methodology creating lattices from a brittle base material using simplified unit cells with two levels of random density distribution to determine if the same benefits apply. Compared to uniform lattices, for the same relative density, disorder increases resistance to loading, increasing compressive apparent elastic modulus and maximum stress, with the effect more pronounced for highly ordered stretching-dominated lattices. However, as the brittle base material results in defect sensitive lattices, the disorder has a minimal impact on strain to failure and energy absorption, with results comparable to uniform structures. Additionally, the influence of non-uniform density distributions on height distortions, known to affect apparent properties is determined, with similar levels of distortion observed compared to uniform lattices. Increasing disorder decreases observed distortions for both geometry types likely due to an improved residual stress distribution, a desirable outcome. The methodology presented in Chapter 5 and initial trends are a starting point for understanding the behaviour of non-uniform

porous metamaterials which have the potential to expand the material property space accessible by synthetic materials.

5.2 Introduction

In Chapter 4, trends and relationships were established for uniform bending- and stretching-dominated porous metamaterials with respect to relative density. Key factors for mechanical performance were measured, including distortion, apparent elastic modulus and failure characteristics such as strain to failure. This chapter seeks to further these relationships, investigating the effect of random density variations within a lattice on the same properties. Such tailored, non-uniform porous metamaterials offer advantages in terms of lightweight load-bearing and energy absorption in applications like aerospace, or nutrient absorption and waste exchange in engineered bone tissue scaffolds for biomedical applications, where matching the stiffness and geometry to that of cancellous bone is key to achieving the desired results [122].

Following a brief introduction and research justification in Section 5.2, the methodology for sample manufacture, mechanical and geometric characterisation is detailed in Section 5.3. In Section 5.4, the impact of the disorder (a measure of randomness) on the height distortion of lattices is compared to the behaviour of uniform bending- and stretching-dominated porous metamaterials. This is followed by an in-depth discussion of the differences that disorder and geometry type can have on mechanical properties such as apparent elastic modulus and failure strain, with comparison to the uniform lattice results from the previous Chapter 4. Key results are summarised in Section 5.5 with a potential use case presented for this research.

5.3 Methodology

5.3.1 Porous Metamaterial Fabrication

Seven types of lattices were manufactured to investigate the influence of varying relative densities and unit cell geometry types on overall specimen height distortions and mechanical properties. Two types of graded lattices (Section 5.3.1.1) and five types of stochastic lattices (Section 5.3.1.2) were studied. A summary of the design parameters for all lattices is given in Table 5.3.1. Within the stretching-dominated lattices, both graded and stochastic lattices (with two levels of disorder, defined in Section 5.3.1.2), were designed to achieve the same average relative density (approximately 0.4), combining unit cells with differing relative density ranges. The same process was applied to bending-dominated lattices to achieve an

Unit Cell Type	**Gradient Type**	**Disorder Value**	**Unit Cell Relative Density Range**	**Average Designed Relative Density**
Bending (BCC)	Graded	N/A	0.16 - 0.50	0.33
Stretching (BCCz)	Graded	N/A	0.18 - 0.62	0.40
Bending (BCC)	Stochastic	0.8	0.16 - 0.50	0.33
Stretching (BCCz)	Stochastic	0.8	0.18 - 0.62	0.40
Bending (BCC)	Stochastic	0.4	0.16 - 0.54	0.33
Stretching (BCCz)	Stochastic	0.4	0.18 - 0.62	0.41
Bending (BCC) and Stretching (BCCz)	Stochastic	0.8	0.16 - 0.36 (BCC) and 0.43 - 0.62 (BCCz)	0.37

TABLE 5.3.1: Summary of Design Parameters for Graded and Stochastic Lattices. Relative density was based on the as-built relative density of uniform lattices, observed in Chapter 4.

average relative density of 0.33. One stochastic lattice combined both bending- and stretching-dominated unit cells for an intermediate relative density of 0.37. Three repeats of each lattice were manufactured in line with the previous investigation (Chapter 4). Additionally, the studies in this thesis were exploratory and prioritised evaluating a larger number of geometry variations, providing a greater insight into potential trends. As such, the number of repeats were limited.

Density variations were achieved by combining unit cells with differing relative densities based on the relative density of uniform lattices with the same as-designed strut diameter. To account for the difference between the as-designed and the as-built relative density observed in Chapter 4, the relative density of each unit cell was determined from Eq. 5.3.1 and Eq. 5.3.2, for the stretching- and bending-dominated geometries respectively, correcting for greater than expected strut diameters. This is a best approximation as there will be minor differences due to excess material between neighbouring unit cells with differing relative densities.

$$\frac{\rho^*}{\rho_s}BCCz = 1.04 \cdot \left(\frac{(1+4\sqrt{3})\pi}{4} \cdot \left(\frac{d}{L}\right)^2 - \frac{11\pi}{6} \cdot \left(\frac{d}{L}\right)^3 \right) + 0.12 \qquad \text{(Eq. 5.3.1)}$$

$$\frac{\rho^*}{\rho_s} BCC = 1.09 \cdot \left(\sqrt{3}\pi \left(\frac{d}{L} \right)^2 - \frac{55\pi}{36} \cdot \left(\frac{d}{L} \right)^3 \right) + 0.1 \qquad \text{(Eq. 5.3.2)}$$

As in Chapters 3 and 4, lattices were manufactured with top and bottom endplates to protect the struts during post-processing and encourage more uniform loading. Samples were manufactured using a Form3 stereolithography printer with Rigid10K resin (layer height of 0.05 mm), a glass-particle reinforced acrylic based resin with a base material elastic modulus of 10 GPa (Formlabs, Massachusetts, United States of America, see Appendix 10 for material data sheets) [123]. Samples were post-processed according to PP2 in Chapter 3, which involved washing samples in IPA for 12 minutes in an ultrasonic bath, followed by at least a 30 minute air dry, 120 minutes under a 5 Pa vacuum, 120 minutes in an oven at 60 °C and an additional 60 minute cure under UV light.

5.3.1.1 Graded Lattices

Three repeats each of one bending- (BCC) and one stretching-dominated (BCCz) graded lattice were designed in MATLAB [154] with the relative density varying continuously within each layer (in the XY plane). For both geometry types, the relative density starts high (H in Fig 5.1) on the outer-most unit cell. The relative density decreases towards the centre of the layer to the minimum relative density (L in Fig 5.1), before increasing back to the higher relative density on the opposite outer-most unit cell. Ranges for the relative density can be found in Table 5.3.1, with the relative density of each unit cell matching an as-built value for the uniform lattices. The as-designed relative density sequence of the bending- and stretching-dominated unit cells were 0.50, 0.42, 0.34, 0.26, 0.16, 0.16, 0.26, 0.34, 0.42, 0.50 and 0.62, 0.51, 0.40, 0.30, 0.18, 0.18, 0.30, 0.40, 0.51, 0.62 respectively. The direction of the gradient was in either the X- or the Y- direction within each layer (example shown in Fig. 5.2), and alternated in the subsequent layer. The average relative density within each layer was constant and therefore equal to the overall relative density of the specimen (0.33 and 0.40 for the graded bending- and stretching-dominated lattices respectively). It also matched the average relative density of the stochastic lattices. There was no relative density variation in the build (Z-) direction as the lowest relative density layer in the build direction would have likely dominated both elastic and failure behaviour. The relative density was varied in both the X- and Y- directions to ensure failure was symmetric and no one direction (X- or Y-), had a dominating effect, as might be the case if the relative density was only varied in one direction. Additionally, the relative density was varied in the X- and Y- directions between alternating layers to introduce a more gradual and less distinct relative density change across two layers compared to varying the relative density in both the X- and Y- directions within one layer, shown by mapping the average relative density of the unit cells across two layers (Fig. 5.3). A more gradual variation in relative density reduces the number of potential failure initiation points, meaning failure is dictated by gradient and not defects.

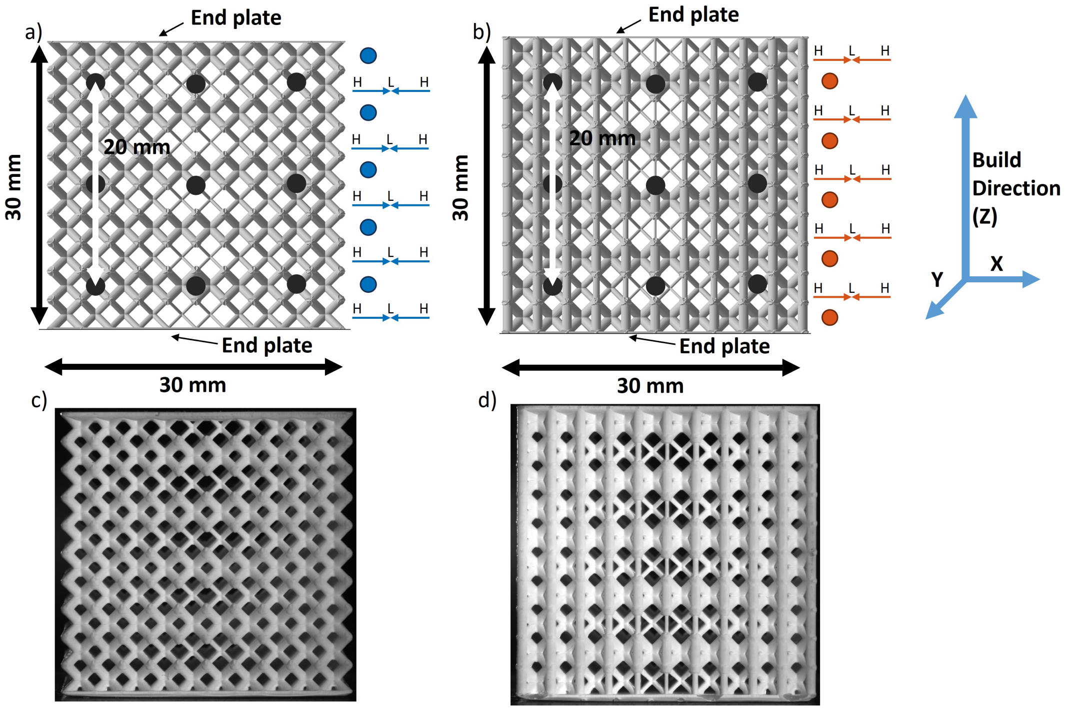

FIGURE 5.1: Graded a) & c) bending-dominated, BCC and b) & d) stretching-dominated, BCCz lattices where vertical struts are aligned with the build direction. H and L indicate the highest and lowest relative density from the relative density range with arrows indicating the variation along the page (X- direction). Blue and orange circles indicate the direction of relative density gradient into the page (Y-direction). Endplates protect the top and bottom struts. Dots marked on the front and back for optical strain measurement with a maximum virtual gauge length of 20 mm. c) and d) are examples of samples prior to testing.

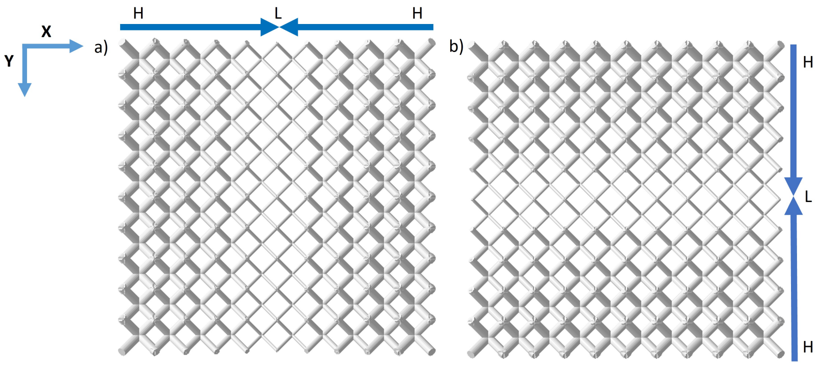

FIGURE 5.2: Relative density variation in a) X- and b) Y- direction within a layer for a bending-dominated sample. H and L indicate the highest and lowest relative density from the relative density range, with arrows indicating the direction of variation. The same pattern of variation is also implemented in the stretching-dominated samples.

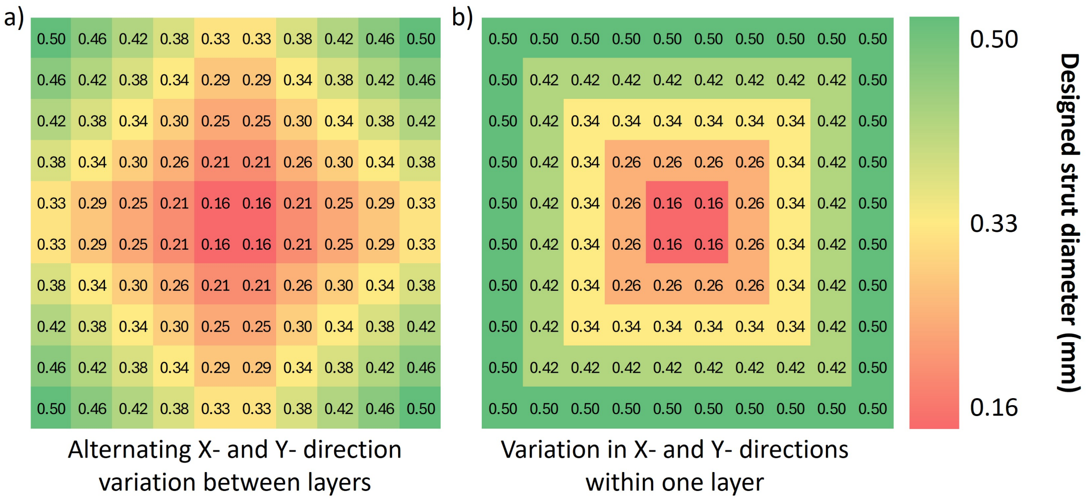

a)

0.50	0.46	0.42	0.38	0.33	0.33	0.38	0.42	0.46	0.50
0.46	0.42	0.38	0.34	0.29	0.29	0.34	0.38	0.42	0.46
0.42	0.38	0.34	0.30	0.25	0.25	0.30	0.34	0.38	0.42
0.38	0.34	0.30	0.26	0.21	0.21	0.26	0.30	0.34	0.38
0.33	0.29	0.25	0.21	0.16	0.16	0.21	0.25	0.29	0.33
0.33	0.29	0.25	0.21	0.16	0.16	0.21	0.25	0.29	0.33
0.38	0.34	0.30	0.26	0.21	0.21	0.26	0.30	0.34	0.38
0.42	0.38	0.34	0.30	0.25	0.25	0.30	0.34	0.38	0.42
0.46	0.42	0.38	0.34	0.29	0.29	0.34	0.38	0.42	0.46
0.50	0.46	0.42	0.38	0.33	0.33	0.38	0.42	0.46	0.50

Alternating X- and Y- direction variation between layers

b)

0.50	0.50	0.50	0.50	0.50	0.50	0.50	0.50	0.50	0.50
0.50	0.42	0.42	0.42	0.42	0.42	0.42	0.42	0.42	0.50
0.50	0.42	0.34	0.34	0.34	0.34	0.34	0.34	0.42	0.50
0.50	0.42	0.34	0.26	0.26	0.26	0.26	0.34	0.42	0.50
0.50	0.42	0.34	0.26	0.16	0.16	0.26	0.34	0.42	0.50
0.50	0.42	0.34	0.26	0.16	0.16	0.26	0.34	0.42	0.50
0.50	0.42	0.34	0.26	0.26	0.26	0.26	0.34	0.42	0.50
0.50	0.42	0.34	0.34	0.34	0.34	0.34	0.34	0.42	0.50
0.50	0.42	0.42	0.42	0.42	0.42	0.42	0.42	0.42	0.50
0.50	0.50	0.50	0.50	0.50	0.50	0.50	0.50	0.50	0.50

Variation in X- and Y- directions within one layer

FIGURE 5.3: Example variation of average strut diameter across two layers for a lattice with a) the relative density varying in the X- and Y- direction in alternating layers and b) the relative density varying in both the X- and Y- directions within each layer.

5.3.1.2 Stochastic Lattices

The relative density of the stochastic lattices was randomly varied, with the degree of variation determined by a Voronoi-based disorder parameter, δ, based upon the work of Aranguren van Egmond *et al.*, [1], [2]. They designed stochastic lattices made up of Voronoi unit cells with varying cell size (and therefore varying relative density), but uniform cell wall thickness, and defined δ as the ratio between the smallest minimum distance between the seed points of two neighbouring Voronoi cells normalised by the seed-to-seed distance of neighbouring regular hexagonal cells.

In a procedure adapted from this work by Aranguren van Egmond [2], a simple sequential inhibition (SSI) algorithm 9.1 was used to determine the cell size variability of 100 randomly seeded Voronoi cells (100 chosen to match the 100 unit cells in a layer). δ was set to 0.8 or 0.4 depending on the stochastic lattice to be created (as specified in Table 5.3.1). The algorithm would pseudo-randomly create new seed points, discarding them if they did not fulfil the disorder criteria, and repeating until the desired number of cells were created. The areas of all Voronoi cells were then calculated and scaled such that the minimum and maximum Voronoi cell areas corresponded to the designed relative density ranges of the stochastic lattice designs in the present work (Table 5.3.1). The Voronoi cell areas were converted to relative density ($Voronoi\ based\ \frac{\rho^*}{\rho_s}$) by scaling to the relative density range using Eq. 5.3.3, where A_V is the area of the Voronoi cell, $A_{V\ min}$ is the minimum Voronoi cell area across all the cells, $A_{V\ max}$ is the maximum Voronoi cell area across all the cells, $\frac{\rho^*}{\rho_s}_{max}$ is the maximum relative density from the relative density range and $\frac{\rho^*}{\rho_s}_{min}$ is the minimum relative density from the relative density range. BCC or BCCz strut diameters corresponding to these relative densities were determined from strut diameter versus relative density plots using Eq. 5.3.2 and Eq. 5.3.1 respectively. These strut diameters were converted into the closest corresponding manufacturable strut diameter, accounting for the difference between as-built and as-designed geometries, as determined previously in Chapter 4, Section 4.4.1. This process of Voronoi cell generation and converted lattice design was repeated until the average relative density of the 100 unit cells was within 1% of the target (chosen to match a corresponding graded lattice). For a single layer, the arrangement/location of the unit cells was randomised using MATLAB's "randi" function, as the locations of the seed points of the Voronoi cells could not be systematically linked to the regular position of the unit cells. The random arrangement of unit cells was repeated for additional layers of the lattice, maintaining both average relative density (similar to graded lattices) and δ throughout by using the same assortment of unit cells. The density was therefore also randomly varied in the Z-direction, with a similar random variation achieved by the Voronoi algorithm used to produce the first layer.

$$Voronoi\ based\ \frac{\rho^*}{\rho_s} = \left((A_V - A_{V\ min}) \cdot \left(\frac{\frac{\rho^*}{\rho_s}_{max} - \frac{\rho^*}{\rho_s}_{min}}{A_{V\ max} - A_{V\ min}} \right) \right) + \frac{\rho^*}{\rho_s}_{min} \qquad \text{(Eq. 5.3.3)}$$

A δ of 0.8 was chosen for stochastic lattice designs as, according to Aranguren van Egmond *et al.*, [1], [2], these structures can have improved failure characteristics compared to fully ordered (uniform) structures in terms of strain to final failure and energy absorption. A δ of 0.4 was also chosen in order to assess expected trends with changes in disorder. Aranguren van Egmond *et al.*, [1] reported that increasing disorder (i.e. decreasing δ) tends to increase strain to failure but to the detriment of maximum stress and energy absorption, for the same relative density. The resulting stochastic lattices are shown in Fig. 5.4.

Stochastic lattices were designed with bending-dominated BCC unit cells, stretching-dominated BCCz unit cells, and also a combination of the two as shown in Fig. 5.5. The combination of bending- and stretching-dominated unit cells can achieve a wider variation of local properties, and thus a wider range of mechanical disorder, in contrast to the geometric disorder captured by δ and design process used above. Stochastic lattices combining BCC and BCCz were designed with a δ of 0.8. Unit cells above a relative density of 0.34 were designated as BCCz, and lower density cells were BCC. This cut-off was chosen because, below a relative density of 0.34, the mechanical properties of BCC and BCCz lattices are relatively small (Fig. 4.15). The location of both the BCC and BCCz unit cells within a layer was randomised as before, using MATLAB's "randi" function.

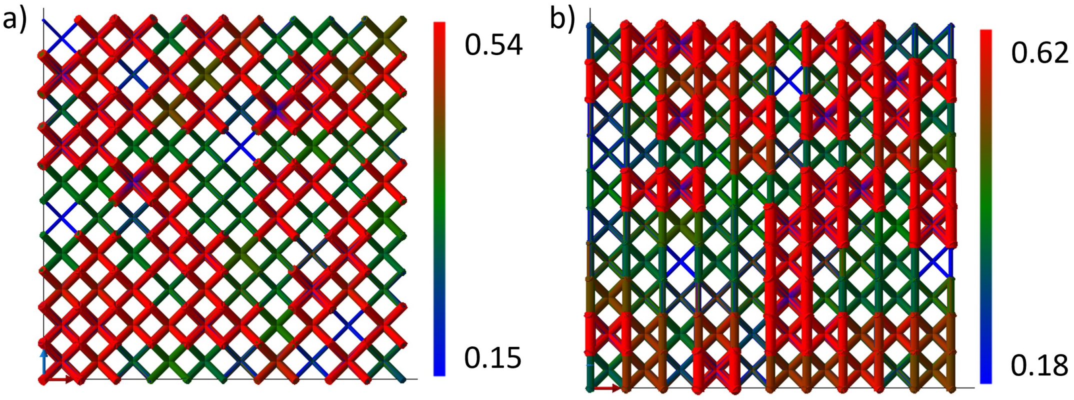

FIGURE 5.4: Example of variation of stochastic a) bending-dominated, BCC and b) stretching-dominated, BCCz lattice with δ = 0.4. The colour bar indicates the relative density of the individual unit cells, with the maximum of the range as red and the minimum as blue.

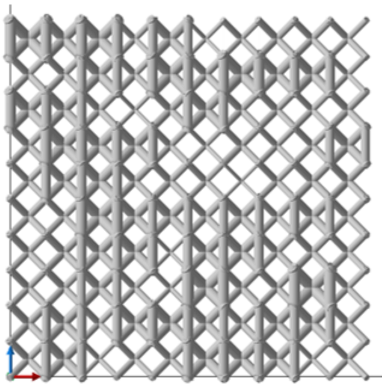

FIGURE 5.5: Mixed stochastic lattice built up from both bending- (BCC) and stretching-dominated (BCCz) unit cells with varying relative densities. High relative density cells (> 0.34) are BCCz and lower relative density cells ($=< 0.34$) are set to BCC. $\delta = 0.8$.

5.3.2 Mechanical Testing

The procedure for carrying out quasi-static compression follows that in the previous investigation (Chapter 4). Samples (n = 21), were quasi-statically compressed with the endplates of all samples adhered to flat metal plates using a cyanoacrylate based adhesive to minimise the effects of height distortions on the loading behaviour of the lattices, as concluded in Chapter 3. Both platen and optical measurements were used to measure strain. Optical measurements account for machine compliance and more accurately capture surface strains for porous materials matching the behaviour as calculated from digital volume correlation [117]. The testing and processing parameters are specified in Chapter 3, Section 4.3.2 and in Appendix 7.2.

The apparent elastic modulus of samples was determined as described in Chapter 4, Section 3.3.2, in a procedure adapted from NPL's 'Measurement Good Practise Guide No. 98: Elastic Modulus Measurement' [129]. Failure characteristics such as final strain to failure and energy absorbed were determined as in Chapter 4, Section 4.3.2, after the procedure to account for the machine compliance with platen data was applied (Chapter 4, Section 4.3.2).

To compare the apparent elastic modulus, maximum stress and energy absorption of the graded and stochastic lattices more easily to uniform lattices, results were normalised using trends from average uniform results of the same geometry type, i.e. bending- or stretching-dominated. The results of the mixed stochastic lattice were normalised to that of the stretching-dominated uniform results.

5.3.3 Geometrical Characterisation

Average width, depth and height measurements (three measurements per direction, measured with SPI callipers, Swiss Precision Instruments, accurate to 0.02 mm) along with mass (measured to four decimal places, AE 240 Mettler Toledo (Ohio, United States) were used to determine the as-built relative density of the graded and stochastic lattices. In Chapter 4, this method was shown to accurately capture the relative density of the lattice once the endplates were accounted for. After both the IPA wash and secondary UV cure, height distortion measurements were captured and measured following the procedure in Chapter 4, Section 4.3.3.

5.4 Results and Discussion

5.4.1 Geometry Characterisation

By applying Eq. 5.3.1 and Eq. 5.3.2 (Chapter 4), the as-designed and as-built relative densities of the gradient and stochastic lattices agreed closely. Minimal differences were observed between lattice types, both for bending- versus stretching-dominated and for graded versus stochastic lattices. However, the as-built relative density for all graded and stochastic lattices was still slightly greater than designed. This was likely due to adjacent unit cells with large differences in relative density having a build-up of excess material at the joints between the neighbouring unit cells (Fig. 5.7). The lowest level of disorder for stochastic lattices (diamond points, δ = 0.8) had the greatest difference.

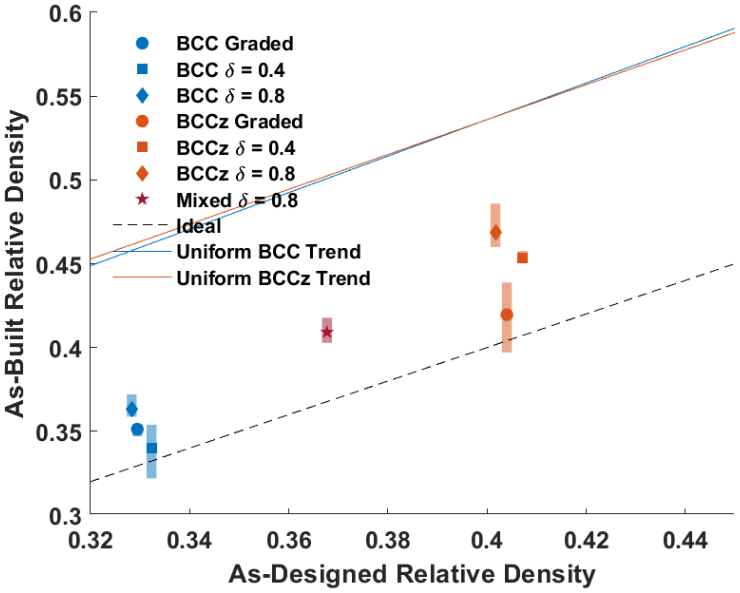

FIGURE 5.6: Comparison between as-designed and as-built relative density for graded (circle) and stochastic (square and diamond) bending- (BCC, blue) and stretching-dominated (BCCz, orange) lattices. The mixed stochastic lattice is given by the red star. Shaded regions indicate the range of data (maximum to minimum). First-order trend lines of the BCC (blue) and BCCz (orange) lattices derived in the previous investigation (Chapter 4) are shown for comparison.

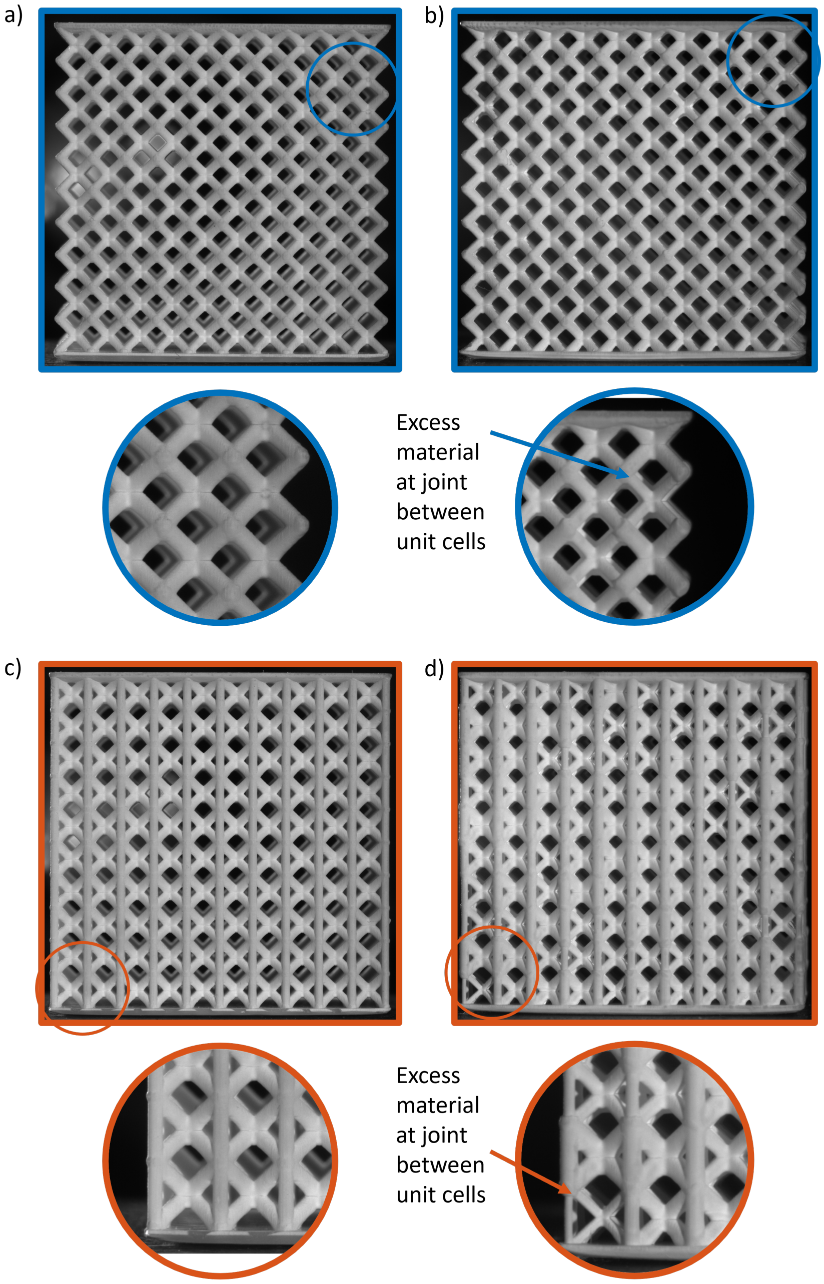

FIGURE 5.7: Excess material between neighbouring cells in stochastic BCC (b) and BCCz (d) lattices. Uniform lattices (a and c) at the same approximate as-built relative density are shown for comparison. Stochastic lattice with $\delta = 0.8$ shown.

5.4.2 Endplate Distortions

Evidence of endplate distortions were seen in all samples both before (Fig. 5.8a) and after (Fig. 5.8b) the secondary cure phase with the average distortion ranging from approximately 50 - 85 μm to 75 - 100 μm respectively. Before the secondary cure phase (Fig. 5.8a), there was no noticeable difference between the non-uniform stretching-dominated lattices (BCCz), with similar average distortions of approximately 85 μm. This was also observed after the secondary cure phase (Fig. 5.8b) with range overlaps between all lattice types. The same trends were not seen for the non-uniform bending-dominated lattices (BCC). Before the secondary cure phase (Fig. 5.8a), the stochastic bending-dominated lattices (square and diamond), had similar average distortions, approximately 25 μm greater than for the graded lattice (circle). After the secondary cure phase (Fig. 5.8b), however, the average distortions for both stochastic and graded lattices are more similar.

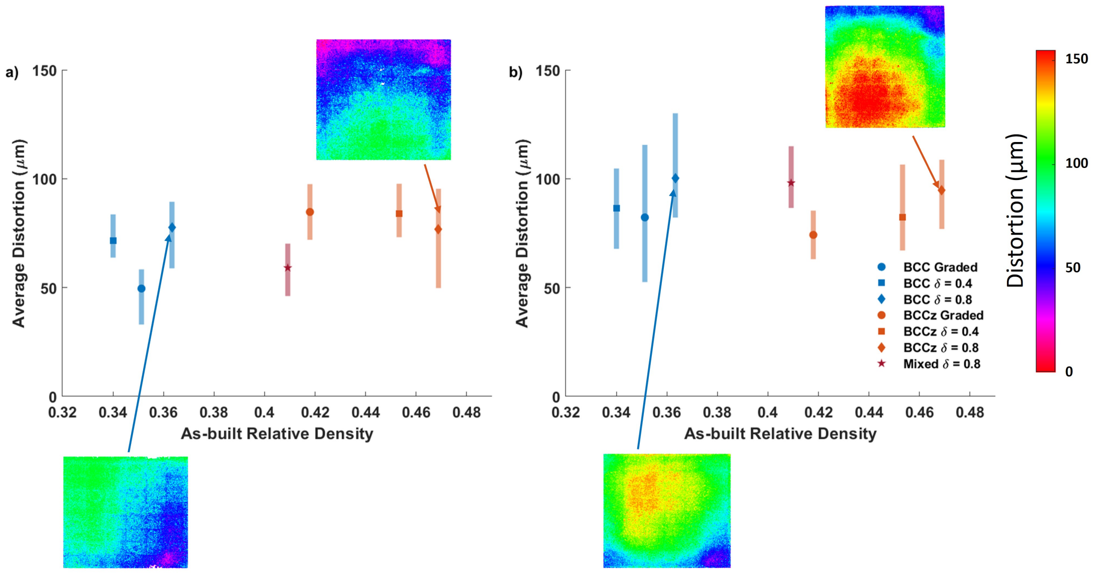

FIGURE 5.8: Average height distortion on the top endplate for graded (circle) and stochastic (square and diamond) BCC (blue) and BCCz (orange) lattices a) before and b) after the secondary cure phase. Data for a mixed stochastic lattice is also shown (red star). The shaded area indicates the range of average height distortion. Representative height distortion plots before the secondary cure phase and the corresponding height distortion plots after the secondary cure phase are shown. Colour bars scaled to the maximum height distortion observed across all plots (BCCz, after the secondary cure phase).

After the secondary cure phase, the shape of the height distortion tends to become more dome-like with the centre of the dome either in the middle or more towards one corner (Fig. 5.8b).

The average distortions for bending-dominated graded and stochastic lattices (blue) before (Fig. 5.9a) and after (Fig. 5.9b) the secondary cure phase are comparable

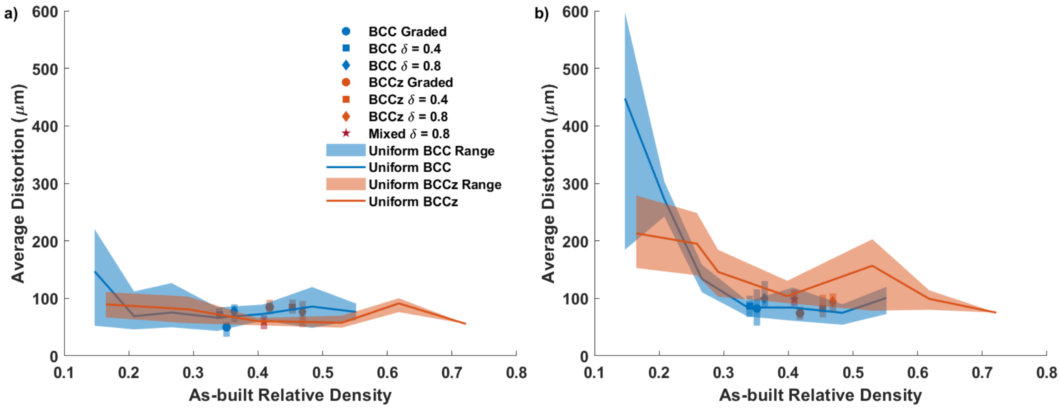

FIGURE 5.9: Average height distortion on the top endplate for graded (circle) and stochastic (square and diamond) BCC (blue) and BCCz (orange) lattices a) before and b) after the secondary cure phase. Data for a mixed stochastic lattice is also shown (red star) compared to results from uniform lattices in Chapter 4. The shaded area indicates the range of average height distortion, for both the uniform and non-uniform lattices.

to uniform lattices with similar as-built relative densities and within the ranges observed. For the non-uniform stretching-dominated lattices (orange, Fig. 5.9), however, before the secondary cure phase (Fig. 5.9a), the average distortion was generally greater than for the uniform stretching-dominated lattices by between 15 to 25 μm with minimal overlap between the ranges. After the secondary cure phase (Fig. 5.9b), the distortion of the non-uniform stretching-dominated lattices was generally less than for the uniform stretching-dominated lattices by between 35 to 40 μm. Although a statistical test cannot be performed with 3 repeats, this is within the variation observed for the uniform lattices. It is therefore hypothesised that relative density has a greater influence on distortion than uniformity/non-uniformity for both bending- and stretching-dominated lattices, especially after the secondary cure phase. A wider range of non-uniform lattices would be required to verify this.

After the secondary cure phase, for both the bending- and stretching-dominated highly disordered stochastic lattices (Fig. 5.9b square points, $\delta = 0.4$), the height distortion was reduced when compared to the more ordered stochastic lattices (Fig. 5.9b diamond points, $\delta = 0.8$). The more disordered lattices (lower δ) have a greater variation in relative density, and therefore a greater chance of unit cells with similar relative densities and stiffnesses being in opposing locations and cancelling out their respective contributions towards distortion. This improves the distribution of residual stresses from the secondary cure phase, resulting in a lower distortion. Both graded bending- and graded stretching-dominated lattices result in further reduced distortions compared to the stochastic lattices after the secondary cure phase (Fig. 5.9b). This too was likely due to better residual stress distribution from the gradient pattern. Within a layer, the position of the unit cells with the same relative density are mirrored about the X- or Y-axis depending on the direction of the gradient. Similar to the highly ordered stochastic lattices, the distortion contributions are therefore likely to counteract each other, reducing overall distortion. From the previous investigation (Chapter 4), increasing relative density, decreased distortion, and with half the external unit cells made up of the highest relative density unit cells (due to the direction of the gradient alternating between layers), they limit the distortion possible, further reducing average distortion.

The more ordered mixed stochastic lattice (red star, $\delta = 0.8$), has a similar level of distortion to the more ordered stochastic bending- and stretching-dominated lattices. After the secondary cure phase, the distortion was approximately between that of both bending- and stretching-dominated uniform lattices.

For relative densities greater than 30%, height distortions for non-uniform lattices appear to be geometry type independent and disorder dependent. More graded and stochastic lattices at varying levels of disorder and relative densities would be required to determine if this holds true at further extremes.

5.4.3 Elastic Behaviour

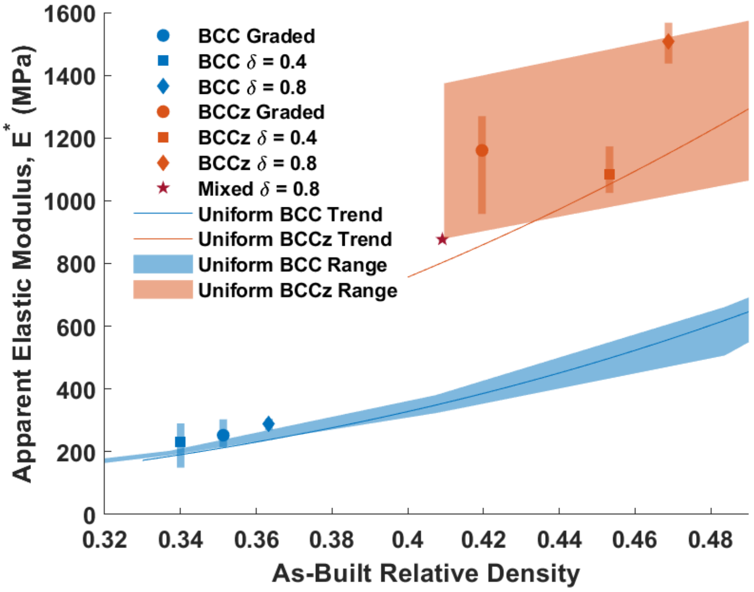

FIGURE 5.10: As-built relative density versus as-built apparent elastic modulus for graded (circle) and stochastic (square and diamond) BCC (blue) and BCCz (orange) lattices, compared to results from uniform lattices from previous investigation (Chapter 4) including range. Data for a mixed stochastic lattice is also shown (red star). Shaded areas/bars indicate the range of apparent elastic modulus, for both the uniform and non-uniform lattices. The mixed stochastic lattice (red star) had a very small range of 885 to 871 MPa, so the range bar is not observable on the plot.

The apparent elastic modulus of the non-uniform stretching-dominated geometries was greater than that for the non-uniform bending-dominated geometries (Fig. 5.10), as expected, partially due to the increased relative density [28].

The apparent elastic modulus of the mixed stochastic lattice (Fig. 5.10, red star) was approximately halfway between that of the bending- and stretching-dominated stochastic lattices with the same disorder parameter of 0.8. To explain this behaviour, one should first look at the stiffness contribution from the bending- and stretching-dominated components of the mixed lattice using the relative contributions to the make up of the lattice and assuming similar behaviours to uniform lattices. The average designed relative density of the BCC unit cells (which make up 60% of the mixed lattice) in the mixed lattice was 0.28, which using Eq. 5.4.1, for a uniform bending-dominated lattice with the same average relative density, results in an apparent elastic modulus of 115 MPa. The average designed relative density for the BCCz unit cells (which make up 40 % of the mixed lattice) in the mixed lattice was 0.83, and using Eq. 5.4.4, for a uniform stretching-dominated lattice with the same average relative density results in an apparent elastic modulus of 5200 MPa. Therefore, the mixed lattice was predicted to have an apparent elastic modulus of 2150 MPa, much greater than the as-built apparent elastic modulus of approximately 880 MPa. The elastic response was therefore not dominated by the combined average response of both the bending- and stretching-dominated unit cells. However, the apparent elastic modulus is similar to a uniform stretching-dominated lattice with the same average as-built relative density of 0.41, similar to the minimum as-designed relative density of the stretching-dominated unit cells within the mixed lattice. To determine whether it is, in fact, the average relative density that dominates the elastic behaviour of the mixed lattice, or the weaker stretching-dominated unit cells, a wider range of mixed stochastic lattices would be required with similar average relative densities but differing stretching-dominated density ranges.

$$\left(\frac{\rho^*}{\rho_s} \leq 0.3\right) E_z^* BCC = 0.88 \cdot E_s \left(\frac{\rho^*}{\rho_s}\right)^{3.41} \qquad \text{(Eq. 5.4.1)}$$

$$\left(\frac{\rho^*}{\rho_s} > 0.3\right) E_z^* BCC = 0.7 \cdot E_s \left(\frac{\rho^*}{\rho_s}\right)^{3.34} \qquad \text{(Eq. 5.4.2)}$$

$$\left(\frac{\rho^*}{\rho_s} \leq 0.3\right) E_z^* BCCz = 0.37 \cdot E_s \left(\frac{\rho^*}{\rho_s}\right)^{1.70} \qquad \text{(Eq. 5.4.3)}$$

$$\left(\frac{\rho^*}{\rho_s} > 0.3\right) E_z^* BCCz = 0.85 \cdot E_s \left(\frac{\rho^*}{\rho_s}\right)^{2.64} \qquad \text{(Eq. 5.4.4)}$$

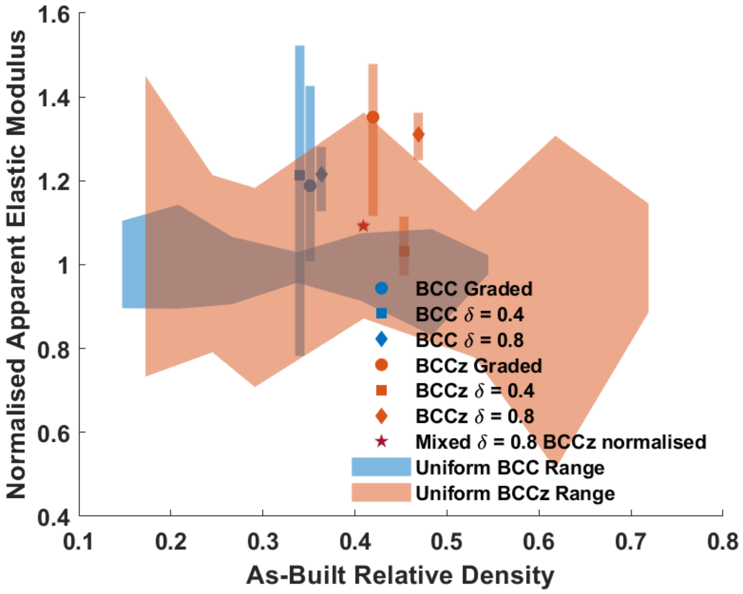

FIGURE 5.11: As-built relative density versus normalised as-built apparent elastic modulus for graded (circle) and stochastic (square, $\delta = 0.4$ and diamond, $\delta = 0.8$) BCC (blue) and BCCz (orange) lattices, compared to results from uniform lattices from previous investigation (Chapter 4). Plots for both the uniform and non-uniform lattices were normalised by trend lines developed for the uniform lattices in the previous investigation (Chapter 4), with Eq. 5.4.1, Eq. 5.4.2, Eq. 5.4.3 and Eq. 5.4.4, to account for any changes due to relative density. Data for a mixed stochastic lattice is also shown (red star), normalised by the trend for uniform stretching-dominated (BCCz) lattices. Shaded areas/bars indicate the range of normalised apparent elastic modulus, for both the uniform and non-uniform lattices. The mixed stochastic lattice (red star) had a very small range of 1.10 to 1.08, so the range bar is not observable on the plot.

Normalising the apparent elastic modulus values of the graded and stochastic lattices, shows that the graded and stochastic bending-dominated lattices (BCC, blue) all behave similarly and result in an apparent elastic modulus approximately 1.2 times that of the uniform lattices, once relative density was considered (Fig. 5.11). There was no observable difference between the two stochastic lattices with differing disorder parameters (0.4 and 0.8), similar to the conclusions of Aranguren *et al.* [1]. Aranguren *et al.*, [1], [2] determined that the normalised apparent elastic modulus was generally independent of disorder and similar to that of fully ordered uniform lattices. The one exception to this was $\delta = 0.3$ (highly disordered), which resulted in a drop of the normalised apparent elastic modulus, which they attributed to tessellation-specific low-density regions. The increased apparent elastic modulus for the non-uniform bending-dominated lattices observed here was likely due to an accumulation of excess material at the joints, observed in Fig. 5.7a, from adjacent unit cells with differing strut diameters. In Chapter 4, it was observed that failure initiates at these joints due to stress concentrations in uniform lattices. With greater material build-up, the joints of the non-uniform lattices are able to withstand increased load, increasing the apparent elastic modulus. Improved as-built geometry characterisation using computed tomography or scanning electron microscopy could verify the extent of material accumulation at such joints and potential contributions to the increased stiffness as carried out by Helgeland *et al.* and Gümrük *et al.* [163], [164].

Similar to the non-uniform bending-dominated lattices, the normalised apparent elastic modulus for the graded (circle) and highly ordered (diamond, δ = 0.8) stretching-dominated lattices are greater than for the uniform lattices (Fig. 5.11). Failure of the uniform stretching-dominated lattices appears to initiate at the joints between struts and within the vertical struts due to buckling. Excess material at the joints for the non-uniform lattices (observed in Fig. 5.7), likely also increases resistance to loading, increasing the apparent elastic modulus compared to uniform lattices. However, this was not observed for the highly disordered (square point, δ = 0.4) stretching-dominated lattice, with a similar apparent elastic modulus to the uniform stretching-dominated lattices once relative density was considered. The highly disordered lattices (δ = 0.4) had a higher proportion of lower density unit cells than highly ordered lattices (δ = 0.8) with over 50% of the unit cells in the highly disordered lattice having a designed relative density of less than 38%, whereas only 35% of the unit cells in the highly ordered lattice had similarly designed relative densities. The highly disordered lattices, therefore, experience lower loads before yield compared to the highly ordered lattices, decreasing apparent elastic modulus.

The considerable range of apparent elastic modulus seen for both bending- and stretching-dominated non-uniform lattices in some cases, means the differences observed are inconclusive without further repeats (Fig. 5.11). Taking the most extreme variation, observed in the highly disordered stochastic bending-dominated group (blue square, δ = 0.4), two of the repeats had an apparent elastic modulus of approximately 250 and 290 MPa, whilst one had an apparent elastic modulus of 150 MPa. Prior to loading, this repeat had a single missing strut in the top right corner of the rear face. Failure initiated along the top row of unit cells on the front face, likely due to this defect. The other two samples had no observable defects and failure initiated more randomly and was more catastrophic. Note, the repeat with the lower apparent elastic modulus was from another build platform, possibly resulting in manufacturing differences.

As observed previously, once the relative density was considered, the mixed stochastic lattice had an apparent elastic modulus similar to the stretching-dominated uniform lattices (Fig. 5.11). The higher density stretching-dominated lattices are likely to take up some of the load from the lower density bending-dominated lattices, resulting in an increased apparent elastic modulus compared to the uniform bending-dominated geometries. However, the presence of these bending-dominated geometries lowers the apparent elastic modulus compared to the more ordered stochastic stretching-dominated geometries.

5.4.4 Failure Behaviour

The failure patterns of the non-uniform lattices were more complex than those for the uniform lattices, however, similar patterns were again observed. The bending-dominated lattices failed suddenly with shear bands evident, Fig. 5.12a). As for the uniform lattices, the angled struts result in angled load transmission, creating a shear force effect, resulting in the failure due to shear bands [161] which form along the joints between struts, known points of stress concentrations. For the stretching-dominated lattices, failure of bottom layer struts (Fig. 5.12b) and due the bottom platen having fewer degrees of freedom than the top platen resulting in stress concentrating along the lower layers) initiated full catastrophic sample failure with shear bands also evident (Fig. 5.12c)) and also due to the angled load transmission as a result of the angled struts. For both the bending- and stretching-dominated lattices, failure tended to initiate at stress concentrations at the junction between thicker and thinner struts, between dissimilar unit cells.

The failure pattern for the mixed stochastic lattices was similar to the stochastic stretching-dominated lattices; randomly distributed individual struts failed first (Fig. 5.12d), normally at junctions. This was followed by the bottom layer experiencing progressive failure (Fig. 5.12e) before the whole sample failed catastrophically with evidence of shear bands (Fig. 5.12f).

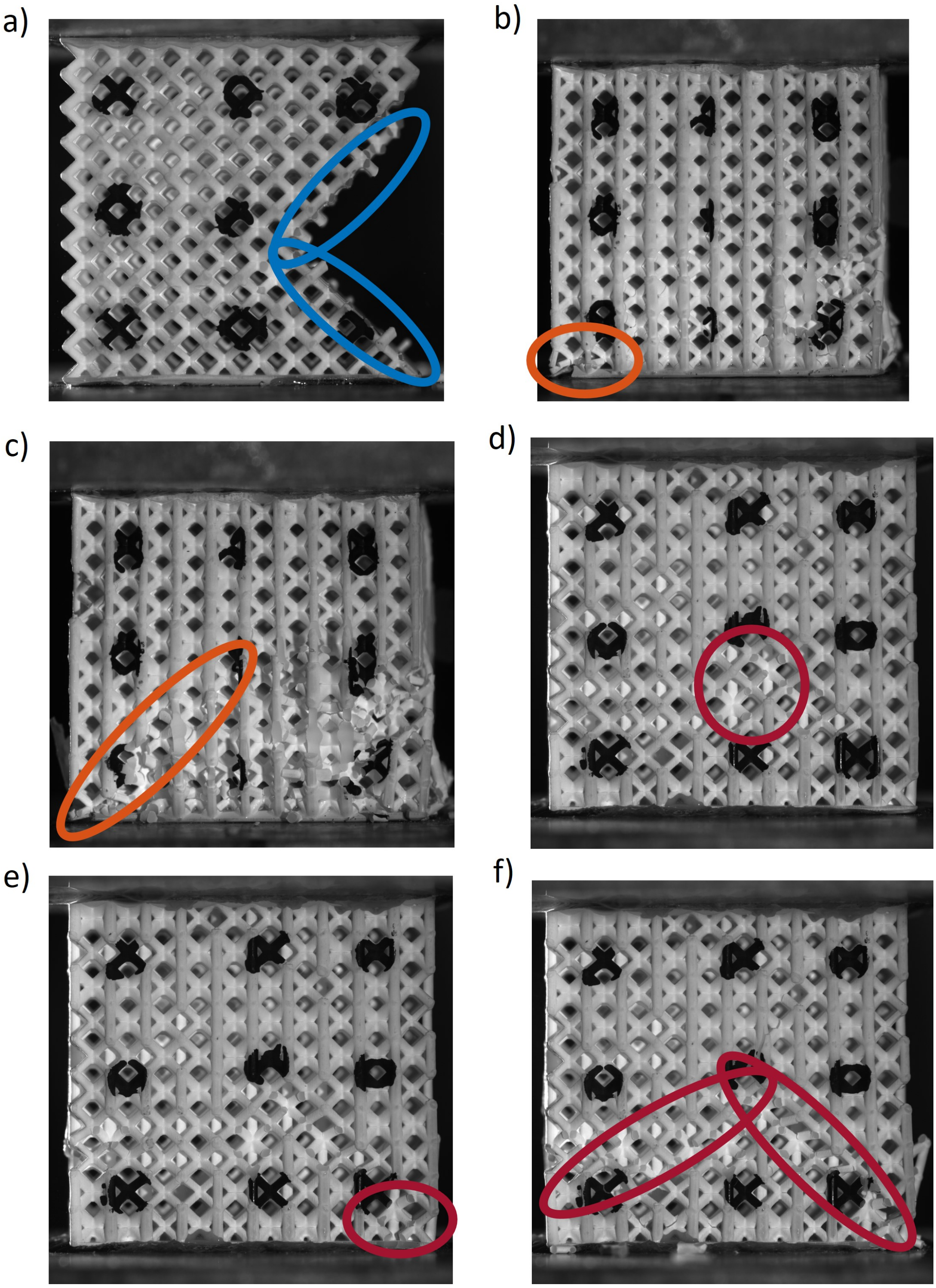

FIGURE 5.12: Representative image for the failure of a) bending-dominated lattices with the shear band highlighted in blue, representative image for the failure of stretching-dominated lattices with b) the initial point of failure and c) the shear band highlighted in orange, representative image for the failure of stochastic mixed (bending- and stretching-dominated) lattices with the d) initial random points of failure, e) bottom layer failure and f) the shear band highlighted in red.

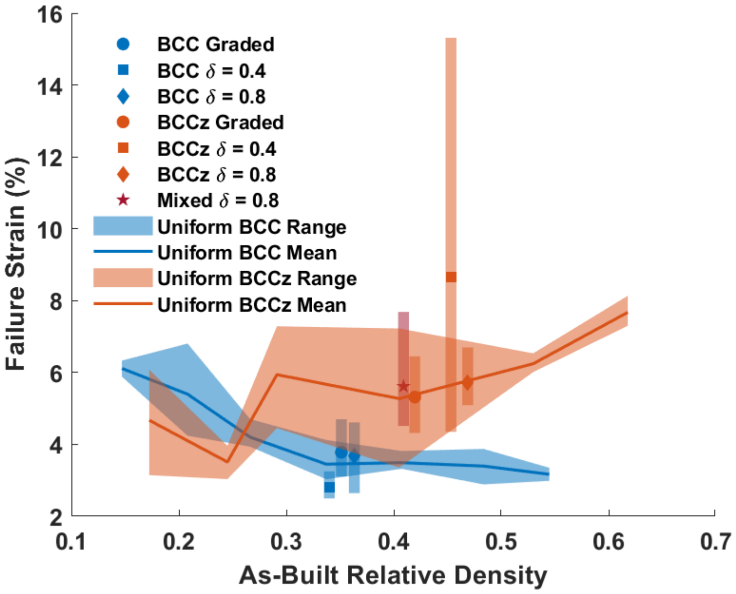

FIGURE 5.13: As-built relative density versus strain at sample failure for graded (circle) and stochastic (square and diamond) BCC (blue) and BCCz (orange) lattices, compared to results from uniform lattices from previous investigation (Chapter 4). Data for a mixed stochastic lattice is also shown (red star). The shaded areas/bars indicate the range of failure strain, for both the uniform and non-uniform lattices.

The non-uniform lattices had similar failure strains to the uniform lattices, with greater strains to failure for the stretching-dominated lattices than the bending-dominated lattices. In terms of geometry, the more ordered non-uniform bending-dominated lattices (graded, circle and stochastic with δ = 0.8, diamond), had a greater failure strain than the more disordered stochastic lattices (square, δ = 0.4) with failure strains of approximately 4 and 3% respectively. This trend of decreasing disorder (increasing δ), increasing strain to failure is in contrast with the findings of Aranguren *et al.* [1], [2] (Fig. 5.14). They determined that for the disorder parameters assessed in this investigation (δ = 0.4 and 0.8), disorder had a negligible impact on the failure strain (Fig. 5.14) [2]. It should be noted that only 3 repeats were performed in this investigation, whereas Aranguren *et al.* performed 12 or 24 repeats depending on the geometry with considerable standard deviations observed. With further repeats, the 1% difference in failure strain for this investigation might therefore also be within observed variations between samples.

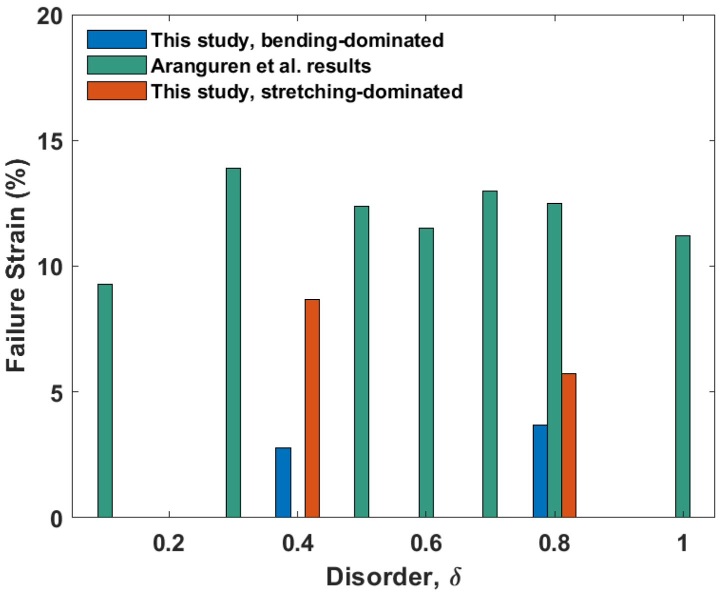

FIGURE 5.14: Variation of failure strain with δ for the stochastic lattices in this investigation (blue and orange) and the 2D Voronoi based lattices investigated by Aranguren *et al.* (green), Results are taken from [2] with error bars determined from 12 repeats for levels of δ and 24 repeats when $\delta = 0.8$ and 1.0.

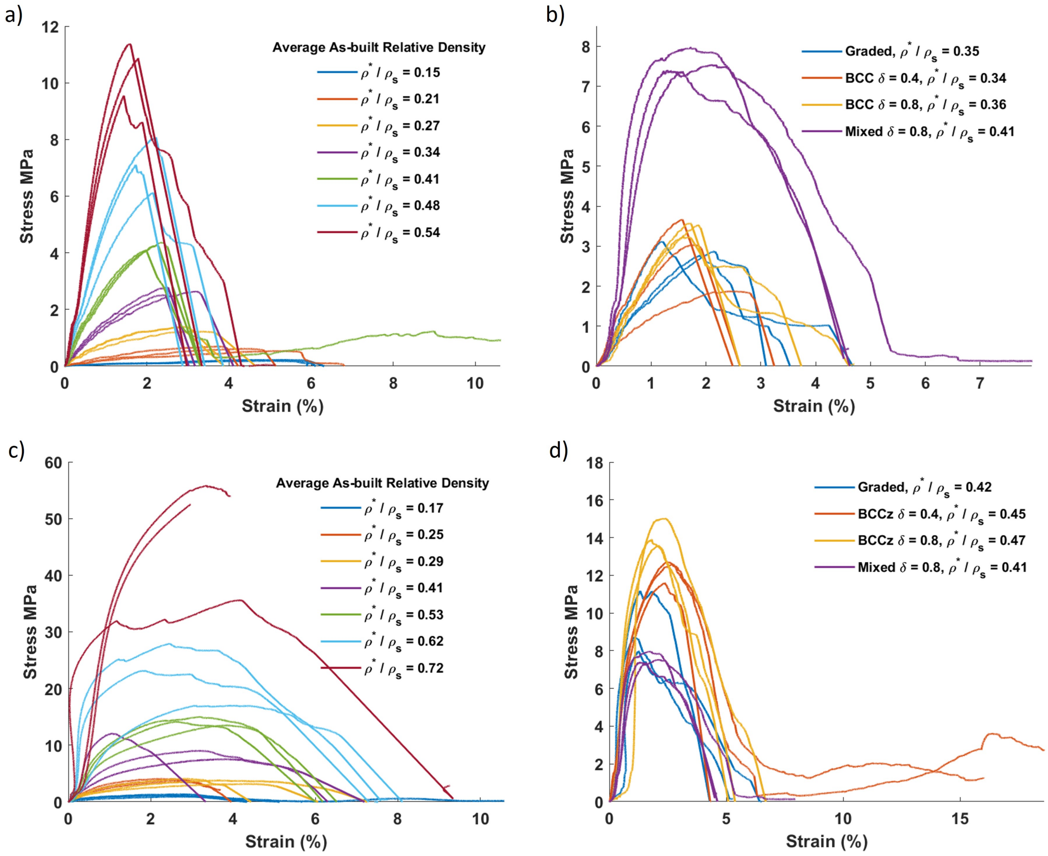

FIGURE 5.15: Stress-strain curves produced from corrected platen data for uniform a) bending- and c) stretching-dominated lattices non-uniform b) bending- and d) stretching-dominated lattices. A mixed stochastic lattice is shown on both plots for the non-uniform lattices (b and d).

For this investigation, the highly ordered bending-dominated lattices experienced multi-stage failure (Fig. 5.15b), suggesting that local cell collapse caused by brittle failure (and evidence by a drop in stress) is followed by a plateau region due to brittle crushing, followed again by the brittle failure and cell collapse of other unit cells. The investigation by Aranguren et al. [1] determined that disorder resulted in multi-stage failure due to more tortuous crack paths, and crack growth being inhibited and deflected. Looking at the failure pattern in the highly ordered stochastic bending-dominated lattices, they experienced failure at random struts, at the junctions between two dissimilar unit cells. Therefore, it is likely that the disorder introduced into the structure is influencing where failure occurs and which cells fail first, resulting in repeated local but not global failure. For the highly disordered bending-dominated lattices, however, only a single-stage failure occurs with a rapid drop in stress and reduced failure strains. The same trend, however, was not observed for the stretching-dominated lattices where the mean failure strain of the more disordered lattice was greater than the more ordered lattice (Fig. 5.13). The range of the highly disordered group of samples was considerable, so any differences noted were not conclusive. For this group of samples, the failure strains are approximately 4, 6 and 15% strain. Plotting the full stress-strain curves (Fig. 5.16) and comparing image data taken during compression reveals that the second repeat failed at around 6% strain.

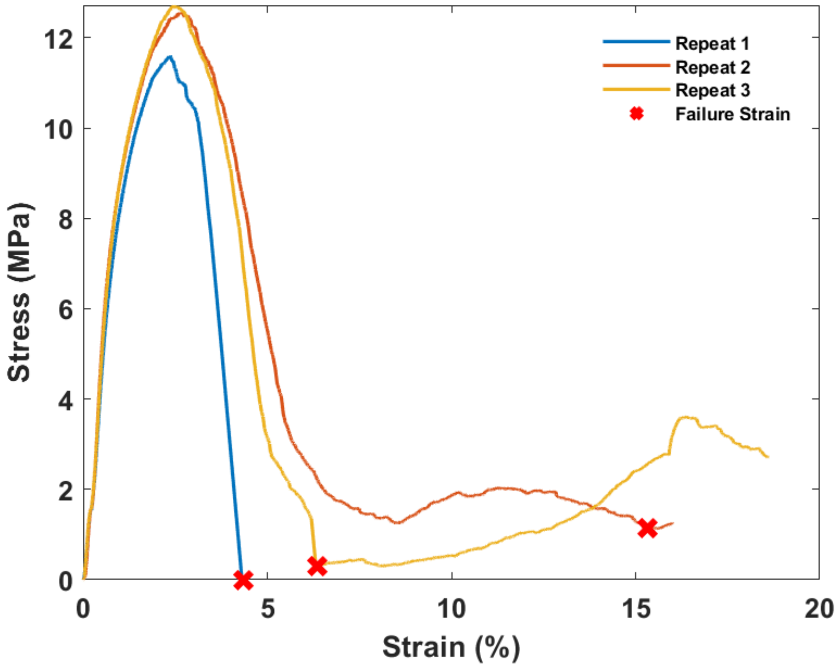

FIGURE 5.16: Stress strain curve for highly disordered stochastic stretching-dominated lattice

This sample was still in contact with the top and bottom platens and a small resultant force still registered. However, for the third repeat, when the sample failed, it was either temporarily not in contact with both platens or the material in contact had failed and could not support load. The resultant force registered temporarily as approximately 0, which was taken as the point for failure strain. There was no observable difference in the failure patterns between the repeats, with the failure perhaps less sudden for the second repeat as more material remained beneath the platen once gross sample failure occurred. Therefore adjusting the failure strain of the second repeat to 6% to be more reflective of when the load is much reduced, the average failure strain for the highly disordered ($\delta = 0.4$) stochastic stretching-dominated group then became 5.6%, comparable to the other non-uniform stretching-dominated lattices. The failure strain of non-uniform stretching-dominated lattices show no dependence on disorder, in agreement with Aranguren (Fig. 5.14 [2]).

The failure strain of the highly ordered mixed stochastic lattice (red star, $\delta = 0.8$), was similar to the uniform stretching-dominated lattice for the same relative density. The relative density and the geometry type appears to dominate the behaviour of failure strain whilst the disorder level of the lattice has a minimal effect.

The failure strain of the non-uniform lattices is greater than that of the base material. Aranguren found that both uniform and stochastic lattices had a failure strain approximately double that of the base material (base material had an elongation at break of 6.83% and lattice failed at approximately 12%) [2]. This corresponds well with the non-uniform bending-dominated lattices in this investigation as the elongation at break of the material is 1.7% and the minimum strain to failure for lattices was 3%. The increase of failure strain compared to the base material is even greater for the non-uniform stretching-dominated lattices, with failure strain approximately 3.5 times greater.

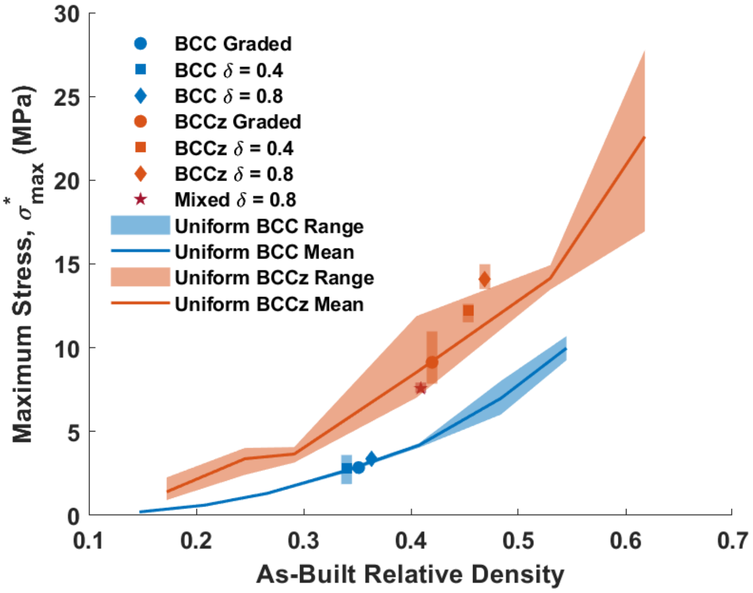

FIGURE 5.17: As-built relative density versus maximum stress for graded (circle) and stochastic (square and diamond) BCC (blue) and BCCz (orange) lattices, compared to results from uniform lattices from the previous investigation (Chapter 4). Data for a mixed stochastic lattice is also shown (red star). Shaded areas/bars indicate the range of maximum stress, for both the uniform and non-uniform lattices. The mixed stochastic lattice (red star), graded (circle) and highly ordered stochastic (diamond, δ = 0.8) BCC lattices all had small ranges, so the range bar is not observable on the plot.

The maximum strength for the stretching-dominated (orange) lattices was greater than for the bending-dominated (blue) lattices (Fig. 5.17). This is expected as the stretching-dominated lattices are stiffer than the bending-dominated lattices for the same relative density and the non-uniform stretching-dominated lattices in this investigation are more dense than the bending-dominated lattices. Fig. 5.17, shows that the more ordered stochastic lattices (diamond points, δ = 0.8) appear to have a greater maximum stress than the more disordered stochastic lattices (square points, δ = 0.4) for both the bending- and stretching-dominated lattices. Maximum stresses were normalised relative to uniform results using equations Eq. 5.4.5 and Eq. 5.4.6 to determine if this was attributable to variations in average relative density or rather to the change in disorder (Fig. 5.18).

$$\sigma^*_{max} BCC = 57.11 \left(\frac{\rho^*}{\rho_s}\right)^{2.88} \qquad \text{(Eq. 5.4.5)}$$

$$\sigma^*_{max} BCCz = 67.16 \left(\frac{\rho^*}{\rho_s}\right)^{2.32} \qquad \text{(Eq. 5.4.6)}$$

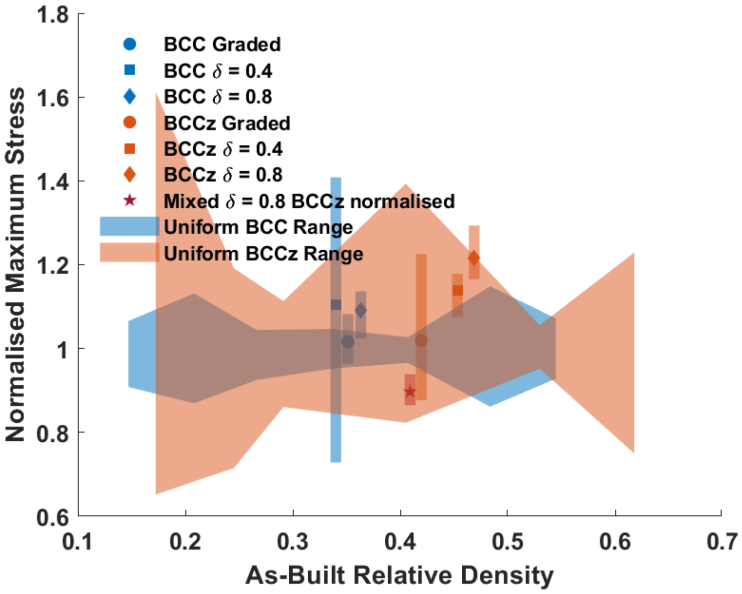

FIGURE 5.18: As-built relative density versus normalised maximum stress for graded (circle) and stochastic (square and diamond) BCC (blue) and BCCz (orange) lattices, compared to results from uniform lattices from previous investigation (Chapter 4). Data for a mixed stochastic lattice is also shown (red star). Plots for both the uniform and non-uniform lattices were normalised by trend lines developed for the uniform lattices in the previous investigation (Chapter 4), with Eq. 5.4.5 and Eq. 5.4.6), to account for any changes due to relative density. Data for a mixed stochastic lattice is also shown (red star), normalised by the trend for uniform stretching-dominated (BCCz) lattices. Shaded areas/bars indicate the range of normalised maximum stress, for both the uniform and non-uniform lattices.

The normalised maximum stress for the bending- and stretching-dominated non-uniform lattices was greater or equal to that of the uniform lattices once the influence relative density was accounted for (Fig. 5.18). The graded lattices of both types of geometries are equivalent to each other and the uniform response of the two geometry types respectively; for a graded lattice, the maximum stress was therefore controlled by geometry and the average relative density. The graded pattern of these lattices, suggests that the loading will be symmetrical around the central axis, i.e. more of the load is taken up by the stiffer outer unit cells, decreasing with each row/column towards the centre. The reduced stiffness of the central lower relative density unit cells is offset by the stiffer more dense unit cells on the outside of the lattice, with the average relative density controlling behaviour.

For both the highly ordered ($\delta = 0.8$) and highly disordered ($\delta = 0.4$) bending- and stretching-dominated lattices, however, the maximum stress was greater than for uniform lattices (Fig. 5.18), in contrast with Aranguren *et al.* [1]. They determined that the maximum stress of a lattice when $\delta = 0.8$ was equivalent to a fully ordered lattice, and decreasing δ further (more disorder) decreased the maximum stress.

Aranguren *et al.* [1], performed tensile tests on 2-dimensional lattices, whereas this investigation analysed 3-dimensional lattices in compression. 3-dimensional lattices have a higher nodal connectivity (number of struts connected to a joint) than 2-dimensional lattices, leading to increased stiffness and strength [165]–[168]. Additionally, brittle materials are stronger in compression than in tension [169], explaining the greater maximum stress for lattices in this investigation compared to Aranguren *et al.* [1]. In compression, cracks generally progress parallel to the loading direction with full sample failure arising from the coalescence of multiple microcracks, a relatively gradual and stable process. In tension, however, crack progression is much more catastrophic, with cracks progressing perpendicular to the loading direction, requiring less energy to fail.

The increase in maximum stress for stochastic lattices over uniform lattices could be due to a build-up of excess material at the joints of the stochastic lattices, known points of failure. The excess material at the joint is influenced by the difference in geometries of adjacent unit cells and flow properties of the uncured material. Assuming comparable amounts of excess material for the two stochastic bending-dominated lattices, the increase in maximum stress compared to uniform lattice is therefore likely similar, as shown in Fig. 5.18. This is not observed for the stochastic stretching-dominated lattices, as whilst failure does initiate at the joints, it also initiates in the vertical struts due to buckling. The more ordered ($\delta = 0.8$) stochastic stretching-dominated lattices are less likely to have areas of lower density compared to the more disordered ($\delta = 0.4$) lattices, increasing maximum stiffness (Fig. 5.18).

Conversely, the mixed stochastic lattice had a maximum stress $\approx$15% less than the stretching-dominated uniform lattices (Fig. 5.18), in accordance with Aranguren *et al.* [1]. The weaker lower density bending-dominated unit cells act as initiation points for failure and fail before the higher density stretching-dominated cells. A higher proportion of the bending-dominated cells are lower density for the mixed lattice than for the stochastic bending-dominated lattices, reducing the maximum stress further.

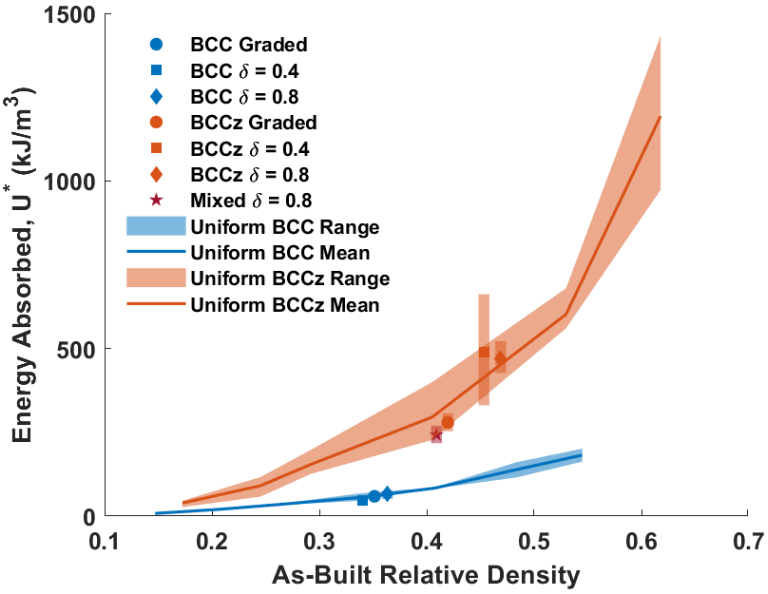

FIGURE 5.19: As-built relative density versus energy absorbed to sample failure for graded (circle) and stochastic (square and diamond) BCC (blue) and BCCz (orange) lattices, compared to results from uniform lattices from previous investigation (Chapter 4). Data for a mixed stochastic lattice is also shown (red star). Shaded areas/bars indicate the range of energy absorbed, for both the uniform and non-uniform lattices. The non-uniform bending-dominated lattices (BCC) and graded stretching-dominated lattices (BCCz) all had small ranges, so the range bar is not observable on the plot.

The energy absorbed to failure was greater for the non-uniform stretching-dominated lattices than the bending-dominated lattices. The more ordered non-uniform lattices (δ = 0.8) appear exhibit increased energy absorption compared to the more disordered stochastic lattices (δ = 0.4). Values were again normalised using equations Eq. 5.4.7 and Eq. 5.4.8 to determine if this increase was due to an increase in the as-built relative density (Fig. 5.20). Additionally, the highly disordered stretching-dominated group (orange square, δ = 0.4), showed considerable variation in energy absorption. This was likely due to the increased failure strain of one of the repeats discussed previously and was therefore adjusted for the normalised plot.

$$U^{*}BCC = 795.44\left(\frac{\rho^{*}}{\rho_{s}}\right)^{2.43} \qquad \text{(Eq. 5.4.7)}$$

$$U^{*}BCCz = 5914.32\left(\frac{\rho^{*}}{\rho_{s}}\right)^{3.39} \qquad \text{(Eq. 5.4.8)}$$

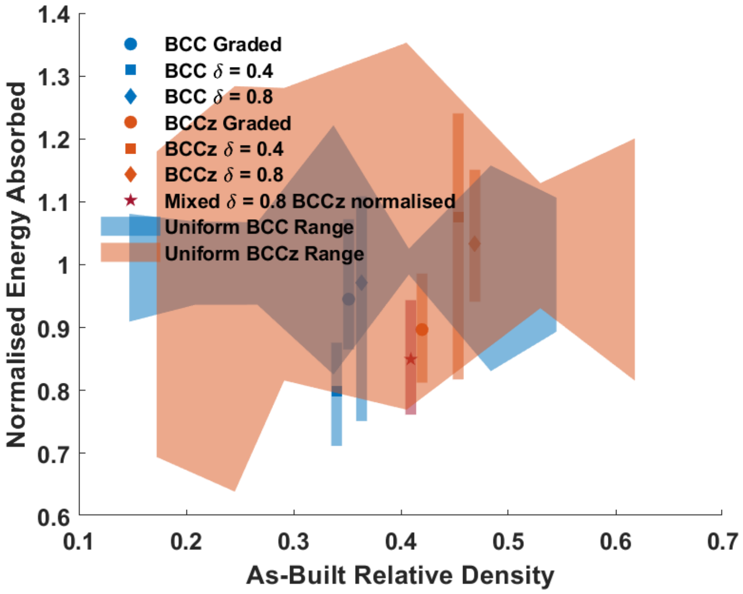

FIGURE 5.20: As-built relative density versus normalised energy absorbed to sample failure for graded (circle) and stochastic (square and diamond) BCC (blue) and BCCz (orange) lattices, compared to results from uniform lattices from previous investigation (Chapter 4). Data for a mixed stochastic lattice is also shown (red star). Plots for both the uniform and non-uniform lattices were normalised by trend lines developed for the uniform lattices in the previous investigation (Chapter 4), with Eq. 5.4.7 and Eq. 5.4.8), to account for any changes due to relative density. Data for a mixed stochastic lattice is also shown (red star), normalised by the trend for uniform stretching-dominated (BCCz) lattices. Shaded areas/bars indicate the range of normalised energy absorbed, for both the uniform and non-uniform lattices.

The highly ordered (diamond points, $\delta = 0.8$) bending- and stretching-dominated lattices showed a similar normalised energy absorption compared to their respective uniform lattices. This aligns with the conclusions of Aranguren *et al.* [1], who found that when $\delta \geq 0.7$, there was no change in energy absorption compared to the uniform lattices. Although the maximum stress of the highly ordered ($\delta = 0.8$) lattices was greater than the uniform lattices (Fig. 5.18), the strain to failure was comparable (Fig. 5.13, suggesting that the final strain had more of an impact on energy absorption. Additionally, the shapes of the highly ordered plots (Fig. 5.15b and d, $\delta = 0.8$), were similar to the higher relative density uniform plots (Fig. 5.15a and c), with relative densities similar to a large proportion of the unit cells in the highly ordered stochastic lattice, indicating similar failure patterns and therefore energy absorption.

Aranguren *et al.* [1], also determined that decreasing δ below 0.7, decreased the energy absorption of stochastic lattices compared to a fully ordered lattice. This was observed for the highly disordered ($\delta = 0.4$) bending-dominated lattice which exhibited energy absorption approximately 80% of that for uniform lattices. The highly disordered ($\delta = 0.4$) bending-dominated lattices experience more catastrophic single-stage failure (Fig. 5.15b) than the highly ordered (δ = 0.8) bending-dominated lattices for which more gradual multi-stage failure was seen (Fig. 5.15b). This difference is likely to cause the drop in energy absorption observed. The highly disordered (δ = 0.4) stretching-dominated lattices, however, had increased energy absorption capabilities compared to the more ordered lattices (δ = 0.8), ≈ 1.08 and ≈ 1.03 times the uniform value respectively. Both stochastic lattices experienced similar failure patterns (Fig. 5.15d) with most of the strength lost during continuous gradual failure. Similar failure likely results in similar energy absorption capabilities further highlighted by the considerable overlap of the ranges.

Although the graded lattices (circle points) have similar strains to failure when compared to the highly ordered stochastic lattices (Fig. 5.13, δ = 0.8), they also exhibit a drop in maximum stress (Fig. 5.18), and subsequently, reduced energy absorption compared to the highly stochastic lattices (Fig. 5.20, δ = 0.4). The energy absorbed for the graded bending-dominated lattices was also ≈5% greater than for the graded stretching-dominated lattices. The graded bending-dominated lattices exhibited more of a multi-stage failure (Fig. 5.15b and d) than the stretching-dominated lattices, with longer plateaus evident, and therefore increased energy absorption. Finally, the mixed highly ordered stochastic lattice (red star, δ = 0.8), showed a decrease in energy absorption compared to other highly ordered stochastic lattices and the uniform stretching-dominated lattices (Fig. 5.20). This is likely due to the lower density bending-dominated unit cells within the lattice.

5.5 Conclusion

Height distortions are consistently observed for additively manufactured uniform and non-uniform lattices, and appear to be related to the level of disorder. Increased disorder (decreasing δ) decreases distortion due to an improved distribution of residual stress caused by curing. Disorder also increases the apparent elastic modulus of lattices compared to uniform lattices, however, these results vary depending on geometry type. Non-uniform lattices increased the apparent elastic modulus compared to uniform lattices by approximately 25%. This increase was seen across all levels of disorder. This increase is likely due to excess material at the joints between struts, points of stress concentration where failure initiates due to differing adjacent strut diameters. However, increasing disorder decreases the apparent elastic modulus for stretching-dominated lattices, with a low level of disorder resulting in a 40% increase in apparent elastic modulus compared to uniform lattices and a high level of disorder resulting in a comparable apparent elastic modulus to uniform lattices. This decrease with increasing disorder (decreasing δ), is likely due to a higher proportion of lower density unit cells in the highly disordered lattice compared to the highly ordered lattices.

The average relative density and geometry type (bending- versus stretching-dominated) determines the strain at failure for non-uniform lattices. For the bending-dominated lattices, an increased level of disorder decreases the strain at failure. This is due to an increased number of lower density unit cells, which promotes more rapid catastrophic failure as opposed to a gradual multi-stage failure observed for highly ordered lattices. For the non-uniform stretching-dominated lattices, however, disorder had a minimal impact on the failure to strain; both levels of disorder resulted in failure at approximately 6% strain, aligning with literature. The failure strain of the non-uniform lattices was at least double that of the base material, with the stretching-dominated lattices showing the greatest increase.

Both maximum stress and energy absorption for non-uniform lattices follow similar trends to uniform lattices with stretching-dominated lattices outperforming bending-dominated lattices. Comparing normalised values, non-uniform stochastic bending- and stretching-dominated lattices have a greater maximum stress than uniform lattices, by at least 15%. Increased material at the joints between struts was observed for both the bending- and stretching stochastic lattices, increasing resistance to loading and maximum stress compared to the uniform lattices as these joints are points of failure initiation. For the bending-dominated lattices, similar maximum stresses are observed for the two levels of disorder as failure only initiates at these joints and similar material accumulation is expected. For stretching-dominated lattices, however, decreasing disorder (increasing δ) increases maximum stress, 15 to 20% compared to uniform lattices. As well as at the joints, failure initiates within the vertical struts due to strut buckling in the stretching-dominated lattices. The higher proportion of lower density unit cells in the highly disordered lattice, therefore results in a decrease in maximum stress compared to the highly ordered lattice.

In terms of energy absorption, the highly ordered stochastic bending- and stretching-dominated lattices exhibit similar normalised energy absorption to their respective uniform lattices, and produced similar failure patterns. Increasing the disorder, however, has opposite effects for bending- and stretching-dominated lattices. For the stretching-dominated lattices, increasing disorder increases the normalised energy absorption by approximately 5% than both uniform and highly ordered non-uniform stretching-dominated lattices. This increase, however, is within the variation observed, confirmed by the similar failure patterns/progression between uniform and non-uniform lattices. For bending-dominated lattices, increasing the disorder decreases the normalised energy by 20% compared to both uniform and highly ordered non-uniform bending-dominated lattices. Increasing the disorder, results in more catastrophic failure, decreasing energy absorption.

Disorder generally increases resistance to loading, leading to an increase in apparent elastic modulus and maximum stress. However, there were minimal improvements in failure to strain and energy absorption compared to uniform lattices. The current work presents a methodology for characterising the mechanical behaviour and properties of disordered lattice structures. While the study highlights trends, the notable variation in results requires additional repeat testing for verification as part of the development process of tailored non-uniform structures that occupy a large material property space.

Chapter 6

Conclusions and Future Work

6.1 Conclusions

This project sought to understand how variations in relative density and different lattice geometries affect distortions and the mechanical behaviour of AM lattices. It has explored lattices made from unit cells with bending- and stretching-dominated mechanical behaviour, and has also explored both uniform assemblies of the same unit cell and non-uniform lattices made up of different unit cells with varying relative densities. Taking natural porous materials as an inspiration, the overall aim was to extend the range of property space occupied by synthetic materials in order to help achieve enhanced, lightweight performance through improved mechanical properties and more efficient allocation of material properties (density and mechanical) according to performance requirements. This was enabled by analytical models from literature that describe the relationship between mechanical properties and relative density of uniform bending- and stretching-dominated lattices. These models were validated and with improvements suggested using empirical fits. These were used to design and manufacture non-uniform lattices with targeted average relative densities and apparent elastic modulus through the assembly of different unit cells, each with individual properties predicted by these analytical models that were validated for uniform lattices. The adaptation of the elastic foundation model also enables an assessment of the mechanical influence of distortions, which can affect loading conditions at the boundaries and were shown to severely reduce the apparent elastic modulus (by 50% at 100 μm of distortion).

All of the data for apparent elastic modulus and density of the lattices in this study (Chapters 3, 4, and 5), both uniform and non-uniform and bending- and stretching-dominated, are compiled and shown on Fig. 6.1. The figure also compares these results with the range of properties for porous natural and alternative synthetic materials. Bone tissue scaffolds have been identified throughout the thesis as one possibility for specific application, and the viability of this is supported by the regions of material space overlapping with that of cancellous bone. Matching the stiffness and relative density of bone tissue scaffolds with the surrounding native bone tissue is a critical requirement for the performance of scaffolds [122]. It is also noteworthy that the relative density and mechanical properties of the lattices in this project span a very wide range of relative densities — comparable to the range of cancellous bone — and this was achieved by only altering the lattice geometry and relative density while maintaining the same base material. At higher relative densities, the elastic moduli for materials in this study are comparable to that of cancellous bone, although at lower relative densities they fall below.

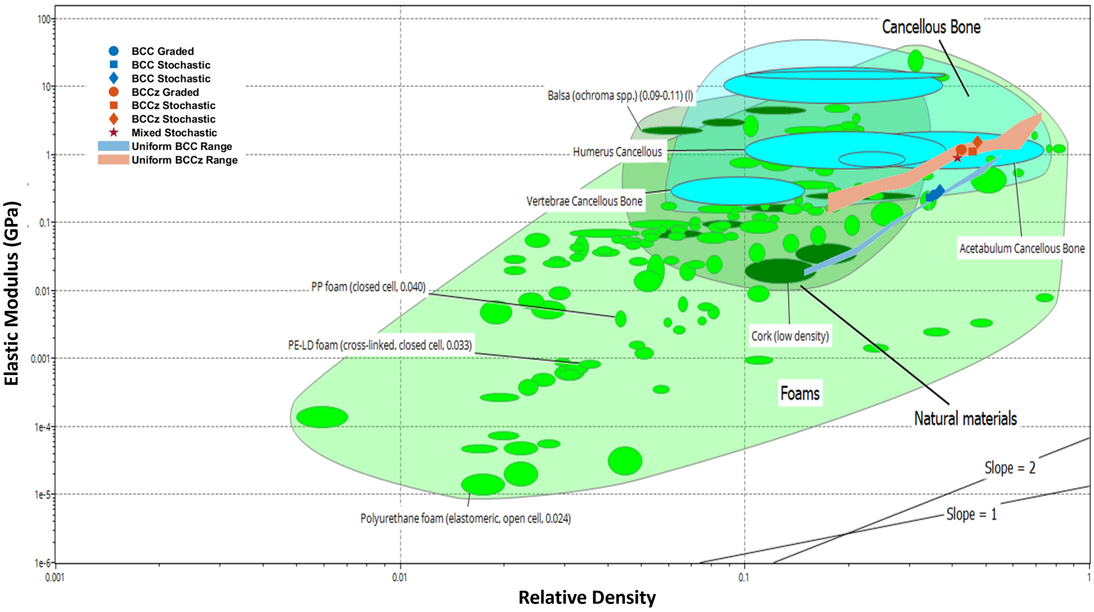

FIGURE 6.1: Ashby map of relative density versus apparent elastic modulus for common natural and synthetic porous materials produced with Granta Selector [170] along with the data for both uniform and non-uniform lattices investigated in this study. A limited number of natural porous materials are shown as there is limited relative density data for them on Granta Selector [170]. The light and dark green, and bright blue shaded regions indicate general property spaces of foams, natural materials and cancellous bone respectively. The smaller bubbles within the shaded regions show the range of properties for more specific materials, examples of which are shown on the plot. Graded (circle) and stochastic (square and diamond) BCC (blue) and BCCz (orange) lattices, compared to results from uniform lattices (shaded regions and lines). Data for a mixed stochastic lattice is also shown (red star).

In addition to the summary of material properties achieved in Fig. 6.1, several key conclusions from this work are listed below.

1. The average intra- and inter-sample apparent elastic modulus of SLA-built lattices varies considerably compared to studies found in the literature (≈13% vs 3%). This was related to variations in the elastic modulus of the base material

both within and between struts (as measured by nanoindentation), as well as variations in strut diameter.

2. Endplate height distortions were observed for all lattice geometries across the full range of as-built relative densities (15 to 70%, depending on geometry type). The distortions were greater after the secondary cure phase due to curing-induced residual stresses, as evidenced by larger height variations and a dome-like shape on the endplate surfaces. The average height distortion was greatest at the lowest relative density at 200 and 450 μm for uniform bending- and stretching-dominated lattices respectively, and decreasing with higher density. The average distortion for all lattices plateaued at a minimum of $\approx$ 100 μm at a relative density of $\sim$ 30%, where Ashby and Gibson suggest a porous material mechanical behaves more like a solid with distributed pores as isolated inclusion. Notably, increasing levels of disorder resulted in lower distortion and was thought to be related to a more even residual stress distribution.
3. Winkler's elastic foundation was adapted to determine the impact that the observed height distortions have on the initial apparent elastic modulus at low levels of strain up to 0.3%. For the specimen size of lattices investigated (30 x 30 x 30 mm), even a distortion of up to 100 μm (a commonly observed by relatively small value amongst the materials in this study) resulted in a 50% decrease in the initial apparent elastic modulus. The initial mechanical behaviour is important for materials that function under small strains such as engineered bone tissue scaffolds.
4. The as-built relative density was greater than the as-designed relative density for all structures. The deviation was 10 - 12 % greater for the uniform structures and at most 5% greater for non-uniform structures. In the uniform lattices, the increase was due to greater than designed strut diameters, primarily due to the stair-stepping effects during SLA AM. New relationships were developed in order to predict the as-built relative density for a given as-designed diameter in uniform lattices, which led to the reduced differences observed in non-uniform lattices. The small difference between as-design and as-built relative density appears to be due to an accumulation of material at the joint between struts.
5. (a) Using as-built relative densities, analytical models for the apparent elastic modulus of specific lattice geometries aligned with as-built apparent elastic modulus measurements for relative densities up to 30 and 50% for the uniform bending- and stretching-dominated structures respectively.

    (b) The accuracy of these models decreases with relative density as slender beam assumptions become less accurate and the excess material at the joints has a more significant stiffening effect relative to the more-compliant, thinner lattices.

(c) Ashby-Gibson analytical models for apparent elastic modulus and density were fit to empirical data to better predict the modulus for uniform lattices. The fitted equations for bending-dominated lattices had higher power-law exponents than stretching-dominated lattices. The exponents were similar to natural porous materials like wood and bone, varying between 1.7 and 3.4.

(d) The apparent elastic modulus for non-uniform bending-dominated lattices was 25% greater than for uniform lattices with the same average relative density. Amongst the non-uniform lattices with the same relative density, no differences in modulus were observed when the level of disorder was varied.

(e) The apparent elastic modulus for non-uniform stretching-dominated lattices was up to 40% greater than for uniform lattices with the same average relative density. Amongst the non-uniform lattices with the same relative density, a reduction in modulus was observed when the level of disorder was increased as a result of the lower density unit cells.

(f) The increases in apparent elastic modulus in non-uniform lattices compared with corresponding uniform lattices of the same unit cell type and average relative density may be attributed to the excess material at the joints, which act to reinforce regions of stress concentrations.

6. The maximum stress and energy absorption of uniform lattices increased with relative density. Stretching-dominated lattices had greater maximum stress and energy absorption than bending-dominated lattices at any given value of relative density over the range examined. The non-uniform lattices exhibited higher maximum stresses than corresponding uniform lattices, which again was thought to be due to excess material at the joints having a stiffening effect. The level of disorder did not impact the maximum stress of non-uniform bending-dominated lattices, but decreased that of stretching-dominated lattices due to the effect of lower density unit cells. Similar levels of energy absorption were observed for the uniform and non-uniform stretching-dominated lattices which exhibited similar failure patterns with most of the stiffness lost upon the first sign of fracture. In contrast, the bending-dominated geometries showed a decrease in energy absorption with increasing disorder. This was thought to be related to the increased proportion of lower density unit cells promoting more catastrophic failure.

7. The strain to failure for both uniform and non-uniform structures was at least double that of the base material. Increasing the relative density of uniform bending-dominated structures decreased the strain to failure, plateauing at a strain of 3.5% at a relative density of approximately 30%. In contrast, uniform stretching-dominated structures exhibited an increased strain to failure with increased relative density. Increased disorder decreased failure strains for non-uniform bending-dominated lattices but did not affect non-uniform stretching-dominated lattices.

Overall, compared to uniform lattices, non-uniform lattices have improved levels of (lower) distortion, (higher) apparent elastic modulus and maximum stress and similar energy absorption capabilities and strain to failure.

The conclusions of this work provide a basis for further development of lightweight porous lattice materials with improved performance, ranges of properties, and models for predicting as-built geometries and behaviour. In doing so, the material property space of synthetic materials can be expanded further into the domain of natural materials that have evolved over millennia to optimise performance and efficiency (as shown in Fig. 6.1). To continue this work and based on the findings of the current work, further investigations are needed, and recommendations are presented in the following section.

Compared to uniform lattices, non-uniform lattices have improved levels of distortion, apparent elastic modulus and maximum stress and similar energy absorption capabilities and strain to failure.

6.2 Future Work

Areas for further investigation have been split into two categories: those that concern characterisation, both geometrical and mechanical, and those that concern the designs of the lattices.

Characterisation

- With geometric variations such as height distortions and variations in strut diameter shown to impact apparent properties, more extensive characterisation of the as-built geometry using computer tomography (CT) is suggested as an initial area for future work. CT can characterise deviations from as-designed geometry throughout the volume instead of just at the surface. Strut diameter variations observed from microscopy could be verified by CT, and strut waviness (known to impact apparent elastic modulus [72], [85], [86], [88]) could be characterised. Additionally, the amount of excess material at the joints both for uniform and non-uniform lattices could be quantified with this excess material hypothesised to increase the apparent elastic modulus and maximum stress for non-uniform lattices.
- The apparent elastic modulus of lattices could be determined from the unloading curve whilst still within the elastic region, free from the effects of compliance and height distortions. This could be used to verify the apparent elastic modulus determined from optical strain measurement techniques which were limited to surface strain measurements, a concern if the sample experienced barrelling due to boundary conditions.
- Digital volume correlation (DVC), can could also be used to measure the internal strain of the lattices, also verifying optical strain measurements. DVC would allow internal geometric defects that potentially lead to stress concentrations to be linked to internal strain measurements with internal failure initiation also potentially identified. The local mechanical response of individual unit cells in non-uniform lattices could also be characterised with DVC and compared to similar uniform lattices. When describing the behaviour of the non-uniform lattices, it has been assumed that each unit cell behaves similarly to the same unit cells in corresponding uniform lattices, however, differing adjacent unit cells and therefore boundary conditions could impact deformation mechanisms and therefore the mechanical response.
- Further to DVC, crack propagation patterns for compressive loading could be investigated to determine load paths, helping to identify the sites of failure initiation and paths of failure propagation in uniform and non-uniform lattices.

Similar failure patterns were observed for uniform and non-uniform lattices, thought to contribute to the comparable energy absorption results. Crack propagation tests could verify if uniform and non-uniform lattices also had similar crack propagation patterns, resulting in similar energy absorptions.

- Finite element analysis could be used to understand the residual stresses within the lattices, both during part manufacture and after post-processing. Part shrinkage and curing could be modelled as thermal effects, allowing residual stresses to be determined. This will provide valuable insight into the origins of endplate distortions and help explain why distortion decreases with relative density.

Altering the lattice designs

- The methodologies developed throughout this project could also be applied to a wider range of manufacturing techniques and materials, including more ductile materials such as metals and more brittle materials such as ceramics. Additively manufactured metallic lattices are often the focus of investigations regarding defects in AM lattices. However, to the author's knowledge, this is somewhat limited concerning global distortions, as observed for height in this project and shown to impact the initial apparent mechanical response. Characterising how these are impacted by the base material would provide valuable insight into lattices made from a broader range of materials. Additionally, characterising the behaviour of lattices made from stiffer and more brittle materials, such as ceramics, could further expand the accessible material property space. The properties of the lattices in this project overlapped with higher-density cancellous bone such as that from the acetabulum, however, lower-density natural materials with similar elastic moduli remain generally inaccessible for synthetic materials. Stiffer ceramic materials have the potential to expand into this space, with their inherent low failure strains improved by utilising stretching-dominated geometries (shown in this investigation to greatly improve failure strain) as well as non-uniform porosity distributions.

- In this work, a limited number of non-uniform bending- and stretching-dominated lattices were investigated, at two levels of density variation and just one overall average relative density for each. Lattices with a larger range of density variation and with different average relative densities could be investigated to confirm and establish trends in mechanical behaviour.

- This project also only investigated one type of mixed non-uniform lattice (combining both bending- and stretching-dominated unit cell geometries), and at just one average value of relative density. Such lattices have the potential for more tailored local mechanical behaviour, which could also include/investigate locally anisotropic behaviour similar to natural porous materials like cancellous bone. Achieving both local and global mechanical behaviours similar to cancellous bone is beneficial for developing engineered bone tissue scaffolds as well as bone analogues used in the preclinical mechanical testing of implants. For bone tissue scaffolds, mimicking local mechanical response could be beneficial for mechanical stimulation of bone growth and healing. For bone analogues, it could be important for recreating the local mechanical response that might affect the loading conditions and potential failure modes of implants.

- It was assumed that endplate contributions to stiffness were minimal in comparison to the full lattice structure as they were very thin (0.2 mm). Their impact on the distortion observed, however, is unknown. Characterising the impact that endplate dimensions, particularly thickness, have upon distortions and therefore apparent properties could help provide insights regarding the mechanisms that contribute to distortion and suggest strategies to minimise it.
- Finally, the methodologies developed in these investigations could be applied to a wider range of unit cell geometries. Although unit cells with the same loading mechanisms (i.e. bending- versus stretching-dominated) behaved similarly, with similar power laws for mechanical property versus relative density relationships, developing models for a wider variety of unit cell geometries would further expand the material property space of synthetic materials. For example, the isotropic stretching-dominated octet geometry has been shown to have greatly improved energy absorption capabilities compared to foams and other additively manufactured lattices [47], [171], resulting in a stiff porous metamaterial with properties closer to high-performance natural porous materials. Finite element analysis could supplement this work by allowing more designs to be evaluated without the need for sample manufacture.

References

[1] D. Aranguren Van Egmond, B. Yu, S. Choukir, *et al.*, “The benefits of structural disorder in natural cellular solids,” 2021.

[2] D. A. Aranguren van Egmond, “Designing for Disorder: The Mechanical Behaviour of Bioinspired, Stochastic Honeycomb Materials,” Ph.D. dissertation, 2018.

[3] N. A. Fleck, V. S. Deshpande, and M. F. Ashby, “Micro-architectured materials: Past, present and future,” *Proceedings of the Royal Society A: Mathematical, Physical and Engineering Sciences*, vol. 466, no. 2121, pp. 2495–2516, 2010, ISSN: 14712946. DOI: `10.1098/rspa.2010.0215`. [Online]. Available: `https://royalsocietypublishing.org/`.

[4] The Editors of Encyclopaedia Britannica, *Roman Road System*, 2018. [Online]. Available: `https://www.britannica.com/technology/Roman-road-system`.

[5] I. McNeil, *An Encyclopaedia of the history of technology*. Routledge, 1990, p. 1062, ISBN: 0-415-01306-2. [Online]. Available: `https://books.google.com/books/about/An_Encyclopedia_of_the_History_of_Techno.html?id=-sXFBQAAQBAJ`.

[6] B. C. White, A. Garland, and B. L. Boyce, “Topological homogenization of metamaterial variability,” *Materials Today*, vol. 53, pp. 16–26, Mar. 2022, ISSN: 1369-7021. DOI: `10.1016/J.MATTOD.2022.01.021`.

[7] S. Gao, W. Liu, L. Zhang, A. Kumar Gain, and A. K. G. Au, “A New Polymer-Based Mechanical Metamaterial with Tailorable Large Negative Poisson’s Ratios,” *Polymers*, vol. 12, no. 7, 2020. DOI: `10.3390/polym12071492`. [Online]. Available: `www.mdpi.com/journal/polymers`.

[8] A. Valipour, M. H. Kargozarfard, M. Rakhshi, A. Yaghootian, and H. M. Sedighi, “Metamaterials and their applications: An overview,” *Proceedings of the Institution of Mechanical Engineers, Part L: Journal of Materials: Design and Applications*, vol. 236, no. 11, pp. 2171–2210, Nov. 2022, ISSN: 20413076. DOI: `10.1177/1464420721995858/ASSET/95C714E7-8F4D-413E-`

9827-F3A6D4066F17/ASSETS/IMAGES/LARGE/10.1177{_}1464420721995858-FIG72.JPG. [Online]. Available: https://journals.sagepub.com/doi/full/10.1177/1464420721995858.

[9] C. Zhang, J. Li, Z. Hu, F. Zhu, and Y. Huang, “Correlation between the acoustic and porous cell morphology of polyurethane foam: Effect of interconnected porosity,” *Materials & Design*, vol. 41, pp. 319–325, Oct. 2012, ISSN: 0261-3069. DOI: 10.1016/J.MATDES.2012.04.031.

[10] H. Yang, S. Xu, D. E. Chitwood, and Y. Wang, “Ceramic water filter for point-of-use water treatment in developing countries: Principles, challenges and opportunities,” *Frontiers of Environmental Science & Engineering*, vol. 14, no. 5, pp. 1–10, May 2020, ISSN: 2095-221X. DOI: 10.1007/S11783-020-1254-9. [Online]. Available: https://link.springer.com/article/10.1007/s11783-020-1254-9.

[11] I. Yakub, A. Plappally, M. Leftwich, *et al.*, “Porosity, Flow, and Filtration Characteristics of Frustum-Shaped Ceramic Water Filters,” *Journal of Environmental Engineering*, vol. 139, no. 7, pp. 986–994, Oct. 2012, ISSN: 0733-9372. DOI: 10.1061/(ASCE)EE.1943-7870.0000669. [Online]. Available: https://ascelibrary.org/doi/abs/10.1061/%28ASCE%29EE.1943-7870.0000669%20https://ascelibrary.org/doi/10.1061/%28ASCE%29EE.1943-7870.0000669.

[12] C. Chen, Y. Kuang, S. Zhu, *et al.*, “Structure-property-function relationships of natural and engineered wood,” *Nature Reviews Materials*, vol. 5, 2020. DOI: 10.1038/s41578-020-0195-z. [Online]. Available: www.nature.com/natrevmats.

[13] J. D. Currey, “The structure and mechanics of bone,” *Journal of Materials Science*, vol. 47, no. 1, pp. 41–54, Jan. 2012, ISSN: 00222461. DOI: 10.1007/S10853-011-5914-9/FIGURES/4. [Online]. Available: https://link.springer.com/article/10.1007/s10853-011-5914-9.

[14] M. F. Ashby, “The CES EduPack Database of Natural and Man-Made Materials,” Tech. Rep., 2007.

[15] L. J. Gibson, M. F. Ashby, and B. A. Harley, *Cellular Materials in Nature and Medicine*. Cambridge: Cambridge University Press, 2010, ISBN: 978-0-521-19544-7.

[16] E. F. Morgan, G. L. Barnes, and T. A. Einhorn, *The Bone Organ System. Form and Function*, Third Edit. Elsevier Inc., 2013, pp. 3–20, ISBN: 9780124158535. DOI: 10.1016/B978-0-12-415853-5.00001-7. [Online]. Available: http://dx.doi.org/10.1016/B978-0-12-370544-0.50003-3.

[17] E. F. Morgan, G. U. Unnikrisnan, and A. I. Hussein, "Bone Mechanical Properties in Healthy and Diseased States," *Annual Review of Biomedical Engineering*, vol. 20, pp. 119–143, 2018, ISSN: 15454274. DOI: `10.1146/annurev-bioeng-062117-121139`.

[18] B. Clarke, "Normal Bone Anatomy and Physiology The Skeleton," *Clin J Am Soc Nephrol*, vol. 3, pp. 131–139, 2008. DOI: `10.2215/CJN.04151206`.

[19] J. Y. Rho, L. Kuhn-Spearing, and P. Zioupos, "Mechanical properties and the hierarchical structure of bone," *Medical Engineering and Physics*, vol. 20, no. 2, pp. 92–102, Mar. 1998, ISSN: 13504533. DOI: `10.1016/S1350-4533(98)00007-1`.

[20] C. J. Hernandez, "Cancellous Bone," in *Handbook of Biomaterial Properties*, 2nd, Springer, 2016, ch. A2, pp. 1–676, ISBN: 9781493933051. DOI: `10.1007/978-1-4939-3305-1`.

[21] N. Reznikov, R. Shahar, and S. Weiner, "Bone hierarchical structure in three dimensions," in *Acta Biomaterialia*, vol. 10, Elsevier Ltd, Sep. 2014, pp. 3815–3826. DOI: `10.1016/j.actbio.2014.05.024`.

[22] P. Zioupos, R. B. Cook, and J. R. Hutchinson, "Some basic relationships between density values in cancellous and cortical bone," *Journal of Biomechanics*, vol. 41, no. 9, pp. 1961–1968, Jan. 2008, ISSN: 0021-9290. DOI: `10.1016/J.JBIOMECH.2008.03.025`.

[23] D. B. Burr, "Bone Morphology and Organization," in *Basic and Applied Bone Biology*, Elsevier, Jan. 2019, pp. 3–26. DOI: `10.1016/b978-0-12-813259-3.00001-4`.

[24] D. Ulrich, B. Van Rietbergen, A. Laib, and P. Ruegsegger, "The ability of three-dimensional structural indices to reflect mechanical aspects of trabecular bone," *Bone*, vol. 25, no. 1, pp. 55–60, Jul. 1999, ISSN: 87563282. DOI: `10.1016/S8756-3282(99)00098-8`.

[25] C. E. Metzger, D. B. Burr, and M. R. Allen, "Anatomy and Structural Considerations," in *Encyclopedia of Bone Biology*, Elsevier, Jan. 2020, pp. 218–232. DOI: `10.1016/b978-0-12-801238-3.62234-1`. [Online]. Available: `https://www.sciencedirect.com/science/article/pii/B9780128012383622341?via%3Dihub`.

[26] J. D. Currey, "Mechanical properties of vertebrate hard tissues," Tech. Rep., 1998.

[27] A. Sombatmai, K. Tapracharoen, V. Uthaisangsuk, S. Msolli, and P. Promoppatum, "Post-yielding and failure mechanism of additively manufactured triply periodic minimal surface lattice structures," *Results in Engineering*, vol. 23, p. 102 364, Sep. 2024, ISSN: 2590-1230. DOI: `10.1016/J.RINENG.2024.102364`.

[28] L. J. Gibson and M. F. Ashby, *Cellular Solids*, 2nd. Cambridge: Cambridge University Press, 1997, ISBN: 9781139878326. DOI: `10.1017/CBO9781139878326`. [Online]. Available: `http://ebooks.cambridge.org/ref/id/CBO9781139878326`.

[29] V. S. Deshpande, M. F. Ashby, and N. A. Fleck, "Foam topology: Bending versus stretching dominated architectures," *Acta Materialia*, vol. 49, no. 6, pp. 1035–1040, Apr. 2001, ISSN: 13596454. DOI: `10.1016/S1359-6454(00)00379-7`.

[30] M. F. Ashby, "The properties of foams and lattices," *Philosophical Transactions of the Royal Society A: Mathematical, Physical and Engineering Sciences*, vol. 364, no. 1838, pp. 15–30, 2006. DOI: `10.1098/rsta.2005.1678`.

[31] Z. Alomar and F. Concli, *A Review of the Selective Laser Melting Lattice Structures and Their Numerical Models*, Dec. 2020. DOI: `10.1002/adem.202000611`.

[32] N. A. Fleck, "An overview of the mechanical properties of foams and periodic lattice materials," *Cellular Metals and Polymers*, Jan. 2004. [Online]. Available: `http://www-mech.eng.cam.ac.uk/profiles/fleck/papers/c51.pdf`.

[33] E. F. Morgan, H. H. Bayraktar, and T. M. Keaveny, "Trabecular bone modulus-density relationships depend on anatomic site," *Journal of Biomechanics*, vol. 36, no. 7, pp. 897–904, Jul. 2003, ISSN: 00219290. DOI: `10.1016/S0021-9290(03)00071-X`.

[34] L. J. Gibson, "The mechanical behaviour of cancellous bone," *Journal of Biomechanics*, vol. 18, no. 5, pp. 317–328, 1985, ISSN: 00219290. DOI: `10.1016/0021-9290(85)90287-8`.

[35] C. R. Calladine, "Buckminster Fuller's "Tensegrity" structures and Clerk Maxwell's rules for the construction of stiff frames," *International Journal of Solids and Structures*, vol. 14, no. 2, pp. 161–172, Jan. 1978, ISSN: 0020-7683. DOI: `10.1016/0020-7683(78)90052-5`.

[36] H. Chen, Q. Han, C. Wang, Y. Liu, B. Chen, and J. Wang, *Porous Scaffold Design for Additive Manufacturing in Orthopedics: A Review*, Jun. 2020. DOI: `10.3389/fbioe.2020.00609`. [Online]. Available: `www.frontiersin.org`.

[37] K. Ushijima, W. J. Cantwell, S. Tsopanos, and M. Smith, "An investigation into the compressive properties of stainless steel micro-lattice structures," *Journal of Sandwich Structures*, vol. 13, no. 3, pp. 303–329, 2011. DOI: `10.1177/1099636210380997`.

[38] R. Gümrük and R. A. Mines, "Compressive behaviour of stainless steel micro-lattice structures," *International Journal of Mechanical Sciences*, vol. 68, pp. 125–139, Mar. 2013, ISSN: 00207403. DOI: `10.1016/j.ijmecsci.2013.01.006`.

[39] T. Tancogne-Dejean and D. Mohr, "Stiffness and specific energy absorption of additively-manufactured metallic BCC metamaterials composed of tapered beams," *International Journal of Mechanical Sciences*, vol. 141, pp. 101–116, Jun. 2018, ISSN: 00207403. DOI: `10.1016/j.ijmecsci.2018.03.027`.

[40] M. Zhang, Z. Yang, Z. Lu, B. Liao, and X. He, "Effective elastic properties and initial yield surfaces of two 3D lattice structures," *International Journal of Mechanical Sciences*, vol. 138-139, pp. 146–158, Apr. 2018, ISSN: 00207403. DOI: `10.1016/j.ijmecsci.2018.02.008`.

[41] S. Ruiz de Galarreta, J. R. Jeffers, and S. Ghouse, "A validated finite element analysis procedure for porous structures," *Materials and Design*, vol. 189, p. 108 546, Apr. 2020, ISSN: 18734197. DOI: `10.1016/j.matdes.2020.108546`.

[42] X. Y. Chen and H. F. Tan, "An effective length model for octet lattice," *International Journal of Mechanical Sciences*, vol. 140, pp. 279–287, May 2018, ISSN: 0020-7403. DOI: `10.1016/J.IJMECSCI.2018.03.016`.

[43] M. R. O'Masta, L. Dong, L. St-Pierre, H. N. Wadley, and V. S. Deshpande, "The fracture toughness of octet-truss lattices," *Journal of the Mechanics and Physics of Solids*, vol. 98, pp. 271–289, Jan. 2017, ISSN: 0022-5096. DOI: `10.1016/J.JMPS.2016.09.009`.

[44] C. Ling, A. Cernicchi, M. D. Gilchrist, and P. Cardiff, "Mechanical behaviour of additively-manufactured polymeric octet-truss lattice structures under quasi-static and dynamic compressive loading," *Materials and Design*, vol. 162, pp. 106–118, Jan. 2018, ISSN: 18734197. DOI: `10.1016/J.MATDES.2018.11.035/MECHANICAL{\_}BEHAVIOUR{\_}OF{\_}ADDITIVELY{\_}MANUFACTURED{\_}POLYMERIC{\_}OCTET{\_}TRUSS{\_}LATTICE{\_}STRUCTURES{\_}UNDER{\_}QUASI{\_}STATIC{\_}AND{\_}DYNAMIC{\_}COMPRESSIVE{\_}LOADING.PDF`.

[45] V. S. Deshpande, N. A. Fleck, and M. F. Ashby, "Effective properties of the octet-truss lattice material," *Journal of the Mechanics and Physics of Solids*, vol. 49, no. 8, pp. 1747–1769, Aug. 2001, ISSN: 0022-5096. DOI: `10.1016/S0022-5096(01)00010-2`.

[46] T. Tancogne-Dejean and D. Mohr, "Elastically-isotropic truss lattice materials of reduced plastic anisotropy," *International Journal of Solids and Structures*, vol. 138, pp. 24–39, May 2018, ISSN: 0020-7683. DOI: `10.1016/J.IJSOLSTR.2017.12.025`.

[47] J. Song, W. Zhou, Y. Wang, *et al.*, "Octet-truss cellular materials for improved mechanical properties and specific energy absorption," *Materials & Design*, vol. 173, p. 107 773, Jul. 2019, ISSN: 0264-1275. DOI: `10.1016/J.MATDES.2019.107773`.

[48] Y. Liu, S. Zhuo, Y. Xiao, G. Zheng, G. Dong, and Y. F. Zhao, "Rapid modeling and design optimization of multi-Topology lattice structure based on unit-Cell library," *Journal of Mechanical Design, Transactions of the ASME*, vol. 142, no. 9, Sep. 2020, ISSN: 10500472. DOI: `10.1115/1.4046812`.

[49] Z. Wu, L. Xia, S. Wang, and T. Shi, "Topology optimization of hierarchical lattice structures with substructuring," *Computer Methods in Applied Mechanics and Engineering*, vol. 345, pp. 602–617, Mar. 2018, ISSN: 00457825. DOI: `10.1016/j.cma.2018.11.003`.

[50] S. Daynes, S. Feih, W. F. Lu, and J. Wei, "Design concepts for generating optimised lattice structures aligned with strain trajectories," *Computer Methods in Applied Mechanics and Engineering*, vol. 354, pp. 689–705, Sep. 2019, ISSN: 00457825. DOI: `10.1016/j.cma.2019.05.053`.

[51] S. Daynes, S. Feih, W. F. Lu, and J. Wei, "Optimisation of functionally graded lattice structures using isostatic lines," *Materials and Design*, vol. 127, pp. 215–223, Aug. 2017, ISSN: 18734197. DOI: `10.1016/j.matdes.2017.04.082`.

[52] H. Yazdani Sarvestani, D. Aranguren van Egmond, I. Esmail, M. Genest, C. Paquet, and B. Ashrafi, "Bioinspired Stochastic Design: Tough and Stiff Ceramic Systems," *Advanced Functional Materials*, vol. 32, no. 6, p. 2 108 492, Feb. 2022, ISSN: 1616-3028. DOI: `10.1002/ADFM.202108492`. [Online]. Available: `https://onlinelibrary.wiley.com/doi/full/10.1002/adfm.202108492%20https://onlinelibrary.wiley.com/doi/abs/10.1002/adfm.202108492%20https://onlinelibrary.wiley.com/doi/10.1002/adfm.202108492`.

[53] S. Choukir, D. A. van Egmond, B. D. Hatton, G. D. Hibbard, and C. V. Singh, "The interplay between constituent material and architectural disorder in bioinspired honeycomb structures," *International Journal of Engineering Science*, vol. 188, p. 103 863, Jul. 2023, ISSN: 0020-7225. DOI: `10.1016/J.IJENGSCI.2023.103863`.

[54] H. Bikas, P. Stavropoulos, and G. Chryssolouris, “Additive manufacturing methods and modeling approaches: A critical review,” *International Journal of Advanced Manufacturing Technology*, vol. 83, no. 1-4, pp. 389–405, Mar. 2016, ISSN: 14333015. DOI: `10.1007/S00170-015-7576-2/METRICS`. [Online]. Available: `https://link.springer.com/article/10.1007/s00170-015-7576-2`.

[55] E. Atzeni, L. Iuliano, and A. Salmi, “On the competitiveness of additive manufacturing for the production of metal parts,” in *9th International Conference on Advanced Manufacturing Systems and Technology*, 2011.

[56] I. J. Solomon, P. Sevvel, and J. Gunasekaran, “A review on the various processing parameters in FDM,” *Materials Today: Proceedings*, vol. 37, no. Part 2, pp. 509–514, Jan. 2021, ISSN: 2214-7853. DOI: `10.1016/J.MATPR.2020.05.484`.

[57] N. Boyard, O. Christmann, M. Rivette, O. Kerbrat, and S. Richir, “Support optimization for additive manufacturing: Application to FDM,” *Rapid Prototyping Journal*, vol. 24, no. 1, pp. 69–79, 2018, ISSN: 13552546. DOI: `10.1108/RPJ-04-2016-0055/FULL/PDF`.

[58] M. Heidari-Rarani, M. Rafiee-Afarani, and A. M. Zahedi, “Mechanical characterization of FDM 3D printing of continuous carbon fiber reinforced PLA composites,” *Composites Part B: Engineering*, vol. 175, p. 107 147, Oct. 2019, ISSN: 1359-8368. DOI: `10.1016/J.COMPOSITESB.2019.107147`.

[59] Q. Ding, X. Li, D. Zhang, G. Zhao, and Z. Sun, “Anisotropy of poly(lactic acid)/carbon fiber composites prepared by fused deposition modeling,” *Journal of Applied Polymer Science*, vol. 137, no. 23, p. 48 786, Jun. 2020, ISSN: 1097-4628. DOI: `10.1002/APP.48786`. [Online]. Available: `https://onlinelibrary.wiley.com/doi/full/10.1002/app.48786%20https://onlinelibrary.wiley.com/doi/abs/10.1002/app.48786%20https://onlinelibrary.wiley.com/doi/10.1002/app.48786`.

[60] A. B. Varotsis, *Introduction to FDM 3D Printing*, 2019. [Online]. Available: `https://www.hubs.com/knowledge-base/introduction-fdm-3d-printing/`.

[61] E. O. Olakanmi, R. F. Cochrane, and K. W. Dalgarno, “A review on selective laser sintering/melting (SLS/SLM) of aluminium alloy powders: Processing, microstructure, and properties,” *Progress in Materials Science*, vol. 74, pp. 401–477, Oct. 2015, ISSN: 0079-6425. DOI: `10.1016/J.PMATSCI.2015.03.002`.

[62] P. Patpatiya, K. Chaudhary, A. Shastri, and S. Sharma, "A review on polyjet 3D printing of polymers and multi-material structures," *Proceedings of the Institution of Mechanical Engineers, Part C: Journal of Mechanical Engineering Science*, vol. 236, no. 14, pp. 7899–7926, Jul. 2022, ISSN: 20412983. DOI: `10.1177/09544062221079506/ASSET/IMAGES/10.1177{\_}09544062221079506-IMG4.PNG`. [Online]. Available: `https://journals.sagepub.com/doi/10.1177/09544062221079506?icid=int.sj-full-text.similar-articles.3`.

[63] A. B. Varotsis, *HP MJF vs. SLS: A 3D printing technology comparison*, 2019. [Online]. Available: `https://www.hubs.com/knowledge-base/hp-mjf-vs-sls-3d-printing-technology-comparison/`.

[64] L. Gregurić, *What Is Material Jetting? – 3D Printing Simply Explained*, 2019. [Online]. Available: `https://all3dp.com/2/what-is-material-jetting-3d-printing-simply-explained/`.

[65] F. d. C. Magalhães, W. d. O. Leite, and J. C. Campos Rubio, "A study of mechanical properties of photosensitive resins used in vat photopolymerization process," *Journal of Elastomers and Plastics*, Oct. 2024, ISSN: 15308006. DOI: `10.1177/00952443241256632/ASSET/IMAGES/LARGE/10.1177{\_}00952443241256632-FIG11.JPEG`. [Online]. Available: `https://journals.sagepub.com/doi/10.1177/00952443241256632?icid=int.sj-full-text.similar-articles.2`.

[66] Formlabs, "Materials Library," Tech. Rep., 2019. [Online]. Available: `https://formlabs-media.formlabs.com/filer_public/ac/89/ac8963db-f54a-4cac-8fe9-fb740a7b06f1/formlabs-materials-library.pdf`.

[67] 3D Systems, "Accura® Materials Selection Guide for Stereolithography – SLA," Tech. Rep., 2021. [Online]. Available: `https://www.3dsystems.com/sites/default/files/2021-08/3d-systems-sla-material-selection-guide-usen-2021-08-06-web.pdf`.

[68] A. B. Varotsis, *Introduction to SLA printing*, 2019. [Online]. Available: `https://www.hubs.com/knowledge-base/introduction-sla-3d-printing/`.

[69] Y. Xu, A. B. Xepapadeas, B. Koos, J. Geis-Gerstorfer, P. Li, and S. Spintzyk, "Effect of post-rinsing time on the mechanical strength and cytotoxicity of a 3D printed orthodontic splint material," *Dental Materials*, vol. 37, no. 5, e314–e327, May 2021, ISSN: 0109-5641. DOI: `10.1016/J.DENTAL.2021.01.016`.

[70] N.-K. Hwangbo, N.-E. Nam, J.-H. Choi, *et al.*, "Effects of the Washing Time and Washing Solution on the Biocompatibility and Mechanical Properties of 3D Printed Dental Resin Materials," *Polymers*, vol. 13, no. 24, p. 4410, Dec. 2021, ISSN: 2073-4360. DOI: `10.3390/POLYM13244410`. [Online]. Available: `https://`

www.mdpi.com/2073-4360/13/24/4410/htm%20https://www.mdpi.com/2073-4360/13/24/4410.

[71] B. Nowacki, P. Kowol, M. Kozioł, P. Olesik, J. Wieczorek, and K. Wacławiak, "Effect of Post-Process Curing and Washing Time on Mechanical Properties of mSLA Printouts," *Materials*, vol. 14, no. 17, p. 4856, Aug. 2021, ISSN: 1996-1944. DOI: 10.3390/MA14174856. [Online]. Available: https://www.mdpi.com/1996-1944/14/17/4856/htm%20https://www.mdpi.com/1996-1944/14/17/4856.

[72] I. Echeta, X. Feng, B. Dutton, R. Leach, and S. Piano, "Review of defects in lattice structures manufactured by powder bed fusion," *The International Journal of Advanced Manufacturing Technology 2019 106:5*, vol. 106, no. 5, pp. 2649–2668, Dec. 2019, ISSN: 1433-3015. DOI: 10.1007/S00170-019-04753-4. [Online]. Available: https://link.springer.com/article/10.1007/s00170-019-04753-4.

[73] X. Gao, F. Okigami, N. Avedissian, and W. Zhang, "An experimental and modeling study on warping in additively manufactured overhang structures," *Additive Manufacturing*, vol. 81, Feb. 2024, ISSN: 22148604. DOI: 10.1016/j.addma.2024.104017.

[74] N. C. Levkulich, S. L. Semiatin, J. E. Gockel, J. R. Middendorf, A. T. DeWald, and N. W. Klingbeil, "The effect of process parameters on residual stress evolution and distortion in the laser powder bed fusion of Ti-6Al-4V," *Additive Manufacturing*, vol. 28, pp. 475–484, Aug. 2019, ISSN: 22148604. DOI: 10.1016/j.addma.2019.05.015.

[75] P. Stavropoulos, P. Foteinopoulos, A. Papacharalampopoulos, and G. Tsoukantas, "Warping in SLM additive manufacturing processes: estimation through thermo-mechanical analysis," *International Journal of Advanced Manufacturing Technology*, vol. 104, no. 1-4, pp. 1571–1580, Sep. 2019, ISSN: 14333015. DOI: 10.1007/s00170-019-04105-2.

[76] P. Lin, M. Wang, V. A. Trofimov, Y. Yang, and C. Song, "Research on the Warping and Dross Formation of an Overhang Structure Manufactured by Laser Powder Bed Fusion," *Applied Sciences 2023, Vol. 13, Page 3460*, vol. 13, no. 6, p. 3460, Mar. 2023, ISSN: 2076-3417. DOI: 10.3390/APP13063460. [Online]. Available: https://www.mdpi.com/2076-3417/13/6/3460.

[77] M. Vatani, F. Barazandeh, A. Rahimi, and A. Sanati Nezhad, "Distortion modeling of SL parts by classical lamination theory," *Rapid Prototyping Journal*, vol. 18, no. 3, pp. 188–193, Apr. 2012, ISSN: 13552546. DOI: 10.1108/13552541211218090/FULL/PDF.

[78] B. Wiedemann, K. H. Dusel, and J. Eschl, "Investigation into the influence of material and process on part distortion," *Rapid Prototyping Journal*, vol. 1, no. 3, pp. 17–22, Jan. 1995, ISSN: 13552546. DOI: 10.1108/13552549510094232/FULL/PDF.

[79] D. Karalekas, D. Rapti, E. E. Gdoutos, and A. Aggelopoulos, "Investigation of Shrinkage-induced Stresses in Stereolithography Photo-curable Resins,"

[80] Q. Huang, J. Zhang, A. Sabbaghi, and T. Dasgupta, "Optimal offline compensation of shape shrinkage for three-dimensional printing processes," *IIE Transactions*, vol. 47, no. 5, pp. 431–441, May 2015, ISSN: 15458830. DOI: 10.1080/0740817X.2014.955599. [Online]. Available: https://www.tandfonline.com/doi/pdf/10.1080/0740817X.2014.955599.

[81] D. Xie, F. Lv, Y. Yang, *et al.*, "A Review on Distortion and Residual Stress in Additive Manufacturing," *Chinese Journal of Mechanical Engineering: Additive Manufacturing Frontiers*, vol. 1, no. 3, p. 100 039, Sep. 2022, ISSN: 2772-6657. DOI: 10.1016/J.CJMEAM.2022.100039. [Online]. Available: https://www.sciencedirect.com/science/article/pii/S2772665722000216.

[82] M. Grasso and B. M. Colosimo, "Process defects and in situ monitoring methods in metal powder bed fusion: a review," *Measurement Science and Technology*, vol. 28, no. 4, p. 044 005, Feb. 2017, ISSN: 0957-0233. DOI: 10.1088/1361-6501/AA5C4F. [Online]. Available: https://iopscience.iop.org/article/10.1088/1361-6501/aa5c4f%20https://iopscience.iop.org/article/10.1088/1361-6501/aa5c4f/meta.

[83] B. Zhang, Y. Li, and Q. Bai, "Defect Formation Mechanisms in Selective Laser Melting: A Review," *Chinese Journal of Mechanical Engineering (English Edition)*, vol. 30, no. 3, pp. 515–527, May 2017, ISSN: 21928258. DOI: 10.1007/S10033-017-0121-5. [Online]. Available: https://www.researchgate.net/publication/318429834_Defect_Formation_Mechanisms_in_Selective_Laser_Melting_A_Review.

[84] I. Kaur and P. Singh, "Critical evaluation of additively manufactured metal lattices for viability in advanced heat exchangers," *International Journal of Heat and Mass Transfer*, vol. 168, p. 120 858, Apr. 2021, ISSN: 0017-9310. DOI: 10.1016/J.IJHEATMASSTRANSFER.2020.120858.

[85] D. Melancon, Z. S. Bagheri, R. B. Johnston, L. Liu, M. Tanzer, and D. Pasini, "Mechanical characterization of structurally porous biomaterials built via additive manufacturing: experiments, predictive models, and design maps for load-bearing bone replacement implants," *Acta Biomaterialia*, vol. 63,

pp. 350–368, Nov. 2017, ISSN: 1742-7061. DOI: 10.1016/J.ACTBIO.2017.09.013.

[86] A. Alghamdi, T. Maconachie, D. Downing, M. Brandt, M. Qian, and M. Leary, "Effect of additive manufactured lattice defects on mechanical properties: an automated method for the enhancement of lattice geometry," *International Journal of Advanced Manufacturing Technology*, vol. 108, no. 3, pp. 957–971, May 2020, ISSN: 14333015. DOI: 10.1007/S00170-020-05394-8. [Online]. Available: https://www.researchgate.net/publication/341618138_Effect_of_additive_manufactured_lattice_defects_on_mechanical_properties_an_automated_method_for_the_enhancement_of_lattice_geometry.

[87] M. Casata, S. Perosanz, C. Garrido, and D. Barba, "A holistic study of the effect of geometrical and processing conditions on the static mechanical performance of LPBF strut elements," *Materials and Design*, vol. 247, Nov. 2024, ISSN: 18734197. DOI: 10.1016/j.matdes.2024.113387.

[88] L. Liu, P. Kamm, F. García-Moreno, J. Banhart, and D. Pasini, "Elastic and failure response of imperfect three-dimensional metallic lattices: the role of geometric defects induced by Selective Laser Melting," *Journal of the Mechanics and Physics of Solids*, vol. 107, pp. 160–184, Oct. 2017, ISSN: 0022-5096. DOI: 10.1016/J.JMPS.2017.07.003.

[89] Y. Amani, S. Dancette, P. Delroisse, A. Simar, and E. Maire, "Compression behavior of lattice structures produced by selective laser melting: X-ray tomography based experimental and finite element approaches," *Acta Materialia*, vol. 159, pp. 395–407, Oct. 2018, ISSN: 1359-6454. DOI: 10.1016/J.ACTAMAT.2018.08.030.

[90] W. Cheng, J. Y. Fuh, A. Y. Nee, Y. S. Wong, H. T. Loh, and T. Miyazawa, "Multi-objective optimization of partbuilding orientation in stereolithography," *Rapid Prototyping Journal*, vol. 1, no. 4, pp. 12–23, Jan. 1995, ISSN: 13552546. DOI: 10.1108/13552549510104429/FULL/PDF.

[91] R. Quintana, J.-W. Choi, K. Puebla, and R. Wicker, "Effects of build orientation on tensile strength for stereolithography-manufactured ASTM D-638 type I specimens," DOI: 10.1007/s00170-009-2066-z.

[92] J. S. Saini, L. Dowling, J. Kennedy, and D. Trimble, "Investigations of the mechanical properties on different print orientations in SLA 3D printed resin," *Proceedings of the Institution of Mechanical Engineers, Part C: Journal of Mechanical Engineering Science*, vol. 234, no. 11, pp. 2279–2293, Jun. 2020, ISSN: 20412983. DOI: 10.1177/0954406220904106/ASSET/D3E8769E-AD19-4F5D-9AFD-C5688366D633/ASSETS/IMAGES/LARGE/10.1177{_}0954406220904106-FIG26.

JPG. [Online]. Available: https://scholar.google.com/scholar_url?url=https://journals.sagepub.com/doi/pdf/10.1177/0954406220904106&hl=en&sa=T&oi=ucasa&ct=usl&ei=WS0vaIvpGOG86rQP8bDQeA&scisig=AAZF9b-HalLvruJbCkS7LyQoVU7H.

[93] A. Kalilayeva, D. Zhumashev, D. Wei, A. Perveen, and D. Talamona, "Investigation of Stereolithography Additively Manufactured Components for Deviations in Dimensional and Geometrical Features," *Polymers*, vol. 16, no. 23, p. 3311, Dec. 2024, ISSN: 20734360. DOI: 10.3390/POLYM16233311. [Online]. Available: https://pmc.ncbi.nlm.nih.gov/articles/PMC11644789/.

[94] A. Unkovskiy, P. H. B. Bui, C. Schille, J. Geis-Gerstorfer, F. Huettig, and S. Spintzyk, "Objects build orientation, positioning, and curing influence dimensional accuracy and flexural properties of stereolithographically printed resin," *Dental Materials*, vol. 34, no. 12, e324–e333, Dec. 2018, ISSN: 0109-5641. DOI: 10.1016/J.DENTAL.2018.09.011. [Online]. Available: https://www.sciencedirect.com/science/article/pii/S0109564118305943#fig0005.

[95] T. Liu, S. Guessasma, J. Zhu, W. Zhang, H. Nouri, and S. Belhabib, "Microstructural defects induced by stereolithography and related compressive behaviour of polymers," *Journal of Materials Processing Technology*, vol. 251, pp. 37–46, Jan. 2018, ISSN: 0924-0136. DOI: 10.1016/J.JMATPROTEC.2017.08.014.

[96] S. Guessasma, L. Tao, S. Belhabib, J. Zhu, W. Zhang, and H. Nouri, "Analysis of microstructure and mechanical performance of polymeric cellular structures designed using stereolithography," *European Polymer Journal*, vol. 98, pp. 72–82, Jan. 2018, ISSN: 0014-3057. DOI: 10.1016/J.EURPOLYMJ.2017.10.034. [Online]. Available: https://www.sciencedirect.com/science/article/pii/S0014305717305311.

[97] Q. Yang, Z. Lu, J. Zhou, K. Miao, and D. Li, "A novel method for improving surface finish of stereolithography apparatus," *International Journal of Advanced Manufacturing Technology*, vol. 93, no. 5-8, pp. 1537–1544, Nov. 2017, ISSN: 14333015. DOI: 10.1007/S00170-017-0529-1/METRICS. [Online]. Available: https://link.springer.com/article/10.1007/s00170-017-0529-1.

[98] O. Santoliquido, P. Colombo, and A. Ortona, "Additive Manufacturing of ceramic components by Digital Light Processing: A comparison between the "bottom-up" and the "top-down" approaches," *Journal of the European Ceramic Society*, vol. 39, no. 6, pp. 2140–2148, Jun. 2019, ISSN: 0955-2219. DOI: 10.1016/J.JEURCERAMSOC.2019.01.044. [Online]. Available: https://www.sciencedirect.com/science/article/pii/S0955221919300561?via%3Dihub.

[99] A. D. Dressler, E. W. Jost, J. C. Miers, D. G. Moore, C. C. Seepersad, and B. L. Boyce, “Heterogeneities dominate mechanical performance of additively manufactured metal lattice struts,” *Additive Manufacturing*, vol. 28, pp. 692–703, Aug. 2019, ISSN: 2214-8604. DOI: 10.1016/J.ADDMA.2019.06.011.

[100] S. Arabnejad, R. Burnett Johnston, J. A. Pura, B. Singh, M. Tanzer, and D. Pasini, “High-strength porous biomaterials for bone replacement: A strategy to assess the interplay between cell morphology, mechanical properties, bone ingrowth and manufacturing constraints,” *Acta Biomaterialia*, vol. 30, pp. 345–356, Jan. 2016, ISSN: 1742-7061. DOI: 10.1016/J.ACTBIO.2015.10.048.

[101] S. Murchio, M. Dallago, F. Zanini, *et al.*, “Additively manufactured Ti–6Al–4V thin struts via laser powder bed fusion: Effect of building orientation on geometrical accuracy and mechanical properties,” *Journal of the Mechanical Behavior of Biomedical Materials*, vol. 119, Jul. 2021, ISSN: 18780180. DOI: 10.1016/j.jmbbm.2021.104495.

[102] P. Mercelis and J. P. Kruth, “Residual stresses in selective laser sintering and selective laser melting,” *Rapid Prototyping Journal*, vol. 12, no. 5, pp. 254–265, 2006, ISSN: 13552546. DOI: 10.1108/13552540610707013/FULL/XML.

[103] S. R. Schricker, “Composite resin polymerization and relevant parameters,” *Orthodontic Applications of Biomaterials: A Clinical Guide*, pp. 153–170, Jan. 2017. DOI: 10.1016/B978-0-08-100383-1.00009-6.

[104] J. S. Ullett, R. P. Chartoff, A. J. Lightman, J. P. Murphy, and J. Lit, “REDUCING WARPAGE IN STEREOLITHOGRAPHY THROUGH NOVEL DRAW STYLES,”

[105] T. Li, Y. Zhang, W. Duan, *et al.*, “A study on the control of the printing accuracy in alumina parts by ceramic stereolithography,” *Journal of the European Ceramic Society*, vol. 44, no. 12, pp. 7149–7159, Sep. 2024, ISSN: 0955-2219. DOI: 10.1016/J.JEURCERAMSOC.2024.04.067.

[106] B. Ping, J. Huang, F. Meng, *et al.*, “Computational and analytical modeling of curing and warping of microdroplet-jet 3D printing photosensitive resins,” *Additive Manufacturing*, vol. 89, p. 104 291, Jun. 2024, ISSN: 2214-8604. DOI: 10.1016/J.ADDMA.2024.104291.

[107] K. Chockalingam, N. Jawahar, and U. Chandrasekhar, “Influence of layer thickness on mechanical properties in stereolithography,” *Rapid Prototyping Journal*, vol. 12, no. 2, pp. 106–113, 2006, ISSN: 13552546. DOI: 10.1108/13552540610652456/FULL/PDF.

[108] C. Yan, L. Hao, A. Hussein, and D. Raymont, "Evaluations of cellular lattice structures manufactured using selective laser melting," *International Journal of Machine Tools and Manufacture*, vol. 62, pp. 32–38, Nov. 2012, ISSN: 0890-6955. DOI: `10.1016/J.IJMACHTOOLS.2012.06.002`.

[109] Z. Dong, Y. Liu, W. Li, and J. Liang, "Orientation dependency for microstructure, geometric accuracy and mechanical properties of selective laser melting AlSi10Mg lattices," *Journal of Alloys and Compounds*, vol. 791, pp. 490–500, Jun. 2019, ISSN: 0925-8388. DOI: `10.1016/J.JALLCOM.2019.03.344`.

[110] Y. Tian, H. Ren, J. He, *et al.*, "Surface roughness improvement of Ti-6Al-4V alloy overhang structures via process optimization for laser-powder bed fusion," *Journal of Manufacturing Processes*, vol. 110, pp. 434–446, Jan. 2024, ISSN: 1526-6125. DOI: `10.1016/J.JMAPRO.2024.01.008`.

[111] A. P. Golhin, R. Tonello, J. R. Frisvad, S. Grammatikos, and A. Strandlie, "Surface roughness of as-printed polymers: a comprehensive review," *The International Journal of Advanced Manufacturing Technology 2023 127:3*, vol. 127, no. 3, pp. 987–1043, May 2023, ISSN: 1433-3015. DOI: `10.1007/S00170-023-11566-Z`. [Online]. Available: `https://link.springer.com/article/10.1007/s00170-023-11566-z`.

[112] V. Lindström, G. Lupo, J. Yang, V. Turlo, and C. Leinenbach, "A simple scaling model for balling defect formation during laser powder bed fusion," *Additive Manufacturing*, vol. 63, p. 103 431, Feb. 2023, ISSN: 2214-8604. DOI: `10.1016/J.ADDMA.2023.103431`.

[113] A. Cuadrado, A. Yánez, O. Martel, S. Deviaene, and D. Monopoli, "Influence of load orientation and of types of loads on the mechanical properties of porous Ti6Al4V biomaterials," *Materials and Design*, vol. 135, pp. 309–318, Dec. 2017, ISSN: 18734197. DOI: `10.1016/j.matdes.2017.09.045`.

[114] R. Goodall, E. Hernandez-Nava, S. N. Jenkins, *et al.*, "The effects of defects and damage in the mechanical behavior of ti6al4v lattices," *Frontiers in Materials*, vol. 6, p. 434 466, Jul. 2019, ISSN: 22968016. DOI: `10.3389/FMATS.2019.00117/BIBTEX`.

[115] L. Salari-Sharif, S. W. Godfrey, M. Tootkaboni, and L. Valdevit, "The effect of manufacturing defects on compressive strength of ultralight hollow microlattices: A data-driven study," *Additive Manufacturing*, vol. 19, pp. 51–61, Jan. 2018, ISSN: 2214-8604. DOI: `10.1016/J.ADDMA.2017.11.003`.

[116] ASTM International, *ASTM D16621 - 16 Test Method for Compressive Properties of Rigid Cellular Plastics*, West Conshohocken, PA, May 2016. DOI: `10.1520/D1621-16`.

[117] A. D. Marter, A. S. Dickinson, F. Pierron, and M. Browne, "A Practical Procedure for Measuring the Stiffness of Foam like Materials," *Experimental Techniques*, vol. 42, no. 4, pp. 439–452, 2018, ISSN: 17471567. DOI: `10.1007/s40799-018-0247-0`. [Online]. Available: `https://link.springer.com/article/10.1007/s40799-018-0247-0`.

[118] S. R. Kalidindi, A. Abusafieh, and E. Ei-Danaf, "Accurate Characterization of Machine Compliance for Simple Compression Testing,"

[119] S. Zhao, M. Arnold, S. Ma, *et al.*, "Standardizing compression testing for measuring the stiffness of human bone," *Bone & Joint Research*, vol. 7, no. 8, pp. 524–538, Aug. 2018, ISSN: 2046-3758. DOI: `10.1302/2046-3758.78.BJR-2018-0025.R1`. [Online]. Available: `https://online.boneandjoint.org.uk/doi/10.1302/2046-3758.78.BJR-2018-0025.R1`.

[120] P. Sousa, S. V. Lomov, and J. Ivens, "Methodology of dry and wet compressibility measurement," *Composites Part A: Applied Science and Manufacturing*, vol. 128, p. 105 672, Jan. 2020, ISSN: 1359-835X. DOI: `10.1016/J.COMPOSITESA.2019.105672`.

[121] A. D. Marter, A. S. Dickinson, F. Pierron, Y. K. (Fong, and M. Browne, "Characterising the compressive anisotropic properties of analogue bone using optical strain measurement," *Proceedings of the Institution of Mechanical Engineers, Part H: Journal of Engineering in Medicine*, vol. 233, no. 9, pp. 954–960, 2019, ISSN: 20413033. DOI: `10.1177/0954411919855150`.

[122] S. S. Lee, X. Du, I. Kim, and S. J. Ferguson, "Scaffolds for bone-tissue engineering," *Matter*, vol. 5, no. 9, pp. 2722–2759, Sep. 2022, ISSN: 2590-2385. DOI: `10.1016/J.MATT.2022.06.003`.

[123] Formlabs, *Form3*, Somerville, Massachusetts, 2021. [Online]. Available: `https://formlabs.com/`.

[124] H. D. Carlton, J. Lind, M. C. Messner, *et al.*, "Mapping local deformation behavior in single cell metal lattice structures," *Acta Materialia*, vol. 129, pp. 239–250, May 2017, ISSN: 1359-6454. DOI: `10.1016/J.ACTAMAT.2017.02.023`.

[125] ASTM International, "ASTM D695-23 Standard Test Method for Compressive Properties of Rigid Plastics," Tech. Rep., 2023.

[126] M. J. Munford, K. C. Ng, and J. R. Jeffers, “Mapping the Multi-Directional Mechanical Properties of Bone in the Proximal Tibia,” *Advanced Functional Materials*, vol. 2004323, pp. 1–9, 2020, ISSN: 16163028. DOI: `10.1002/adfm.202004323`.

[127] F. Linde and I. Hvid, “Stiffness behaviour of trabecular bone specimens,” *Journal of Biomechanics*, vol. 20, no. 1, pp. 83–89, Jan. 1987, ISSN: 0021-9290. DOI: `10.1016/0021-9290(87)90270-3`.

[128] MatchID EU, *MatchID*, 2022. [Online]. Available: `https://www.matchid.eu/en`.

[129] J. D. Lord and R. Morrell, “A national measurement good practice guide No. 98: Elastic Modulus Measurement,” Tech. Rep. 98, 2006, pp. 1–40.

[130] J. Schindelin, I. Arganda-Carreras, E. Frise, *et al.*, “Fiji: an open-source platform for biological-image analysis,” *Nature Methods 2012 9:7*, vol. 9, no. 7, pp. 676–682, Jun. 2012, ISSN: 1548-7105. DOI: `10.1038/nmeth.2019`. [Online]. Available: `https://www.nature.com/articles/nmeth.2019`.

[131] Micromaterials Ltd., *Micromaterials Vantage System*, Wrexham, UK.

[132] W. C. Oliver and G. M. Pharr, “Measurement of hardness and elastic modulus by instrumented indentation: Advances in understanding and refinements to methodology,” *Journal of Materials Research*, vol. 19, no. 1, pp. 3–20, Jan. 2004, ISSN: 08842914. DOI: `10.1557/JMR.2004.19.1.3/METRICS`. [Online]. Available: `https://link.springer.com/article/10.1557/jmr.2004.19.1.3`.

[133] A. Mokhtari, N. Tala-Ighil, and Y. A. Masmoudi, “Nanoindentation to Determine Young’s Modulus for Thermoplastic Polymers,” *Journal of Materials Engineering and Performance*, vol. 31, no. 4, 2022. DOI: `10.1007/s11665-021-06386-9`. [Online]. Available: `https://doi.org/10.1007/s11665-021-06386-9`.

[134] K. L. Johnson, *Contact Mechanics*. Cambridge University Press, May 1985, ISBN: 9780521255769. DOI: `10.1017/CBO9781139171731`. [Online]. Available: `https://www.cambridge.org/core/books/contact-mechanics/E3707F77C2EBCE727C3911AFBD2E4AC2`.

[135] C. B. Burson-Thomas, A. S. Dickinson, and M. Browne, “Quantifying Joint Congruence With an Elastic Foundation,” *Biomedical Engineering*, vol. 144, no. 10, 2022. DOI: `10.1115/1.4054276`. [Online]. Available: `http://asmedigitalcollection.asme.org/biomechanical/article-pdf/144/10/101003/6878131/bio_144_10_101003.pdf`.

[136] S. Bhattacharya, H. E. Demirci, G. Nikitas, *et al.*, "Physical modeling of interaction problems in geotechnical engineering," *Modeling in Geotechnical Engineering*, pp. 205–256, Jan. 2021. DOI: `10.1016/B978-0-12-821205-9.00017-4`.

[137] A. C. Lamprea-Pineda, D. P. Connolly, and M. F. M. Hussein, "Beams on elastic foundations-A review of railway applications and solutions," *Transportation Geotechnics*, vol. 33, p. 100 696, 2022. DOI: `10.1016/j.trgeo.2021.100696`. [Online]. Available: `https://doi.org/10.1016/j.trgeo.2021.100696`.

[138] T. G. Chandler and D. Vella, "Validity of Winkler's mattress model for thin elastomeric layers: beyond Poisson's ratio," *Proceedings of the Royal Society A*, vol. 476, no. 2242, Oct. 2020, ISSN: 14712946. DOI: `10.1098/RSPA.2020.0551`. [Online]. Available: `https://royalsocietypublishing.org/doi/10.1098/rspa.2020.0551`.

[139] P. Chen, L. Xu, and Z. Li, "Study on prediction method of initial stiffness of self-centering energy dissipation braces," *Engineering Structures*, vol. 247, p. 113 226, Nov. 2021, ISSN: 0141-0296. DOI: `10.1016/J.ENGSTRUCT.2021.113226`.

[140] B. Lozanovski, D. Downing, P. Tran, *et al.*, "A Monte Carlo simulation-based approach to realistic modelling of additively manufactured lattice structures," *Additive Manufacturing*, vol. 32, p. 101 092, Mar. 2020, ISSN: 2214-8604. DOI: `10.1016/J.ADDMA.2020.101092`.

[141] H. Lei, C. Li, J. Meng, *et al.*, "Evaluation of compressive properties of SLM-fabricated multi-layer lattice structures by experimental test and μ-CT-based finite element analysis," *Materials & Design*, vol. 169, p. 107 685, May 2019, ISSN: 0264-1275. DOI: `10.1016/J.MATDES.2019.107685`.

[142] R. Oftadeh, M. Perez-Viloria, J. C. Villa-Camacho, A. Vaziri, and A. Nazarian, *Biomechanics and Mechanobiology of Trabecular Bone: A Review*, Jan. 2015. DOI: `10.1115/1.4029176`. [Online]. Available: `http://asmedigitalcollection.asme.org/biomechanical/article-pdf/137/1/010802/6091457/bio_137_01_010802.pdf`.

[143] P. Pivonka, A. Park, and M. R. Forwood, "Functional adaptation of bone: The mechanostat and beyond," in *CISM International Centre for Mechanical Sciences, Courses and Lectures*, vol. 578, Springer International Publishing, 2018, pp. 1–60. DOI: `10.1007/978-3-319-58845-2{\_}1`. [Online]. Available: `https://link.springer.com/chapter/10.1007/978-3-319-58845-2_1`.

[144] H. M. Frost, "Bone "mass" and the "mechanostat": A proposal," *The Anatomical Record*, vol. 219, no. 1, pp. 1–9, 1987, ISSN: 10970185. DOI: 10.1002/AR.1092190104.

[145] Formlabs, *SLA vs. DLP vs. MSLA vs. LCD: Guide to Resin 3D Printers — Formlabs*. [Online]. Available: https://formlabs.com/uk/blog/resin-3d-printer-comparison-sla-vs-dlp/?srsltid=AfmBOoq9m2a06DUHdPsXpf-9U0c994i-UteD77nP1HQdcXCsPA6q9hUv.

[146] A. Vyas, V. Garg, S. B. Ghosh, and S. Bandyopadhyay-Ghosh, "Photopolymerizable resin-based 3D printed biomedical composites: Factors affecting resin viscosity," *Materials Today: Proceedings*, vol. 62, pp. 1435–1439, Jan. 2022, ISSN: 2214-7853. DOI: 10.1016/J.MATPR.2022.01.172.

[147] A. Licciulli, C. Esposito Corcione, A. Greco, V. Amicarelli, and A. Maffezzoli, "Laser stereolithography of ZrO2 toughened Al2O3," *Journal of the European Ceramic Society*, vol. 25, no. 9, pp. 1581–1589, Jun. 2005, ISSN: 0955-2219. DOI: 10.1016/J.JEURCERAMSOC.2003.12.003.

[148] S. Corbel, O. Dufaud, and T. Roques-Carmes, "Materials for Stereolithography," in *Stereolithography: Materials, Processes and Applications*, Springer US, 2011, pp. 141–159. DOI: 10.1007/978-0-387-92904-0{_}6. [Online]. Available: https://www.researchgate.net/publication/278693190_Materials_for_Stereolithography.

[149] K. Rooney, Y. Dong, A. Pramanik, and A. K. Basak, "Additive Manufacturing in Australian Small to Medium Enterprises: Vat Polymerisation Techniques, Case Study and Pathways to Industry 4.0 Competitiveness," *Journal of Manufacturing and Materials Processing*, vol. 7, no. 5, Oct. 2023, ISSN: 25044494. DOI: 10.3390/JMMP7050168. [Online]. Available: https://www.researchgate.net/publication/373840127_Additive_Manufacturing_in_Australian_Small_to_Medium_Enterprise_Vat_Polymerisation_Techniques_Case_Study_and_Pathways_to_Industry_40_Competitiveness.

[150] C. Arnold, L. Riß, J. Hey, and R. Schweyen, "Dimensional Accuracy of Different Three-Dimensional Printing Models as a Function of Varying the Printing Parameters," *Materials 2024, Vol. 17, Page 3616*, vol. 17, no. 14, p. 3616, Jul. 2024, ISSN: 1996-1944. DOI: 10.3390/MA17143616. [Online]. Available: https://www.mdpi.com/1996-1944/17/14/3616/htm%20https://www.mdpi.com/1996-1944/17/14/3616.

[151] J. Metelkova, L. Vanmunster, H. Haitjema, and B. Van Hooreweder, “Texture of inclined up-facing surfaces in laser powder bed fusion of metals,” *Additive Manufacturing*, vol. 42, p. 101 970, Jun. 2021, ISSN: 2214-8604. DOI: `10.1016/J.ADDMA.2021.101970`.

[152] H. Gonabadi, A. Yadav, and S. Bull, “Mechanical Characterisation of Polymeric Materials Using Nanoindentation,” in *Contact Problems for Soft, Biological and Bioinspired Materials*, Springer, Cham, 2022, pp. 139–180, ISBN: 978-3-030-85175-0. DOI: `10.1007/978-3-030-85175-0{\_}8`. [Online]. Available: `https://link.springer.com/chapter/10.1007/978-3-030-85175-0_8`.

[153] M. R. VanLangingham, J. S. Villarrubia, W. F. Guthrie, and G. F. Meyers, “Nanoindentation of polymers: an overview,” *Macromolecular Symposia*, vol. 167, no. 1, pp. 15–44, 2001.

[154] The MathWorks Inc., *MATLAB*, Natick, Massachusetts, United States, 2020.

[155] C. B. Finfrock, “Temperature and Strain Rate Dependence of the Martensitic Transformation and Mechanical Properties in Advanced High Strength Steels,” Ph.D. dissertation.

[156] S. Chava and S. Namilae, “Continuous evolution of processing induced residual stresses in composites: An in-situ approach,” *Composites Part A: Applied Science and Manufacturing*, vol. 145, p. 106 368, Jun. 2021, ISSN: 1359-835X. DOI: `10.1016/J.COMPOSITESA.2021.106368`.

[157] M. H. Luxner, J. Stampfl, and H. E. Pettermann, “Finite element modeling concepts and linear analyses of 3D regular open cell structures,” *Journal of Materials Science*, vol. 40, no. 22, pp. 5859–5866, Nov. 2005, ISSN: 00222461. DOI: `10.1007/S10853-005-5020-Y/METRICS`. [Online]. Available: `https://link.springer.com/article/10.1007/s10853-005-5020-y`.

[158] L. J. Gibson, “Biomechanics of cellular solids,” *Journal of Biomechanics*, vol. 38, no. 3, pp. 377–399, Mar. 2005, ISSN: 0021-9290. DOI: `10.1016/J.JBIOMECH.2004.09.027`.

[159] E. Hernández-Nava, C. J. Smith, F. Derguti, *et al.*, “The effect of density and feature size on mechanical properties of isostructural metallic foams produced by additive manufacturing,” *Acta Materialia*, vol. 85, pp. 387–395, Feb. 2015, ISSN: 1359-6454. DOI: `10.1016/J.ACTAMAT.2014.10.058`.

[160] A. Mortensen, Y. Conde, A. Rossoll, and C. San Marchi, "Scaling of conductivity and Young's modulus in replicated microcellular materials," *Journal of Materials Science*, vol. 48, no. 23, pp. 8140–8146, Dec. 2013, ISSN: 00222461. DOI: `10.1007/S10853-013-7626-9/FIGURES/4`. [Online]. Available: `https://link.springer.com/article/10.1007/s10853-013-7626-9`.

[161] F. H. Öztürk, İ. A. Karamanlı, and A. Temiz, "Strut-based design optimization for improving mechanical properties of lattice structures," *International Journal of Mechanics and Materials in Design*, pp. 1–18, Apr. 2025, ISSN: 15738841. DOI: `10.1007/S10999-025-09751-X/FIGURES/4`. [Online]. Available: `https://link.springer.com/article/10.1007/s10999-025-09751-x`.

[162] J. Bauer, L. R. Meza, T. A. Schaedler, R. Schwaiger, X. Zheng, and L. Valdevit, *Nanolattices: An Emerging Class of Mechanical Metamaterials*, Oct. 2017. DOI: `10.1002/adma.201701850`.

[163] E. Helgeland, A. Rashad, E. Campodoni, *et al.*, "Dual-crosslinked 3D printed gelatin scaffolds with potential for temporomandibular joint cartilage regeneration," *Biomedical Materials (Bristol)*, vol. 16, no. 3, May 2021, ISSN: 1748605X. DOI: `10.1088/1748-605X/ABE6D9`. [Online]. Available: `https://www.researchgate.net/publication/349356959_Dual-crosslinked_3D_printed_gelatin_scaffolds_with_potential_for_temporomandibular_joint_cartilage_regeneration`.

[164] R. Gümrük, R. A. W. Mines, and S. Karadeniz, "Static mechanical behaviours of stainless steel micro-lattice structures under different loading conditions," *Materials Science and Engineering: A*, vol. 586, pp. 392–406, 2013. DOI: `10.1016/j.msea.2013.07.070`. [Online]. Available: `http://dx.doi.org/10.1016/j.msea.2013.07.070`.

[165] S. B. Segletes, "An Examination of Connectivity across 3-D Cubic-Lattice Networks," Tech. Rep., 2021.

[166] S. Kechagias, R. N. Oosterbeek, M. J. Munford, S. Ghouse, and J. R. Jeffers, "Controlling the mechanical behaviour of stochastic lattice structures: The key role of nodal connectivity," *Additive Manufacturing*, vol. 54, p. 102 730, Jun. 2022, ISSN: 2214-8604. DOI: `10.1016/J.ADDMA.2022.102730`.

[167] H. Gu, M. Pavier, and A. Shterenlikht, "Experimental study of modulus, strength and toughness of 2D triangular lattices," *International Journal of Solids and Structures*, vol. 152-153, pp. 207–216, Nov. 2018, ISSN: 0020-7683. DOI: `10.1016/J.IJSOLSTR.2018.06.028`.

[168] X. Y. Zhang, G. Fang, L. L. Xing, W. Liu, and J. Zhou, "Effect of porosity variation strategy on the performance of functionally graded Ti-6Al-4V scaffolds for bone tissue engineering," *Materials and Design*, vol. 157, pp. 523–538, Nov. 2018, ISSN: 18734197. DOI: `10.1016/J.MATDES.2018.07.064`.

[169] M. Iskander and N. Shrive, "Fracture of brittle and quasi-brittle materials in compression: A review of the current state of knowledge and a different approach," *Theoretical and Applied Fracture Mechanics*, vol. 97, pp. 250–257, Oct. 2018, ISSN: 0167-8442. DOI: `10.1016/J.TAFMEC.2018.08.014`.

[170] Granta Design, *CES EduPack*, 2019.

[171] M. Mohsenizadeh, F. Gasbarri, M. Munther, A. Beheshti, and K. Davami, "Additively-manufactured lightweight Metamaterials for energy absorption," *Materials & Design*, vol. 139, pp. 521–530, Feb. 2018, ISSN: 0264-1275. DOI: `10.1016/J.MATDES.2017.11.037`.

Chapter 7

Appendix A

This appendix will focus on the appendices of the first technical chapter, Chapter 3.

7.1 Post-processing Variation

The effects of 6 different post-processing methods were investigated (summarised in Table 7.1.1) on the elastic modulus of BCCz lattices manufactured in the same way as those for the main investigation; Form3 with Rigid 10K resin, BCCz unit cell with an as-design strut diameter of 0.46 mm and 10 unit cells in each direction, additional vertical strut aligned with the build direction and endplates on the top and bottom faces.

Condition	**Heated**	**Under Vacuum**	**Vacuum and Heat (PP2)**	**Manufacturer Recommended (PP1)**	**Shorter Wash**	**Shorter Cure**
Wash 1 (UB)	7	7	7	10	7	7
Wash 2 (UB)	5	5	5	10	5	5
Heat	60 °C	N	60 °C	N	N	N
Vacuum	N	Y, 2 hrs	Y, 2 hrs	N	N	N
Cure	1 hr	1 hr	1 hr	1 hr	1 hr	45 mins

TABLE 7.1.1: Post-processing conditions trialled in phase one with key differences being highlighted with boxes. UB – ultrasonic bath.

Samples were unadhered and were compressively tested according to the methods outlines in the study and elastic modulus was calculated using strain from the machine platen ('Crosshead') and optical measurements from point tracking ('Optical') (Fig. 7.1).

Across the post-processing methods, the average elastic modulus calculated from optical strain measurements was greater than when calculated using the machine

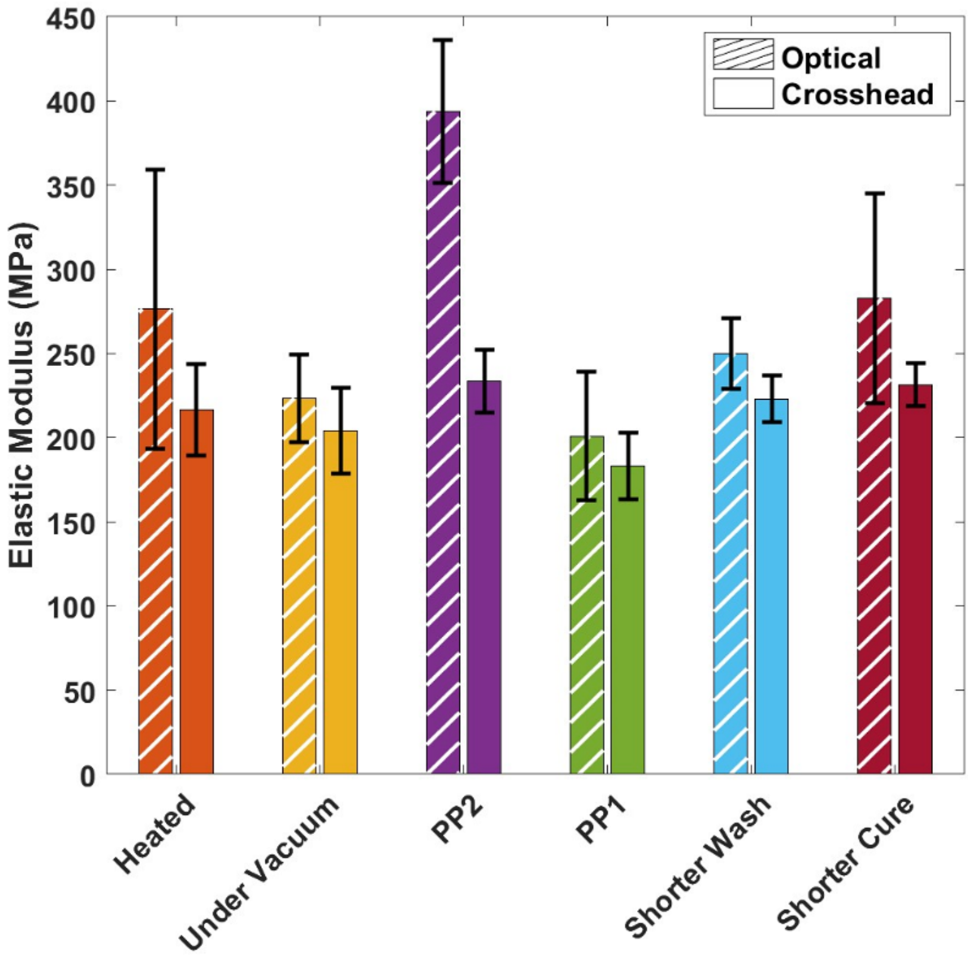

FIGURE 7.1: Variation in apparent elastic modulus for six different post-processing methods calculated using both optical strain measurements and cross-head displacement.

crosshead displacement. Local variability in loads, especially for unadhered samples cannot be captured using the machine platens and is evidenced by the greater variation of the optical plots shown with the error bars.

The average elastic modulus differs between post-processing methods with the samples held under a vacuum and subsequently heated (PP2) resulting in the greatest average modulus (394 MPa). The minimum elastic modulus (201 MPa) is observed for samples which were not exposed to any addition heating and experienced longer washing cycles (PP1), suggesting that the washing agent, isopropyl alcohol may have a softening effect. PP2 has an average elastic modulus approximately 200 MPa greater than PP1, greater than the similar standard deviations for both groups, 38 and 42 MPa for PP1 and PP2 respectively. More repeats were required to verify the difference between the two post-processing methods as well as additional tests such as nanoindentation to help identify why such differences occurred.

7.2 MatchID Noise Study

For point tracking, as with similar non-contact measurement techniques like digital image correlation, there are a variety of image processing settings that need to be chosen to suit the data/deformation and minimise computational costs. Based on the expected small deformations the following settings in MatchID were set:

- Correlation criterion: Zero-Normalised Sum of Squared Differences (ZNSSD)
- Interpolation: Local Bicubic Spline
- Shape Function: Affine

Additionally, to maximise correlation success between images, the reference image from which a correlation was calculated from was updated each image, i.e. n and n – 1 were compared with n as the image number.

The subset and step sizes can also be varied to maximise spatial resolution, minimise computing cost and maximise accuracy. The following subset and steps sizes (in pixels) were evaluated:

Subset Size	**Step Size**
399	115
299	90
245	70
199	60
99	30

TABLE 7.2.1: Subset and step size variation for noise study. Subsets were chosen in increments of 100 pixels with 245 pixels chosen to try and improve upon 199 and 299 pixels.

To evaluate the different sizes, the optical strain at each position was averaged over the first 13 images of one of the adhered PP2 samples, before the sample was loaded, Fig. 7.2. When evaluating subset sizes, it is important to keep in mind that increasing subset size reduces noise but also increases computational cost. For each virtual extensometer, we determined the smallest subset size that was still within the plateau of the plot. For the middle extensometer (FM), subset size has a negligible impact on strain so the optimal subset size would be 99 pixels. For the right and left extensometers, however the subset sizes greater than 245 and 199 pixels respectively show deviations from the plateau. From these subset sizes, the maximum size, pixels was chosen to minimise noise across the sample.

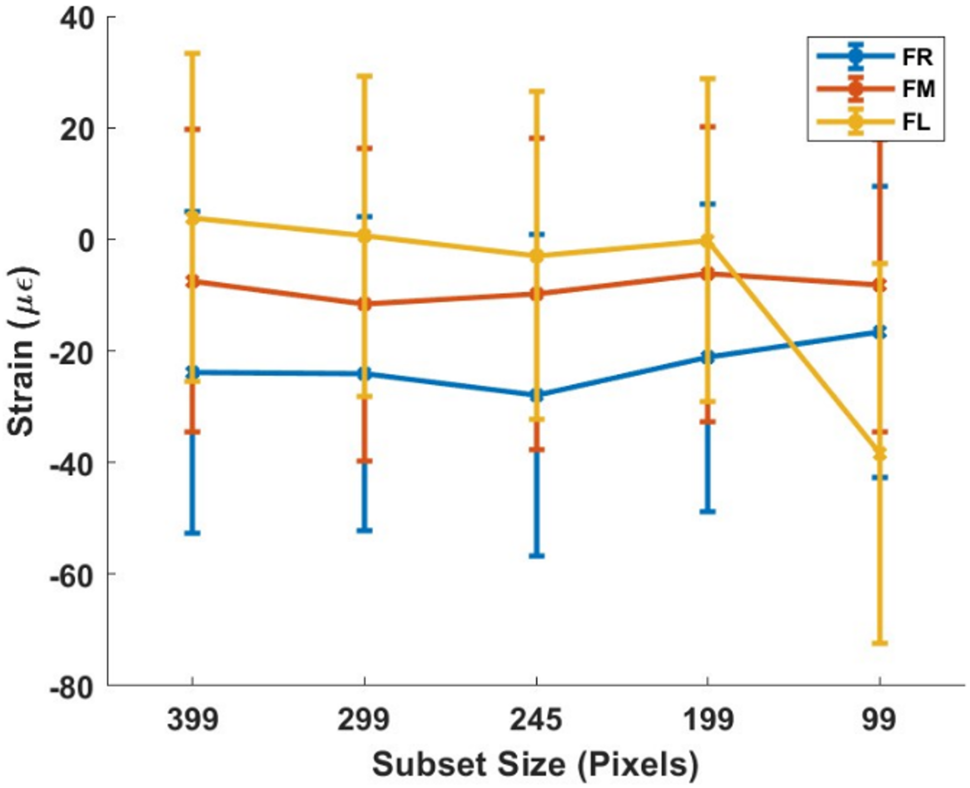

FIGURE 7.2: Variation in strain across an unloaded sample with varying subset size.

7.3 Integration of Elastic Foundation Model for Dome with Peak in the Centre

Elastic modulus E_s, is related to stress, σ, and strain, ε by:

$$E_s = \frac{\sigma}{\varepsilon} \quad \text{(Eq. 7.3.1)}$$

Strain is defined by equation 2 with u_z as the change in length and L as the original length of the springs.

$$\varepsilon = \frac{u_z}{L} \quad \text{(Eq. 7.3.2)}$$

Eq. 7.3.1 can then be rewritten to make σ the subject to give:

$$\sigma = \frac{E_s \Delta L}{L} \quad \text{(Eq. 7.3.3)}$$

The original length of the springs is equal to the thickness of the elastic material in the elastic foundation model, h. The change in length depends on both the displacement,

x, and the position of the spring as a function of position in x and y, and the major (a) and minor (b) semi-axes of the elliptical paraboloid based on the curvature of the indenter as in Eq. 7.3.4:

$$u_z = x\left(1 - \frac{x^2}{a^2} - \frac{y^2}{b^2}\right) \qquad \text{(Eq. 7.3.4)}$$

The stress as a function of position can therefore be defined as:

$$\sigma = \frac{E_s x}{h}\left(1 - \frac{x^2}{a^2} - \frac{y^2}{b^2}\right) \qquad \text{(Eq. 7.3.5)}$$

The total force, P, is determined by integrating the area, $A(\sigma)$ as a function of the stress:

$$P = \int_{\sigma(min)}^{\sigma(max)} A(\sigma)\, d\sigma \qquad \text{(Eq. 7.3.6)}$$

The area of an ellipse is defined as:

$$A = \pi a^{'} b^{'} \qquad \text{(Eq. 7.3.7)}$$

Where $a^{'}$ and $b^{'}$ are the major and minor semi-axes that vary with the displacement and therefore stress.

To find $a^{'}$ and $b^{'}$ in terms of stress, x and y, some limits can be defined.

At a particular displacement, x, $a^{'} = x$, when $y = 0$ (along the x axis) and $b^{'} = y$, when $x = 0$ (along the y axis).

Therefore, to find $a^{'}$:

$$\sigma(a^{'}, 0) = \frac{E_s x}{h}\left(1 - \frac{a^{'2}}{a^2} - \frac{0^2}{b^2}\right) \qquad \text{(Eq. 7.3.8)}$$

Which simplifies to:

$$\sigma = \frac{E_s x}{h}\left(1 - \frac{a^{'2}}{a^2}\right) \qquad \text{(Eq. 7.3.9)}$$

And making $a^{'}$ the subject yields:

$$a' = a\left(1 - \frac{\sigma h}{E_s x}\right)^{\frac{1}{2}} \tag{Eq. 7.3.10}$$

The same procedure applied for b', yields:

$$b' = b\left(1 - \frac{\sigma h}{E_s x}\right)^{\frac{1}{2}} \tag{Eq. 7.3.11}$$

$A(\sigma)$ then becomes:

$$A(\sigma) = \ \pi\ a\left(1 - \frac{\sigma h}{E_s x}\right)^{\frac{1}{2}}\ b\left(1 - \frac{\sigma h}{E_s x}\right)^{\frac{1}{2}} \tag{Eq. 7.3.12}$$

Which simplifies to:

$$A(\sigma) = \ \pi\ ab\left(1 - \frac{\sigma h}{E_s x}\right) \tag{Eq. 7.3.13}$$

For the integration, we need to define the maximum and minimum stress. The minimum stress is 0, whilst the maximum stress is at the peak of the indenter at the maximum displacement, x, and is equal to $\frac{E_s x}{h}$.

The integral then becomes:

$$P = \int_0^{\frac{E_s x}{h}} \pi ab\left(1 - \frac{\sigma h}{E_s x}\right)\ d\sigma \tag{Eq. 7.3.14}$$

The integral then simplifies as:

$$P = \ \pi ab \int_0^{\frac{E_s x}{h}} 1 - \frac{\sigma h}{E_s x}\ d\sigma \tag{Eq. 7.3.15}$$

Which becomes:

$$P = \ \pi ab\left[\sigma - \frac{\sigma^2 h}{2E_s x}\right]_0^{\frac{E_s x}{h}} \tag{Eq. 7.3.16}$$

And:

$$P = \ \pi ab\left(\frac{E_s x}{h} - \left(\left(\frac{E_s x}{h}\right)^2 \cdot \left(\frac{h}{2E_s x}\right)\right)\right) \tag{Eq. 7.3.17}$$

And finally simplifies out as:

$$P = \frac{E_s \pi abx}{2h} \tag{Eq. 7.3.18}$$

Which for an axisymmetric elliptic paraboloid where the major and minor semi-axes are equal, is:

$$P = \frac{E_s \pi a^2 x}{2h} \tag{Eq. 7.3.19}$$

7.4 Integration of Elastic Foundation Model for Dome with Peak in the Corner

The steps for determining the force exerted on the lattice when the peak of dome is in a corner is much the same as when the peak is in the centre. The key difference is that the radius of the dome at the base is now double with the shape now modelled as a quarter of a larger dome (Fig. 7.3 a) instead of a full smaller dome (Fig 7.3 b).

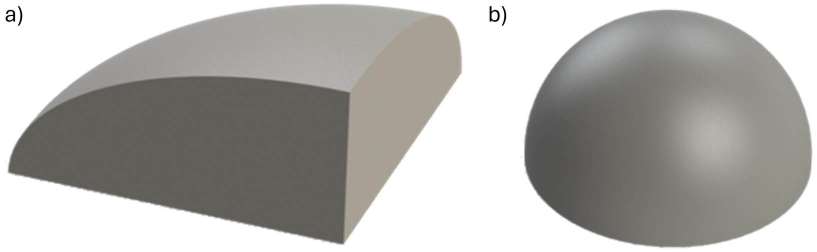

FIGURE 7.3

The area of the cross-section is now a quarter of an ellipse, and Eq. 7.3.6 then becomes:

$$P = \int_{\sigma(min)}^{\sigma(max)} \frac{A(\sigma)}{4}\, d\sigma \tag{Eq. 7.4.1}$$

The increase in radius is accounted for after the integration and the additional ¼ term can be taken outside the integral so Eq. 7.3.15 becomes:

$$P = \frac{\pi ab}{4} \int_{0}^{\frac{E_s x}{h}} 1 - \frac{\sigma h}{E_s x}\, d\sigma \tag{Eq. 7.4.2}$$

Leading to a final simplified equation:

$$P = \frac{E_s \pi abx}{8h} \tag{Eq. 7.4.3}$$

Which, similar to previously for an axisymmetric elliptic paraboloid where the major and minor semi-axes are equal, becomes:

$$P = \frac{E_s \pi a^2 x}{8h} \tag{Eq. 7.4.4}$$

7.5 Method for accounting for the 'toe-in' region adapted from NPL's 'Measurement Good Practice Guide No. 98: Elastic Modulus Measurement' [129]

```
%% need to extract stress strain data
% 'F:\TSRL_Grad\Tests\', 'F:\TSRL_230524\Tests\','F:\Chp2\', 'F:\Chp1\', 'F:\TSRL_Grad2\Tests\'
base_dir = 'F:\TSRL_Grad2\Tests\'; %setting the directory of the files to be made %Change
struct_name_save = 'stress_strain_Grad2';
full_half = 'half'; %change
start_char = 21; %change 20 for grad, 22 for 230524 9 for chp2, 9 for chp1 21 for grad2
end_char = 15; %change
file_list = dir([base_dir  '**/*stress_strain_' full_half '.csv']);
file_list = struct2cell(file_list)';
if full_half == 'full'
    mkdir ([base_dir 'Results\CURRENT\IndividualGraphs']);
end

stress_strain_all.(full_half) = struct;

for i = 1:length(file_list)
    name = file_list{i,2};
    name = name(start_char:end-end_char);
    name = replace(name,'.','_');
    front_back = file_list{i,1};
    front_back = front_back(1:end-23);
    name = [front_back '_' name];
    data = readmatrix([file_list{i,2} '\' file_list{i,1}]);
    count = 1;
    for j = 1:2:size(data,2)
        strain(:,count) = data(:,j+1);
        stress(:,count) = data(:,j);
        count = count + 1;
    end
    stress_strain_all.(full_half).(name).strain = strain * -100;
    stress_strain_all.(full_half).(name).stress = stress;
    clear strain stress
end

%%
%base_dir = 'F:\Chp1\'; %setting the directory of the files to be made
%full_half = 'full';
% stress_strain_all_og = load([base_dir 'Results\stress_strain_all.mat']);
names_fields = fieldnames(stress_strain_all.(full_half));
ind = contains(names_fields,["front","back"]);
names_fields(ind == 0) = [];
if full_half == 'full'
    list_exten = {'L','M','R'};
elseif full_half == 'half'
    list_exten = {'TL','BL','TM','BM','TR','BR'};
end
% list_exten = {'TL','L','BL','TM','M','BM','TR','R','BR'};

%Run this one first to determine if you need to manually redo the start
%point of any of the plots
```

```
tiledlayout(7,round(length(names_fields)/6));
for i = 1:length(names_fields)
    nexttile
%     figure
    name_sample = names_fields{i};
    strain_all = stress_strain_all.(full_half).(name_sample).strain;
    stress_all = stress_strain_all.(full_half).(name_sample).stress;
    for j = 1:size(strain_all,2)
        strain = strain_all(:,j);
        stress = stress_all(:,j);
        [stress,strain] = filter_stress_strainv2(strain,stress,0);
        % need to have the first point at (0,0) before we start
        validrows = ~any(isnan(strain),2);
        idx = find(validrows);
        idx = idx(1);
        stress_strain_all.(full_half).(name_sample).strain_realign_all(:,j) = strain_all(:,j) - ...
        strain(idx);
        stress_strain_all.(full_half).(name_sample).stress_realign_all(:,j) = stress_all(:,j) - ...
        stress(idx);
        stress_strain_all.(full_half).(name_sample).strain_realign_all(1:idx,j) = 0;
        stress_strain_all.(full_half).(name_sample).stress_realign_all(1:idx,j) = 0;
        strain = strain - strain(idx);
        stress = stress - stress(idx);
        stress_strain_all.(full_half).(name_sample).strain_filter(:,j) = strain;
        stress_strain_all.(full_half).(name_sample).stress_filter(:,j) = stress;
        plot(strain,stress);
        xlim([0 0.2]);
        hold on;
        title(name_sample)
    end
end
%%
% here you manually arrange the start points of the plots you identify in
% %the plot before

names_correct = {};


names_skip = {};



%full_half = 'full'
names_fields = fieldnames(stress_strain_all.(full_half));
ind = contains(names_fields,["front","back"]);
names_fields(ind == 0) = [];
if full_half == 'full'
    list_exten = {'L','M','R'};
elseif full_half == 'half'
    list_exten = {'TL','BL','TM','BM','TR','BR'};
end
%%
skip = 0; %number of tests to skip (mainly for repeating test)
ResultsT = table;
vis = 0;
for i = skip +1 :length(names_fields)
    name_sample = names_fields{i};
    if contains(name_sample,names_skip)
        continue;
    end
    strain_all = stress_strain_all.(full_half).(name_sample).strain_filter;
    stress_all = stress_strain_all.(full_half).(name_sample).stress_filter;
    for j = 1:size(strain_all,2)
        strain = strain_all(:,j);
        stress = stress_all(:,j);
        %if the sample is the one that needs individual adjustment
        TF = contains(name_sample,names_correct);
        if TF == 1
            prompt = convertCharsToStrings(['Do you want to skip altering extensometer, ' ...
            name_sample '_' list_exten{j} ', Y or N? ']);
            skip_exten = input(prompt,"s");
            if skip_exten == 'Y' || skip_exten == 'y'
                %do nothing
            else
```

```
                %do something
                [stress,strain,stress_adjust,strain_adjust] = pick_start(strain,stress);
                stress_strain_all.(full_half).(name_sample).stress_realign_all(:,j) = ...
                stress_strain_all.(full_half).(name_sample).stress_realign_all(:,j) - stress_adjust;
                stress_strain_all.(full_half).(name_sample).strain_realign_all(:,j) = ...
                stress_strain_all.(full_half).(name_sample).strain_realign_all(:,j) - strain_adjust;
                stress_strain_all.(full_half).(name_sample).strain_filter(:,j) = strain;
                stress_strain_all.(full_half).(name_sample).stress_filter(:,j) = stress;
            end
        end

        %calculating an initial estimate for modulus
        [mod,r2,eq] = point2_modv2(strain,stress,vis);
        x_intercept = -(eq(0))/(mod/100);
        count = 1;
        while x_intercept > 0.001  %if the x_intercept is larger than 0.001 then run again ...
        or if its tried 1000 times to optimise and cant get closer
            if count > 1000
                break
            end
            [stress,strain,stress_adjust,strain_adjust] = realign_start(strain,stress,eq,vis);
            stress_strain_all.(full_half).(name_sample).stress_realign_all(:,j) = ...
            stress_strain_all.(full_half).(name_sample).stress_realign_all(:,j) - stress_adjust;
            stress_strain_all.(full_half).(name_sample).strain_realign_all(:,j) = ...
            stress_strain_all.(full_half).(name_sample).strain_realign_all(:,j) - strain_adjust;
            [mod,r2,eq] = point2_modv2(strain,stress,vis);
            x_intercept = -(eq(0))/(mod/100);
            count = count + 1;
        end

        %save the realignment
        stress_strain_all.(full_half).(name_sample).strain_filter_realign(:,j) = strain;
        stress_strain_all.(full_half).(name_sample).stress_filter_realign(:,j) = stress;

        %calculating the modulus
        [mod,r2,eq] = point2_mod_force0v2(strain,stress,vis);
        intermediate_table = table({[name_sample '_' list_exten{j}]});
        intermediate_table(1,2:3) = {mod, r2}; %copying over the relevant data
        ResultsT = [ResultsT;intermediate_table];
        a = figure;
        plot(strain,stress); hold on;
        ylim([0 max(stress)]); xlim([0 max(strain)]);
        plot(eq);
        xlabel('Strain (%)'); ylabel('Stress (MPa)');
        legend({'Adjusted Data','Linear Fit'});
        hold off
        saveas(a,[base_dir 'Results\CURRENT\IndividualGraphs\' name_sample '_' list_exten{j} ...
        '_' full_half '.fig']);
        saveas(a,[base_dir 'Results\CURRENT\IndividualGraphs\' name_sample '_' list_exten{j} ...
        '_' full_half '.png']);
        close(a);
        clear stress strain
    end
end
close all;
% save the table
writetable(ResultsT,[base_dir 'Results\CURRENT\Summary_Data_MATLAB_' full_half '.xlsx'],'Sheet',1); ...
%writing the information from all the samples
%% save the structure
save([base_dir 'Results\CURRENT\' struct_name_save '.mat'],'-struct','stress_strain_all');...
%do this once youve done half processing too
% writetable(ResultsT,[base_dir 'Results\Summary_Data_matlab.xlsx'],'Sheet',1); ...
%writing the information from all the samples
clear all

function [stress,strain] = filter_stress_strainv2(strain,stress,vis)
    %strain needs to be in percent
    %stress needs to be in MPa
    %removes the data that is below the rebalanacing point
    %removes the data past maximum force

    if nargin == 2
        vis = 0;
    end
```

```

    x = strain;
    y = stress;

    if vis == 1
        figure;
        plot(x,y);
    end

    for i = 1:(length(y)*0.75) %your assuming that it has gone past the initial region or ...
    rebalancing once its 75% of the way through the test but hasnt failed yet.
        test(i,1) = abs(y(i+1)/y(i));
    end
    [~,idx] = min(test);
    idx = idx +1; %the index of the start of the rebalancing
    x(1:idx) = NaN; %making everything before the rebalancing NaN
    y(1:idx) = NaN; %making everything before the rebalancing NaN

    %removing less than or equal to 0 stress. This is after everything
    %before the reset is NaNd
    correction = y <= 0;
    corr_vals = find(correction);
    idx = min(corr_vals);
    if idx < (length(y)*0.1)
        x(1:idx) = NaN; %removing everything before the last value that is NaN
        y(1:idx) = NaN;
    end

    corr_vals = flip(corr_vals); %flipping the idx so we can start from the highest number to set NaN

    for k = 1:length(corr_vals)
        x(corr_vals(k)) = NaN;
        y(corr_vals(k)) = NaN;
    end

    if vis == 1
        figure;
        plot(x,y)
    end

    %removing 0 strain (apart from the first)
    idx = find(~isnan(x),1); %find the first non NaN variable
    idx = [idx:idx+10]'; %any zeros in the first 10 numbers are to be ignored
    correction = x == 0;
    corr_vals = find(correction);
    for i = 1:length(idx)
        check = idx(i);
        corr_vals(corr_vals == check) = [];
    end %now we have a list of indexs with 0 strain

    for i = 1:length(corr_vals)
        check = corr_vals(i);
        x(check) = NaN;
        y(check) = NaN;
    end

    [~,idx] = max(y); %making everything the same length as the original matrix
    x(idx+1:end) = NaN;
    y(idx+1:end) = NaN;

    if vis == 1
        figure;
        plot(x,y)
    end

%     % cleaning up the data to remove an NaNs
%     validrows = ~any(isnan(x),2);
%     strain = x(validrows);
%     stress = y(validrows);
    strain = x;
    stress = y;
end

function [stress,strain,stress_adjust,strain_adjust] = pick_start(strain,stress)
```

```
    figure;
    h = plot(strain,stress);
    info = 'click on the datatips button and select the point you want to reset the start to';
    disp(info)
    blank = input('Press enter to continue once done ');
    dt = findobj(h,'Type','datatip');
    stress_adjust = dt.Y;
    strain_adjust = dt.X;
    strain = strain - dt.X;
    stress = stress - dt.Y;
    check = strain==0;
    idx = find(check);
    strain(1:idx-1) = NaN;
    stress(1:idx-1) = NaN;
end

function [mod,r2,eq] = point2_modv2(strain,stress,vis)
    %strain needs to be in percent
    %stress needs to be in MPa
    %mod = modulus
    %r2 = rsquared of fit
    %line = equation of line that describes the linear portion

    if nargin == 2
        vis = 0;
    end

    % cleaning up the data to remove an NaNs
    validrows = ~any(isnan(strain),2);
    strain = strain(validrows);
    stress = stress(validrows);

    %removing the point past yield
    check = strain(:,:)<=(0.2);
    idx = find(check == 0,1,'first');% finding the first instance of greater than 0.2
    strain(idx:end) = [];
    stress(idx:end) = [];

    %plotting stress strain graph
    if vis == 1
        figure; scatter(strain,stress);
    end

    ft1 = fittype('a*x+b'); %
    [p,gof] = fit(strain,stress,ft1,'StartPoint',[0.1 0]);
    coeffvals = coeffvalues(p);
    mod = coeffvals(1)*100;
    r2 = gof.rsquare;
    eq = p;
    if vis == 1
        hold on
        plot(eq);
    end
end

function [mod,r2,eq] = point2_mod_force0v2(strain,stress,vis)
    %strain needs to be in percent
    %stress needs to be in MPa

    if nargin == 2
        vis = 0;
    end

    % cleaning up the data to remove an NaNs
    validrows = ~any(isnan(strain),2);
    strain = strain(validrows);
    stress = stress(validrows);

    %removing the point past yield
    check = strain(:,:)<=(0.2);
    idx = find(check == 0,1,'first');% finding the first instance of greater than 0.2
    strain(idx:end) = [];
    stress(idx:end) = [];

```

```
        %plotting stress strain graph
        if vis == 1
            figure; scatter(strain,stress);
        end

        ft1 = fittype('a*x'); %forcing the polynomial through 0,0
        [p,gof] = fit(strain,stress,ft1,'StartPoint',0.1);
        mod = p(1)*100;
        r2 = gof.rsquare;
        eq = p;
        if vis == 1
            hold on
            plot(eq);
        end
    end

    function [stress,strain,stress_adjust,strain_adjust] = realign_start(strain,stress,eq,vis)
        %strain needs to be in percent
        %stress needs to be in MPa
        %you need to repeat this till the y incercept is less than a value (and
        %then you can force it through 0,0)

        if nargin == 2
            vis = 0;
        end

        leng = length(strain);

        % cleaning up the data to remove an NaNs
        validrows = ~any(isnan(strain),2);
        strain = strain(validrows);
        stress = stress(validrows);

        %finding the point where the straightline intersects with the data
        x2 =[-0.1;0;0.01;0.02;0.03;0.05;(max(strain))];
        y2 = feval(eq,x2);
        [x0,y0,~,~] = intersections(strain,stress,x2,y2,1);
        if vis == 1
            figure; plot(strain,stress);
            hold on
            plot(x2,y2);
        end

        %setting the intersection point as the start
        strain = strain - x0(1);
        stress = stress - y0(1);

        %outputting the adjusting values
        strain_adjust = x0(1);
        stress_adjust = y0(1);

        %making the first point 0
        idx = (strain<0);
        stress(idx==1) = [];
        strain(idx == 1) = [];

        strain = strain - strain(1);
        stress = stress - stress(1);

        %adding nans to the end to make it the same size as original

        strain(end+1:leng,:) = missing;
        stress(end+1:leng,:) = missing;

        %plotting stress strain graph
        if vis == 1
            figure; scatter(strain,stress);
        end
    end
```

Chapter 8

Appendix B

This appendix will focus on the appendices of the second technical chapter, Chapter 4.

8.1 Analysing Height Distortions

```
%import as matrix
%everything is in um
%need to run this twice - pre and post
% base_dir = 'C:\Users\msn1g16\OneDrive\Documents\PhD\Images\Distortion_Calc\';
base_dir = 'C:\Users\msn1g16\OneDrive\Documents\PhD\Images\Distortion_Calc\dis_other\';
save_struct_name = [base_dir 'Distortion_Vals_all.mat'];
pre_post = 'Post';
base_dir = [base_dir pre_post '\'];
file_list = dir([base_dir  '**/*.xyz']); %finds to location of all data files
file_list = struct2cell(file_list)';
% distortion_info = struct;
T = table;
info_table = load('C:\Users\msn1g16\OneDrive\Documents\PhD\Images\Distortion_Calc\info_table_post.mat');
struct_name = fieldnames(info_table.info_table_post);

resave = 1;
%%
for i = 1:length(file_list) %repeat for for all the files in the directory
    data = load([file_list{i,2} '\' file_list{i,1}]); %loading the data of the first file
    %calculating the pixel size in y
    [C,ia,ic] = unique(data(:,1),'stable'); %sorting to the find all the same values in x
    for j = 1:length(C)
        idx = (ic == j);
        y_temp = sort(data(idx,2));
        if size(y_temp,1) < 2
            continue
        end
        for k = 1:length(y_temp)-1
            pix_y_temp(k,1) = y_temp(k) - y_temp(k+1);
        end
        pix_size_y(j,1) = mode(pix_y_temp);
    end
    pix_size_y = abs(mode(pix_size_y));
    %calculating the pixel size in x
    [C,ia,ic] = unique(data(:,2),'stable'); %sorting to the find all the same values in y
    for j = 1:length(C)
        idx = (ic == j);
        x_temp = sort(data(idx,1));
        if size(x_temp,1) < 2
            continue
        end
        for k = 1:length(x_temp)-1
            pix_x_temp(k,1) = x_temp(k) - x_temp(k+1);
        end
```

```
            pix_size_x(j,1) = mode(pix_x_temp);
        end
        pix_size_x = abs(mode(pix_size_x));

        pix_size = pix_size_x * pix_size_y;

        %now we can starting processing the data
        %some of the data is stored in um in which we need to divide by 1000 to
        %convert to mm, otherwise its stored as m in which case we need to
        %multiply by 1000
        if (max(data(:,1)) - (min(data(:,1)))) > 2000
            dis_data = data./1000; %working in mm
            pix_size = pix_size/(1000^2);
        else
            dis_data = data.*1000;
            pix_size = pix_size * 1000^2;
        end
        sample_name = file_list{i,1};
        sample_name = sample_name(1:end-4); %change number 9 depending on the name of your folder

        idx_1 = matches(info_table.(struct_name{1}).Name(:),sample_name);

        %removing data above and below min and max as decided by the user - moi
        %code below makes it user defined
        prompt = convertCharsToStrings(['What is the min height distortion of the sample in mm ...
        , ' sample_name '? ']);
        min_dis = input(prompt);
        prompt = convertCharsToStrings(['What is the max height distortion of the sample in mm ...
        , ' sample_name '? ']);
        max_dis = input(prompt);
        % min_dis = info_table.(struct_name{1}).Min(idx_1);
        % max_dis = info_table.(struct_name{1}).Max(idx_1);

        idx = (dis_data(:,3) > max_dis); %removing data above the max height distortion
        dis_data(idx,:) = [];
        idx = (dis_data(:,3) < min_dis); %removing data below the max height distortion
        dis_data(idx,:) = [];
        %removing edge data (0.5 mm from each edge)
        idx = (dis_data(:,1) > (max(dis_data(:,1))-0.5));
        dis_data(idx,:) = [];
        idx = (dis_data(:,1) < (min(dis_data(:,1))+0.5));
        dis_data(idx,:) = [];

        idx = (dis_data(:,2) > (max(dis_data(:,2))-0.5));
        dis_data(idx,:) = [];
        idx = (dis_data(:,2) < (min(dis_data(:,2))+0.5));
        dis_data(idx,:) = [];
        z_alt(:,1) = dis_data(:,3) - min(dis_data(:,3));

        if resave == 1
            % prompt = convertCharsToStrings(['Rotation angle clockwise for ' sample_name '? If no ...
            rotation is required write 0. ']);
            % theta = input(prompt);
            theta = info_table.(struct_name{1}).Rot(idx_1);
            theta = deg2rad(-theta);
            x_rot = dis_data(:,1)*cos(theta) - dis_data(:,2)*sin(theta);
            y_rot = dis_data(:,1)*sin(theta) + dis_data(:,2)*cos(theta);
            z_rot = dis_data(:,3);

            %will need to flip all LR
            figure;
            scatter3(-x_rot,y_rot,z_rot,5,z_rot,'filled') %LR flipped
            grid off
            c = hsv;
            c = flipud(c);
            colormap(c)
            colorbar
            view(2)
            axis off
            graphname = [base_dir 'HeightMaps\Original\' sample_name];
            saveas(gcf,graphname,'fig');
            saveas(gcf,graphname,'png');

            figure;
```

```
            scatter3(-x_rot,y_rot,z_alt,5,z_alt,'filled') %LR flipped
            grid off
            c = hsv;
            c = flipud(c);
            colormap(c)
            colorbar
            view(2)
            axis off
            graphname = [base_dir '\HeightMaps\Adjusted\' sample_name];
            saveas(gcf,graphname,'fig');
            saveas(gcf,graphname,'png');
            close all
        end

        as_design_relden = info_table.(struct_name{1}).("As Des")(idx_1);
        as_built_relden = info_table.(struct_name{1}).("As Built"){idx_1};
        T.Var1{i} = (sample_name); %name
        T{i,2} = as_design_relden; %as-designed relative density
        T{i,3} = as_built_relden; %as-built relative density
        T{i,4} = max(z_alt); %max distortion
        T{i,5} = mean(z_alt); %total average distortion per mm2
        %fitting a plane to the data
        f1 = fit([dis_data(:,1),dis_data(:,2)],z_alt,'poly11');
        z_vals_plane = feval(f1,dis_data(:,1),dis_data(:,2));
        Sa = sum(abs(z_alt - z_vals_plane));
        T{i,6} = Sa; %Sa from ISO 25178 2:2022
        clear data pix_size pix_size_y pix_size_x pix_x_temp pix_y_temp z_vals_plane ...
        z_alt z_rot x_rot x_temp y_rot y_temp Sa sample_name
        clear idx min_dis max_dis theta idx_1
    end
    T.Properties.VariableNames(1) = "Sample";
    T.Properties.VariableNames(2) = "As-Design Rel Den";
    T.Properties.VariableNames(3) = "As-built rel den";
    T.Properties.VariableNames(4) = convertCharsToStrings([pre_post ' Cure Dist']);
    T.Properties.VariableNames(5) = convertCharsToStrings([pre_post ' Cure Dis/mm2']);
    T.Properties.VariableNames(6) = convertCharsToStrings([pre_post ' Sa']);

    distortion_info.(pre_post).av_specimen = T;
    %save(save_struct_name,"distortion_info",'-mat');
    %% summarising the distortion vals
    load('C:\Users\msn1g16\OneDrive\Documents\PhD\Images\Distortion_Calc\Distortion_Vals_all.mat');
    struct_name = fieldnames(distortion_info);
    names_den = load('C:\Users\msn1g16\OneDrive\Documents\PhD\Images\Distortion_Calc\names_den.mat');
    names_den = names_den.names_den;

    for j = 1:length(struct_name)
        data_specimen = distortion_info.(struct_name{j}).av_specimen;

        temp = distortion_info.(struct_name{j}).av_specimen{:,2:end};
        [C,ia,ic] = unique(temp(:,1));
        data = [];
        data2 = {};
        for i = 1:length(C)
            idx = (ic == i);
            temp2 = temp(idx,:);
            temp3 = mean(temp2,1);
            %temp3(:,2) = [];

            temp3(1,end+1) = std(temp2(:,2));
            temp3(1,end+1) = std(temp2(:,3));
            temp3(1,end+1) = std(temp2(:,4));
            temp3(1,end+1) = std(temp2(:,5));

            temp3(1,end+1) = min(temp2(:,3));
            temp3(1,end+1) = max(temp2(:,3));
            temp3(1,end+1) = min(temp2(:,4));
            temp3(1,end+1) = max(temp2(:,4));
            temp3(1,end+1) = min(temp2(:,5));
            temp3(1,end+1) = max(temp2(:,5));
            %temp3 = array2table(temp3);
            data = [data;temp3];
            idx_2 = find(names_den.("Design Rel Den") == (round(temp3(1),4)));
            data2{end+1} = names_den.Name{idx_2};
            clear temp3 temp2
```

```
    end


    data2 = table(data2');
    data = array2table(data);
    data = [data2,data];
    data.Properties.VariableNames(1) = "Sample";
    data.Properties.VariableNames(2) = "As-Design Rel Den";
    data.Properties.VariableNames(3) = "As-Built Rel Den";
    data.Properties.VariableNames(4) = convertCharsToStrings(['Av Dis ' struct_name{j} ' Cure']);
    data.Properties.VariableNames(5) = convertCharsToStrings(['Av Dist/mm2 ' struct_name{j} ' Cure']);
    data.Properties.VariableNames(6) = convertCharsToStrings(['Av Sa ' struct_name{j} ' Cure']);
    data.Properties.VariableNames(7) = "std as-built rel den";
    data.Properties.VariableNames(8) = convertCharsToStrings(['std dis max ' struct_name{j} ' Cure']);
    data.Properties.VariableNames(9) = convertCharsToStrings(['std av dis/mm2 ' struct_name{j} ' Cure']);
    data.Properties.VariableNames(10) = convertCharsToStrings(['std av Sa ' struct_name{j} ' Cure']);
    data.Properties.VariableNames(11) = convertCharsToStrings(['Min max ' struct_name{j} ' Cure']);
    data.Properties.VariableNames(12) = convertCharsToStrings(['Max max ' struct_name{j} ' Cure']);
    data.Properties.VariableNames(13) = convertCharsToStrings(['Min av dis ' struct_name{j} ' ...
    cure /mm2 (mm)']);
    data.Properties.VariableNames(14) = convertCharsToStrings(['Max av dis ' struct_name{j} ' ...
    cure /mm2 (mm)']);
    data.Properties.VariableNames(15) = convertCharsToStrings(['Min av Sa ' struct_name{j} ' Cure']);
    data.Properties.VariableNames(16) = convertCharsToStrings(['Max av Sa ' struct_name{j} ' Cure']);

    distortion_info.(struct_name{j}).av_sample = data;

end
save('C:\Users\msn1g16\OneDrive\Documents\PhD\Images\Distortion_Calc\Distortion_Vals_all.mat', ...
"distortion_info",'-mat')
```

8.2 Applying the Compliance Correction

```
function [F_corr,dis_corr,stress_corr,strain_corr] = correct_compliance(E_pt,E_eq,A,L,F,d_i)

% E_pt is the elastic modulus as calculated with point tracking - we're
%assuming its accurate in MPa
% E_eq is the elastic modulus from the instron/the elastic modulus including
%compliance in MPa- calculated from the instron without the correction
%applied
% A is the cross-sectional area in mm2
% L is the original length of the sample in mm
% F is the force data (from the instron) (in kN)
% d_i is the displacement from the instron machine (in mm)
% d_corr is the corrected displacement from the instron (corrected to
% account for machine compliance
% F_corr is the corrected force from the instron machine - just corrected
% to have everything as 0 we're assuming this is in N
% stress_corr is the zeroed stress from the instron machine - in GPa
% strain_corr is the corrected and zeroed strain from the instron

F_corr = (F - F(1)); %zeroing the force and changing to SI units
d_i_corr = (d_i - d_i(1)); %zeroing the displacment and changing to SI units
E_pt = E_pt / 1000; %in GPa
E_eq = E_eq / 1000; %in GPa
% k_pt = (E_pt*A)/L;
% k_eq = (E_eq*A)/L;
% k_L = 1/((1/k_eq)-(1/k_pt));

dis_corr = d_i_corr - (((F.*L)/A).*((E_pt-E_eq)/(E_pt * E_eq)));
dis_corr = dis_corr - dis_corr(1);

stress_corr = (F_corr/A);
strain_corr = dis_corr/L;
end
```

Chapter 9

Appendix C

This appendix will focus on the appendices of the third technical chapter, Chapter 5.

9.1 Using Voronoi Cells to Create Stochastic Lattices

The following code is adapted from the thesis of Aranguren van Egdmond [1]

```
%% SIMPLE SEQUENTIAL INHIBITION PROCESS%%
% Source: After Martinez and Martinez, Ref. [125]
% Description: Provides pseudo-random dispersion of Voronoi seed points according to input parameters
% (desired regularity), A (basal area), and n (desired number of cells)
% taken from the thesis of Derek Alexandre Aranguren van Egmond.
% https://www.proquest.com/docview/2140317200?%20Theses&fromopenview= ...
true&parentSessionId=IoVha00uZE3P32mRA1E8jbKyrUS0jfjJPmMToCaJXw8%3D&pq-origsite=gscholar&sourcetype= ...
Dissertations%20&parentSessionId=f5OHGHiyt2yrqXClDPTtIIsc2KGhpUrFph1BV9FrnEc%3D
%%
%For 30x30 surface, with n=100 seeds, delta = s/r = 0.8 (optimal disorder
%paramter as in the hamilton paper
% tiledlayout(2,4);
% for ratio = 0.1:0.1:0.8
% format short
clear all; %clearing the work space
L = 3; %unit cell size
d = 0.3:0.01:1.0; %all the possible strut diams
rho_r = ((1+ 4*sqrt(3))*(pi()/4)*(d/L).^2)-((11*pi()/6)*((d/L).^3)); %calculating the relative ...
density for BCCz
rho_r_adjusted = (1.05.*(rho_r))+0.12; %adjusted for as-built rel den
% rho_r = sqrt(3)*pi()*((d/L).^2); %BCC
% rho_r_adjusted = -0.49.*(rho_r.^2) + 1.06*rho_r + 0.09;
max_rel = 0.72;
min_rel = 0.17;
target_rel = 0.4;

mean_rel_del = 0.45; %setting an initial value for the mean relative density

while mean_rel_del>(target_rel+0.01) || mean_rel_del<(target_rel-0.01)
    ratio = 0.4; %desired delta value
    n = 100; %No. of cells
    A = 30*30; %Basal area
    r = sqrt((2*A)/(sqrt(3)*n));
    s = ratio*r;
    % Generate the vertices for the regions - UNITS IN mm!
    rx = [0 30 30 0 0];
    ry = [0 0 30 30 0];
    X = zeros(n,2);
    %Generate the first event:
    X(1,:) = csbinproc(rx,ry,1); %csbinproc returns a 2D Poisson distribution
    i = 1;
```

```matlab
        %Generate the other events:
        while i<n
            [sx, sy] = csbinproc(rx,ry,1);
            xt = [sx, sy ; X(1:i,:)];

            %Find distance between the events:
            dist = pdist(xt);

            %Find distance between candidate event and others that have been
            %generated already
            ind = find(dist(1:i) <= s);
            if isempty(ind)
                %We keep the event:
                i = i+1;
                X(i,:) = [sx, sy];
            end
        end
        X_zeros = [X zeros(size(X,1),1)];
        %Verify that all are no closer than inhibition distance:
        dist = pdist(X);
        delhat = min(dist);
        %plot the results:
        xx = X(:, 1);
        yy = X(:, 2);
        % nexttile;
        % scatter(xx,yy,'.');
        % title(num2str(ratio));

        %% Jakob Sievers (2024). VoronoiLimit(varargin) ...
        (https://www.mathworks.com/matlabcentral/fileexchange/34428-voronoilimit-varargin), ...
        MATLAB Central File Exchange. Retrieved December 4, 2024.
        addpath 'C:\Users\msn1g16\OneDrive\Documents\PhD\Other MATLAB\VoronoiLimit.m';...
        %this bounds the voronoi cells to the size of the lattice


        bs_ext=[0 30 30 0;0 0 30 30]';
        [V,r,XY]=VoronoiLimit(xx,yy,'bs_ext',bs_ext,'figure','off');
        % [vx,vy] = voronoi(xx,yy);
        % DT = delaunayTriangulation(xx,yy);
        % [V,r] = voronoiDiagram(DT);


        area_voronoi = [];
        for i = 1:length(r)
            vertex_nums = r{i};
            x_vals = [];
            y_vals = [];
            for j = 1:length(vertex_nums)
                x_vals = [x_vals; V(vertex_nums(j),1)];
                y_vals = [y_vals; V(vertex_nums(j),2)];
            end
            area_voronoi = [area_voronoi;polyarea(x_vals,y_vals)];
        end

        area_rel_conv = (max_rel-min_rel)/(max(area_voronoi) - min(area_voronoi));
        rel_den_voronoi = ((area_voronoi-(min(area_voronoi))).*area_rel_conv)+ min_rel;

        rel_den_voronoi_corrected = [];
        diams_voronoi_corrected = [];
        for i = 1:length(rel_den_voronoi)
            temp = abs(rho_r_adjusted - rel_den_voronoi(i));
            [~,idx] = min(temp);
            rel_den_voronoi_corrected = [rel_den_voronoi_corrected; rho_r_adjusted(idx)];
            diams_voronoi_corrected = [diams_voronoi_corrected; d(idx)];
        end
        mean_rel_del = mean(rel_den_voronoi_corrected)
    end
    mean_rel_del


    %% Summary
    % This is a script to make a combined unit cell structure given the unit
    % cell type, strut diameter and location of unit cell. The whole thing
    % should only take 20 seconds including the user input re stl file name
```

```
% clear all; close all
addpath 'C:\Users\msn1g16\OneDrive\Documents\PhD\Other MATLAB\GIBBON_functions';
addpath 'C:\Users\msn1g16\OneDrive\Documents\PhD\Other MATLAB\stlwrite';

%% Setting up the variables to describe your unit cells
num_layers = 10; %number of unit cells in the z direction
num_rows = 10; %number of unit cells in the y direction
num_columns = 10; %number of unit cells in the x direction

dim_z = 3.00; %dimension of unit cell in mm in z direction
dim_y = 3.00; %dimension of unit cell in mm in y direction
dim_x = 3.00; %dimension of unit cell in mm in x direction

err_val = 100; %radius is divided by this to determine the acceptable error
% when drawing the circles for the cylinder.

unit_type = "BCCz"; %unit cell type
diameters = diams_voronoi_corrected;

%% Visualisation and STL variables
vis = 0; %on/off (1/0) variable to visualise your structure
name = 'Grad_Voronoi_Random_BCCz_0.4disorder'; %name you want to give your stl file
base_dir ='C:/Users/msn1g16/OneDrive/Documents/PhD/Other MATLAB/STL files'; ...
%base directory that you're saving your STL in

%% Creating a the structure with a set diameter
Volume = struct; % create a structure to put the relavant information in.
letter = ["A","B","C","D","E","F","G","H","I","J","K","L","M","N","O","P","Q","R","S","T","U",...
"V","W","X","Y","Z"]; %begining name of the layer. Will use notation like a chessboard
g = 0; %counting variable for the layer
for i = 1:num_layers
    h = 0; %counting variable for the y coordinates
    rand_int = randi([1 100], 10,10);
    for j = 1:num_rows
        t = 0; %counting variable for the x coordinates
        for k = 1:num_columns
            Volume.("L"+i).(letter(j)+k).coordinate = [t,h,g]; ...
            %coordinate of the top left hand corner of the cube
            Volume.("L"+i).(letter(j)+k).d = diameters(rand_int(j,k));
            Volume.("L"+i).(letter(j)+k).unit_cell = unit_type;
            t = t + dim_x;
        end
        h = h + dim_y;
    end
     g = g + (dim_z*1);
end


%% Initial single unit cell

verts_one = [0 0 0; dim_x 0 0;dim_x dim_y 0;0 dim_y 0;...
    0 0 dim_z;dim_x 0 dim_z;dim_x dim_y dim_z;0 dim_y dim_z;...
    dim_x/2 dim_y/2 dim_z/2]; %initial coordinates of vertices one unit cell
%this is the same for BCC, BCCz and FCCm.

verts_RD_d_octet_one = [0 0 0; dim_x 0 0;dim_x dim_y 0;0 dim_y 0;...
    0 0 dim_z;dim_x 0 dim_z;dim_x dim_y dim_z;0 dim_y dim_z;...
    0 dim_y/2 dim_z/2;dim_x/2 dim_y dim_z/2;dim_x dim_y/2 dim_z/2;dim_x/2 0 dim_z/2;...
    dim_x/2 dim_y/2 0;dim_x/2 dim_y/2 dim_z;...
    dim_x/4 dim_y/4 dim_z/4; dim_x*0.75 dim_y/4 dim_z/4; dim_x*0.75 dim_y*0.75 dim_z/4;dim_x/4 ...
    dim_y*0.75 dim_z/4;...
    dim_x/4 dim_y/4 dim_z*0.75; dim_x*0.75 dim_y/4 dim_z*0.75; dim_x*0.75 dim_y*0.75 ...
    dim_z*0.75; dim_x/4 dim_y*0.75 dim_z*0.75];
%the vertices list for RD and diamond unit cells

%BCC
segments_BCC_one = [1 9; 2 9; 3 9; 4 9; 5 9; 6 9; 7 9; 8 9]; ...
%joining of vertices to create BCC cell

%BCCz
segments_BCCz_one = [1 9; 2 9; 3 9; 4 9; 5 9; 6 9; 7 9; 8 9; 1 5; 2 6; 3 7; 4 8]; ...
%joining of vertices to create BCCz cell

%FCCm
```

```
segments_FCCm_one = [ 1 6; 2 5; 2 7; 3 6; 4 7; 3 8; 4 5; 1 8];

%RD
segments_RD_one = [1 15; 2 16;3 17;4 18;13 15;13 16;13 17;13 18;9 15;9 19;9 22;9 18;...
    10 18;10 17;10 21;10 22;11 16;11 17;11 20;11 21;12 15;12 16;12 19;12 20;...
    14 19;14 20;14 21;14 22;5 19;6 20;7 21;8 22];

%Diamond
segments_diamond_one = [2 16;4 18;13 16;13 18;...
    9 18;9 19;10 18;10 21;11 21;11 16;12 16;12 19;...
    5 19;7 21;14 19;14 21];

%Octet
segments_octet_one = [1 6; 2 5; 2 7; 3 6; 4 7; 3 8; 4 5; 1 8;...
    5 7; 6 8;  1 3; 2 4;...
    9 10; 10 11; 11 12; 12 9;...
    14 9; 9 13; 13 11; 11 13;
    14 10; 10 13; 13 12; 12 14];

%% Initialising changing variables

verts_new = []; %matrix that will be changed throughout loop to reflect the correct unit cell. ...
Its quicker to preassign variables and then change
line_num = 1; %number of lines (used for the structures)

%% Initialising more variables to make all the unit cells

unit_struct = struct; %initialising structure to keep track of all the vertices and faces

%% Plotting the cylinders for all the unit cells
for i = 1:num_layers %repeating for all unit cells in x direction (layers)
    for j = 1:num_rows %(number of rows)
        for k = 1:num_columns %(number of columns)
            if Volume.("L"+i).(letter(j)+k).unit_cell== "RD" || Volume.("L"+i).(letter(j)+k).unit_cell ... ==
            "Diamond" || Volume.("L"+i).(letter(j)+k).unit_cell == "Octet"
                verts_one = verts_RD_d_octet_one;
            end
            verts_new(:,1) = verts_one(:,1)+(Volume.("L"+i).(letter(j)+k).coordinate(1)); ...
            %new vertex coordinates x
            verts_new(:,2) = verts_one(:,2)+(Volume.("L"+i).(letter(j)+k).coordinate(2)); ...
            %new vertex coordinates y
            verts_new(:,3) = verts_one(:,3)+(Volume.("L"+i).(letter(j)+k).coordinate(3)); ...
            %new vertex coordinates z
            if Volume.("L"+i).(letter(j)+k).unit_cell=="BCC"
                segments_unit_cell = segments_BCC_one;
            elseif Volume.("L"+i).(letter(j)+k).unit_cell=="BCCz"
                segments_unit_cell = segments_BCCz_one;
            elseif Volume.("L"+i).(letter(j)+k).unit_cell=="FCCm"
                segments_unit_cell = segments_FCCm_one;
            elseif Volume.("L"+i).(letter(j)+k).unit_cell=="RD"
                segments_unit_cell = segments_RD_one;
            elseif Volume.("L"+i).(letter(j)+k).unit_cell=="Diamond"
                segments_unit_cell = segments_diamond_one;
            elseif Volume.("L"+i).(letter(j)+k).unit_cell=="Octet"
                segments_unit_cell = segments_octet_one;
            end
            seg_num = size(segments_unit_cell,1); %number of line segements
            %things that stay the same during the loop
            radius = (Volume.("L"+i).(letter(j)+k).d)/2; %radius of struts in unit cell
            e = radius/err_val; %error that is acceptable
            th = acos(2*(1-e/radius)^2 -1);
            num_verts = ceil(2*pi()/th); %number of vertices required to define the circle
            [V_cyl_initial,F_cyl]=cylinder_meshv2(radius,num_verts,'Caps',true);...
            %Unit cylinder with caps and the required radius
            %The cylinder_mesh is the only thing that is required from
            %gptoolbox TODO try and find a way not to use the toolbox as
            %its a pain to install
            for a = 1:seg_num %repeating for each line segment
                un = segments_unit_cell(a,1); deux = segments_unit_cell(a,2); %vertex numbers to refer to
                P1 = verts_new(un,:); P2 = verts_new(deux,:); %coordinates of vertices
                % Find the rotation matrix between a straight line and the real line
                d = diff([P1;P2]);
                height = sum(sqrt(sum(d.*d,2)))+(1.5*radius); ...
                %length of the line which is the height of the cylinders
```

```
                V_cyl = V_cyl_initial;
                V_cyl(:,3) = height * V_cyl(:,3); %scaling to get the correct height
                [M]=rigidTransformationMatrixDirect([0 0 0;0 0 height],[P1;P2]); ...
                %calculating the transformation matrix (translation and rotation)
                V_cyl = tform((M),V_cyl); %Rotate vertices with rotation matrix
                unit_struct.faces.("line"+line_num) = F_cyl; %saving faces to structure for each line
                unit_struct.vertices.("line"+line_num) = V_cyl; ...
                %saving vertices to structure for each line
                line_num = line_num + 1;
            end
            values_faces = struct2cell(unit_struct.faces); %extracting the faces
            values_vertices = struct2cell(unit_struct.vertices); %extracting the vertices
            [Volume.("L"+i).(letter(j)+k).faces,Volume.("L"+i).(letter(j)+k).vertices]=...
            joinElementSets(values_faces,values_vertices);%combining faces and vertices
            unit_struct = struct; %reinitialising the variable
        end
    end
end

%% Collating all the vertices and faces
All_Vertices = {};
All_Faces = {};

for i = 1:num_layers %number of layers (L1, L2, L3, ... etc)
    for j = 1:num_rows %y coordinates (A, B, C, ... etc)
        for k = 1:num_columns %rows (A1, A2, A3, ... etc)
            All_Vertices{end+1,1} = Volume.("L"+i).(letter(j)+k).vertices;
            All_Faces{end+1,1} = Volume.("L"+i).(letter(j)+k).faces;
        end
    end
end

[All_Faces,All_Vertices]=joinElementSets(All_Faces,All_Vertices);%combining faces and vertices

if vis == 1
    cFigure; gpatch(All_Faces,All_Vertices);
    view(3); axis equal
end

%% Saving the STL file (ca c'est plus vite que GIBBON)
filename = [base_dir '/' name '.stl'];
if isfile(filename)
    disp(['The file already exists. You will be given an option to rename the file,'...
          'overwrite the file or exit the process']) % File exists.
    rename_opt = input('Do you want to rename the file? Y/N, ','s');
    if rename_opt == 'Y'
        name = input('New stl filename is: ','s'); %renaming the file
        filename = [base_dir '/' name '.stl'];
    elseif rename_opt == 'N'
        overwrite = input('Do you want to overwrite the current file? Y/N, ','s');
        if overwrite == 'Y'
            %do nothing as the file will automatically be rewritten if you
            %proceed as normal
        elseif overwrite == 'N'
            exit_opt = input('You will now exit the script, press enter to continue','s'); ...
            %exiting the script
            return;
        end
    end
else
    disp('The file does not exist so proceed as normal')% File does not exist.
end

stlwrite(filename,All_Faces,All_Vertices); %saving the file

%% Post processing
% There isn't much post processing that needs to be done, just adding the
% flats/end plates in autodesk netfabb.
%1. Add parts and perform automatic simple repair
%2. Move part to platform center
%3. Add box (31 x 31 x 0.2) and move to platform center
%4. Merge parts
%5. Rotate merge parts 180 deg in Y axis
%6. Add box (31 x 31 x 0.2) and move to platform center
```

```
    %7. Merge parts
    %8. Export as STL
```

Chapter 10

Appendix D

This appendix contains the material data sheets for the Rigid 10K resin used in this project.

formlabs **ENGINEERING RESIN**

Rigid 10K Resin

Resin for Rigid, Strong, Industrial-Grade Prototypes

This highly glass-filled resin is the stiffest material in our engineering portfolio. Choose Rigid 10K Resin for precise industrial parts that need to withstand significant load without bending. Rigid 10K Resin has a smooth matte finish and is highly resistant to heat and chemicals.

Short-run injection molds and inserts

Heat resistant and fluid exposed components, jigs, and fixtures

Simulates stiffness of glass and fiber-filled thermoplastics

Aerodynamic test models

(V1) **FLRG1001** (V1.1) **FLRG1011**

Prepared 10/07/2020

Rev. 06 26/06/2024

Material Properties	METRIC				METHOD
	Green	**Post-Cured** for 60 min at 70 °C[1]	**Post-Cured** for 60 min at 70 °C and 125 min at 90 °C[2]	**Post-Cured** for 60 min at 70 °C and Media Blasted	
Tensile Properties	METRIC				METHOD
Ultimate Tensile Strength	55 MPa	65 MPa	53 MPa	88 MPa	ASTM D638-14
Tensile Modulus	7.5 GPa	10 GPa		11 GPa	ASTM D638-14
Elongation at Break	2%	1%		1.7%	ASTM D638-14
Flexural Properties	METRIC				METHOD
Flexural Strength	84 MPa	126 MPa	103 MPa	158 MPa	ASTM D790-15
Flexural Modulus	6 GPa	9 GPa	10 GPa	9.9 GPa	ASTM D790-15
Impact Properties	METRIC				METHOD
Notched Izod	16 J/m	16 J/m	18 J/m	20 J/m	ASTM D256-10
Unnotched Izod	41 J/m	47 J/m	41 J/m	130 J/m	ASTM D4812-11
Thermal Properties	METRIC				METHOD
Heat Deflection Temp. @ 0.45 MPa	65 °C	163 °C	218 °C	238 °C	ASTM D648-16
Heat Deflection Temp. @ 1.8 MPa	56 °C	82 °C	110 °C	92 °C	ASTM D648-16
Thermal Expansion, 0-150 °C	48 μm/m/°C	47 μm/m/°C	46 μm/m/°C	41 μm/m/°C	ASTM E831-13

Material Properties	IMPERIAL				METHOD
	Green	**Post-Cured for 60 min at 70 °C**[1]	**Post-Cured** for 60 min at 70 °C and 125 min at 90 °C[2]	**Post-Cured** for 60 min at 70 °C and Media Blasted	
Tensile Properties	IMPERIAL				METHOD
Ultimate Tensile Strength	7980 psi	9460 psi	7710 psi	12700 psi	ASTM D638-14
Tensile Modulus	1090 ksi	1480 ksi	1460 ksi	1600 ksi	ASTM D638-14
Elongation at Break	2%	1%		1.70%	ASTM D638-14
Flexural Properties	IMPERIAL				METHOD
Flexural Strength	12200 psi	18200 psi	15000 psi	22900 psi	ASTM D790-15
Flexural Modulus	905 ksi	1360 ksi	1500 ksi	1440 ksi	ASTM D790-15
Impact Properties	IMPERIAL				METHOD
Notched Izod	0.3 ft-lb/in			0.37 ft-lb/in	ASTM D256-10
Unnotched Izod	0.8 ft-lb/in	0.9 ft-lb/in	0.7 ft-lb/in	2.5 ft-lb/in	ASTM D4812-11
Thermal Properties	IMPERIAL				METHOD
Heat Deflection Temp. @ 0.45 MPa	149 °F	325 °F	424 °F	460 °F	ASTM D648-16
Heat Deflection Temp. @ 1.8 MPa	133 °F	180 °F	230 °F	198 °F	ASTM D648-16
Thermal Expansion, 0-150 °C	27 μin/in/°F	26 μin/in/°F	26 μin/in/°F	23 μin/in/°F	ASTM E831-13

ELECTRICAL CHARACTERIZATION

Property	Frequency	Value	Standard
Dielectric Constant (D_k)	1 GHz	3.4	ASTM D150-22
Dielectric Constant (D_k)	10 GHz	3.3	ASTM D2520-21
Loss Tangent (D_f)	1 GHz	0.036	ASTM D150-22
Loss Tangent (D_f)	10 GHz	0.0074	ASTM D2520-21
Volume Resistivity	-	1.1 x 10^{15} Ω•cm	ASTM D257-14
Surface Resistivity	-	6.9 x 10^{13} Ω	ASTM D257-14
Dielectric Strength	-	458 V/mil	ASTM D149-20

TOXIC GAS GENERATION

Testing Standard BSS 7239 (comparable to NFPA No. 258)	Maximum allowed concentration per BSS 7239 (ppm)	Flaming Mode (ppm)	Non-Flaming Mode (ppm)
Hydrogen Cyanide (HCN)	150	1	0.5
Carbon Monoxide (CO)	3500	50	10
Nitrous Oxides (NOx)	100	< 2	
Sulfur Dioxide (SO2)	100	< 1	
Hydrogen Fluoride (HF)	200	< 1.5	
Hydrogen Chloride (HCl)	500	1	< 1

SMOKE DENSITY

SPECIFIC OPTICAL DENSITY

Testing Standard	@ 90 sec	@ 4 min	Maximum
ASTM E662 Flaming Mode	2	95	132
ASTM E662 Non-Flaming Mode	0	1	63

FLAMMABILITY

Testing Standard	Rating
UL 94 Section 7 (3 mm)	HB

SOLVENT COMPATIBILITY

Percent weight gain over 24 hours for a printed and post-cured 1 x 1 x 1 cm cube immersed in respective solvent:

Solvent	24 hr weight gain, %	Solvent	24 hr weight gain, %
Acetic Acid 5%	< 0.1	Isooctane (aka gasoline)	0
Acetone	< 0.1	Mineral oil (light)	0.2
Isopropyl Alcohol	< 0.1	Mineral oil (Heavy)	< 0.1
Bleach ~5% NaOCl	0.1	Salt Water (3.5% NaCl)	0.1
Butyl Acetate	0.1	Sodium Hydroxide solution (0.025% PH 10)	0.1
Diesel Fuel	0.1	Water	< 0.1
Diethyl glycol Monomethyl Ether	0.4	Xylene	< 0.1
Hydraulic Oil	0.2	Strong Acid (HCl conc)	0.2
Skydrol 5	0.6	Tripropylene glycol monomethyl ether	0.4
Hydrogen peroxide (3%)	< 0.1		

All testing specimens were printed using Form 3.

[1] Data was obtained from parts printed using Form 3, 100 µm and post-cured with a Form Cure for 60 minutes at 70 °C.

[2] Data was obtained from parts printed using Form 3, 100 µm and post-cured with a Form Cure for 60 minutes at 70 °C and an additional thermal cure at 90 °C for 125 minutes.

Safety Data Sheet

According to Regulation (EC) No. 1272/2008 (CLP) and (EC) No. 1907/2006 (REACH)

Initial preparation date: 2020.08.05

Rigid 10K Resin

SECTION 1: Identification of the substance/mixture and of the company/undertaking

1.1 Product identifier

Product Name: Rigid 10K Resin

Product code: FLRG1001

1.2 Relevant identified uses of the substance or mixture and uses advised against

Relevant identified uses: For use in Formlabs SLA Printers

Uses advised against: Not determined or not applicable.

Reasons why uses advised against: Not determined or not applicable.

1.3 Details of the manufacturer/supplier of the safety data sheet

Manufacturer:	**Supplier:**
United States	**Germany**
Formlabs, Inc	Formlabs GmbH
35 Medford St	Nalepastr. 18
Suite 201 Somerville, MA 02143	12459 Berlin
+1 617 855 0762	+49 30 555 795 880
sds@formlabs.com	

1.4 Emergency telephone number:

1-800-424-9300 (24/7)

SECTION 2: Hazard(s) identification

2.1 Classification of the substance or mixture:

Classification according to Regulation (EC) No. 1272/2008 (CLP):

Skin sensitization, category 1
Chronic aquatic hazard, category 2

Hazard-determining components of labeling:

Urethane Dimethacrylate
Isobornyl Methacrylate

Additional Information: None

2.2 Label elements

Labelling according to Regulation (EC) No 1272/2008 (CLP)

Hazard pictograms:

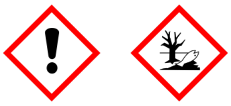

Signal word: Warning

Hazard statements:

H317 May cause an allergic skin reaction
H411 Toxic to aquatic life with long lasting effects

Precautionary statements:

P261 Avoid breathing dust/fume/gas/mist/vapors/spray
P272 Contaminated work clothing should not be allowed out of the workplace
P280 Wear protective gloves/protective clothing/eye protection/face protection
P273 Avoid release to the environment

P302+P352 IF ON SKIN: Wash with plenty of soap and water
P333+P313 If skin irritation or rash occurs: Get medical advice/attention
P363 Wash contaminated clothing before reuse
P391 Collect spillage
P501 Dispose of contents/container in accordance with local/regional/national regulations

2.3 Other hazards: None known

SECTION 3: Composition/information on ingredients

3.1 Substance: Not applicable.

3.2 Mixture:

Identification	**REACH Registration No.**	**Name**	**Classification according to Regulation (EC) No. 1272/2008 (CLP)**	**Weight %**
CAS number: 72869-86-4 EC number: 276-957-5	–	Urethane Dimethacrylate	Skin Sens. 1; H317 Aquatic Chronic 2; H411	15-25
CAS number: 7534-94-3 EC number: 231-403-1	–	Isobornyl Methacrylate	Skin Irrit. 2; H315 STOT SE 3 (RI); H335 Aquatic Chronic 3; H412 Eye Irrit. 2; H319	7-10
CAS number: 7631-86-9 EC number: 231-545-4	–	Filler	Not classified	55-75

Additional information: None
Full Text of H and EUH statements: See section 16

SECTION 4: First aid measures

4.1 Description of first aid measures

General notes:

Show this Safety Data Sheet to the doctor in attendance.

Following inhalation:

If inhaled, remove person to fresh air and place in a position comfortable for breathing. If respiratory symptoms develop or persist, seek medical advice/attention.

Following skin contact:

Wash affected area with plenty of soap and water. Remove contaminated clothing and launder before reuse. If skin irritation develops or persists, seek medical advice/attention.

Following eye contact:

Rinse eyes with plenty of water for several minutes. Remove contact lenses if present and easy to do so. Protect unexposed eye. If symptoms develop or persist, seek medical advice/attention.

Following ingestion:

If swallowed, DO NOT induce vomiting unless told to do so by a physician or poison control center. Rinse mouth with water. Never give anything by mouth to an unconscious person. If spontaneous vomiting occurs, place on the left side with head down to prevent aspiration of liquid into the lungs. If symptoms develop or persist, seek medical advice/attention.

Self-Protection of the first aider:

Not determined or not available.

4.2 Most important symptoms and effects, both acute and delayed

Acute symptoms and effects:

Dermal exposure may cause an allergic skin reaction. Symptoms may include irritation, redness, pain, rash, inflammation, itching, burning and dermatitis.

Delayed symptoms and effects:

Effects are dependent on exposure (dose, concentration, contact time).

4.3 Indication of any immediate medical attention and special treatment needed

Specific treatment:

Not determined or not available.

Notes for the doctor:

Treat symptomatically.

SECTION 5: Firefighting measures

5.1 Extinguishing media

Suitable extinguishing media:

Water mist/fog, carbon dioxide, dry chemical, or alcohol resistant foam.

Unsuitable extinguishing media:

Do not use water jet.

5.2 Special hazards arising from the substance or mixture:

Thermal decomposition may produce irritating/toxic fumes/gases.

5.3 Advice for firefighters

Personal protection equipment:

Not determined or not applicable.

Special precautions:

Avoid contact with skin, eyes, hair and clothing. Do not breathe fumes/gas/mists/aerosols/vapors/dusts. Move containers from fire area if safe to do so. Use water spray/fog for cooling fire exposed containers. Avoid unnecessary run-off of extinguishing media which may cause pollution.

SECTION 6: Accidental release measures

6.1 Personal precautions, protective equipment and emergency procedures:

Evacuate unnecessary personnel. Ventilate area. Extinguish any sources of ignition. Wear recommended personal protective equipment (see Section 8). Avoid contact with skin, eyes and clothing. Avoid breathing mist, vapor, dust, fume and spray. Do not walk through spilled material. Wash thoroughly after handling.

6.2 Environmental precautions:

Prevent further leakage or spillage if safe to do so. Prevent from reaching drains, sewers and waterways. Discharge into the environment must be avoided.

6.3 Methods and material for containment and cleaning up:

Do not touch damaged containers or spilled material unless wearing appropriate personal protective clothing. Stop leak if you can do it without risk. Contain and collect spillage and place in suitable container for future disposal. Dispose of in accordance with all applicable regulations (see Section 13).

6.4 Reference to other sections:

For personal protective equipment see Section 8. For disposal see Section 13.

SECTION 7: Handling and storage

7.1 Precautions for safe handling:

Use appropriate personal protective equipment (see Section 8). Use only with adequate ventilation. Avoid breathing mist/vapor/spray/dust. Do not eat, drink, smoke, or use personal products when handling chemical substances. Avoid contact with skin, eyes and clothing. Wash affected areas thoroughly after handling. Keep away from incompatible materials (See Section 10). Keep containers tightly closed when not in use.

7.2 Conditions for safe storage, including any incompatibilities:

Store in cool, dry, well-ventilated location out of direct sunlight. Keep away from food and beverages. Protect from freezing and physical damage. Store away from heat, open flames and other sources of ignition. Keep container tightly sealed. Store away from incompatible materials (See Section 10).

7.3 Specific end use(s):

Refer to Section 1 (Recommended Use).

SECTION 8: Exposure controls/personal protection

8.1 Control parameters

Only those substances with limit values have been included below.

Occupational Exposure limit values:

No occupational exposure limits noted for the ingredient(s).

Biological limit values:

No biological exposure limits noted for the ingredient(s).

Derived No Effect Level (DNEL):

Not determined or not applicable.

Predicted No Effect Concentration (PNEC):

Not determined or not applicable.

Information on monitoring procedures:

Not determined or not applicable.

8.2 Exposure controls

Appropriate engineering controls:

Emergency eye wash stations and safety showers should be available in the immediate vicinity of use or handling. Provide adequate ventilation to maintain the airborne concentrations of vapor, mists, and/or dusts below the applicable workplace exposure limits, while observing recognized national standards (or equivalent).

Personal protection equipment

Eye and face protection:

Safety glasses or goggles. Use eye protection equipment that has been tested and approved by recognized national standards (or equivalent).

Skin and body protection:

Chemical resistant, impervious gloves approved by the appropriate standards. Gloves must be inspected prior to use. Avoid skin contact with used gloves. Appropriate techniques should be used to remove used gloves and contaminated clothing. Personal protective equipment for the body should be selected based on the task being performed and the risks involved and should be approved by a specialist before handling this product. Ensure that all personal protective equipment is approved by recognized national standards (or equivalent).

Respiratory protection:

If engineering controls do not maintain airborne concentrations below the applicable workplace exposure limits, or to an acceptable level (if exposure limits have not been established), a respirator approved by recognized national standards (or equivalent) must be worn.

General hygienic measures:

When handling chemical products, do not eat, drink or smoke. Wash hands after handling, before breaks, and at the end of the workday. Avoid contact with skin, eyes and clothing. Wash contaminated clothing before reuse. Perform routine housekeeping.

Environmental exposure controls:

Emissions from ventilation or work process equipment should be checked to ensure they comply with the requirements of environmental protection legislation.

Product (substance / mixture) related measures to prevent exposure:	Not determined or not applicable.
Instruction measures to prevent exposure:	Not determined or not applicable.
Organisational measures to prevent exposure:	Not determined or not applicable.
Technical measures to prevent exposure:	Not determined or not applicable.

Risk management measures to control exposure:
Not determined or not applicable.

SECTION 9: Physical and chemical properties

9.1 Information on basic physical and chemical properties

Appearance	White Liquid
Odor	Characteristic acrylate
Odor threshold	Not determined or not available.
pH	Not determined or not available.
Melting point/freezing point	Not determined or not available.
Initial boiling point/range	>100°C
Flash point (closed cup)	>93.5°C
Evaporation rate	Not determined or not available.
Flammability (solid, gas)	Not Flammable
Upper flammability/explosive limit	Not determined or not available.
Lower flammability/explosive limit	Not determined or not available.
Vapor pressure	Not determined or not available.
Vapor density	Not determined or not available.
Density	1.63 g/cm3
Relative density	Not determined or not available.
Solubilities	Not determined or not available.
Partition coefficient (n-octanol/water)	Not determined or not available.
Auto/Self-ignition temperature	Not determined or not available.
Decomposition temperature	Not determined or not available.
Dynamic viscosity	1896 cps @ 25°C; 933 cps @ 35°C
Kinematic viscosity	Not determined or not available.
Explosive properties	Not determined or not available.
Oxidizing properties	Not determined or not available.

9.2 Other information

SECTION 10: Stability and reactivity

10.1 Reactivity:

Not reactive under recommended handling and storage conditions.

10.2 Chemical stability:

Stable under recommended handling and storage conditions.

10.3 Possibility of hazardous reactions:

Hazardous reactions are not anticipated under recommended conditions of handling and storage.

10.4 Conditions to avoid:

Extreme heat, open flames, hot surfaces, sparks, ignition sources and incompatible materials.
Avoid storage >38°C (100°F) and exposure to light/direct sunlight and heat.

10.5 Incompatible materials:

Polymerization initiators, including peroxides, strong oxidizing agents, alcohols, copper, copper alloys, carbon steel, iron, rust, and strong bases.

10.6 Hazardous decomposition products:

Under normal conditions of storage and use, hazardous decomposition products should not be produced.

SECTION 11: Toxicological information

11.1 Information on toxicological effects

Acute toxicity

Assessment: Based on available data, the classification criteria are not met.

Product data: No data available.

Substance data:

Name	Route	Result
Isobornyl Methacrylate	oral	LD50 Rat: >2000 mg/kg
	dermal	LD50 Rabbit: >3000 mg/kg

Skin corrosion/irritation

Assessment: Based on available data, the classification criteria are not met.

Product data:

No data available.

Substance data:

Name	Result
Isobornyl Methacrylate	Causes skin irritation

Serious eye damage/irritation

Assessment: Based on available data, the classification criteria are not met.

Product data:

No data available.

Substance data:

Name	Result
Isobornyl Methacrylate	Causes serious eye irritation

Respiratory or skin sensitization

Assessment:

May cause an allergic skin reaction.

Product data:

No data available.

Substance data:

Name	Result
Urethane Dimethacrylate	May cause an allergic skin reaction.

Carcinogenicity

Assessment: Based on available data, the classification criteria are not met.

Product data: No data available.

Substance data: No data available.

International Agency for Research on Cancer (IARC): None of the ingredients are listed.

National Toxicology Program (NTP): None of the ingredients are listed.

Germ cell mutagenicity

Assessment: Based on available data, the classification criteria are not met.

Product data: No data available.

Substance data: No data available.

Reproductive Toxicity

Assessment: Based on available data, the classification criteria are not met.

Product data:

No data available.

Substance data: No data available.

Specific target organ toxicity (single exposure)

Assessment: Based on available data, the classification criteria are not met.

Product data:

No data available.

Substance data:

Name	Result
Isobornyl Methacrylate	May cause respiratory irritation

Specific target organ toxicity (repeated exposure)

Assessment: Based on available data, the classification criteria are not met.

Product data:

No data available.

Substance data: No data available.

Aspiration toxicity

Assessment: Based on available data, the classification criteria are not met.

Product data:

No data available.

Substance data: No data available.

Information on likely routes of exposure:

No data available.

Symptoms related to the physical, chemical and toxicological characteristics:

No data available.

Other information:

No data available.

SECTION 12: Ecological information

12.1 Toxicity

Acute (short-term) toxicity

Assessment: Based on available data, the classification criteria are not met.

Product data: No data available.

Substance data:

Name	Result
Isobornyl Methacrylate	LC50 Danio rerio: 1.79 mg/L (96 hours)
	EC50 Daphnia magna: 2.57 mg/L (48 hours)

Chronic (long-term) toxicity

Assessment:

Toxic to aquatic life with long lasting effects.

Product data: No data available.

Substance data:

Name	Result
Isobornyl Methacrylate	NOEC Daphnia magna: 0.233 mg/L (21 days)

12.2 Persistence and degradability

Product data: No data available.

Substance data:

Name	**Result**
Urethane Dimethacrylate	This substance is not readily biodegradable.
Isobornyl Methacrylate	Readily biodegradable

12.3 Bioaccumulative potential

Product data: No data available.

Substance data: No data available.

12.4 Mobility in soil

Product data: No data available.

Substance data:

Name	**Result**
Urethane Dimethacrylate	This substance is expected to distribute between the water column and organic soil and sediment particles.

12.5 Results of PBT and vPvB assessment

Product data:

PBT assessment: This product does not contain any substances that are assessed to be a PBT.
vPvB assessment: This product does not contain any substances that are assessed to be a vPvB.

Substance data:

PBT assessment:

Urethane Dimethacrylate	This substance is not PBT.
Isobornyl Methacrylate	This substance in not PBT

vPvB assessment:

Urethane Dimethacrylate	This substance is not vPvB.
Isobornyl Methacrylate	This substance is not vPvB

12.6 Other adverse effects: No data available.

12.7 Hazard to the ozone layer

Assessment: Based on available data, the classification criteria are not met.
Product data: No data available.
Substance data: No data available.

SECTION 13: Disposal considerations

13.1 Waste treatment methods

13.1.1 Product / Packaging disposal:
Do not discharge into public wastewater or surface waters. It is the responsibility of the waste generator to properly characterize all waste materials according to applicable regulatory entities.

Waste codes / waste designations according to LoW: Not determined or not available.

13.1.2 Waste treatment-relevant information: Not determined or not available.

13.1.3 Sewage disposal-relevant information: Not determined or not available.

13.1.4 Other disposal recommendations: Dispose in a safe manner in accordance with local and national regulations. Do not allow the product to be released into the environment.

SECTION 14: Transport information

International Carriage of Dangerous Goods by Road/Rail (ADR/RID)

UN number	UN 3082

UN proper shipping name	Environmentally hazardous liquid, N.O.S. Methacrylate Polymer
UN transport hazard class(es)	9 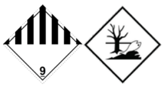
Packing group	III
Environmental hazards	Marine Pollutant
Special precautions for user	None
Additional Information	This product is not regulated as a dangerous good when transported in sizes of < 5L or <5 kg provided the packaging meets the general provisions of 4.1.1.1, 4.1.1.2 and 4.1.1.4 to 4.1.1.8.

International Carriage of Dangerous Goods by Inland Waterways (ADN)

UN number	UN 3082
UN proper shipping name	Environmentally hazardous liquid, N.O.S. Methacrylate Polymer
UN transport hazard class(es)	9 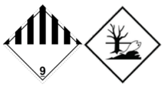
Packing group	III
Environmental hazards	Marine Pollutant
Special precautions for user	None
Additional Information	This product is not regulated as a dangerous good when transported in sizes of < 5L or <5 kg provided the packaging meets the general provisions of 4.1.1.1, 4.1.1.2 and 4.1.1.4 to 4.1.1.8.

International Maritime Dangerous Goods (IMDG)

UN number	UN 3082
UN proper shipping name	Environmentally hazardous liquid, N.O.S. Methacrylate Polymer
UN transport hazard class(es)	9 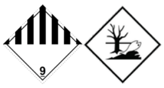
Packing group	III
Environmental hazards	Marine Pollutant
Special precautions for user	None
Additional Information	This product is not regulated as a dangerous good when transported in sizes of < 5L or <5 kg provided the packaging meets the general provisions of 4.1.1.1, 4.1.1.2 and 4.1.1.4 to 4.1.1.8.

International Air Transport Association Dangerous Goods Regulations (IATA-DGR)

UN number	UN 3082
UN proper shipping name	Environmentally hazardous liquid, N.O.S. Methacrylate Polymer
UN transport hazard class(es)	9 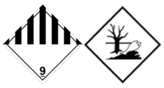
Packing group	III
Environmental hazards	Marine Pollutant
Special precautions for user	None

Additional Information	This product is not regulated as a dangerous good when transported in sizes of ≤ 5L or ≤ 5 kg provided the packaging meets the general provisions of 5.0.2.4.1, 5.0.2.6.1 and 5.0.2.8.

Transport in bulk according to Annex II of MARPOL and the IBC Code	
Bulk Name	None
Ship type	None
Pollution category	None

SECTION 15: Regulatory information

15.1 Safety, health and environmental regulations/legislation specific for the substance or mixture.

European regulations

Inventory listing (EINECS): All ingredients are listed or exempt.

REACH SVHC candidate list: None of the ingredients are listed.

REACH SVHC Authorizations: None of the ingredients are listed.

REACH Restriction: None of the ingredients are listed.

Water hazard class (WGK) (Product):

Water hazard class (WGK) (Substance):

Ingredient Name	CAS	Class
Urethane Dimethacrylate	72869-86-4	Water hazard class 1: slightly hazardous to water
Isobornyl Methacrylate	7534-94-3	Water hazard class 1: slightly hazardous to water

Other regulations

Germany TA Luft: None of the ingredients are listed.

15.2 Chemical Safety Assessment

No Chemical Safety Assessment has been carried out for this substance/mixture by the supplier.

SECTION 16: Other information

Abbreviations and Acronyms: None

Classification procedure:

Classification according to Regulation (EC) No. 1272/2008 (CLP)	Method Used
Skin sensitization, category 1	Calculation method
Chronic aquatic hazard, category 2	Calculation method

Summary of classification(s) in section 3:

Skin Sens. 1	Skin sensitization, category 1
Skin Irrit. 2	Skin irritation, category 2
STOT SE 3 (RI)	Specific target organ toxicity - single exposure, category 3, respiratory tract irritation
Aquatic Chronic 3	Chronic aquatic hazard, category 3
Eye Irrit. 2	Eye Irritation, category 2

Summary of hazard statements in section 3:

H317	May cause an allergic skin reaction
H315	Causes skin irritation
H335	May cause respiratory irritation
H412	Harmful to aquatic life with long lasting effects
H319	Causes serious eye irritation

Disclaimer:

This product has been classified in accordance with EC No. 1272/2008 (CLP) and EC No. 1907/2006 (REACH). The information provided in this SDS is correct, to the best of our knowledge, based on information available. The information given is designed only as a guidance for safe handling, use, storage, transportation and disposal and is not to be considered a warranty or quality specification. The information relates only to the specific material designated and may not be valid for such material used in combination with any other materials, unless specified in the text. The responsibility to provide a safe workplace remains with the user.

Initial preparation date: 2020.08.05

End of Safety Data Sheet